EXOTIC COLLECTIVE EXCITATIONS AT HIGH SPIN:

TRIAXIAL ROTATION AND OCTUPOLE CONDENSATION

A Dissertation

Submitted to the Graduate School

of the University of Notre Dame

in Partial Fulfillment of the Requirements

for the Degree of

Doctor of Philosophy

by

Xiaofeng Wang, B.S., M.S.

_____

Umesh Garg, Director

_____

Robert V. F. Janssens, Director

Graduate Program in Physics

Notre Dame, Indiana

December 2007

EXOTIC COLLECTIVE EXCITATIONS AT HIGH SPIN:

TRIAXIAL ROTATION AND OCTUPOLE CONDENSATION

Abstract

by

Xiaofeng Wang

In this thesis work, two topics, triaxiality and reflection asymmetry, have been discussed. Band structures in ^{163}Tm were studied in a "thin" target experiment as well as in a DSAM lifetime measurement. Two new excited bands were shown to be characterized by a deformation larger than that of the yrast sequence. These structures have been interpreted as Triaxial Strongly Deformed bands associated with particle-hole excitations, rather than with wobbling. Moreover, the Tilted-Axis Cranking calculations provide a natural explanation for the presence of wobbling bands in the Lu isotopes and their absence in the neighboring Tm, Hf and Ta nuclei. A series of so-called "unsafe" Coulomb excitation experiments as well as one-neutron transfer measurements was carried out to investigate the role of octupole correlations in the ^{238,240,242}Pu isotopes. Some striking differences exist between the level scheme and deexcitation patterns seen in ^{240}Pu, and to a lesser extent in ^{238}Pu, and those observed in ^{242}Pu and in many other actinide nuclei such as ^{232}Th and ^{238}U, for example. The differences can be linked to the strength of octupole correlations, which are strongest in ^{240}Pu. Further, all the data find a natural explanation within the recently proposed theoretical framework of octupole condensation.

Dedicated to my wife *Canli*

in heartful recognition of

her love and encouragement.

CONTENTS

FIGURES

TABLES

PREFACE

Shell structure is one of the cornerstones of our description of atomic nuclei. Systems with none or a small number of nucleons outside a closed shell are generally spherical, while those away from closed shells are usually deformed because of the long-range forces between valence nucleons. The purpose of this thesis is to explore two exotic modes of collectivity that have only been proposed recently.

Direct evidence for triaxial nuclear shapes has, historically, been difficult to obtain. Nevertheless, early in the 21st century, evidence was found in nuclei with proton number $Z \sim 70$ and mass $A \sim 165$ for wobbling, a collective mode uniquely associated with triaxiality. In the present work, the properties of band structures discovered in a nucleus close to those where wobbling was reported are examined. It is shown that these bands are associated with triaxial rotation, but not wobbling.

During the past year, the concept of octupole condensation has been proposed in order to account for band structures observed in some neutron-deficient actinide nuclei. In the present work, the strength of octupole correlations in plutonium isotopes is investigated. It is shown that the rotational sequences observed in ^{240}Pu find a natural interpretation within the new concept.

For clarity and ease of reading, this thesis is divided into five chapters. In the first, the theoretical concepts relevant to the problems under discussion are described. The second chapter is devoted to the various experimental techniques

and data analysis methods. In the next chapter, the results obtained for Triaxial Strongly Deformed bands in ^{163}Tm are discussed; a general introduction of triaxiality in nuclei is followed by the presentation of the data and a detailed interpretation. The fourth chapter discusses an investigation of octupole correlations in three even-even Pu isotopes ($A = 238, 240, 242$). The first three sections of this chapter contain a general introduction on reflection asymmetry in nuclei, a motivation of the present work and relevant information about the experiments and the data analysis. The data for each nucleus are then presented one by one in the next three sections, and this is followed by the interpretation within the available models. Finally, this thesis ends with a brief summary of the present work and a perpective on possible future measurements.

ACKNOWLEDGMENTS

This thesis is a summation of my research efforts over the past four and one half years. In this long and hard period, I worked with as much wisdom and enthusiasm as I am capable of, but, honestly, I do not think that I could have finished this job without the help and support of many people. Here, I would like to deeply thank every contributor to this work from the bottom of my heart. Please forgive me if some of their names are not mentioned within the limited available space.

Dr. Umesh Garg, my advisor at Notre Dame, opened the door for me and introduced me to the world of nuclear physics, which may become my lifetime career. He is a mentor for me not only in work, but also in life.

Dr. Robert Janssens is my advisor at Argonne. I feel very lucky that I was able to work on my thesis in his group, at the side of a wonderful instrument – Gammasphere. His guidance and enthusiasm throughout the course of this work were determinant for its accomplishment. The things that have made a great impact on me in the past years and will stay with me in the future are his profound knowledge of science as well as his positive attitude towards work and life.

My gratitude also goes to Drs. Stefan Frauendorf and Takashi Nakatsukasa; their excellent theoretical work made a nice interpretation of the data possible.

Drs. Frank Moore, Michael Carpenter, Torben Lauritsen, Shaofei Zhu, Con-

Physics Department and the administrative staffs therein (Allan Bernstein, Colleen Tobolic, Janet Bergman, Barbara Weller, Barbara Fletch, Jennifer Maddox, Shelly Goethals, Shari Herman, Sandy Trobaugh, Lesley Krueger *et al.*) for all the help I received in the past years.

Last, family is most important for everyone. I would not have accomplished anything without the love and support from my family. My Mom and Dad gave me birth, education and love, I cannot adequately express my gratitude to them in any word. This thesis is dedicated to my wife, Canli, for her love, support and encouragement.

CHAPTER 1

THEORETICAL BACKGROUND

1.1   Fundamental properties of nucleus

Since the discovery of the atomic nucleus following the famous Rutherford scattering experiment [1] in 1911, numerous facts regarding this small (10^{-14} to 10^{-15} m in diameter, only one ten-thousandth of an atom in size), but heavy (about 99.9% of an atom in mass) object have been studied and characterized. The well-known properties of the nucleus include the fact that (i) it consists of protons, positively charged particles, and neutrons, electrically neutral particles; (ii) between nucleons a strong, but short-ranged nuclear force exists, which overcomes the Coulomb repulsion and results in a bound system; (iii) the binding energy per nucleon, which originates from the fact that the mass of a given nucleus is less than the sum of its constituent nucleons, keeps increasing as a function of mass until reaching a maximum of about 8 MeV at mass number A $\sim$ 60, and above this value remains approximately constant [2] (see Figure 1.1); and, (iv) the nuclear force saturates as indicated by the trend of the binding energy per nucleon as a function of mass and by the fact that the nuclear density is almost constant.

There is strong evidence that nuclei with certain numbers of protons (Z) or neutrons (N) are more stable than others. This is seen, for example, in the neutron
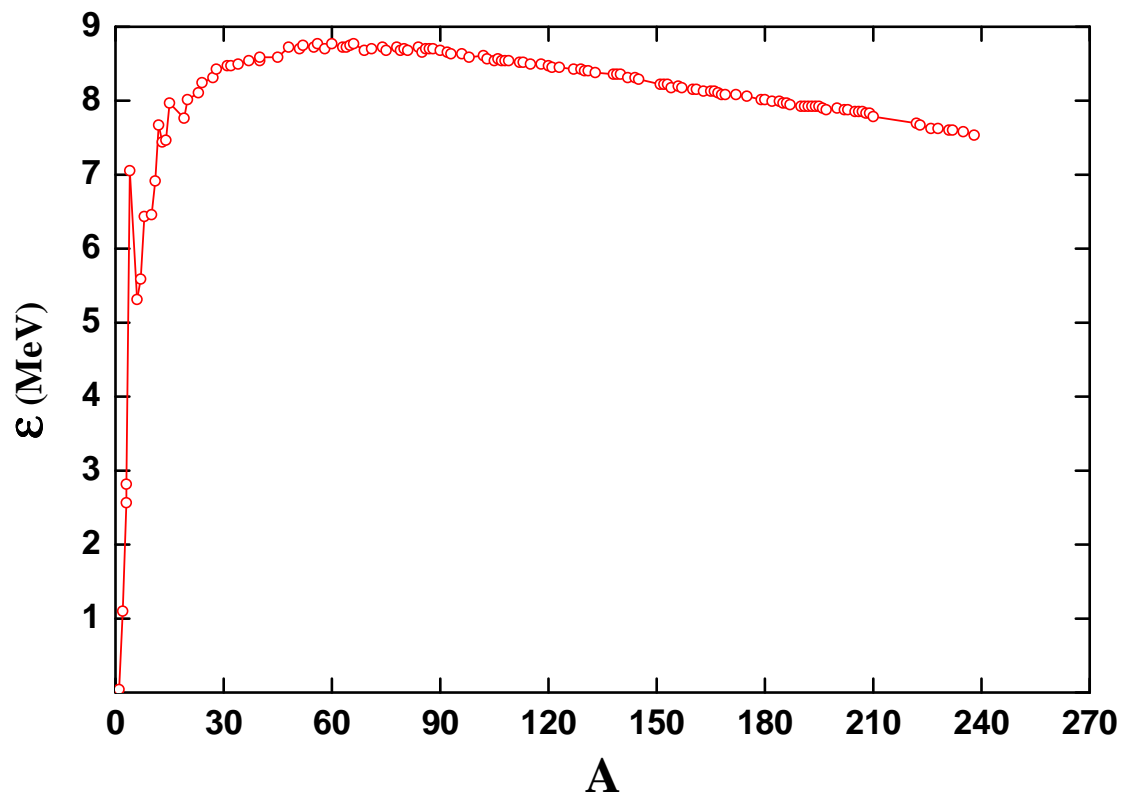
Figure 1.1. Average binding energy per nucleon ε as a function of atomic mass number A. Adapted from Ref. [2].

and proton separation energy, the energy of first excited states, *etc.* These specific
N or Z numbers, called "magic numbers", provide an insight into the fact that the
nucleons inside nucleus occupy shells, similar to those occupied by the electrons
surrounding the nucleus of the atom. On the other hand, the existence of the
collective motion of a large number of nucleons in a nucleus, *e.g.*, the collective
rotation and vibration of the nucleus, *etc.*, to be discussed later in this chapter,
is also firmly supported by a large number of experimental observations. It is the
occupation of shells by two types of nucleons that gives the nucleus its special
character. Such occupation is under some conditions responsible for the so-called
single-particle aspects of nuclear structure and under some other accounts for
its collective behavior. Understanding these two fundamental modes and the
interplay between them is one of the most important goals of nuclear structure
research.

1.2   Shell model and deformation

1.2.1   The nuclear shell model

In order to account for the shell structure found in the nucleus, the Nuclear
Shell Model [3, 4] was developed, and it has proved to be a most successful model.
In the shell model, each nucleon is described as moving in an average potential
generated by all the other nucleons, the so-called mean field potential. Hence, the
ordering and energy of nuclear states can be calculated by choosing an appropriate
form of the potential and solving the Schrödinger equation:

$$\left[-\frac{\hbar^2}{2m}\nabla^2 + V(r) \right] \psi(r) = e\,\psi(r). \tag{1.1}$$

One of the applicable potentials can be expressed as,

$$V(r) = \frac{1}{2}m(\omega r)^2 + \beta\, l^2 + \alpha\, \vec{l} \cdot \vec{s}, \qquad (1.2)$$

where $\vec{l}$ is the orbital angular momentum and $\vec{s}$ is the intrinsic spin. The first term, the harmonic oscillator potential, leads to the sequence of levels given in the left column of Figure 1.2, where N is the principal quantum number. This first term accounts only for the first three magic numbers. The addition of a l^2 term removes some of the degeneracy, as shown in the middle column of Figure 1.2, but it still does not result in the correct magic numbers. Therefore, an additional spin-orbit coupling term $\left(\vec{l} \cdot \vec{s}\right)$ [4] is necessary to obtain the sequence of levels in the right column where the "magic numbers", $e.g.$, 2, 8, 20, 28, 50, 82, 126, 184, can be understood. The states obtained in this way are occupied by the nucleons in an order of ascending energy starting from the lowest level while obeying the Pauli Exclusion Principle, $i.e.$, a maximum of two nucleons can fill into any single level.

The intrinsic spin of a nucleon is $1/2$, so for a given l there are two values of total angular momentum j, $j = l \pm 1/2$, corresponding to different spin orientations with respect to the direction of the orbital angular momentum. In spectroscopic notation, the j value is added as a subscript, for example, $1p_{1/2}$ and $1p_{3/2}$, and the multiplicity of the states is $2j + 1$. As can be seen in Figure 1.2, for $l > 3$, the energy splitting between $j + 1/2$ and $j - 1/2$ states will be large enough to lower the $j + 1/2$ state from one oscillator shell (N) to the shell below $(N - 1)$. Such levels are known as intruder states and are of opposite parity, $\pi = (-1)^l$, to the shell that they eventually occupy.

It should be noted that the magic numbers mentioned here apply to nuclei
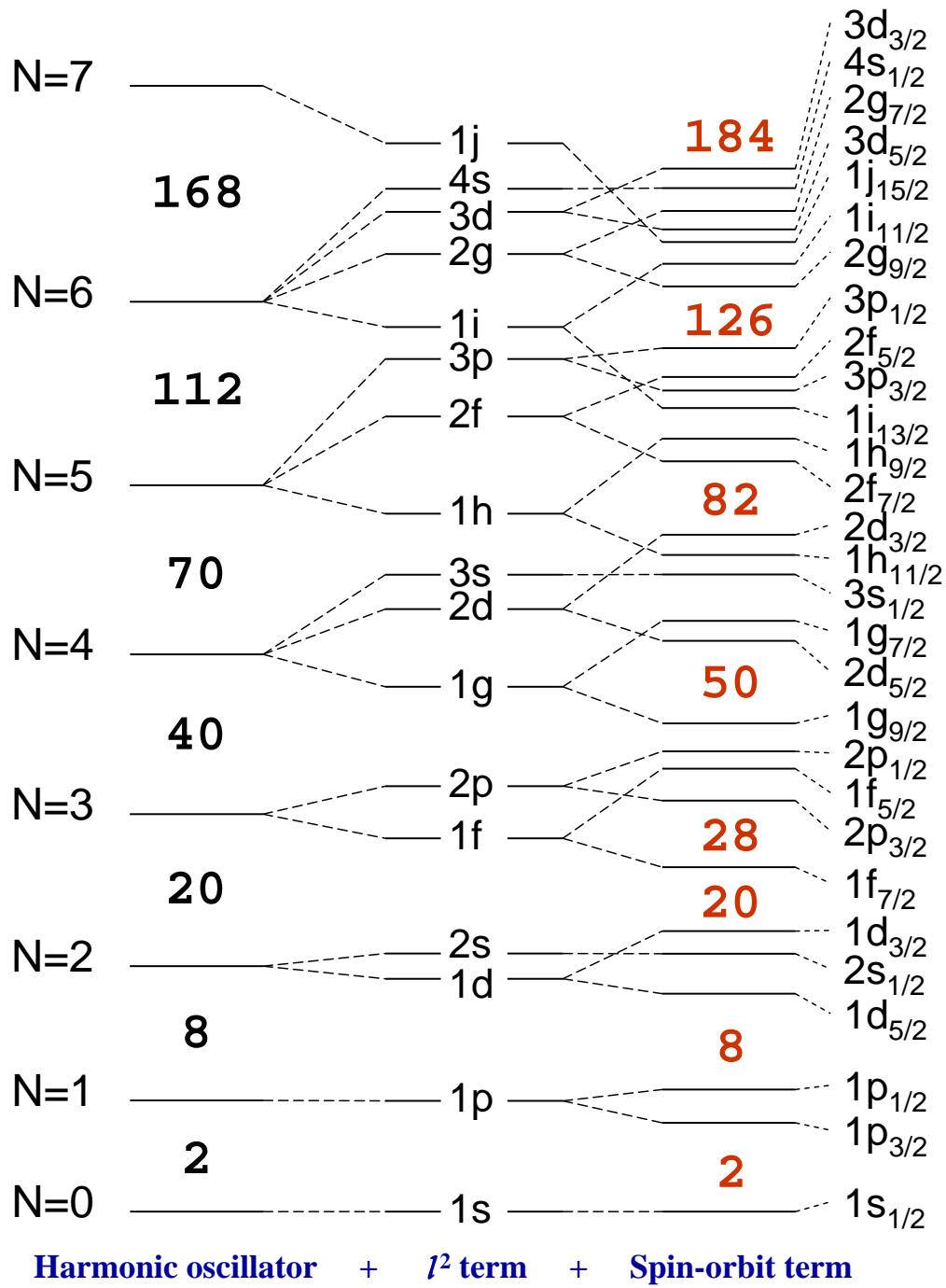
Figure 1.2. Energy levels from calculations using a modified oscillator potential. The three columns of states correspond to the three terms in the potential, and the numbers shown in the right column with red color are the "magic numbers" (see text for details). Adapted from Ref. [2].

close to stablity and recent evidence [5] indicates that these numbers are modified for exotic, neutron-rich nuclei. It is also worth pointing out that the scheme of proton states is slightly different at high energy from that of neutrons because of Coulomb repulsion.

Another often used and more realistic potential is the Woods-Saxon (WS) potential,

$$V(r) = -V_0[1 + exp^{(\frac{r-R_0}{a})}]^{-1} + \alpha(r)\,\vec{l} \cdot \vec{s}, \qquad (1.3)$$

where $R_0 = r_0 A^{1/3}$, $V_0 \approx 50\ MeV$, $a \approx 0.5\ fm$ and $r_0 \approx 1.2\ fm$. It can also reproduce the "magic numbers" and the shell structure. In the WS potential, the total angular momentum, $j = l + s$, and the parity, $\pi = (-1)^l$, are the only good quantum numbers [6].

Until this point, the nuclear problem is considered as one where each nucleon is treated as an independent particle moving in an average potential representing the effective interaction of all other nucleons with the one being described. This description is often referred to as the mean-field approximation. The assumption above is not accurate and, in fact, the nuclear problem should be treated as a many-body problem, due to the mutual interactions between the nucleons. These types of interactions, called residual interactions, must be taken care of if an accurate description of the nucleus is to be achieved.

1.2.2   Deformation

The Shell Model, using the nuclear potentials with spherical symmetry described above, has been successful in explaining many of nuclear phenomena and in predicting the properties of spherical or near-spherical nuclei, in which the number of nucleons outside a closed shell is small. However, when considering nu-

clei away from closed shells, the residual interactions between the valence nucleons (nucleons beyond a closed shell) can not be described by the spherical Shell Model. In such nuclei, the long-range effective forces between valence nucleons will lead to collective motion. In some cases, these collective effects can be strong enough to drive to a breaking of the spherical symmetry, and a permanent deformation of the nucleus is then established as the total energy of nuclear system with a deformed shape becomes lower than that associated with a spherical shape. The nuclear shape can be described using a radius vector in terms of a set of shape parameters $\alpha_{\lambda\mu}$ in the following way:

$$R(\theta, \phi) = R_0 \left(1 + \alpha_{00} + \sum_{\lambda=1}^{\infty} \sum_{\mu=-\lambda}^{\lambda} \alpha_{\lambda\mu} Y_{\lambda\mu}(\theta, \phi) \right), \qquad (1.4)$$

where $R(\theta, \phi)$ is the distance from the center of the nucleus to the surface at angles (θ, ϕ), R_0 is the radius of a sphere having the same volume as the deformed nucleus, the factor α_{00} is due to nuclear volume conservation, and $Y_{\lambda\mu}(\theta, \phi)$ is a spherical harmonic function of θ and ϕ.

In expression 1.4, the lowest multipole, $\lambda = 1$, corresponds to a shift of the position of the center of mass. It can be easily eliminated by requiring the origin of the coordinate system to coincide with the center of mass. The terms associated with $\lambda = 2$ represent the quadrupole deformation. In such a case, the nucleus is either of oblate deformation (with two equal semi-major axes) or of prolate deformation (having two equal semi-minor axes), or of triaxial deformation (having three unequal axes). The latter case is one of the two foci of this thesis work. The $\lambda = 3$ terms introduce octupole deformation, which is reflection asymmetric with a pear shape as one of the typical shapes; this is the other emphasis of this work. For the issues addressed in the present thesis, the $\lambda = 4$ (hexadecapole) and higher

7

order terms are sufficiently small that they can be ignored.

In the case of pure quadrupole deformation, Eq. 1.4 can be simplified to

$$R(\theta, \phi) = R_0 \left(1 + \alpha_{20} Y_{20}(\theta, \phi) + \alpha_{22} Y_{22}(\theta, \phi) + \alpha_{22} Y_{2-2}(\theta, \phi)\right). \quad (1.5)$$

The choice of an appropriate coordinate system where the principal axis is lined up with the axis of symmetry of the nuclear shape leads to $\alpha_{21} = \alpha_{2-1} = 0$, $\alpha_{22} = \alpha_{2-2}$. Using the so-called Lund convention (shown in Figure 1.3), the coefficients α_{20} and α_{22} can be expressed as

$$\alpha_{20} = \beta_2 \cos\gamma \quad (1.6)$$

$$\alpha_{22} = \beta_2 \sin\gamma, \quad (1.7)$$

where the parameters β_2 and γ represent the excentricity and non-axiality of the nuclear shape, respectively (see Figure 1.3), and are defined by the Lund convention as:

$$\frac{R_x - R_0}{R_0} = \sqrt{\frac{5}{4\pi}} \beta_2 \cos(\gamma - \frac{2}{3}\pi) \quad (1.8)$$

$$\frac{R_y - R_0}{R_0} = \sqrt{\frac{5}{4\pi}} \beta_2 \cos(\gamma - \frac{4}{3}\pi) \quad (1.9)$$

$$\frac{R_z - R_0}{R_0} = \sqrt{\frac{5}{4\pi}} \beta_2 \cos\gamma. \quad (1.10)$$

For axially symmetric deformation, $\gamma = 0$, β_2 can be derived from the equations above as:

$$\beta_2 = \frac{4}{3} \sqrt{\frac{\pi}{5}} \frac{\Delta R}{R_0}, \quad (1.11)$$

where $\Delta R \ (= R_z - R_x)$ is the difference between the major (R_z) and minor
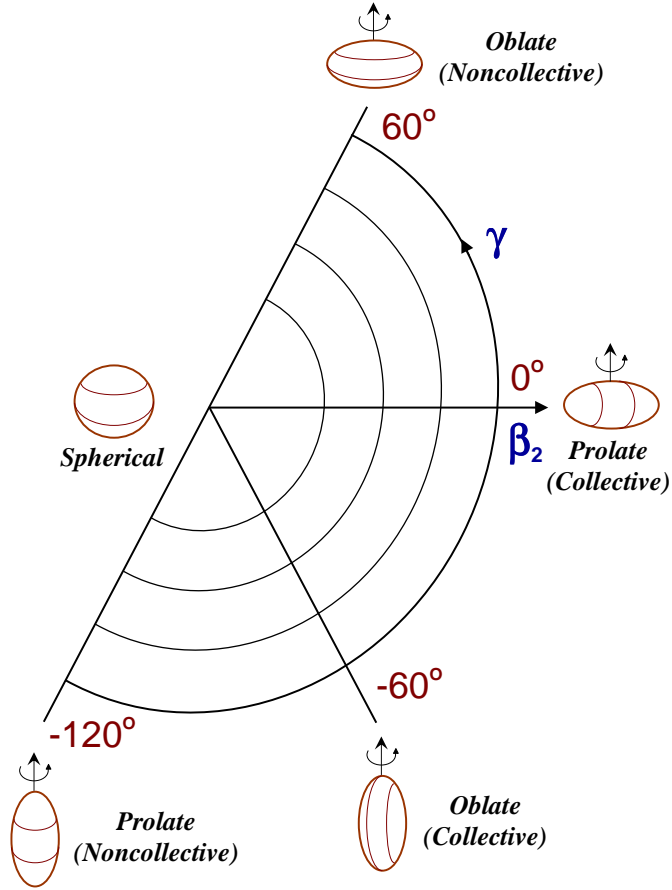
Figure 1.3. The nuclear deformations described in the Lund convention.
Adapted from Ref. [7].

(R_x) axis of the ellipsoid. It can be concluded from Eq. 1.11 that $\beta_2 < 0$ for oblate deformation, in which $R_z < R_x$, whereas $\beta_2 > 0$ for a prolate shape, in which $R_z > R_x$. Typical values for β_2 found in nuclei are: $0.2 - 0.3$ for normal deformation and $0.4 - 0.6$ for superdeformation. Another popular deformation parameter ε_2 is often used in the literature. For small deformation,

$$\varepsilon_2 \approx \frac{\Delta R}{R_0} = \frac{3}{4}\sqrt{\frac{5}{\pi}}\beta_2 = 0.946\beta_2. \tag{1.12}$$

The parameter γ is the one to describe the degree of triaxiality. As can be seen in Figure 1.3, the nuclei are axially deformed only when γ is equal to multiples of $60°$, while intermediate values of γ describe various degrees of triaxiality with the maximum degree of triaxial deformation being reached when γ is an odd multiple of $30°$.

1.2.3 The deformed shell model

As was mentioned above, the spherical Shell Model has difficulies when dealing with issues regarding deformed nuclei. Therefore, the deformed shell model was introduced.

The modified harmonic oscillator potential, *i.e.*, Nilsson potential [8], allows to take deformation into account. The Hamiltonian in this case can be written as:

$$H_{Nilsson} = \frac{-\hbar^2}{2m}\nabla^2 + \frac{m}{2}\left(\omega_x^2 x^2 + \omega_y^2 y^2 + \omega_z^2 z^2\right) - 2\kappa\hbar\omega_0\left[\vec{l}\cdot\vec{s} - \mu\left(l^2 - \langle l^2\rangle_N\right)\right],$$
$$\tag{1.13}$$

where the $\left(\vec{l}\cdot\vec{s}\right)$ term represents the spin-orbit force, and the $(l^2 - \langle l^2\rangle_N)$ term was introduced by Nilsson to simulate the flattening of the nuclear potential at the bottom of the well (as obtained with a WS potential). The factors κ and

μ determine the strength of the spin-orbit and l^2 term, respectively. The $\omega_{x,y,z}$ terms are the one-dimensional oscillator frequencies which can be expressed as a function of the deformation. In the axially-symmetric case,

$$\omega_x^2 = \omega_y^2 = \omega_0^2 \left(1 + \frac{2}{3}\varepsilon_2\right), \ \omega_z^2 = \omega_0^2 \left(1 - \frac{4}{3}\varepsilon_2\right), \tag{1.14}$$

where ω_0 is the oscillator frequency ($\hbar\omega_0 = 41A^{-1/3}MeV$) in the spherical potential, for which $\varepsilon_2 = 0$. Using the deformation-dependent Hamiltonian, the single-particle energies can be calculated as a function of the deformation ε_2. A plot of single-particle energies versus deformation is known as a Nilsson diagram; two examples of which are given in Figures 1.4 and 1.5 for $50 \leq Z \leq 82$ and $N \geq 126$, respectively.

The Nilsson orbitals can be characterised by the so-called asymptotic quantum numbers

$$\Omega[Nn_z\Lambda] \tag{1.15}$$

where N is the principal quantum number from the harmonic oscillator, Ω is the projection of the single-particle angular momentum onto the symmetry axis (z), Λ is the projection of the orbital angular momentum onto the symmetry axis and n_z is the number of oscillator quanta along the symmetry axis. While N and Ω are strictly valid quantum numbers for the Hamiltonian (Eq. 1.13), n_z and Λ become good quantum numbers only for large deformations and are approximate quantum numbers otherwise. The parity of the state, π, is determined by $(-1)^N$. The projection of the intrinsic spin of the nucleon onto the symmetry axis is $\Sigma(= \pm\frac{1}{2})$, thus we can define $\Omega = \Lambda \pm \frac{1}{2}$. The asymptotic quantum numbers for the Nilsson model are shown schematically in Figure 1.6.
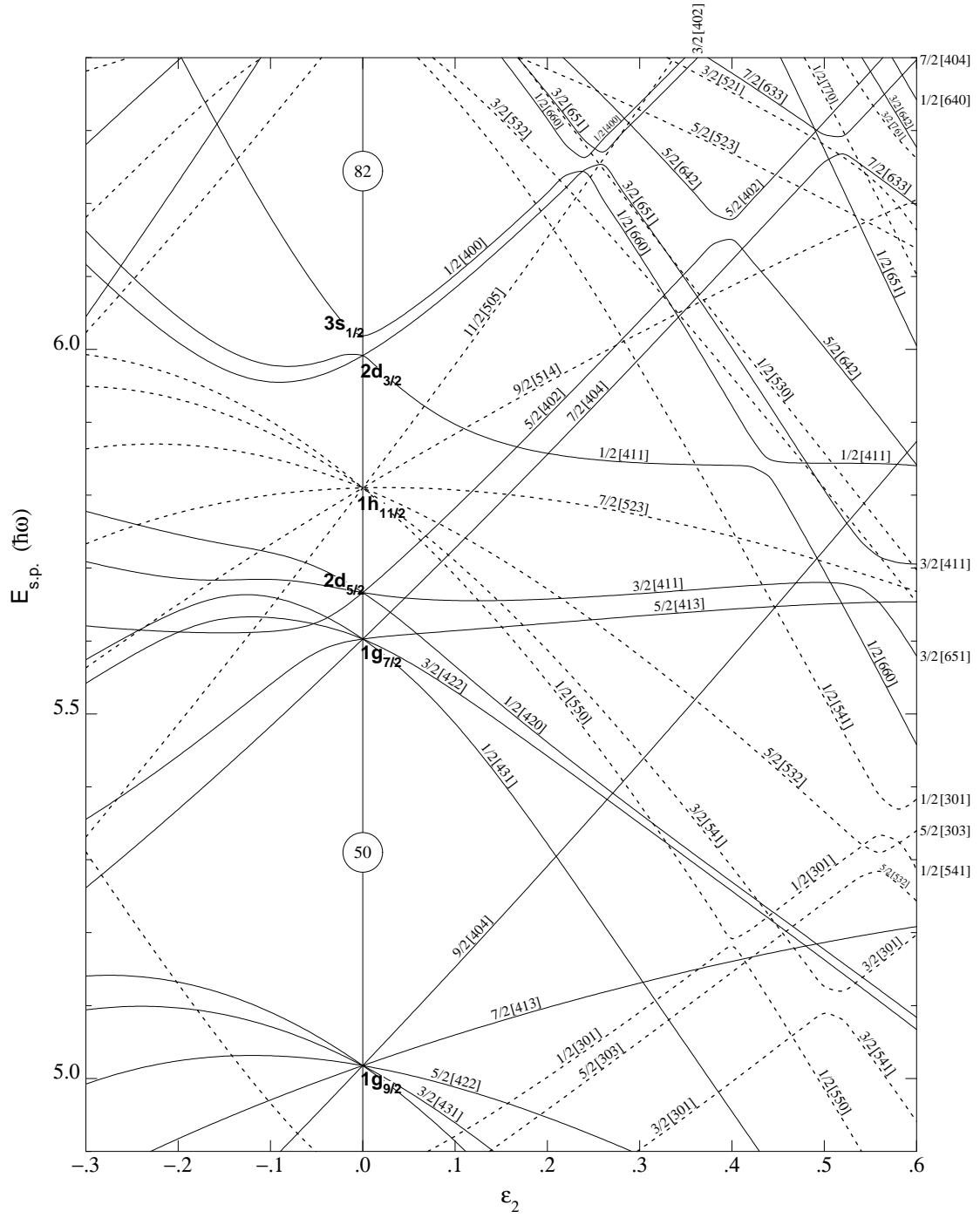
Figure 1.4. Nilsson diagram for protons, $50 \leq Z \leq 82$. Adapted from Ref. [9].

Figure 1.5. Nilsson diagram for neutrons, $N \geq 126$. Adapted from
Ref. [9].

13
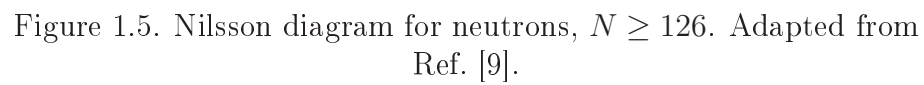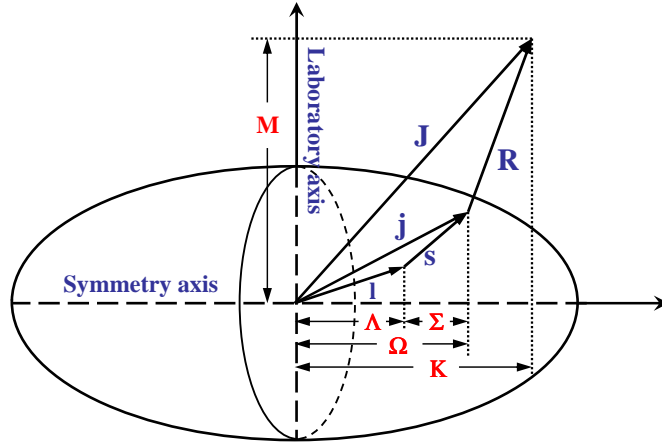
Figure 1.6. Asymptotic quantum numbers for the Nilsson model: R is the angular momentum of collective rotation; M and K are the projections of the total angular momentum J onto the laboratory axis and the symmetry axis respectively, and K is equal to Ω if no collective rotation occurs or the axis of collective rotation is perpendicular to the symmetry axis. Adapted from Ref. [7].

It should also be remembered that if N is even, then $(n_z + \Lambda)$ must also be even. Similarly if N is odd, then $(n_z + \Lambda)$ must be odd. It can be seen in Figure 1.4 and Figure 1.5 that at zero deformation, the $(2j + 1)$-fold degeneracy of a given j state is not lifted. When the deformation is introduced, the j states split into two-fold degenerate levels, the number of which for a state j is $(j + \frac{1}{2})$.

Many properties of nuclear excitations based on orbitals in the Nilsson model can be understood with these quantum numbers. For example, in Figure 1.5, it can be seen that the $j_{15/2}$ shell, with negative parity, π, lies in a region of predominantly positive-parity orbits. As a result, the various trajectories of the orbits of $j_{15/2}$ parentage are rather straight and the associated wavefunctions are rather pure, while the orbits in the neighboring shells, $e.g.$, $d_{5/2}$, $g_{7/2}$, are bent and changing slopes much more often. Two levels with the same Ω and π quantum

numbers can not cross because the deformed potential couples them and causes a repulsion. In contrast, only levels with different Ω or π cross, because the axial symmetric, reflection symmetric potential has no matrix elements due to its symmetry. Hence, it is just the high-K values and negative parities of $j_{15/2}$ orbits, being different from those of the neighboring orbits, that lead to the above observation in the Nilsson diagram.

In order to calculate the total energy of the nucleus, a summation of all populated single-particle energies can be made. The big shell gaps at finite values of ε_2, seen in the Nilsson diagram, suggest the existence of stable deformations. Thus, within the framework of the Nilsson model, it is possible to predict the magnitude of the deformation for nuclei away from closed shells. This is only a very rough estimate. An accurate method is described in the following section.

1.2.4 The Strutinsky-shell correction

The method to predict the existence of stable, deformed nuclei by calculating the total energy of the nuclear system with the shell model, described earlier, has proved to be successful in interpreting many microscopic aspects of the nucleus, mostly properties of excited states relative to the ground state. However, it fails to accurately reproduce some of the bulk properties of the nucleus, such as the total binding energy. In contrast, another approach, the liquid drop model [10], where the nucleus is described in analogy to a liquid drop, has difficulty in predicting properties related to shell structure, but is often able to provide an adequate interpretation of the macroscopic properties of the nucleus. A new approach that can incorporate the advantages of both of these models was proposed by Strutinsky [11, 12] to accurately reproduce, for example, the observed nuclear

ground-state energies. In the Strutinsky approach, the total energy E_{tot} is split into two terms: the first is a macroscopic term, E_{ldm}, derived from the liquid drop model, and the second is the microscopic term E_{shell}, which accounts for the fluctuations in the shell energy,

$$E_{tot} = E_{ldm} + E_{shell}(protons) + E_{shell}(neutrons). \qquad (1.16)$$

In Eq. 1.16, the E_{shell} quantity is calculated independently for protons and neutrons. It is defined by the difference between the actual discrete level density and a "smeared" level density. The actual discrete level density g consists of a sequence of δ-functions, and the smeared density $\tilde{g}$ uses a Gaussian distribution instead. The respective definitions are:

$$g(e) = \sum_i \delta(e - e_i), \qquad (1.17)$$

and

$$\tilde{g}(e) = \frac{1}{\gamma\sqrt{\pi}} \sum_i f_{corr}\left(\frac{e - e_i}{\gamma}\right) exp\left(-\frac{(e - e_i)^2}{\gamma^2}\right). \qquad (1.18)$$

Here, γ is an energy of the order of the shell spacing $\hbar\omega_0$, $\sim 8MeV$, and f_{corr} is a correction function for keeping unchanged the long-range variation over energies much larger than $\hbar\omega_0$. The shell energy E_{shell} can thus be calculated using

$$E_{shell} = 2\sum_i e_i - 2\int e\tilde{g}(e)\, de, \qquad (1.19)$$

where the factor 2 arises because of the double degeneracy of the deformed levels. Calculations using this method have predicted well, for example, the existence of stable reflection-asymmetric deformation in nuclear ground states [13, 14].

1.3   Rotation and cranked shell model

1.3.1   Nuclear rotation and rotational band

Because of deformation, discussed earlier, the collective rotation of the nucleus becomes possible. This started attracting people's attention early in the 1950s [15, 16, 17]. In a quantum mechanical description, a system with a symmetry axis (conveniently named as the z-axis) is given by a wave function which is an eigenfunction of the angular momentum operator $\vec{J}_z$, and any rotation about this axis produces only a phase change. The rotating system has, therefore, the same wave function and the same energy as the ground state. This simply means that this system can not rotate about the symmetry axis collectively [18]. The spherical nuclei are symmetric with respect to any axis, therefore, it is not possible to observe collective rotation in them. In the case of an axially deformed nucleus, there is a set of axes of rotation, perpendicular to the symmetry axis. A rotation around such an axis is presented schematically in Figure 1.7, and it gives rise to a distinct rotational pattern.

Here, the rotational angular momentum $\vec{R}$ is generated by the collective motion of many nucleons about the axis x, which is perpendicular to the symmetry axis z. The intrinsic angular momentum, $\vec{J}$, is the sum of the angular momenta of the nucleons, $i.e.$, $\vec{J} = \sum_{i=1}^{A} \vec{j}_i$. The total angular momentum $\vec{I}$ is then $\vec{I} = \vec{R} + \vec{J}$, and its projection onto the symmetry axis z, K, is equal to the sum of the projection of the angular momentum $\vec{j}$ of the individual nucleons onto the symmetry axis, $i.e.$, $\Omega = \sum_{i=1}^{A} \Omega_i$, in this case.

The classical kinetic energy of the rotating rigid body is, $E = \frac{L^2}{2\Im}$, where L is the angular momentum and $\Im$ is the moment of inertia. In analogy, for a quantum system, the rotational energy is the expectation value of the Hamiltonian
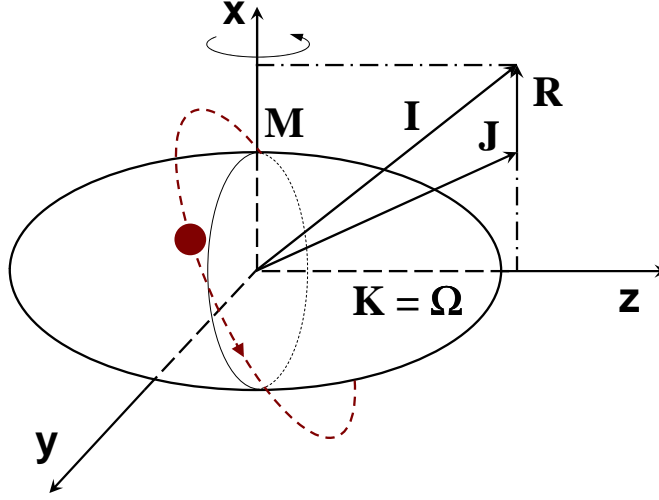
Figure 1.7. Schematic coupling of angular momenta for collective rotation of an axially deformed nucleus: $\vec{R}$ is the collective angular momentum, $\vec{J}$ is the intrinsic angular momentum, and K is the projection of the total angular momentum, $\vec{I}$ $(= \vec{R} + \vec{J})$, onto the symmetry axis z. Adapted from Ref. [19].

of rotation. For the rotating nuclear system schematically described in Figure 1.7, the Hamiltonian of rotation is given by:

$$H_{rot} = \frac{\hbar^2}{2\Im} I_x^2 \approx \frac{\hbar^2}{2\Im} \left[I^2 - I_z^2 \right],$$ (1.20)

where I_x, I_z are the projection of the total angular momentum $\vec{I}$ onto the axis of rotation x and onto the symmetry axis z, respectively. The approximation assumes that the x and y components of $\vec{J}$ can be neglected (strong coupling), which is often the case.

The state of the rotating system can be described in terms of three quantum numbers, the total angular momentum (I), its projection onto the axis of rotation (M), and its projection onto the symmetry axis (K). Hence, the energy of the

rotating system can be obtained:

$$E_{rot} = \frac{\hbar^2}{2\Im} \left[I(I+1) - K^2 \right].$$

(1.21)

It can be seen in Figure 1.7 that the quantum number K is associated with the intrinsic degrees of freedom of the valence nucleons, thus, in the energy of Eq. 1.21, one term depends on intrinsic degrees of freedom, and the other depends on the total angular momentum of the system. The latter, generally called the rotational energy, can be written as:

$$E = \frac{\hbar^2}{2\Im} I(I+1).$$

(1.22)

The total wavefunction of the rotating system Ψ_{MK}^I is the combination of the rotational wavefunction (D_{MK}^I) and the single-particle wavefunction (ϕ_K), and can be expessed as:

$$\Psi_{MK}^I = \left(\frac{2I+1}{16\pi^2} \right)^{1/2} \left[\phi_K D_{MK}^I + (-)^{I+K} \phi_{-K} D_{M-K}^I \right].$$

(1.23)

In this expression, the second term reflects the property that a rotation by π around the axis of rotation leaves the system unchanged. This rotational invariance results in two degenerate states, ϕ_K and ϕ_{-K}, which form a single series of rotational states with spins give by:

$$I = K, \ K+1, \ K+2, ...$$

(1.24)

The phase factor $(-)^{I+K}$ is called the signature. If the J_x and J_y components are

taken into account,

$$
\begin{aligned}
H_{rot} &= \frac{\hbar^2}{2\Im} \left[(I_x - J_x)^2 + (I_y - J_y)^2 \right] \\
&= \frac{\hbar^2}{2\Im} (I^2 - I_z^2 - 2I_xJ_x - 2I_yJ_y + J_x^2 + J_y^2).
\end{aligned}
\qquad (1.25)
$$

The new terms compared with Eq. 1.20, I_xJ_x and I_yJ_y, are called Coriolis interactions. They represent the influence of rotation on the motion of the individual nucleons. Among other things, they disturb the regular sequence (Eq. 1.24). According to the signature quantum number, $\alpha = (-1)^{I+K}$, the states of Eq. 1.24 can be divided into two distinct sets with an opposite value of the signature:

$$
I = K, \; K+2, \; K+4, ... \qquad (1.26)
$$

and

$$
I = K+1, \; K+3, \; K+5, ..., \qquad (1.27)
$$

and, each set of states is just a so-called rotational band. This means that the rotational bands are restricted to favored bands and unfavored partners with opposite signature. In an odd-A nucleus, for example, the levels in the favored bands possess spins, $I = \frac{1}{2}, \; \frac{5}{2}, ...$, while the unfavored partner bands are characterized by spins, $I = \frac{3}{2}, \; \frac{7}{2}, ...$, and opposite signature.

In the excitation mode of rotation, a nucleus deexcites mostly in the form of emitting γ rays, therefore, it is necessary to briefly introduce the fundamental properties of the γ rays here.

As shown in Figure 1.8, the energy of a γ ray that decays from an initial level

with energy E_i to a final level with energy E_f is:

$$E_\gamma = E_i - E_f. \tag{1.28}$$

Since each nuclear state has a definite angular momentum I, and parity π, a photon must take out angular momentum $\vec{L}$ (its eigenvalue is L) and parity π in accordance with the conservation laws:

$$\vec{I_i} - \vec{L} = \vec{I_f}, \tag{1.29}$$

$$\pi_i \times \pi = \pi_f. \tag{1.30}$$

The angular momentum of the photon, L, is called its multipolarity. For each multipolarity, two types of γ transitions are possible: the electric transition (EL) or the magnetic transition (ML). Electric transitions have angular momentum L and parity $\pi^E = (-)^L$, while the magnetic ones are characterized by angular momentum L and parity $\pi^M = (-)^{L+1}$. Therefore, the selection rules for any γ ray are:

$$
\begin{aligned}
|I_i - I_f| \leq \quad L \quad &\leq (I_i + I_f), \\
1 \leq \quad L \quad &\leq (I_i + I_f) \quad for \ I_i = I_f > 0; \\
\pi_i \pi_f \ &= \ (-)^L \quad for \ EL, \\
\pi_i \pi_f \ &= \ (-)^{L+1} \quad for \ ML.
\end{aligned} \tag{1.31}
$$

Since the photon has an intrinsic spin of 1, a γ transition from $I_i = 0$ state to $I_f = 0$ state can not occur. Often, the so-called stretched $E2$ transitions, $i.e.$, γ decays from levels with an angular momentum I to levels with an angular
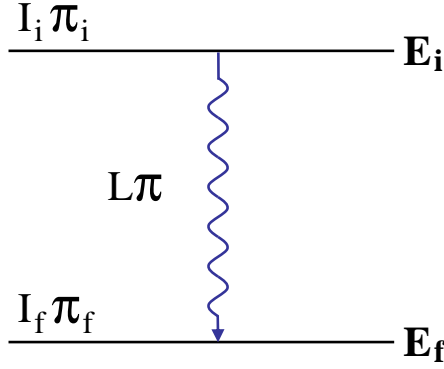
Figure 1.8. Scheme of a γ ray. Adapted from Ref. [2].

momentum $(I - 2)$ and the same parity, dominate in a rotational band, while the $E1$ transitions, $i.e.$, γ decays from levels with the angular momentum I to levels with the angular momentum $(I \pm 1)$ and the opposite parity, dominate inter-band deexcitations, especially in the case of octupole bands discussed in detail in this thesis work.

It is also worth to note that the real nucleus is intermediate between two extremes, a rigid body and a superfluid, as the measured moments of inertia are less than the rigid body values at low spin and larger than those calculated for the rotation of a superfluid. Furthermore, experimentally the moment of inertia of nucleus is found to change as a function of spin. For the rotating nucleus, the important angular rotational frequency, ω, can be written as

$$\hbar\omega = \frac{dE(I)}{dI_x} = \frac{dE(I)}{d(\sqrt{I(I+1) - K^2})}, \tag{1.32}$$

where I_x is called the aligned angular momentum and is the projection of the total angular momentum I onto the rotation axis. In the simplest case, $K = 0$. For a rotational band, where states are linked by $E2$ transitions, the angular rotational

frequency can be approximated as

$$\hbar\omega = \frac{E(I) - E(I-2)}{\sqrt{I(I+1)} - \sqrt{(I-2)(I-1)}} \simeq \frac{E_\gamma}{2}, \qquad (1.33)$$

where E_γ is the energy of γ ray between two consecutive levels in the rotational band. For a rotational band, two spin-dependent moments of inertia, which are related to two different aspects of nuclear dynamics, have been introduced in terms of the derivatives of the excitation energy with respect to the aligned angular momentum. The kinematic moment of inertia is the first order derivative

$$\Im^{(1)} = I_x \left(\frac{dE}{dI_x}\right)^{-1} \hbar^2 = \hbar \frac{I_x}{\omega}, \qquad (1.34)$$

and can be used to express the transition energy, E_γ, in a rotational band with Eq. 1.22 as:

$$E_\gamma = E(I) - E(I-2) = \frac{\hbar^2}{\Im^{(1)}}(2I - 1) \qquad (1.35)$$

through Eq. 1.21; while the dynamical moment of inertia is the second order derivative:

$$\Im^{(2)} = \left(\frac{d^2 E}{dI_x^2}\right)^{-1} \hbar^2 = \hbar \frac{dI_x}{d\omega}, \qquad (1.36)$$

and can be related to the energy spacing of consecutive γ rays in a rotational band

$$\Delta E_\gamma = \frac{4\hbar^2}{\Im^{(2)}}. \qquad (1.37)$$

Moreover, the two moments of inertia have the following relation,

$$\Im^{(2)} = \frac{d}{d\omega}\left(\omega \Im^{(1)}\right) = \Im^{(1)} + \omega \frac{d\Im^{(1)}}{d\omega}, \qquad (1.38)$$

23

and $\Im^{(1)} \simeq \Im^{(2)}$ if $\Im^{(1)}$ is constant in a band.

1.3.2 Pairing interaction

The pairing interaction is a force responsible for binding together two identical nucleons with opposite intrinsic spins in the same orbit, and this interaction is such that the energy of the configuration of opposite spins for the two nucleons is much lower than the one of any other configuration. The existence of pairing forces in the nucleus is firmly supported by many experimental results, for example: (1) the ground state of even-even nuclei always has 0^+ spin and parity, (2) the ground-state spin of odd-mass nuclei is always determined by the spin of the last nucleon, which is the only unpaired one, and (3) the binding energy of an odd-mass nucleus is found to be always smaller than the average values for two neighboring even-even nuclei. The strength of the pairing interaction, G, which favors the maximum spatial overlap between the wave functions of nucleons, is lower for protons $(G_p = \frac{17}{A}MeV)$ than for neutrons $(G_n = \frac{23}{A}MeV)$. The Hamiltonian describing pairing is usually written in the form:

$$H_{pair} = -GP^+P - \mu\hat{N}, \tag{1.39}$$

where P^+ and P are pair creation and annihilation operators, respectively, μ is the chemical potential, and $\hat{N}$ is the number operator.

Near to the Fermi surface, $i.e.$, near the last filled level, some unoccupied orbits are present. The pairing interaction scatters pairs of nucleons with $J^\pi = 0^+$ from occupied states j into empty states j' and this will result in a "smearing" of the Fermi surface. In the absence of pairing, the Fermi surface would be a sharp rectangle (see Figure 1.9).

24
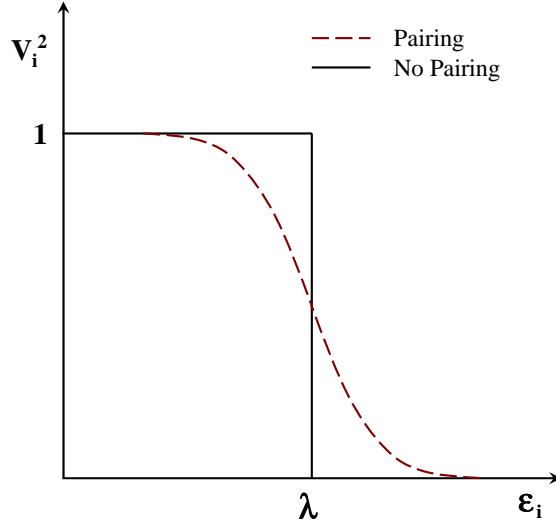
Figure 1.9. Schematic representation of the smearing of the Fermi surface due to the pairing interaction. Adapted from Ref. [20].

The smearing of the Fermi surface leads to the concept of quasi-particles [21, 22], where particle and hole wave functions are combined. The probability that a state i is occupied by a hole is given by the expression:

$$U_i^2 = \frac{1}{2} \left[1 + \frac{(\varepsilon_i - \lambda)}{\sqrt{(\varepsilon_i - \lambda)^2 + \Delta^2}} \right], \tag{1.40}$$

while the corresponding expression for the occupation by a particle is given as:

$$V_i^2 = \frac{1}{2} \left[1 - \frac{(\varepsilon_i - \lambda)}{\sqrt{(\varepsilon_i - \lambda)^2 + \Delta^2}} \right], \tag{1.41}$$

where ε_i is the single particle energy, and λ is the average Fermi energy associated with a certain particle number (see Ref. [23] for a detailed discussion of these quantities). The probabilities are normalised such that $U_i^2 + V_i^2 = 1$. It can be seen that, far below the Fermi surface $(\varepsilon_i \ll \lambda)$ $V_i^2 = 1$, and far above the Fermi

25

surface $(\varepsilon_i \gg \lambda)$ $U_i^2 = 1$. Close to the Fermi surface, the occupation probabilities are mixed. Following the treatment described in Ref. [21], the quasi-particle energy can be expressed by:

$$E_{qp}(n, p) = \sqrt{(\varepsilon_i - \lambda)^2 + \Delta^2}. \tag{1.42}$$

As the nucleus rotates, the induced Coriolis force, in analogy to the one of the classical rotations, competes with the pairing interaction and attempts to break the pair and align the individual angular momenta of the two nucleons with the rotation axis. More generally, the rotational motion weakens the pairing interaction in the nucleus, *i.e.*, while some pairs of nucleons are broken and align at specific rotational frequencies, pairing is affected for all pairs. This is known as the Coriolis anti-pairing effect (CAP) [24].

1.3.3 The cranked shell model

In order to understand the interplay between the collective and intrinsic degrees of freedom of the nucleons, the cranked shell model (CSM) was developed by Bengtsson and Frauendorf [25], built on the original cranking concepts introduced by Inglis in 1954 [26]. In this model, the nucleons can be viewed as particles independently moving in an average potential, which rotates around the principal axis (x), which is perpendicular to the symmetry axis of the nucleus (an example is shown in Figure 1.7).

The cranking model is formulated in the body-fixed frame. The transformation from the laboratory frame to the body-fixed frame can be made easily using the the rotation operator, $\Re = e^{-i\omega t j_x/\hbar}$, where j_x is the projection of the total angular momentum onto the rotational axis x. The time-dependent Schrödinger equation

of a single particle in the laboratory system can be written as:

$$i\hbar \frac{\partial \phi^l}{\partial t} = h^l \phi^l. \tag{1.43}$$

Using the rotation operator $\Re$, the wavefuction in the laboratory frame ϕ^l can be expressed in terms of the intrinsic wavefunction ϕ^0,

$$\phi^l = \Re \phi^0, \tag{1.44}$$

and the Hamiltonian in the laboratory frame h^l can be expressed in terms of the intrinsic Hamiltonian h^0, *i.e.*, the non-rotating Hamiltonian expressed in the body-fixed frame,

$$h^l = \Re h^0 \Re^{-1}. \tag{1.45}$$

Hence, the time-dependent Schrödinger equation of a single particle in the intrinsic (body-fixed) frame can be obtained,

$$i\hbar \frac{\partial \phi^0}{\partial t} = (h^0 - \omega j_x)\phi^0, \tag{1.46}$$

by replacing ϕ^l and h^l with the expressions 1.44 and 1.45, respectively, and computing the time derivation in Eq. 1.43. The single-particle cranking Hamiltonian h^ω becomes:

$$h^\omega = h^0 - \omega j_x, \tag{1.47}$$

where the term ωj_x represents the Coriolis and centrifugal forces resulting from the rotating frame. The eigenvalue of the single-particle cranking Hamiltonian,

e_ν^ω, derived from the Schrödinger equation,

$$h^\omega |\nu^\omega> = e_\nu^\omega |\nu^\omega>, \tag{1.48}$$

is the single-particle Routhian, where $|\nu^\omega>$ is the single-particle eigenfunction in the rotating frame. Taking into account the pairing interaction, the single-particle (quasi-particle) cranking Hamiltonian becomes:

$$h^\omega = h^0 - \omega j_x - \Delta(P^+ + P) - \mu \hat{N}, \tag{1.49}$$

where Δ is the pair gap. For a given configuration, the total Routhian e' can be deducted by diagonalizing as:

$$e' = \sum_i e_\nu^\omega(i). \tag{1.50}$$

The single-particle (quasi-particle) aligned angular momentum (alignment), which is the projection of angular momentum onto the axis of rotation, can be obtained from the slope of the single-particle (quasi-particle) Routhian versus the rotational frequency, i.e., $i_x^\omega = -\frac{de_\nu^\omega}{d\omega}$. Similar to the Routhian, the total alignment, i_x, is given as:

$$i_x = \sum_i i_x^\omega(i). \tag{1.51}$$

Therefore, after being appropriately transformed into the rotating frame (to be discussed in Sec. 1.3.4), the measured Routhian e' and alignment values i_x as a function of the rotational frequency ω can be compared with the results of calculations from Eqs. 1.50 and 1.51.

Since the non-rotating single-particle wavefunctions are not eigenfunctions of

j_x, the rotation leads to a mixing of the single-particle states and breaks the time-reversal symmetry. Thus, for the single-particle states the only remaining good quantum numbers are the parity, π, which is a conserved quantum number as long as the shape of the potential can be expanded in even multipoles, and the signature, α, which is related to the properties of a nucleonic state under a rotation by 180° around an axis (x) perpendicular to the symmetry axis. The signature is defined by:

$$\Re_x(\pi)\phi_\alpha = e^{-i\pi j_x}\phi_\alpha = e^{-i\pi\alpha}\phi_\alpha, \qquad (1.52)$$

where ϕ_α denotes a wavefunction with signature α. While the parity is $+$ or $-$, the signature of a single particle state can be written as $+\frac{1}{2}$ or $-\frac{1}{2}$ conventionally. In a non-rotating potential (if $\omega = 0$, $h^\omega = h^0$), the time-reversed states with the quantum number $+\Omega$ and $-\Omega$, $i.e.$, the projection of spin onto the symmetry axis (z), are energetically degenerate. Although they do not have a good signature with respect to a rotation perpendicular to the symmetry axis, it is always possible to form linear combinations of π and α. These linear combinations can then be used as basis states when solving the cranking equation 1.48. which is then split into four independent sets of equations, each one corresponding to a particular combination of the parity, π, and the signature, α. The solutions, $i.e.$, Routhians of quasi-particles, can therefore be classified by the quantum numbers (π, α), which have four available values: $(+, +\frac{1}{2})$, $(+, -\frac{1}{2})$, $(-, +\frac{1}{2})$, and $(-, -\frac{1}{2})$. The Routhians are calculated as a function of the rotational frequency, $\hbar\omega$, for a given deformation and pairing gap using the cranking equation. They are usually summarized through quasi-particle diagrams. An example is given in Figure 1.10 which presents the quasi-proton diagram calculated for ^{164}Er [27]. In the figure,

the trajectories (orbitals) are labeled by (π, α), and it is especially noticeable that orbitals with the same (π, α) do not cross; they rather come within some energy and then repel each other. The interaction regions can be interpreted as virtual crossings between different quasi-particle configurations, resulting in changes in alignment and energy. The experimental observation associated with a virtual crossing between the occupied and unoccupied quasi-particle orbitals is characterized by a sudden, large increase of the angular momentum along with a decrease in rotational frequency; *i.e.*, the curve bends back and up. The same happens in a plot of the moment of inertia vs. the rotational frequency. This phenomenon has been called "backbending". It was first observed in the ground state rotational bands of ^{162}Er and ^{158,160}Dy [28]. The underlying physical explanation is the decoupling of a pair of high-j quasi-particles from time reversed orbitals, where they have opposite intrinsic spins, and the alignment of their spins with the rotational axis (x) due to the increase of the Coriolis force with rotation [29]. Hence, the rearrangement of the quasi-particle configuration of the nucleus represents the rotational alignment of a pair of quasi-particles.

1.3.4 Transfering the experimental data to the intrinsic frame of nucleus

As described earlier in this section, the Cranking shell model provides an opportunity to make predictions about the properties of a nuclear system, particularly the alignment i_x and the quasi-particle energy (Routhian) e', in the rotating frame of reference. On the other hand, the measured values of the alignment and Routhian can be extracted from experimental data. Hence, after transferring the data from the laboratory frame to the rotating frame, a comparison between experiment and theory can be made to give the data an appropriate theoretical
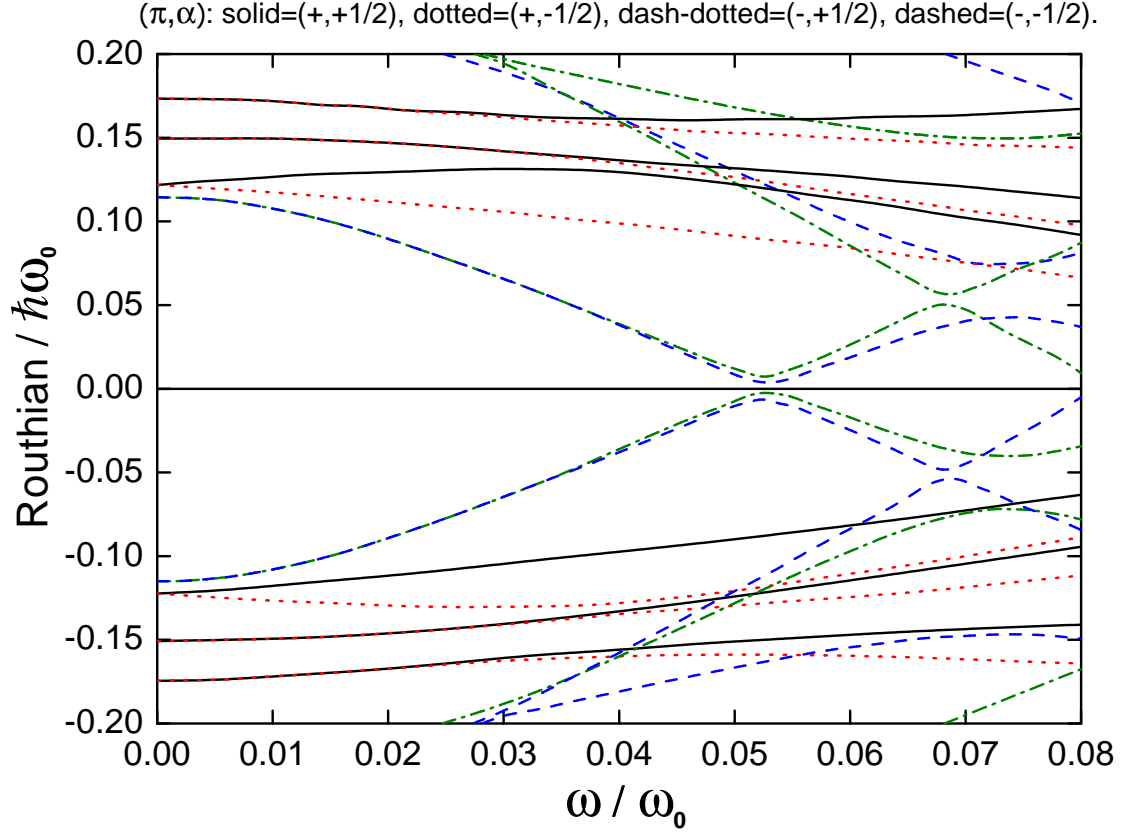
Figure 1.10. Quasi-proton Routhians of ^{164}Er calculated with the following parameters: the quadrupole deformation, $\varepsilon_2 = 0.258$; the hexadecapole deformation (a high-order term in Eq. 1.4 in Sec. 1.2.2), $\varepsilon_4 = 0.001$; the triaxiality, $\gamma = 0°$; the pairing gap, $\Delta = 0.111~MeV$; and the Fermi energy, $\lambda = 5.812~MeV$. Further details about these parameters may be found in Refs. [25, 30], and the energy scale $\hbar\omega_0$ is defined in Ref. [30] (for a spherical shape, commonly, $\hbar\omega_0 = 41A^{-1/3}~MeV$). The figure is taken from Ref. [27].

interpretation as well as to test how well the model predicts the experimental observations.

For a rotational band, where states are linked by $E2$ transitions, the angular rotational frequency ω can be derived by using the transformed expression of Eq. 1.33 in Sec. 1.3.1,

$$\hbar\omega(I+1) = \frac{E_\gamma(I)}{\sqrt{(I+2)(I+3)-K^2} - \sqrt{I(I+1)-K^2}}, \qquad (1.53)$$

from the measured γ-ray energy $E_\gamma(I)$ (for the transition $(I+2)\to I$), the spin I, and the known K value which represents the projection of I onto the axis of symmetry. The two spin-dependent moments of inertia can then be deduced from the measured E_γ and spin I values for three consecutive levels in the band, $e.g.$, $I+2$, I, and, $I-2$, through applying the following formula which are deduced from Eqs. 1.34 and 1.36:

$$\Im^{(1)}(I+1) = \hbar^2 \frac{(I+1)_x}{\hbar\omega(I+1)}; \qquad (1.54)$$

$$\Im^{(2)}(I) = \hbar^2 \frac{(I+1)_x - (I-1)_x}{\hbar\omega(I+1) - \hbar\omega(I-1)}, \qquad (1.55)$$

where $I_x = \sqrt{I(I+1)-K^2}$, $(I+1)_x$ and $(I-1)_x$ are in the same form with only I substituted by $I+1$ and $I-1$, respectively, and, $\hbar\omega(I-1)$ is deduced by replacing I with $I-2$ in Eq. 1.53. For the simplest case, in which $K=0$, $\omega = \frac{E_\gamma}{2\hbar}$, and, $\Im^{(2)}(I) = \frac{4\hbar^2}{\Delta E_\gamma}$, where ΔE_γ $(= E_\gamma(I) - E_\gamma(I-2))$ is the energy spacing of consecutive γ rays in the band.

The experimental Routhian is given in terms of the excitation energy of level $E(I)$, the angular frequency ω, and the angular momentum on the symmetry axis

I_x as:

$$E_{exp}^{\omega}(\omega) = \frac{1}{2}[E(I) + E(I+2)] - \hbar\omega(I+1)(I+1)_x. \tag{1.56}$$

To evaluate the quasi-particle contribution alone, a reference energy must be sub-tracted in order to eliminate the contribution of the rotating core. This is com-monly done by parameterizing the moments of inertia $\Im^{(1)}$, $\Im^{(2)}$ as functions of the rotational frequency ω, as described in Ref. [31]:

$$\Im^{(1)}(\omega) = J_0 + J_1\omega^2; \tag{1.57}$$

$$\Im^{(2)}(\omega) = J_0 + 3J_1\omega^2, \tag{1.58}$$

J_0 and J_1 are called Harris parameters. Hence, the fits of measured $\Im^{(1)}$ and $\Im^{(2)}$ values, obtained from Eqs. 1.54 and 1.55, in the form of Eqs. 1.57 and 1.58, where ω values are extracted from Eq. 1.53, will give the value of the Harris parameters. The reference aligned angular momentum $I_x^{ref}(\omega)$ can be deduced by using the expression as:

$$I_x^{ref}(\omega) = J_0\,\omega + J_1\,\omega^3, \tag{1.59}$$

and the reference energy is given by:

$$E_{ref}^{\omega}(\omega) = -\int I_x^{ref}(\omega)\,d\omega \simeq -\frac{1}{2}J_0\omega^2 - \frac{1}{4}J_1\omega^4 + \frac{\hbar^2}{8J_0}, \tag{1.60}$$

omitting the last term, if $J_0 = 0$. Finally, the experimental Routhian $e'(\omega)$ in the rotating frame, refering to the quasi-particle contribution alone, is written as:

$$e'(\omega) = E_{exp}^{\omega}(\omega) - E_{ref}^{\omega}(\omega), \tag{1.61}$$

and, in the same manner, the experimental alignment $i_x(\omega)$ in the rotating frame, which reflects the quasi-particle contribution only, can be given as:

$$i_x(\omega) = I_x(\omega) - I_x^{ref}(\omega), \tag{1.62}$$

where $I_x(\omega)$ is just $(I+1)_x$ defined above.

1.3.5 Shape vibrations

In addition to rotation, vibration is also one of the collective excitation modes of the nucleus. One of the foci of this work is the nature of octupole vibrations in the Pu isotopes. It corresponds to a type of oscillation of the shape of the nucleus. When a spherical nucleus absorbs small amounts of energy, its density distribution can start to vibrate around the spherical shape. The magnitude of this vibration can be described by the coefficients $\alpha_{\lambda\mu}$, defined in Eq. 1.4 in Sec. 1.2.2. For small amplitude vibrations, the Hamiltonian for a vibration of multipole order λ, which is actually the difference between the energy of the deformed shape corresponding to the vibration and the energy of the nucleus at rest, can be written as:

$$H_\lambda = \frac{1}{2} C_\lambda \sum_\mu |\alpha_{\lambda\mu}|^2 + \frac{1}{2} D_\lambda \sum_\mu \left| \frac{d\alpha_{\lambda\mu}}{dt} \right|^2. \tag{1.63}$$

With the assumption that the different modes of vibrational excitation are independent from one another, the classical equation of motion can be obtained from the above Hamiltonian,

$$D_\lambda \frac{d^2\alpha_{\lambda\mu}}{dt^2} + C_\lambda \alpha_{\lambda\mu} = 0. \tag{1.64}$$

Therefore, a small vibration can be considered as an harmonic oscillation with the amplitude, $\alpha_{\lambda\mu}$, and the angular frequency, $\omega_\lambda = \left(\frac{C_\lambda}{D_\lambda} \right)^{1/2}$. The vibrations

are quantized. The quanta are called phonons, and $\hbar\omega_\lambda$ is quantity of vibrational energy for the multipole λ. Each phonon is a boson carrying angular momentum $\lambda\hbar$ and a parity $\pi = (-1)^\lambda$. The different modes of low order vibrational excitation $(\lambda = 0, 1, 2, 3)$ are illustrated in Figure 1.11.
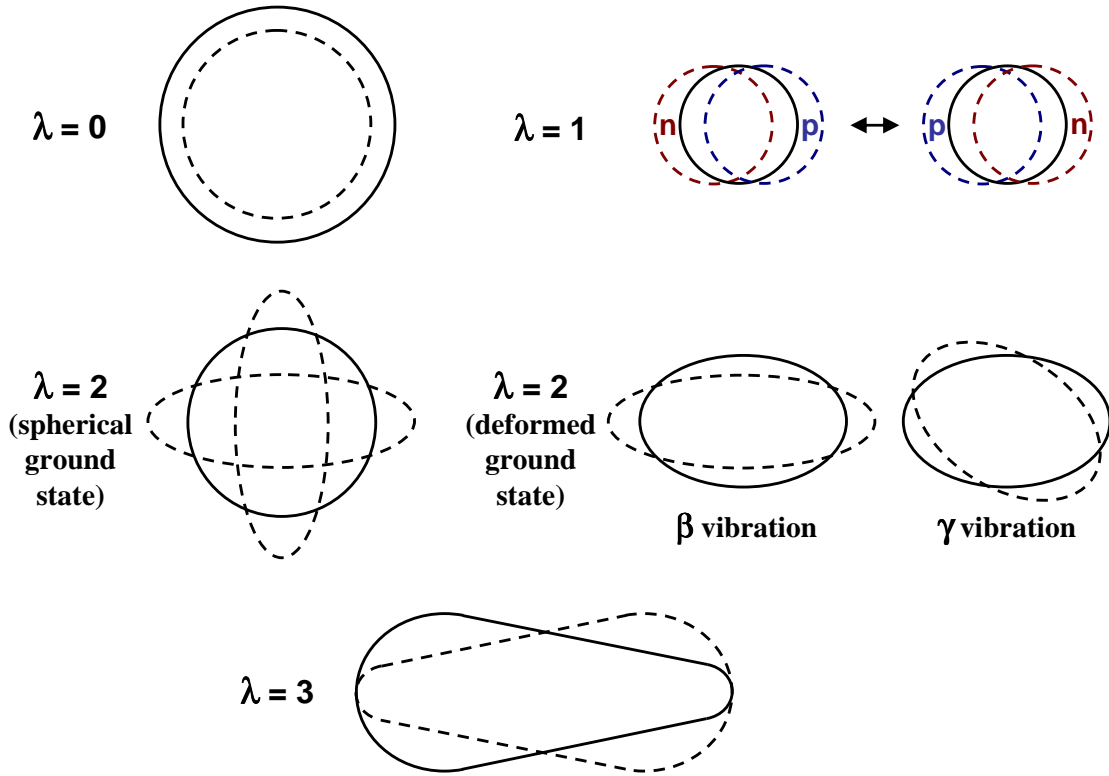
Figure 1.11. A schematic illustration of the different modes of the nuclear vibration.

1.4   Electromagnetic properties of deformed nuclei

1.4.1   Electric quadrupole moment

The nuclear quadrupole moment is one of the most important properties of a deformed nucleus, and the observation of large quadrupole moments in nuclei away from closed shells is one of the direct evidences for the existence of stable nuclear deformation. The intrinsic quadrupole momemt, Q_0, in the body fixed frame of a deformed nucleus rotating about its z-axis can be defined in terms of the charge distribution in the nucleus, $\rho_e(r)$, and, hence, of the nuclear shape, as:

$$Q_0 = \int (3z^2 - r^2)\rho_e(r)\,d^3r \approx \frac{8Z}{5}\frac{a-b}{a+b}\,r_0^2,\tag{1.65}$$

where a and b are the lengths of the major and minor axes of nucleus, respectively, and $r_0 = \frac{a+b}{2}$. Therefore, the nuclear quadrupole moment is a direct measure of the nuclear deformation, i.e., for a spherical shape, $Q_0 = 0$; for a prolate shape, $Q_0 > 0$; and for an oblate nucleus, $Q_0 < 0$. The Q_0 moment can also be related to the deformation parameter, β_2. In axially symmetric nuclei with quadrupole deformation only, the first order expression can be given as:

$$Q_0 = \frac{3Z}{\sqrt{5\pi}}r_0^2\beta_2.\tag{1.66}$$

Generally, the experimental quadrupole moments measured in the laboratory frame are the spectroscopic quadrupole moments, Q_{spec}, which will be discussed in Chapter 3. As shown in Ref. [32], the intrinsic quadrupole moment, Q_0 can be obtained by projecting the spectroscopic quadrupole moment onto the frame of

reference fixed on the nucleus through the following relation:

$$Q_0 = \frac{(I+1)(2I+3)}{3K^2 - I(I+1)} Q_{spec},$$

(1.67)

where K is the projection of I onto the symmetry axis, as described in Sec. 1.3.1.
For a $K = 0$ band, such as the ground state band in even-even nuclei, this relation
has the simpler form:

$$Q_0 = \frac{(I+1)(2I+3)}{I(2I-1)} Q_{spec}.$$

(1.68)

Moreover, as shown in Ref. [33], the experimental transition quadrupole mo-
ment, Q_t, which can be derived from the measurement of the lifetime of a state
(see below), is related to the Q_0 moment by the relation:

$$Q_t(I+1) = \sqrt{Q_0(I)Q_0(I+2)}.$$

(1.69)

1.4.2 Magnetic moment

In contrast to the nuclear electric moment, the nuclear magnetic moment re-
flects the contribution of the individual nucleons inside the nucleus. It is conve-
nient to separate the orbital and spin contributions of the neutrons and protons.
The magnetic moment operator can be expressed as:

$$\hat{\mu} = \mu_N \sum_{i=1}^{A} [g_{li} l_i + g_{si} s_i],$$

(1.70)

where μ_N is the nuclear magneton, g_{li} and g_{si} are the orbital and the spin gyro-
magnetic ratios (the gyromagnetic ratio is the ratio of the magnetic dipole moment
to the angular momentum of a nucleus), respectively. Besides this contribution,
the rotation of the core as a whole, $i.e.$, the collective rotation, contributes to the

nuclear magnetic moments. In units of the nuclear magneton, the latter contribution is proportional to the angular momentum of rotation, R. Combining all of the contributions together, the magnetic moment operator can be written after some mathematical treatment as:

$$\hat{\mu} = g_R I + [g_K - g_R]\frac{K^2}{I+1}.$$ (1.71)

The observed nuclear magnetic moment is the expectation value of the magnetic moment operator on a nuclear state $|I, K>$:

$$\mu = \langle I, K | \hat{\mu}_z | I, K \rangle,$$ (1.72)

where I is the total angular momentum, K is the projection of I onto the symmetry axis, and the z-axis is the axis of rotation.

1.4.3   Gamma-ray transition probability and branching ratio

As described in Sec. 1.3.1, in the process of nuclear deexcitation between two levels of energy E_i and E_f ($E_i > E_f$), a γ ray or a conversion electron is emitted, which carries the energy and angular momentum difference between initial and final states. The angular momentum of the γ ray (photon) always has an integer value of at least 1, and the photon can be of electric or magnetic character.

As described in Ref. [34, 35], the transition probability for a γ ray of multipolarity L from an excited state a to a final state b is given by,

$$T(L) = \frac{8\pi(L+1)}{L[(2L+1)!!]^2}\left(\frac{1}{\hbar}\right)\left(\frac{E_\gamma}{\hbar c}\right)^{2L+1}B(L),$$ (1.73)

where the reduced transition probability $B(L)$ for $a{\rightarrow}b$ is

$$B(L) = (2J_a + 1)^{-1}|\langle\psi_b\|\varkappa(L)\|\psi_a\rangle|^2, \qquad (1.74)$$

and $\varkappa$ is the electromagnetic operator. The reduced transition probability, $B(L)$, represents a sum of squared $\varkappa(L, \mu)$ matrix elements over the m substates of the final state and an average over the m substates of the initial state [36]. An approximation to single-particle matrix elements is often used to calculate an approximate unit of strength, which is called Weisskopf unit [34],

$$B(EL)_W \;\; = \;\; (1/4\pi)[3/(3+L)]^2(1.2A^{1/3})^{2L} \quad [e^2fm^{2L}], \qquad (1.75)$$

$$B(ML)_W \;\; = \;\; (10/\pi)[3/(3+L)]^2(1.2A^{1/3})^{2L-2} \quad [\mu_0{}^2fm^{2L-2}], \quad (1.76)$$

where A is the mass number, fm is femtometer (10^{-15} m), and the units e^2 and $\mu_0{}^2$ are $e^2 = 1.44 \; MeV \; fm$ and $\mu_0{}^2 = (e\hbar/2M_pc)^2 = 0.01589 \; MeV \; fm^3$.

In this work, the observed γ rays are of E1, E2 or M1 character, and the reduced transition probabilities for these three basic cases can be written according to Eq. 1.73,

$$B(E1) \;\; = \;\; 6.288{\times}10^{-16}(E_\gamma)^{-3}\lambda(E1) \quad [e^2fm^2], \qquad (1.77)$$

$$B(E2) \;\; = \;\; 8.161{\times}10^{-10}(E_\gamma)^{-5}\lambda(E2) \quad [e^2fm^4], \qquad (1.78)$$

$$B(M1) \;\; = \;\; 5.687{\times}10^{-14}(E_\gamma)^{-3}\lambda(M1) \quad [\mu_0{}^2], \qquad (1.79)$$

where E_γ is the γ-ray energy in MeV, and $\lambda(XL)$ (X is E or M) can be measured experimentally using the relation with the γ-ray intensity, $I(XL)$ (the summation

goes over all of the emitted γ rays from the initial state a),

$$\lambda(XL) \propto \frac{I(XL)}{\sum I(XL)}. \qquad (1.80)$$

Furthermore, within a rotational band, it is possible to express the reduced transition probabilities of E1, E2 and M1 transitions in terms of the dipole moment (unit: $e\ fm$), D_0, the intrinsic quadrupole moment (unit: $e\ (fm)^2$), Q_0, and the gyromagnetic ratios, g_K and g_R, respectively, as:

$$B(E1) = \frac{3}{4\pi}e^2 D_0{}^2|\langle J_a K10|J_b K\rangle|^2, \qquad (1.81)$$

$$B(E2) = \frac{5}{16\pi}e^2 Q_0{}^2|\langle J_a K20|J_b K\rangle|^2, \qquad (1.82)$$

$$B(M1) = \frac{3}{4\pi}\left(\frac{e\hbar}{2Mc}\right)^2 |\langle J_a K20|J_b K\rangle|^2 (g_K - g_R)^2 K^2, \qquad (1.83)$$

where J_a, J_b and K are the total angular momenta described earlier and the projection onto symmetry axis.

Hence, it is possible to derive from the γ-ray intensities the experimental branching ratios of the reduced probabilities by using equations 1.77 to 1.83 in this section:

$$\frac{B(E1)}{B(E2)} = 7.705{\times}10^{-7}\ \frac{E_\gamma^5(E2)}{E_\gamma^3(E1)}\frac{I(E1)}{I(E2)} \quad [fm^{-2}], \qquad (1.84)$$

and

$$\frac{B(M1)}{B(E2)} = 6.9685{\times}10^{-5}\ \frac{E_\gamma^5(E2)}{E_\gamma^3(M1)}\frac{I(M1)}{I(E2)} \quad [\mu_0{}^2 e^{-2} fm^{-4}]. \qquad (1.85)$$

These measured branching ratios can be compared with the results of theoretical calculations, and the information brought by the comparison may help us understand some important properties of the nucleus studied. The branching ratios will

be discussed in further details in the following chapters.

CHAPTER 2

EXPERIMENTAL TECHNIQUES

It is well known to nuclear physics experimentalists that there are two basic phases to every research project in nuclear structure: producing the nuclei in the desired conditions and collecting all useful physical signals from the experiment. In order to achieve the first aspect an appropriate reaction must be selected, while the second requires proper instrumentation and a powerful data acquisition system.

2.1 Reaction and target

2.1.1 Fission barrier and angular momentum

The work in this thesis focuses on phenomena in nuclei at high spin. Therefore, nuclei with large amounts of angular momentum must be produced with the chosen reaction. Often, a fusion-evaporation reaction with two heavy ions is the best option since a light projectile would only bring a small amount of angular momentum in the nucleus. However, this method is limited by the maximum amount of angular momentum a nucleus can accomodate while remaining stable against fission. This number is given qualitatively in Figure 2.1, from a calculation [37] done within the liquid drop model.
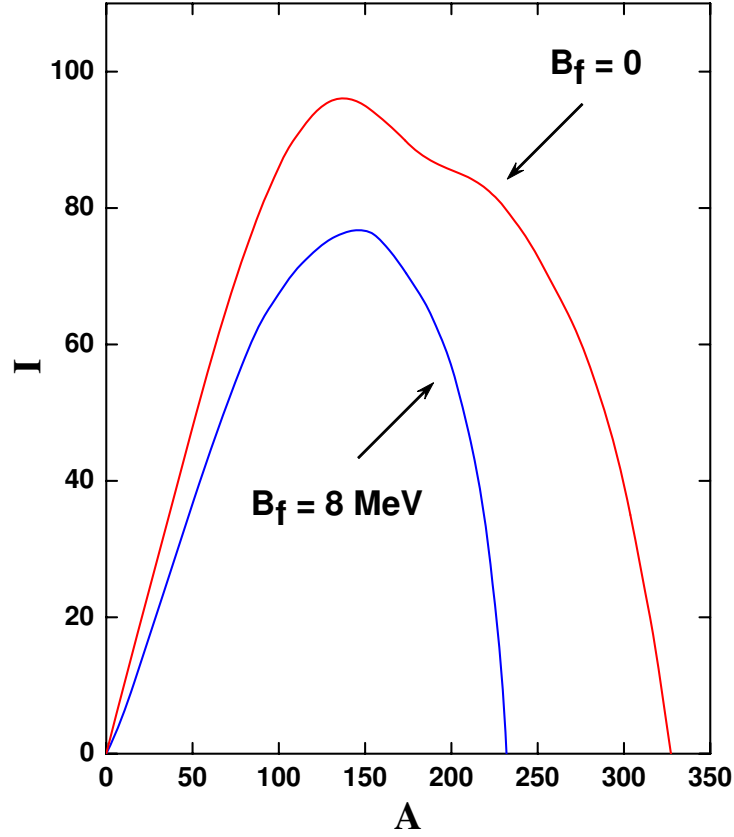
Figure 2.1. The maximum angular momentum, as a function of mass number, which a nucleus can acquire before fission occurs in the liquid drop model. The upper curve represents the angular momentum at which the fission barrier vanishes, while the lower curve represents the angular momentum for which the fission barrier is 8 MeV, $i.e.$, a condition where fission does not compete effectively with neutron evaporation. Adapted from Ref. [19].

In terms of the size and energy of the projectile, the maximum amount of angular momentum can be calculated using the following approximate relation:

$$l_{max} = \sqrt{2 A_B E_B b},$$ (2.1)

where A_B and E_B are the mass and energy of the projectile, and b is the classical impact parameter. This parameter plays an important role in the fusion process and can be defined in terms of the distance between the centers of the beam and target nuclei.

2.1.2 Fusion-evaporation reaction

In the first part of this thesis work, the nucleus ^{163}Tm was populated with high angular momentum via an heavy-ion induced fusion evaporation reaction, i.e., (HI, xn) reaction. In such a reaction, the target and projectile nuclei collide and fuse together. In a very short time ($\sim 10^{-22}$ s), they either separate via fast fission or form a compound nucleus; this is schematically illustrated in Figure 2.2. The idea of compound nucleus formation was first suggested by Niels Bohr in 1936 [38].

The compound nucleus is in a state of extreme excitation, and typically it may have an excitation energy of about 40 MeV and very large angular momentum, up to 70 $\hbar$. However, it can only exist for $\sim 10^{-20}$ s [34] before starting to get rid of its excess angular momentum and excitation energy. At first, the compound nucleus will deexcite in the most efficient way, particle emission, in which charged-particle emission (proton and alpha particles) is hindered by the Coulomb barrier and neutron evaporation usually dominates, until the process is no longer energetically possible. Each of the emitted neutrons carries away an

44
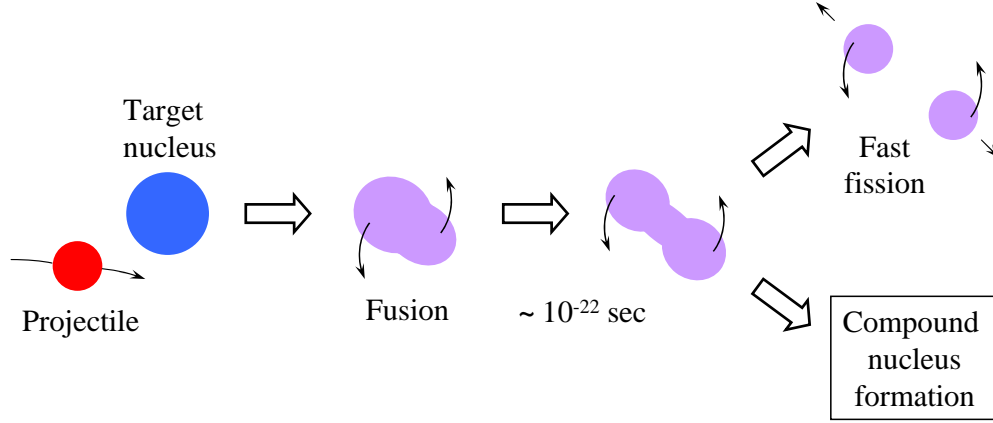
Figure 2.2. A schematic illustration of fusion-evaporation reaction
(process of compound nucleus formation).

excitation energy of on average $8 - 10 \ MeV$. The centrifugal barrier inhibits neutrons with considerable amount of orbital angular momentum from escaping [39], thus, most of the evaporated neutrons are in $l = 0$ or 1 states (l is the quantum number of orbital angular momentum). Hence, through the process of neutron evaporation, the nucleus loses most of the excitation energy, but only little angular momentum. Following particle emission, the nucleus, which is still in a state with a rather high excitation energy and a correspondingly large level density, will continue to deexcite through the emission of statistical γ rays. These γ rays are usually high energy dipole transitions, carrying away large amounts of excitation energy, but again very little angular momentum. As the nucleus approaches the yrast line, *i.e.*, the line which connects the states with the lowest energy for a given spin, the decay proceeds mostly through stretched quadrupole transitions (though other multipolarities also contribute) which remove the bulk of the angular momentum. When the level density is still high, these transitions form an unresolved continuum of γ rays. Finally, as soon as the level density becomes

low enough, the nucleus continues to decay by discrete transitions carrying lower energy (compared to statistical γ rays) until the ground state is reached. These γ rays will form cascades along, or parallel to, the yrast line.

In order to have the compound nucleus formed and obtain the particular final nucleus of interest in an (HI, xn) reaction, some factors have to be considered before the experiment: (1) the target and beam should be available; (2) the energy of the projectile must be larger than the Coulomb barrier (in MeV), E_{CB},

$$E_{CB} = \frac{1.44 Z_1 Z_2}{1.16(A_1^{1/3} + A_2^{1/3} + 2)}, \qquad (2.2)$$

and can often be estimated (particularly for $A > 100$) appropriately using the empirical expression:

$$E_{pk}(x) = \frac{1 + A_1/A_2}{-Q_x + \alpha x}, \qquad (2.3)$$

where Q_x is the Q value for the given (HI, xn) reaction, α is about 6 MeV [40], and A_1 and A_2 refer to the mass of projectile and target, respectively; (3) as few as possible open reaction channels; (4) the maximum angular momentum, l_{max}, which can be estimated classically by the formula:

$$l_{max} = \frac{\sqrt{\mu(E_0 - E_{CB})}}{4}(A_1^{1/3} + A_2^{1/3})\hbar \qquad (2.4)$$

with $\mu = A_1 A_2/(A_1 + A_2)$ and E_0 being the incident beam energy, should be comparable to the spins of levels of interest.

2.1.3 "Unsafe" Coulomb excitation

For the second part of this thesis work, the study of the properties of octupole correlations at high spin in the ^{238,240,242}Pu isotopes, we need to carefully examine

the feasibility of populating the desired states via fusion-evaporation reactions. In the framework of the liquid drop model, it is found empirically that no nucleus can survive fission if the condition $\frac{Z^2}{A} \geq 50$ is satisfied. Obviously, the Pu isotopes of interest nearly satisfy this criterion. Moreover, the height of the fission barrier is inversely proportional to the value of the angular momentum. As can be seen in Figure 2.1, the high-spin states in the Pu isotopes of interest, $A \sim 240$, are located beyond the curve of stability against fission, where $B_f = 8\ MeV$. Therefore, fusion-evaporation reactions can not be used effectively in work on these Pu isotopes, and another approach is required.

The so-called "unsafe" Coulomb excitation (Coulex) technique, which was pioneered by D. Ward, *et al*. [41] and proved to be successful in earlier work on actinide nuclei [42, 43, 44], was exploited in this thesis. In this technique, a thick target, consisting of a target layer and a thick stopper foil is bombarded by a heavy beam (high Z) of energies $\sim 10 - 15\%$ above the Coulomb barrier (Eq. 2.2). Thus, the dominant process is Coulomb excitation of the target and the projectile, but by raising the energy above the barrier, higher spin states are populated more strongly. In addition, transfer reactions will populate neighboring nuclei and provide an opportunity to investigate their structural properties as well. Unfortunately, the high beam energy will also generate fission and this process introduces background in the spectra. As shown in Ref. [41], the deexcitation from states fed in unsafe Coulex can be selectively studied with detection systems comprising a number of Compton-suppressed Ge spectrometers plus a high-efficiency sum energy/multiplicity inner array, *e.g.*, Gammasphere. By gating on the γ-ray multiplicity, the longest rotational cascades, *i.e.*, the sequences involving the highest spin levels, can be selected. Under such conditions, most

of the γ rays are emitted after the excited nucleus has come to rest in the thick target, and the majority of transitions in a collective cascade are measured with the intrinsic resolution of the Ge detectors. This feature is especially useful in the actinide nuclei where many collective bands are characterized by nearly degenerate transition energies. In this technique, weak cascades that are not seen in the traditional particle-γ Coulex experiments can be resolved in γ-γ coincidence measurements. This technique has no limit on the thickness of the target material, and in some special cases, $e.g.$, ^{238}U [41], a thick foil of the material can be used both as a target and as a stopper.

One of the deficiencies of this unsafe Coulex technique is that it is not possible to reliably measure absolute transition probabilities from the γ yields. However, for the present work, this is not critical since only level schemes and relative γ-ray intensities are discussed. Another potential drawback of this technique originates in the Doppler broadening of transitions emitted from the highest spin states with lifetimes shorter than the stopping time. This effect makes such transitions harder to resolve. Fortunately, this drawback can also be overcome to some extent by obtaining and analyzing the angular spectra, as will be discussed in detail in Chapter 4.

2.1.4 Target preparation

A crucial precondition for a successful experiment is the making of good targets. The quality of the targets may affect much the quality of final data. In the first part of this thesis work, the lifetime measurement of ^{163}Tm, a thick target of isotopically enriched ($\geq 99\%$) ^{130}Te backed by Au and Pb was used. The preparation of this target was fairly routine for the ANL target maker. In contrast, in the

other part of this thesis work, the targets, ^{239,240,242}Pu (backed by thick ^{197}Au), are radioactive ($T_{1/2} \sim 10^3 - 10^5$ years). As a result, the making and handling of these Pu targets were carried out very carefully in accordance with radiation safety concerns.

2.2 ATLAS and accelerating ions

All experiments in this thesis work were performed at ATLAS (Argonne Tandem Linear Accelerator System) in the Physics Division at Argonne National Laboratory. ATLAS is the world's first superconducting linear accelerator for heavy ions at energies in the vicinity of the Coulomb barrier, and it consists of a sequence of sections of superconducting rf cavities where each accelerates charged atoms and then feeds them into the next section for additional energy gain. The beams are provided by one of two "injector" accelerators, either a 9 million volts (MV) electrostatic tandem Van de Graaff, or a new 12 MV low-velocity linac coupled to an electron cyclotron resonance (ECR) ion source. The beam from one of these injectors is sent onto the 20 MV "booster" linac, and then finally into the 20 MV "ATLAS" linac section. High precision heavy-ion beams, with the size of ≤ 1 mm in diameter and pulses of ≤ 500 ps separated by 82 ns intervals, ranging over all possible elements, from Hydrogen to Uranium, can be accelerated to energies of $7 - 17$ MeV per nucleon and delivered to one of three target areas.

2.3 Gamma-ray detection

2.3.1 Interactions of gamma rays with matter

With the appropriate beam and target, the nuclei to be studied are produced in a high-spin experiment, hence, the next step must be detecting the emitted γ

rays, which carry most of the useful physical information, and, possibly, charged particles as well. It is the interaction of electromagnetic radiation with matter (detector material) that makes the detection of γ rays possible. For the energy range of γ rays in high-spin research, $10\,keV\ <\ E_\gamma\ <\ 10\,MeV$, only three major processes need to be considered, neglecting other small effects. These processes are the photoelectric absorption, Compton scattering, and pair production.

In the case of photoelectric absorption, an incident photon is completely absorbed by an atom in the material, and one of the atomic electrons is ejected because of the energy deposited by photon. In Compton scattering, an incident γ ray is inelastically scattered by an electron over an angle θ, and a portion of γ-ray energy is transferred to the electron. The third process, pair production, is effective when the incident γ-ray energy is larger than $1.022\,MeV$, *i.e.*, twice of the rest mass of an electron. An electron/positron pair may be generated in the material, and, after slowing down, the positron will annihilate with one of the atomic electrons producing two γ rays of energy $511\,keV$.

2.3.2 Germanium detector

In order to detect the γ rays efficiently and accurately using the three processes just mentioned, the material of the detector must have a good enough absorption efficiency. This can be provided by a material of high atomic number (Z). The best energy resolution is generally provided by semiconductors, *i.e.*, materials which can to first order be viewed as a reservoir of loosely bound electrons. Of all types of semiconductor detectors, the High-Purity Germanium (HPGe) detectors are the best ones to satisfy the above requirements. They are widely applied in modern γ-ray spectroscopy experiments. An HPGe detector is a large reverse-biased *p-n*

diode junction, as shown in Figure 2.3. The depletion region is a region of net zero charge in a *p-n* junction. The reverse high voltage has the effect of enlarging the depletion region and, thus, the active volume for the radiation detection.
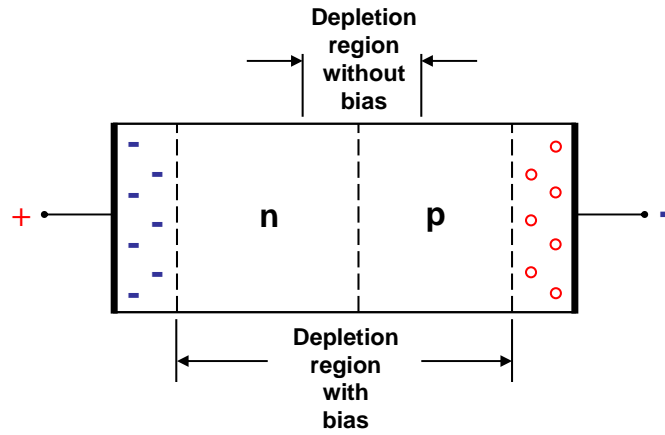
Figure 2.3. Reverse-biased *p-n* junction.

Any γ ray interacting with the germanium crystal, through the three processes described in Sec. 2.3.1, produces electron-hole pairs in the depletion region. These electron-hole pairs will then be swept to the edges of the detector, because of the electric gradient, and constitute an electric current. In the detector material, multiple processes, *e.g.*, typically a Compton scattering followed by another Compton event or by a photoelectric absorption, occur for an incident γ ray. Moreover, the photopeak efficiency increases considerably with the rising of the active volume (width of depletion region), therefore, the use of larger volume detectors is desirable.

The energy required to create an electron-hole pair in germanium is only about 3 eV. Thus, an incident γ ray with a typical energy of hundreds of keV can produce a large number of such pairs, leading to good resolution and small statistical fluctuations. The energy resolution ΔE_{in} (FWHM, $i.e.$, full width at half maximum) of any HPGe detector due to statistical fluctuations is given in the unit of keV as:

$$\Delta E_{in} = 2.36\sqrt{F\epsilon E_\gamma} = 4.06\sqrt{F E_\gamma}, \qquad (2.5)$$

where $\epsilon = 2.96\ eV$ is the average ionization energy, E_γ is the γ-ray energy in units of MeV, and, F is a constant, called the Fano factor (for the interested reader, please see Chapter 5 of Ref. [45]). The Fano factor for a semiconductor has been studied experimentally in the work of Ref. [46] and was shown to be between 0 and 1.

For an in-beam γ-ray experiment, the energy resolution of the Ge detector is often dominated by the Doppler broadening due to the motion of the recoiling nucleus and the opening angle $\Delta\theta_D$ of the Ge detector. The energy of a Doppler shifted γ ray emitted from a recoiling nucleus with the velocity $\beta = v/c$ (c is the speed of light) and observed at an angle θ relative to the beam direction, $i.e.$, detector angle, can be written as:

$$E_\gamma = E_{\gamma 0}\frac{\sqrt{1 - \beta^2}}{1 - \beta\cos\theta}, \qquad (2.6)$$

where E_γ is the enery of the γ ray collected by a detector at the angle θ and $E_{\gamma 0}$ is the nominal energy of the γ ray (as emitted by recoils at rest). As shown in Figure 2.4, according to Eq. 2.6, the Doppler broadening ΔE_D can be given in

terms of β, θ and $\Delta\theta_D$ ($= 2\delta\theta$; $\delta\theta$ is the variation of the detector angle θ) as:

$$\Delta E_D = |E_\gamma(\theta + \delta\theta) - E_\gamma(\theta - \delta\theta)| = E_{\gamma 0}\beta\sqrt{1 - \beta^2}\frac{\sin\theta}{(1 - \beta\cos\theta)^2}\Delta\theta_D. \quad (2.7)$$

It can be easily concluded that, for a given detector opening angle $\Delta\theta_D$, the energy of detected γ rays will be maximally broadened at the angle $\theta = 90°$. Besides ΔE_{in} and ΔE_D, the energy resolution of a Ge detector is also affected by ΔE_R, $i.e.$, the Doppler broadening due to the angle spread of the recoils, and ΔE_V, $i.e.$, the Doppler broadening due to the velocity distribution of the recoils.

Based on the above discussion, the FWHM of the photon peaks, $i.e.$, the total energy resolution of a Ge detector ΔE_γ, is expressed as (unit used generally: keV):

$$\Delta E_\gamma^2 = \Delta E_{in}^2 + \Delta E_D^2 + \Delta E_R^2 + \Delta E_V^2. \quad (2.8)$$

The detection efficiency of HPGe detectors depends on the energy of the collected γ ray, and reaches a maximum in the energy range of $200 - 400\ keV$. The relation of the efficiency with the γ-ray energy will be discussed in detail in Sec. 2.5.1.

HPGe detectors are operated at temperatures of around $77\ K$, in order to reduce noise from electrons which may be thermally excited across the small band gap in Ge $(0.67\ eV)$ at room temperature. This is achieved through thermal contact of the Ge crystal with a dewar of liquid nitrogen (LN_2), using a copper rod.
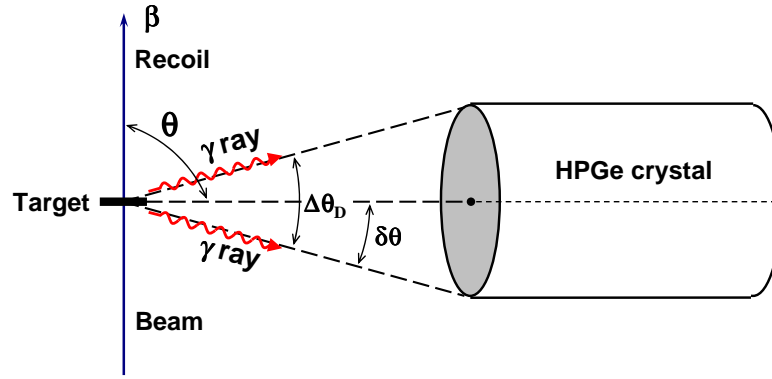
Figure 2.4. Illustration for the discussion of Doppler broadening.

2.3.3   Compton suppression and BGO detector

Compton scattering, as discussed in Sec. 2.3.1, is a major process in γ-ray detection. Many γ rays which enter the Ge detector will not deposit their full energy, leading to a large Compton continuum. One way to reduce the contribution of scattered γ rays in the spectrum is to surround the Ge detector with a BGO (Bismuth Germanate) detector which detects γ rays Compton-scattered out of the Ge crystal and then provides a signal to electronically suppress the partial energy pulse left in the Ge detector. Figure 2.5 schematically indicates the working principle of Compton suppression. With suppression shielding (the Ge and BGO are operated in anti-coincidence, which means that if an event occurs at the same time in both detectors, the event is rejected), the γ ray which deposits all of its energy in the Ge detector, for example γ_1, is only detected by the Ge detector and, hence, will be accepted, while the γ ray which deposits only part of its energy and is scattered out of the Ge detector, for example γ_2, is detected by both the Ge and BGO detector (a signal is generated to veto the HPGe readout), and, hence, will be discarded.
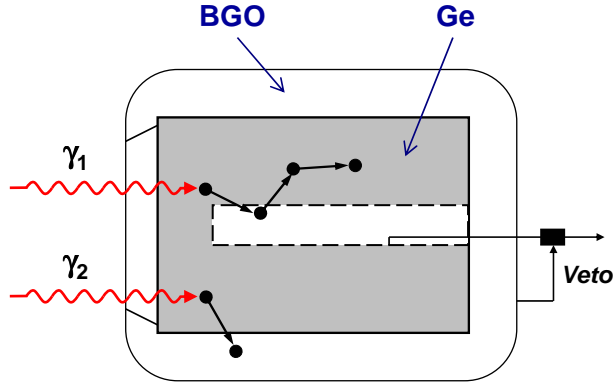
Figure 2.5. Working principle of Compton suppression.

BGO is a pure inorganic scintillator crystal. The reason to choose BGO detectors as Compton suppression shields, in spite of the notoriously low energy resolution of this material, is that, they have good timing properties (like other scintillator detectors), which is desirable for coincidence work, and high density ($7.3 \; g/cm^3$) and, hence, high efficiency (almost 100% efficiency due to the large atomic number of $_{83}$Bi), which is suitable for shielding closely and tightly in large detector arrays. For γ-ray spectroscopy, the better the ratio of full-energy to partial-energy events (called the peak-to-total, or P/T ratio), the cleaner the γ-ray spectra will be. It has been proved that the P/T ratio can be improved considerably by Compton suppression. An example of the effect of Compton suppression on the spectrum from the decay of a ^{60}Co source is shown in Figure 2.6. In this figure, it can be seen that the P/T ratio is increased from about 0.25 for the bare crystal to about 0.60 when Compton suppression is activated, while the photopeak is not affected appreciably [47].
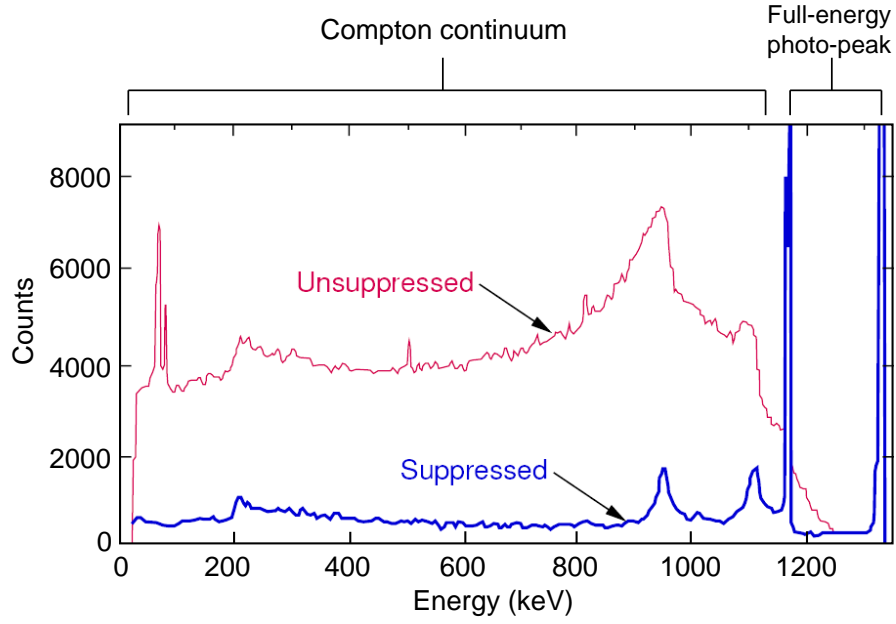
Figure 2.6. Effect of Compton suppression on the spectrum from the decay of a ^{60}Co source. Taken from Ref. [47].

2.3.4 Gammasphere detector array

In an experimental work studying nuclear phenomena associated with high spin states, an average of $20 - 30$ γ rays are emitted in any single coincidence event (a γ-ray cascade). Therefore, a detection system capable of dealing simultaneously with a large number of γ rays with good resolution and good efficiency is required. This has led to the development of large scale γ-ray detector arrays, such as Gammasphere [48], which was constructed early in 1990s, and is presently the most powerful γ-ray spectrometer in the world.

Gammasphere is an array of spherical shape (the diameter is about 6 feet and the weight is about 12 tons), consisting of up to 110 (101 in operation when running the experiments for this thesis work) Compton-suppressed HPGe detectors (HPGe + BGO) which cover almost 4π in solid angle around the target. The angle with

respect to the beam direction of each ring of detectors and the maximum number of detectors that can be put in each ring can be found in Table 2.1.

The performance of the Gammasphere array depends on four factors [49]: the peak-to-total ratio, the energy resolution ΔE_γ, the effective solid angle, and the resolving power R. The energy resolution is defined in terms of the FWHM of a γ ray of average energy, as discussed in Sec. 2.3.2, and ΔE_{in} is about 2 keV for 1.3 MeV γ rays, which is good for high-precision spectroscopy. With such large solid angle coverage (almost 4π), Gammasphere is perfectly suited to measure $5 - 10$ coincident γ rays in a high multiplicity cascade with $20 - 30$ transitions emitted in a nuclear reaction. As described in Sec. 2.3.3, the P/T ratio in a γ-ray spectrum is considerably improved by the Compton suppression. For a γ-ray event with fold n (*i.e.*, with n prompt coincident γ rays), the resolving power of Gammasphere R is proportional to the quantity $\left(\frac{P/T}{\Delta E_\gamma}\right)^n$. The total efficiency of Gammasphere is 10% for 1.3 MeV γ rays. The characteristics of Gammasphere mentioned above make it an ideal device for studying high-spin phenomena in atomic nuclei. A picture of Gammasphere located at ATLAS is shown in Figure 2.7.

2.3.5 Gammasphere electronics

In order to detect two or more coincident γ rays using the Gammasphere array, the electronic circuitry, which contains a number of amplifiers and discriminators for each Compton suppressed unit, must be employed to determine whether the detected γ-ray events satisfy the preset minimum coincidence requirement, *i.e.*, the trigger condition.

Gammasphere (GS) is usually set to have a three-fold trigger for a common high-spin experiment without the use of any external detector. The first level

TABLE 2.1

ANGLE AND MAXIMUM NUMBER OF DETECTORS (DETS) FOR
EACH RING OF GAMMASPHERE

Ring No.	Angle	Maximum number of dets
1	17.27°	5
2	31.72°	5
3	37.38°	5
4	50.07°	10
5	58.28°	5
6	69.82°	10
7	79.19°	5
8	80.71°	5
9	90.00°	10
10	99.29°	5
11	100.81°	5
12	110.18°	10
13	121.72°	5
14	129.93°	10
15	142.62°	5
16	148.28°	5
17	162.73°	5

Figure 2.7. Gammasphere detector array at ANL.

of triggering is called the pre-trigger, of which the value is often set to be "4". This means that, once four or more Ge detectors of GS have fired simultaneously, *i.e.*, each of at least four Ge detectors detect a γ ray within a time window of $200 - 800$ nanoseconds (ns) (the γ rays are required to be in coindence not only with one other, but also with the beam burst), the logic will block any further acquisition. Then, the next 1 microsecond (μs) will be used to check the master trigger, set to be "3" typically, which guarantees that at least three "clean" (no veto signal generated) Ge detectors have fired in this event; *i.e.*, at least three Ge energies remain after checking the Compton suppression through the coincidence with the respective BGO detectors. Finally, a late trigger will generally spend 6 μs to inspect the pile-up status with the purpose of excluding the possibility that more than one γ ray was absorbed by a single Ge detector in the event. If all these conditions are fulfilled, the event is a valid one, and it will take another

8 μs for the GS acquisition system to read out all the relevant information. If in any one of the above steps, the minimum coincidence requirement is not met, the acquisition is reset within ~ 1 μs to be available for incoming signals. More details about the GS electronics can be found in Ref. [50].

2.4   Lifetime measurements

2.4.1   Introduction

The lifetimes of nuclear states, or more fundamentally, the electromagnetic transition matrix elements extracted from them, are vitally important to studies of the structure of nuclei. These electromagnetic matrix elements, of which the relation with the corresponding γ-ray probability was described in Eq. 1.74 in Sec. 1.4.3, provide one of the most important connections between theoretical model wave functions and data. It has become routine to ask of a nuclear model its prediction for the lifetimes of the nuclear states of interest and to judge the model's success by how well these reproduce the experimental data [36]. The feasibility of nuclear lifetime measurements has greatly improved, due to technological advances in electronics, computers, accelerators, and above all, γ-ray detectors. The appearance of large scale γ-ray spectrometers, such as the Gammasphere array, exemplifies this spectacular progress. Without such a powerful device, lifetime measurements of short-lived states in the triaxial stongly deformed (TSD) bands of ^{163}Tm (to be discussed in Chapter 3) using the Doppler shift attenuation method (DSAM) technique (Sec. 2.4.2) would hardly be conceivable.

It is worth to mention the three most basic and widely applicable direct experimental techniques: the electronic technique, the recoil distance method (RDM) and the Doppler shift attenuation method. The time and γ-ray energy domains in

which these techniques can be applied are illustrated in Figure 2.8. The electronic technique, RDM and DSAM are used typically in the indicated time regions with time accuracies of 1, 10, and 15%, respectively, but with consirable variation depending on the detailed experimental conditions. Although there are lifetimes (τ) for which more than one of these techniques can be used, each technique has its favorable timing region, and these regions are approximately [36]:

$$
\begin{aligned}
\tau \quad &> \quad 10^{-10} \; sec \qquad electronic \; technique; \\
5 \times 10^{-12} \; sec \; < \quad \tau \quad &< \quad 10^{-10} \; sec \qquad RDM; \\
\tau \quad &< \quad 5 \times 10^{-12} \; sec \qquad DSAM.
\end{aligned}
\tag{2.9}
$$

In addition to these three basic direct techniques, there are several indirect methods and other special direct techniques which are often competitive with the three basic direct ones for the determination of lifetimes. The indirect techniques include: resonance fluorescence, capture cross-section measurements, Coulomb excitation, inelastic electron scattering, inelastic particle scattering, *etc*. Other direct ones include: microwave and channeling techniques, *etc*. The interested reader can refer to Ref. [36] for further details.

According to the selection rule defined in Eq. 2.9, and the theoretical prediction of lifetimes, we selected the DSAM technique to measure the lifetimes of TSD bands in ^{163}Tm, which is one of the foci of this thesis work and will be discussed in detail in Chapter 3.

2.4.2 DSAM technique

In accordance with the boundaries described in Figure 2.8, to determine the lifetimes of nuclear states between 10^{-12} s and 10^{-15} s, a Doppler Shift Atten-
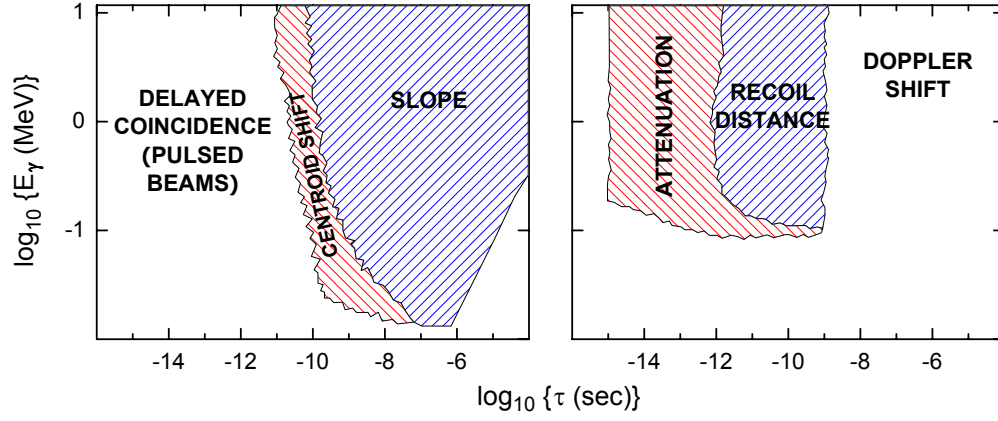
Figure 2.8. Schematics of the applicable regions of lifetime (τ) and γ-ray energy (E_γ) for the three basic direct techniques of lifetime measurements. The left figure is for the electronic techniques, and the right one is for the RDM and DSAM (see Ref. [36] for the detailed explanation of labels used in the figure). The regions are only crudely delineated and the boundaries indicated should not be taken as absolutely excluding nearby regions, but rather as an historical indication of the past use of these methods. Taken from Ref. [36].

uation Method (DSAM) measurement is performed. Typically, a target used in a DSAM experiment has the configuration of multiple layers, for example, as shown in Figure 2.9, the target for the ^{163}Tm lifetime measurements consisted of a 0.813 mg/cm^2-thick layer of the actual target material, ^{130}Te, evaporated on a 15 mg/cm^2 thick Au foil backed by a 15 mg/cm^2 layer of Pb. The thickness of the target was chosen to fully stop the recoiling evaporation residues in the Au layer, while the projectiles came to rest in the additional Pb foil.

In Figure 2.9, the principle of the DSAM technique is schematically illustrated for the ^{163}Tm lifetime measurements. A ^{37}Cl beam particle, with an energy of 165 MeV, reacts with a ^{130}Te target nucleus via a fusion-evaporation reaction, and, hence, a recoiling ^{163}Tm residue with an initial velocity $\beta_0 = v_0/c$ is formed after four neutrons are evaporated from the compound nucleus. The nucleus ^{163}Tm will then travel at a velocity $\beta(t) = v(t)/c$, which decreases with time as the nucleus slows down in the ^{130}Te target layer, and the Au backing, until it is completely stopped. During the slowing down process in the thick target, a γ ray of nominal energy $E_{\gamma 0}$ emitted from the recoiling nucleus will be measured by a HPGe detector at the angle θ, because of the Doppler shift, with the actual energy:

$$E_\gamma = E_{\gamma 0} \frac{(1 - \beta^2)^{1/2}}{1 - \beta \cos\theta}. \tag{2.10}$$

For small values of β, $e.g.$, $\beta \sim 2\%$ in the ^{163}Tm case, Eq. 2.10 is commonly substituted by its first order approximation:

$$E_\gamma = E_{\gamma 0}(1 + \beta \cos\theta). \tag{2.11}$$

The ability of a given material to decelerate the recoiling nuclei is parameterized

in terms of the stopping power. The appropriate calculation of the stopping power of the target and backing material leads to the determination of the velocity of the nucleus as a function of time by using the relation:

$$\frac{dE}{dx} = -M\frac{dv}{dt},$$

(2.12)

where $\frac{dE}{dx}$ is the stopping power of the material that the recoil is traveling in, M is the mass of the recoiling nucleus and $\frac{dv}{dt}$ is the change rate of the velocity v. The stopping power of material depends mainly on two processes: Coulomb collisions with the electrons of the atom of the target or backing material and nucleus-nucleus collisions with the target or backing material. A detailed discussion about stopping powers can be found in Ref. [50], and the value of the stopping power for a certain material can be obtained using computer codes and tabulations such as SRIM 2003 [51].

Experimentally, there are three different scenarios to consider. First, for states with very short lifetimes and feeding times (the lifetimes of feeder states), as is the case for the TSD bands in ^{163}Tm, the velocity distribution of the nucleus is narrow and all γ rays associated with these levels are emitted before the complete stopping of the nucleus. Hence, several Doppler-shifted, well-defined peaks will be visible in a spectrum obtained for a specific angle. Second, for lifetimes and feeding times approaching the stopping time of the nucleus in the backing, the associated peaks in the spectrum present distinct lineshapes with the γ-ray intensity distributed between energies corresponding to the stopped and full velocity components. Finally, for states with long lifetimes or long feeding times, all associated γ rays have no Doppler shift as the emission of these transitions occurs after the nucleus has come to rest in the backing material. For the first case, $i.e.$,
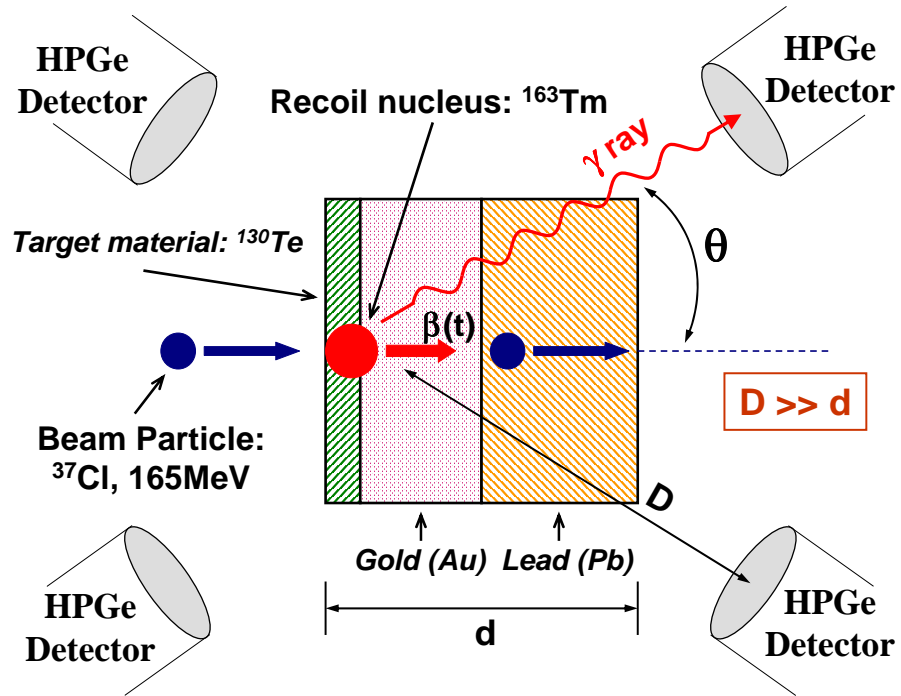
Figure 2.9. Schematic illustration of the DSAM principle (see text for the interpretation). $D \sim 20\ cm$, is the distance between target and detector, while $d \sim 10^{-6}\ m - 10^{-3}\ m$, is the thickness of target.

the fully Doppler-shifted transitions, it is straightforward that the average energy of such a transition, $\overline{E_\gamma}$, *i.e.*, the centroid of the corresponding γ peak, can be determined experimentally from the spectrum obtained at a specific angle θ, and the measured value of the average velocity β_{ave} will then be extracted by using Eq. 2.11. The important fraction of full Doppler shift, $F(\tau)$, is defined in terms of β_{ave} as:

$$F(\tau) = \beta_{ave}/\beta_0. \tag{2.13}$$

On the other hand, Eq. 2.12 has established a "clock" to measure time from the instant of fusion until the final stopping of the recoiling nucleus in the backing material. The velocity $v(t)$ as a function of time can be calculated using SRIM 2003 [51] containing the necessary information on stopping powers. Thus, the experimental $F(\tau)$ values for the states of interest and the calculated velocity $v(t)$ for the recoiling nucleus are then used to calculate the states lifetimes from the expression:

$$F(\tau) = \int_0^\infty \frac{N_k(t)}{N_0} \frac{v(t)}{v_0} \, d\,t, \tag{2.14}$$

where $N_k(t)$ is the population of state k at time t, which is a function of all the lifetimes of all its feeding states and N_0 is the initial number of nuclei at state k or a state that will decay to state k at time $t = 0$. The analytical solution to the population of state k is given by the Bateman equation:

$$N_k(t) = N_0 \prod_{i=1}^{k-1} \lambda_i \times \sum_{j=1}^{k} \frac{e^{-\lambda_j t}}{\prod_{l \neg j}^{k}(\lambda_l - \lambda_j)}, \tag{2.15}$$

where $\lambda_i = 1/\tau_i$, and τ_i is the mean lifetime of state i. For more precise results, the branching ratios, internal convertion coefficients, and side feeding cascades should be considered also, but these effects are small compared to the uncertainty

$\sim 15\%$ associated with the limited knowledge of stopping powers. The simultaneous solution of all lifetimes in the band is accomplished with a χ^2 minimization procedure in a program that attempts to fit the experimental $F(\tau)$ values with the expression of Eq. 2.14. Error bars for the lifetimes can be determined by allowing the minimum of the total Chi-square χ^2_{min} of the fit to change by ± 1 [52]. Similarly, if the $F(\tau)$ values of states in a rotational band are measured, the transition quadrupole moment Q_t and its error can be derived via running a set of fitting codes, which will be discussed in detail in Chapter 3.

2.5 Data analysis techniques

Once all the experimental data have been recorded on a storage medium, $e.g.$, a magnetic tape or a hard drive, the off-line analysis process begins. For a typical Gammasphere experiment, for example the six-day run of the ^{163}Tm lifetime measurement, Gammasphere would collect more than 1.5×10^9 coincidence events with fold ≥ 3 ($i.e.$, with at least three prompt coincident γ rays), and, hence, the total size of recorded data is huge, typically larger than 100 Giga Bytes (GB). On the other hand, the raw data commonly contains a large number of contaminant γ rays from several kinds of background, which have to be subtracted in order to obtain the useful information from the data (the background subtraction will be discussed in detail in Sec. 2.5.3). Moreover, even in the records of the "clean" γ rays emitted from the nuclei of interest, some of the information that is part of standard GS data stream, for example, the energy and time information from the individual BGOs, $etc.$, is not necessary for our purpose and can be eliminated in a presort of the data.

2.5.1 Calibration

Before dealing with the actual data of experiments, the calibration data should be analyzed. These were obtained by placing γ-ray sources (nuclei with γ rays of well-known energy, intensity, *etc.*), at the target position of Gammasphere. The purpose of these calibrations is to determine the relation between the channel number and the actual energy value, and to establish the detection efficiency of the GS detectors. The ^{56}Co, ^{152}Eu, ^{182}Ta, and ^{243}Am sources were chosen in the present work to cover the energy range from about 50 keV to around 1.4 MeV.

For any single detector, the recorded energy channel number, x, can be related to the actual energy of a γ ray, E_γ, by using the polynomial form:

$$E_\gamma = a_0 + a_1 x + a_2 x^2 + \dots \tag{2.16}$$

For most cases, the first- or the second-order approximation is sufficient for GS data. In this thesis work, the second-order relation was employed and the coefficints a_0, a_1 and a_2 for each detector were determined by using the "ENCAL" codes from the Radware software package [53].

In order to determine the relative intensity of the transitions within a cascade, the spectrum has to be corrected for the detection efficiency. This efficiency can be obtained by fitting a function to a set of measured data points (photopeak intensities) from a calibration source or to a combination of several sets of normalized data points from different calibration sources, as the relative intensity of each calibration transition is well known. The efficiency of GS detectors can be described by the following relation:

$$\epsilon = \exp\left[(A + Bx + Cx^2)^{(-G)} + (D + Ey + Fy^2)^{(-G)}\right]^{(-1/G)}, \tag{2.17}$$

where ϵ is the relative efficiency, x and y are given by:

$$x = \ln(E_\gamma/E_1) \qquad y = \ln(E_\gamma/E_2), \qquad (2.18)$$

and E_γ is in keV, $E_1 = 100\ keV$, $E_2 = 1000\ keV$. The seven parameters A, B, C, D, E, F and G can be determined by fitting the experimental data points with the "EFFIT" codes in Radware. A, B and C describe the efficiency at low energies (typically $E_\gamma \le 200\ keV$), while D, E and F have the same role for higher energies. In the fitting procedure, the parameter C is in general not required, and is by default fixed to be zero by the "EFFIT" codes. The last parameter G is an interaction parameter between the two regions. As shown in Figure 2.10, which is the total relative efficiency of all GS detectors for the experiment on the Pu isotopes (to be discussed in Chapter 4), the efficiency curve turns over around 200 keV. The parameter G determines the efficiency in the region where the curve turns over: the larger G is, the sharper the turnover at the top will be.

In Figure 2.10, it is also worth noting the sharp decrease of the curve in the low-energy region. This phenomenon arises from two main factors: (i) the absorption of low-energy γ rays in the target and the materials between the target and the Ge crystal in the detector; (ii) cut-offs due to the electronics. Low-energy γ rays are characterized by relatively poor timing in large Ge crystals [45]. As a result, the signal may be too late to be accepted either by the GS acquisition system or in the subsequent analysis.

Similarly, the relative detection efficiency of a GS detector (or all detetors in a detector ring) for a γ ray of specific energy can be extracted from the calibration data. These relative efficiencies will be useful later in measuring the lifetimes of states in Chapter 3 and deriving the multipolarities of transitions in Chapter 4.
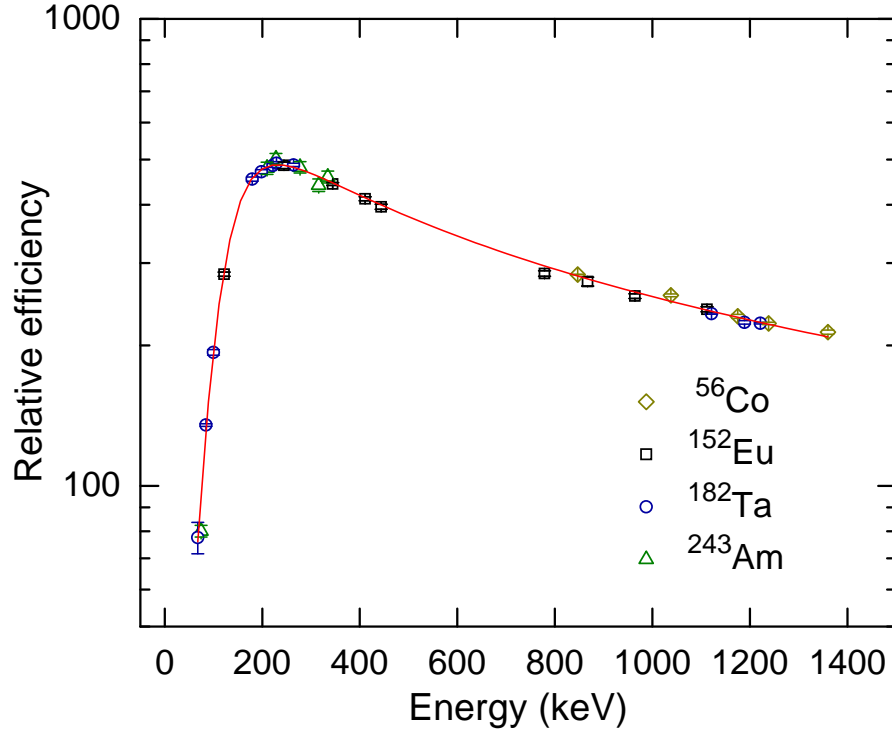
Figure 2.10. Relative efficiency curve for all GS detectors as a function of energy for the experiment on the Pu isotopes (Chapter 4). The fitting line, obtained by running the the "EFFIT" codes, represents the best-fit values of the seven parameters described in the text: $A = 5.7531214$, $B = 2.5643179$, $C = 0.0$, $D = 5.9341712$, $E = -0.62089050$, $F = -0.048151560$, and $G = 9.3074818$.

2.5.2 Blue database and Radware software package

For a large array of HPGe detectors such as GS, a dramatic increase in its effective sensitivity is realized through the dispersion of less-correlated background γ rays over a space of increased coincidence fold. Moreover, it has been shown in Ref. [54] that there exists an optimal analysis fold which is sufficiently high to dilute background γ-ray correlations and yet sufficiently low to maintain adequate statistics in the strong correlations observed in nuclear de-excitations. For GS, this fold has been found to be 4 in most cases, and, hence, the best sensitivity of the array is achieved with coincidence events of fold 4 or higher. For the analysis of coincidence data at these folds, the traditional histogram-based techniques, such as the Cube or Hypercube in Radware, becomes impractical because of the storage constraints. With the purpose to overcome the difficulty of efficient storage of and access to high-fold coincidence data, a new tool, the so-called Blue database, was developed by M. Cromaz, *et al.* [55] in 2000.

Blue is a library of routines which enables one to create and query a database specifically tailored to the storage of γ-ray coincidence events. A specialized indexing scheme which adapts to the density distribution of each particular dataset allows data to be retrieved quickly. Unlike traditional data-storage techniques for high-fold γ-ray coincidence events, the BLUE database stores the data in its original fold without unfolding. With Blue, the raw data can be sorted into several database files. Each BLUE database file corresponds to the ensemble of all coincidence events of a given fold n ($n = 1, 2, 3, ...$), each event in the file for n-fold data is stored as an array of n dimension, *e.g.*, the array $evt[n]$, and each element in the array ($evt[0]$, ..., $evt[n-1]$) remains encoded, not only with the γ-ray energy and time information, but also with the auxiliary information, *e.g.*,

the detector identification (Det-ID). The data structure of γ-ray events stored in the Blue database is schematically illustrated in Figure 2.11. Nevertheless, for certain experiments, *e.g.*, the Pu measurements to be discussed in Chapter 4, some auxiliary information of events, for example: the sum of energy absorbed by all detectors (H: sum energy), the total number of all detectors which fired promptly (K: multiplicity), *etc.*, need to be saved for the subsequent analysis. In such cases, the $(n+1)$-dimension arrays are used for storing the n-fold events instead of the regular n-dimension ones in the Blue database, since, with the new data structure, the last element in each array, being free of storing individual γ rays, is perfect to contain a number generated by encoding the necessary auxiliary information.

The specific data structure of BLUE is such that producing background-subtracted spectra at a given detector angle under specific coincidence requirements can be achieved efficiently with the method described in the next section. Such spectra are essential for studying the important Doppler-shifted or Doppler-broadened γ transitions in Chapters 3 and 4, as they are analyzed in detail by using the "GF3" codes in Radware.

Moreover, the Cube or Hypercube files of Radware format (regular ones or ones under specific pregating conditions) can also be generated quickly through querying the corresponding Blue database instead of sorting the raw data that has much larger size and less organized structure. The Cube or Hypercube obtained in this way can then be viewed with the help of the "LEVIT8R" or "4DG8R" codes in Radware to, for example, search for new transitions or band structures.
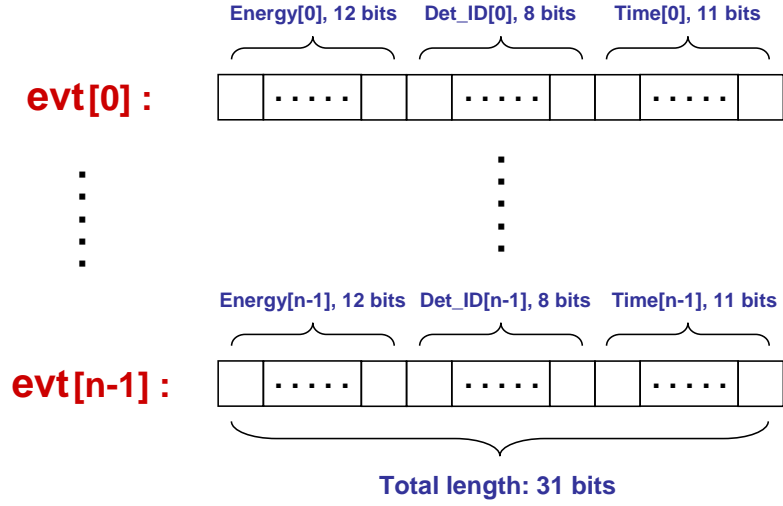
Figure 2.11. A schematic illustration of a n-fold γ-ray event *evt* stored in Blue database file. The total length of each element in the array can be as large as 32 bits (it is 31 bits in this example), while the length of individual parameter, *i.e.*, energy, or time or Det-ID, can be changed according to user's requirements.

2.5.3 Background subtraction

The proper identification of background is one of the key issues in the analysis of γ-ray spectroscopic experiments. The background contamination in such experiments is mainly of two types. The first one is the so-called "random" coincidence events, in which two or more detectors fire promptly with respect to one another but the γ rays they receive are not correlated. An example of this situation would be the γ rays emitted from a ^{240}Pu nucleus of the target and from a ^{197}Au nucleus from the backing material in the "unsafe" Coulex experiment described in Chapter 4. The other contamination arises from Compton scattering, in which the γ ray only deposits a portion of its full energy in the detector as discussed in Sec. 2.3.1.

These "random" γ peaks in spectra can be removed by using complex gating

conditions for sorting the data into the spectra (the 1-dimension histograms), or matrices (the 2-dimension histograms), or Cubes (the 3-dimension histograms), or Hypercubes (the 4-dimension histograms). Generally, such gating conditions include a window on the γ-ray time relative to the beam clock RF, a window on the multiplicity in the events, K, and a window on the sum energy in the events, H, in addition to the regular coincidence requirement with known transitions. The time window can be determined by investigating the distribution of γ-ray time as a function of γ-ray energy. As can be seen in Figure 2.12, the curves represent sample data from ^{238,240,242}Pu unsafe Coulex measurements. For γ rays in the energy range $316 - 357\ keV$, the time window can easily be set within a narrow range around the middle, strongest peak (the centroid is at about channel 1024), $e.g.$, channels $885 -$ 1054. In contrast, for γ rays in the energy range $59 - 72\ keV$, a broad time window, $e.g.$, channels $500 - 1054$, should be chosen as the contrast of intensity between the middle peak and its neighboring peaks is low. This observation is due to the relatively poor timing response of Ge detectors for low-energy ($E_\gamma < 200\ keV$) γ rays. Additionally, for the energy range $E_\gamma > 200\ keV$, the γ-ray spectra can be even cleaner. The possibility that those random contaminant γ rays are distributed in any single beam burst is even. Hence, if the qualifying γ rays with time positioned within the time window of the next beam burst (relative to the middle one), $e.g.$, channels $805 - 884$ in Figure 2.12, under the exactly same gating conditions are subtracted with proper normalization from the gated spectrum containing the γ rays with time positioned within the time window of the middle peak, $e.g.$, channels $885 - 1054$ in Figure 2.12, in principle, the resulting spectra will be free of the random contaminations after the above processing. With the gating condition of time window only (or plus gates on some known transitions),
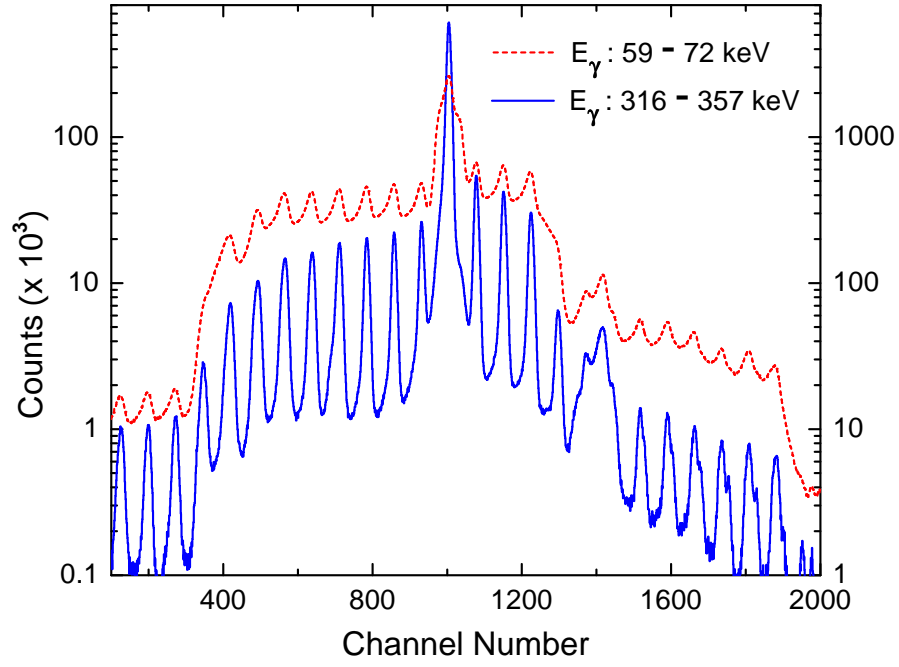
Figure 2.12. The distributions of time for γ rays in the energy range 316 $-$ 357 keV and γ rays in the energy range 59 $-$ 72 keV, respectively, taken from the data on the ^{238,240,242}Pu Coulex experiments. The channel number on the horizontal axis can be translated into real time, the time difference between consecutive peaks being 82 ns.

the preliminary histograms can be produced and some strong transitions will be observed in the analysis.

The process to determine the appropriate K and H coincidence windows is explained with the example of the ^{240}Pu Coulex data. As illustrated in Figs. 2.13 and 2.14, the distributions in multiplicty K and sum energy H for the events associated with the contaminant 279 keV transition of ^{197}Au, with the 250 keV γ ray ($10^+ \rightarrow 8^+$ in the yrast band) of ^{240}Pu, and with the 469 keV line ($22^+ \rightarrow 20^+$ in the yrast band) of ^{240}Pu, were obtained from the same data. Based on the comparisons from Figure 2.13, the following conclusions can be drawn: (i) the absolute intensity of the transition from the Coulex of ^{197}Au is

much larger than the one of any transition from the Coulex of the ^{240}Pu target (considering that the scales of counts associated with the 279 keV, 250 keV and 469 keV lines are 1×10^6, 4×10^4 and 1.5×10^4, respectively); (ii) the contaminant ^{197}Au Coulex transition favors low multiplicity, in a narrow range, $1 \leq K \leq 9$, while the events containing the transitions from the nucleus of interest, ^{240}Pu, have much higher multiplicities, in a broad range, $1 \leq K \leq 30$; (iii) a trend can be clearly seen, *i.e.*, the higher the spin of the transition involved, the larger the multiplicity. A similar phenomenon can be observed in the comparison of the sum energies in Figure 2.14, even though the discrimination is less pronounced than in Figure 2.13. Therefore, taking into account also that the probability of fission goes up with multiplicity, the optimal K and H windows were set to be 6 − 20 and 4 − 35, respectively, in order to eliminate as much as possible background while keeping adequate statistics for true coincidence events.

The second source of background, Compton scattering, results in a continuous spectrum for each γ ray transition. As described in Sec. 2.3.3, the efforts to minimize background using active Compton suppression shielding have led to significant improvements of the P/T ratios in γ-ray spectra. However, it is important to note that even with the best performance of current shields, only $\sim$ 60% of γ rays from a monochromatic 1 MeV source are detected as photopeaks leaving a $\sim$ 40% probability for a γ ray to be detected as background. Therefore, such background is still an important factor affecting data analysis, and it has to be subtracted properly in order to acquire more useful information from the spectrum.

If the data is stored in the traditional symmetric Cube or Hypercube file with decomposing each event with higher multiplicity into several 3- or 4-fold arrays,
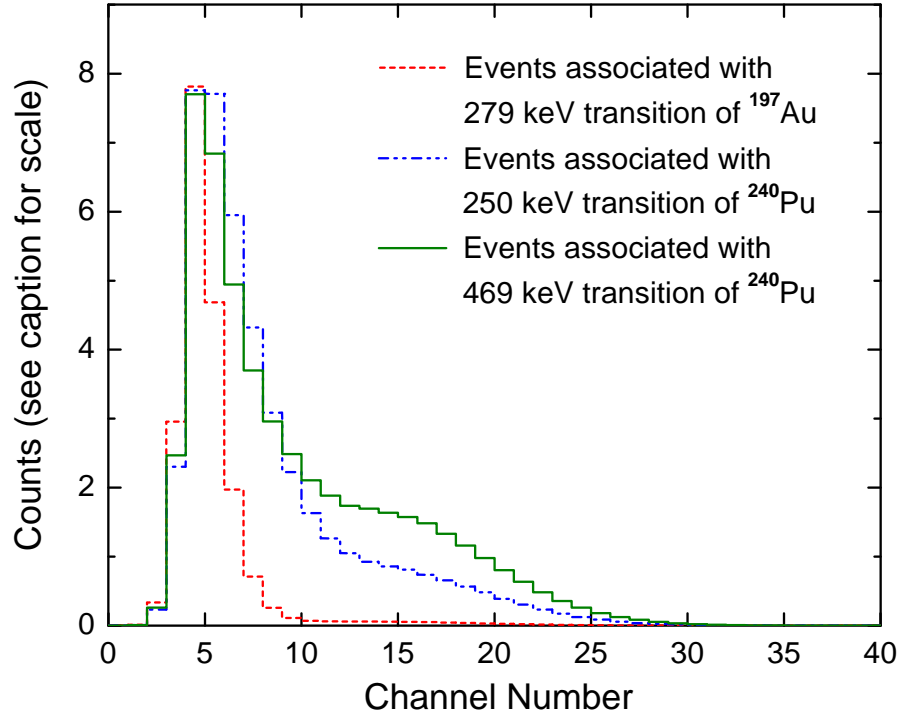
Figure 2.13. Multiplicity distributions for events associated with the contaminant 279 keV transition in ^{197}Au (scale of counts: 1×10^6), with the 250 keV γ ray ($10^+ \rightarrow 8^+$ in the yrast band) of ^{240}Pu (scale of counts: 4×10^4), and with the 469 keV line ($22^+ \rightarrow 20^+$ in the yrast band) of ^{240}Pu (scale of counts: 1.5×10^4). The channel number on the horizontal axis represents the total number of detectors firing in prompt coincidence.
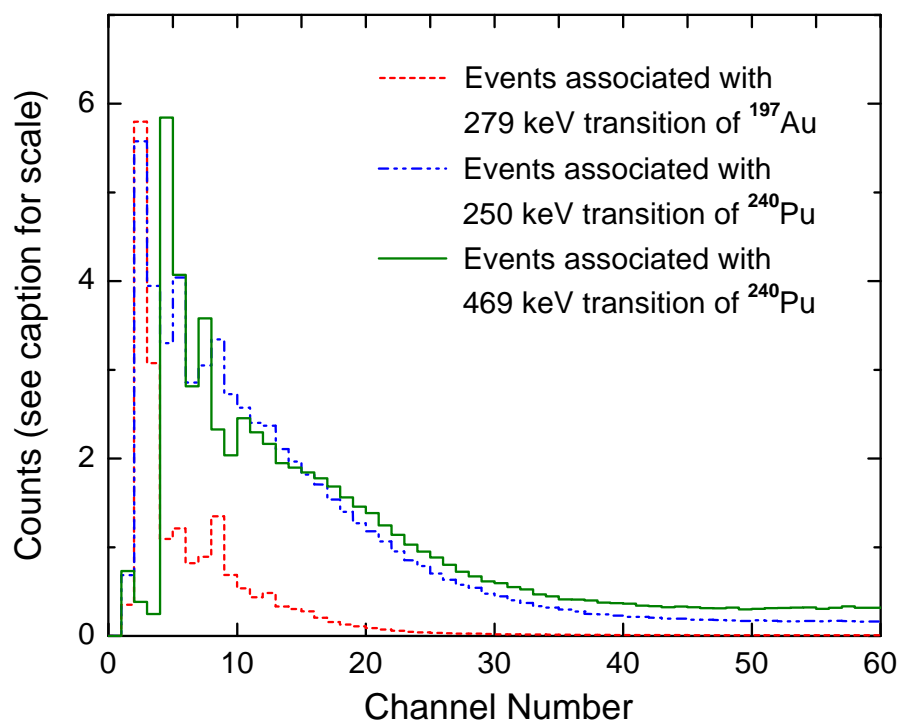
Figure 2.14. Sum-energy distributions for events associated with the contaminant 279 keV line in ^{197}Au (scale of counts: 1×10^6), with the 250 keV transition ($10^+ \rightarrow 8^+$ in the yrast band) in ^{240}Pu (scale of counts: 2×10^4), and with the 469 keV γ ray ($22^+ \rightarrow 20^+$ in the yrast band) in ^{240}Pu (scale of counts: 7×10^3). The channel number on the horizontal axis can be translated into energy units.

i.e., unfolding, the background will be subtracted automatically in the analysis with the codes "LEVIT8R" or "4DG8R" of Radware which adopts the method described in Ref. [56]. However, in some cases, *e.g.*, in a DSAM or angular distribution (to be discussed in the next section) analysis, the spectra generated at certain angles with complex gating conditions are needed, and, thus, it is convenient to store the data including the auxiliary information in its native fold via the Blue database technique. For the data of such unsymmetric format, the algorithm of subtracting background in Ref. [56] is not valid. Hence, a new method was developed by K. Starosta, *et al.* [57], which has proven to be successful in the analysis of a number of DSAM measurements, including the ^{163}Tm lifetime measurement in this thesis work. The principle of the new method is introduced briefly below by using an example of double gating on events of fold three and higher (for the interested reader, please refer to Ref. [57] for the details of this method). Any γ ray detected in the spectrum may be either a peak (P) or a background (B). Denoting the first and the second gating transitions by γ_1 and γ_2, respectively, the events can be grouped into four classes, *i.e.*, PP, PB, BP and BB, which are defined in Table 2.2.

The objective is to obtain the spectrum $S_{pp}(j)$ which corresponds to class (1) from the double-gated spectrum $S_{tt}(j)$ which corresponds to the sum of all four classes. The task is accomplished following the subtraction of the appropriate background spectrum in the expression:

$$S_{pp}(j) = S_{tt}(j) - [N_{pb}S_{pb}(j) + N_{bp}S_{bp}(j) + N_{bb}S_{bb}(j)], \qquad (2.19)$$

where N_{pb}, N_{bp} and N_{bb} represent the number of events in classes (2), (3) and (4),

TABLE 2.2

CLASSES OF EVENTS FOR DOUBLE GATING (SEE TEXT FOR DETAILS)

Class	γ_1	γ_2
(1)	Peak	Peak
(2)	Peak	Background
(3)	Background	Peak
(4)	Background	Background

respectively, and $S_{pb}(j)$, $S_{bp}(j)$ and $S_{bb}(j)$ are the normalized spectra extracted for these classes:

$$\sum_j S_{pb}(j) = \sum_j S_{bp}(j) = \sum_j S_{bb}(j) = 1. \qquad (2.20)$$

With some appropriate assumptions, the Eq. 2.19 can then be simplified into:

$$S_{pp}(j) = S_{tt}(j) - N \left(\frac{b_2^{g1}}{N^{g1}} S^{g1}(j) + \frac{b_1^{g2}}{N^{g2}} S^{g2}(j) - \frac{b_1 b_2^{g1} + b_2 b_1^{g2}}{2} \frac{1}{T} P(j) \right), \quad (2.21)$$

where b_1^{g2} denotes the background to total (B/T) ratio for γ_1 in the spectrum single gated on γ_2, $i.e.$, the conditional probability that γ_1 is detected in background while γ_2 is detected in either manner, similarly, b_2^{g1} denotes the B/T ratio for γ_2 in the spectrum single gated on γ_1; b_1 and b_2 denote the B/T ratios for γ_1 or γ_2 in the total projection spectrum $P(j)$ ($T = \sum_j P(j)$), respectively; $S^{g1}(j)$ and $S^{g2}(j)$ represent the spectrum single gated on γ_1 and the one single gated on γ_2, respectively, and, $N^{g1} = \sum_j S^{g1}(j)$, $N^{g2} = \sum_j S^{g2}(j)$. However, for γ rays

in the background subtracted spectrum $S_{pp}(j)$ there is a certain probability for peak detection and a certain probability for background detection as a result of Compton scattering; therefore, the smooth background in true coincidence with gating transitions is not removed by the algorithm defined in Eqs. 2.19 and 2.21. The shape of the smooth background $B(j)$ is then defined based on the total projection of the data according to the prescription of Ref. [53], and then the average probability for a γ ray being detected in the background can be expressed as: $b^T = \frac{\sum_j B(j)}{T}$. Hence, the final clean spectrum with background subtraction can be written as:

$$
\begin{aligned}
S_{pp}^F(j) &= S_{pp}(j) - b^T \frac{\sum_j S_{pp}(j)}{N^B} B(j) \\
&= S_{tt}(j) - N\big(\frac{b_2^{g1}}{N^{g1}} S^{g1}(j) + \frac{b_1^{g2}}{N^{g2}} S^{g2}(j) - \frac{b_1 b_2^{g1} + b_2 b_1^{g2}}{2} \frac{1}{T}[P(j) - B(j)] \\
&\quad + [1 - b_1^{g2} - b_2^{g1}] \frac{1}{T} B(j)\big).
\end{aligned}
\tag{2.22}
$$

The effect of proper background subtraction with this method is demonstrated by the comparison of a background-subtracted spectrum with data without subtraction in Figure 2.15. It can be seen clearly that some peaks which can be observed in the spectrum without background subtraction disappear in the spectrum with background subtraction, while some peaks which are absent or too weak to be determined in the spectrum without background subtraction appear in the properly subtracted spectrum.

2.5.4 Level scheme and gamma-ray angular distribution

By analyzing a large number of spectra gated on transitions of interest, the various coincidence relations of γ rays emitted in the deexcitation of a nucleus are
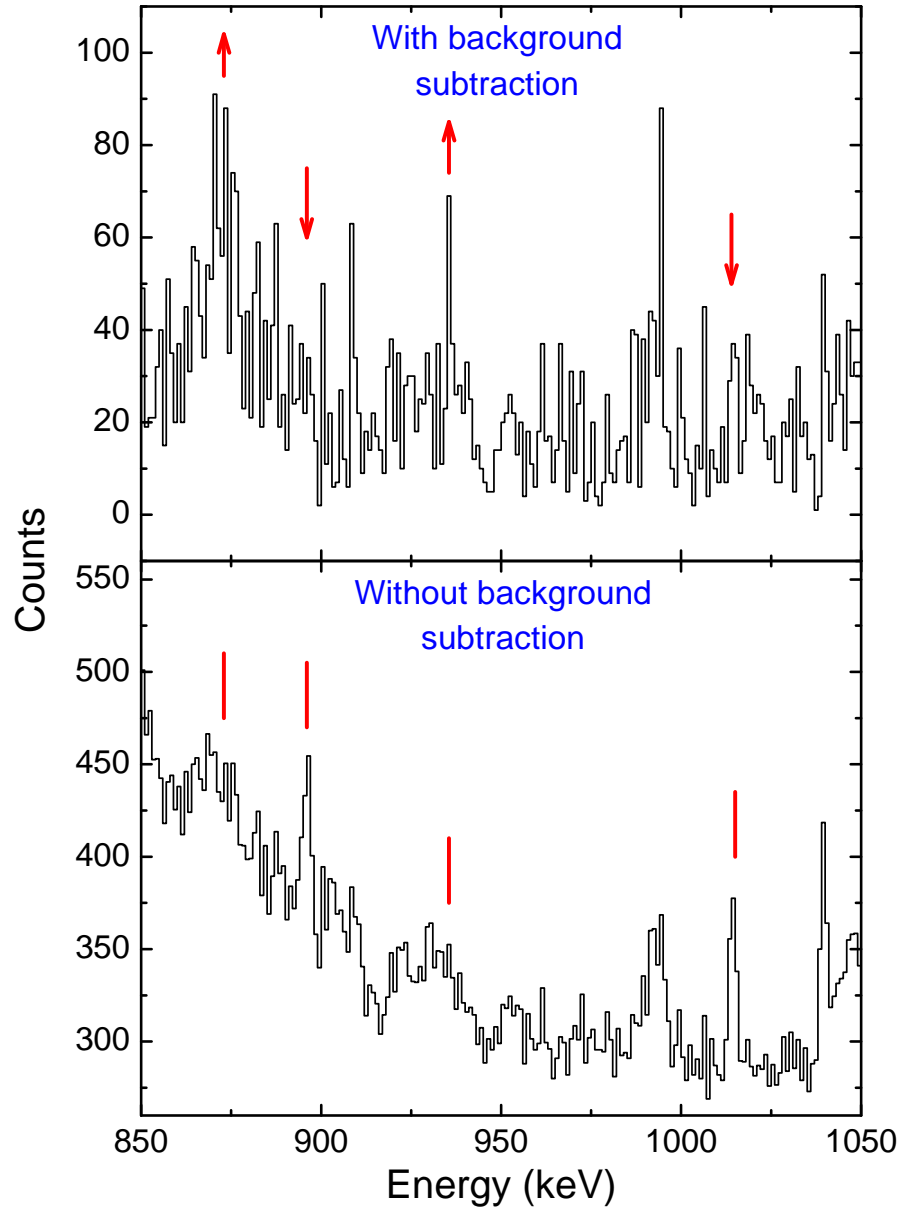
Figure 2.15. Comparison between a background-subtracted spectrum and the spectrum without background subtraction double-gated on the same transitions of the band TSD1 in ^{163}Tm (see Sec. 3.2.2 in Chapter 3 for the band configuration). The method presented in Ref. [57] was used for background subtraction. The spectra are summed over Gammasphere rings 2 to 5. Note the appearance of the true peaks (marked with ↑ symbols) and the disappearance of the background peaks (marked with ↓ symbols) in the background-subtracted spectrum; see text for details.

studied. Hence, with the help of Radware, the level scheme of the nucleus can generally be constructed using the techniques described in the literature, such as Refs. [7] and [58]. Nevertheless, a specific method for identifying those high-spin transitions which are very weak and perhaps Doppler-shifted or -broadened will be introduced in Chapter 4. In a level scheme, transitions within a rotational band are assumed to be of $E2$ character, while transitions between bands which carry one or two units of angular momentum normally correspond to either $E2$, $E1$, or $M1$ multipolarity. In order to determine the multipolarities of γ rays, the angular distribution of each γ ray involved will be studied. The angular distribution is defined in the expression of γ-ray intensity $(W(\theta))$ as a function of the angle θ with respect to beam direction as:

$$W(\theta) = A_0[1 + A_2 P_2(\cos\theta) + A_4 P_4(\cos\theta)], \qquad (2.23)$$

where $P_2(\cos\theta)$ and $P_4(\cos\theta)$ are the Legendre polynomials, A_0 represents the γ-ray intensity, and the coefficients A_2 and A_4 depend on the multipolarity (L) of the γ ray. Typical values of the A_2 and A_4 coefficients are summarized in Table 2.3.

With the help of a powerful detector array, such as GS, and of the proper data storage technique, the Blue database, these angular distribution coefficients A_0, A_2, A_4 can be extracted from data conveniently for transitions with sufficient statistics. Hence, the multipolarities of these γ rays can be determined through the comparison of measured A_2 and A_4 coefficients with typical values. In most of cases, the band heads, *i.e.*, the lowest-spin level in a band, have been observed in particle-decay (for example: β-decay) experiments. Sometimes, the yrast cascade was also established previously. Normally, the spins and parities of these known

TABLE 2.3

TYPICAL VALUES OF ANGULAR DISTRIBUTION
COEFFICIENTS A_2, A_4 FOR γ RAYS WITH DIPOLE (D),
QUADRUPOLE (Q), OR MIXED DIPOLE-QUADRUPOLE ($D+Q$)
MULTIPOLARITY. NOTE THAT ΔI DENOTES THE DIFFERENCE
OF SPIN BETWEEN INITIAL AND FINAL STATES, WHILE L
REPRESENTS THE MULTIPOLARITY. TAKEN FROM REF. [59]

ΔI	L	Sign of A_2	Sign of A_4	Typical value of A_2	Typical value of A_4
2	Q	$+$	$-$	$+0.3$	-0.1
1	D	$-$		-0.2	0.0
1	Q	$-$	$+$	-0.1	$+0.2$
1	$D+Q$	$+/-$	$+$	-0.8 to $+0.5$	0.0 to $+0.2$
0	D	$+$		$+0.35$	0.0
0	Q	$-$	$-$	-0.25	-0.25
0	$D+Q$	$+/-$	$-$	-0.25 to $+0.35$	-0.25 to 0.0

states have been determined. Therefore, if the multipolarities of the transitions
connecting the states of interest to those known levels (the yrast or low-spin states
with known spins and parities) are obtained in an angular distribution measure-
ment, the spins and parities of associated states will be assigned in accordance
with Eqs. 1.29 and 1.30 in Chapter 1.

CHAPTER 3

TRIAXIAL STRONGLY DEFORMED BANDS IN ^{163}Tm

3.1   Triaxiality in nuclei

3.1.1   Introduction

It is well known that the shape of a nucleus can be either deformed or spherical (see the discusssion in Sec. 1.2.2 of Chapter 1). In most deformed nuclei the quadrupole deformation is dominant, and, so far, nuclear spectra have been associated mostly with axially symmetric deformed shapes, $i.e.$, with either prolate or oblate deformation. However, triaxial deformation (for example, a nuclear shape with parameters: $\varepsilon_2 > 0$ and $|\gamma| \sim 20°$), $i.e.$, deformation implying the breaking of axial symmetry, has attracted much attention over the past decades since it opens a new dimension to the study of collective nuclear rotation in the sense that the rotation of axially symmetric nuclei becomes a limit to a more general description. Triaxiality relates to a nucleus with a shape characterized by three unequal principal body-fixed axes. Its occurence in nuclei has been a longstanding prediction of nuclear structure theory. In such triaxial nuclei, the mass distribution and, therefore, the moment of inertia is different along each of the three principal axes.

As discussed in Sec. 1.2.4 of Chapter 1, the calculation of the total energy of the nuclear system with the Strutinsky-shell correction, $i.e.$, the Strutinsky method, has proved to be successful in predicting where in the nuclear landscape deforma-

tion occurs. However, in order to account for collective rotation, the Strutinsky method must be transferred to the rotating frame of reference. Hence, when calculating the total energy of a rotating nucleus, Routhians are often used which represent the energy in the rotating frame. The results of such calculations are called Total Routhian Surfaces (TRS) [60, 61]. On the other hand, in the classical book of nuclear theory by Bohr and Mottelson [9], it was suggested that: "...there is no clear-cut evidence for the occurence of stable nuclear deformation without axial symmetry... It is possible, however, that such shapes may be encountered for states with high angular momentum...". Therefore, the more recent TRS calculations predict the occurrence of stable triaxial deformation at high spin, *i.e.*, the rotation has a direct impact on global nuclear deformation. For example, as can be seen in Figure 3.1, the TRS calculations for the $N \sim 94$ and $Z \sim 71$ region by the means of the so-called "Ultimate Cranker" (UC) model [62], based on a modified harmonic oscilator potential, predict two stable triaxial minima $(\varepsilon_2, \gamma) = (0.38, \pm 20°)$ at high spin. The calculations have by now been validated by experimental results - see Ref. [63]. Triaxiality in this region will be discussed further in Sec. 3.1.3.

Experimental signatures for a triaxial shape are difficult to establish, and, as a result, conclusive evidence has only appeared in the last few years, although the phenomenon was predicted more than 25 years ago. Triaxiality has now been invoked to describe various phenomena, including so-called chiral bands and wobbling bands. Both types of collective structures are now widely accepted as unique fingerprints for triaxiality.
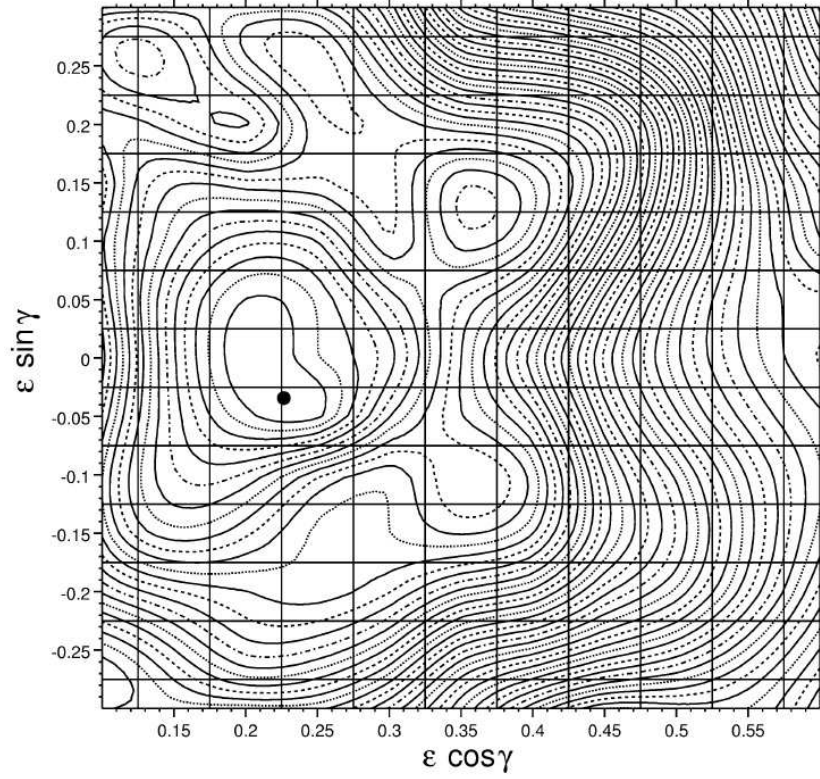
Figure 3.1. Total Routhian Surface (TRS) for the $N \sim 94$ and $Z \sim 71$ region calculated by means of the "Ultimate Cranker" (UC) model [62] at $I^\pi = 61/2^+$. A normal deformed minimum at $\varepsilon_2 = 0.23$ and two triaxial strongly deformed minima at $(\varepsilon_2, \gamma) = (0.38, \pm 20°)$ are clearly seen. Adapted from Ref. [63].

3.1.2 Triaxiality and chiral bands

One of the best examples for chirality in nature is our hands – the left hand can not be superimposed upon the right hand by means of rotation. More generally, any object with chirality can not be superimposed on its mirror image by means of a rotation only. Chirality often appears in molecules and is typical of biomolecules. Nuclei had originally been thought to be chiral symmetric, *i.e.*, not exhibiting chirality, because they consist of only two species of nucleons and have relatively simple associated shapes as compared to molecules. However, if the angular momentum $\vec{J}$ does not lie on any of the three principal axes in a triaxial nucleus, the combination of the three axes with $\vec{J}$ becomes chiral [64]. Figure 3.2 illustrates how chirality emerges from the combination of dynamics (the angular momentum) and geometry (the triaxial shape). When nuclei are triaxially deformed with $\gamma \sim 30°$, the moments of inertia along the three principal axes will satisfy the relation $\Im_s \sim \Im_l < \Im_i$, where l, s and i represent the long, short and intermediate axes, respectively. Let's consider a nucleus with one (or more) proton in an orbital just above the Fermi surface (particle) and one (or more) neutron just below the Fermi surface (hole). The protons align their angular momentum j_π along the axis s. This orientation maximizes the overlap of their orbitals with the triaxial density, which corresponds to minimal energy, since the core-particle interaction is attractive. The orientation of the angular momentum of neutron holes is aligned along the axis l and minimizes the overlap of their orbitals with the triaxial density, reflecting the fact that the core-hole interaction is repulsive. The collective angular momentum of the core R is preferably oriented along the intermediate axis i, which has the largest moment of inertia, because the density distribution achieves the largest deviation from rotational symmetry with respect

to this axis. The total angular momentum, J, therefore, is out of any of the planes determined by the three principal axes. With respect to the frame defined by the three axes, a system with such total angular momentum has either a left-handed configuration (J') or a right-handed one (J). Reverting the direction of the component of the angular momentum on the axis i changes the chirality.

The left-handed and right-handed configurations are related to each other by $|l\rangle = \mathcal{T}\mathcal{R}_y(\pi)|r\rangle$ [64]. The operator $\mathcal{T}\mathcal{R}_y(\pi)$ is the time reversal operator combined with rotation about the y-axis by 180°. The simplest model case was considered as a high-j particle and a high-j hole coupled to a triaxial rotor with ratios $\Im_i = 4\Im_s = 4\Im_l$ between the moments of inertia. It was first studied by Frauendorf and Meng [65, 66]. They showed that the experimental signature of chiral rotation consists of two $\Delta I = 1$ bands of the same parity with nearly degenerate energy, i.e., the so-called chiral doublet bands, which are connected by $E2$ and $M1$ mixed transitions. The interband $E2$ transitions are strongly suppressed, as compared to the inband $E2$ transitions, whereas the interband and inband $M1$ transitions are comparable in strength. Of course, there is always the possibility of two planar bands that are accidentally degenerate and would mimic chirality. Hence, evidence for the phenomenon should rest on all the signatures described above.

So far, a number of pairs of nearly degenerate $\Delta I = 1$ sequences of the same parity have been seen in odd-odd nuclei with mass A $\sim$ 100 [67, 68, 69] and A $\sim$ 130 [70, 71] and have been interpreted as chiral doublets. However, it is also worth to point out that the argument of chirality in nuclei is based only on the symmetry of the rotating triaxial nucleus, and is independent of how the three components of the angular momentum are composed [64]. Therefore, chirality is expected for all configurations that have substantial angular momentum components along the
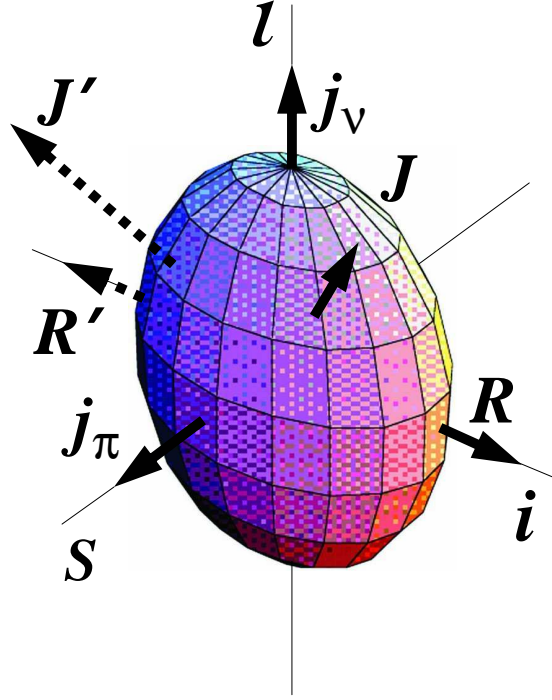
Figure 3.2. Chirality in nuclei. l, s and i represent long, short and intermediate axes, respectively. j_π and j_μ are angular momenta originating from the protons and neutron holes near to the Fermi surface. R is angular momentum of the collective rotation. The total angular momenta J and J', corresponding to two opposite angular momenta, R and R', respectively, introduce the left-handed and right-handed configurations. The figure is adapted from Ref. [7].

three principal axes, no matter how the individual components are composed. It is of fundamental importance to find a composite chiral pair of rotational bands in a system with more than two quasi-particles in order to clearly establish the general geometric character of this phenomenon. Such is the case in ^{135}Nd [72], a nucleus studied by the Notre Dame group, for which strong experimental evidence is available at the present time both in terms of energies of the chiral partner bands and in terms of the inband and interband transitions rates.

3.1.3 Trixial strongly deformed band and wobbling

Unlike the chiral bands, which are associated with a special arrangement of the angular momenta with respect to the triaxial shape and the small deformation of the nucleus ($\varepsilon_2 \sim 0.2$), rotational sequences measured in A $\sim 160 - 175$ nuclei [63, 73, 74, 75, 76, 77, 78, 79, 80, 81, 82, 83, 84, 85] have been associated with stable triaxial deformation in a strongly deformed well, as predicted by theory [62, 75] for this mass region. Because these observed sequences have relatively large deformation ($\varepsilon_2 \sim 0.4$), which agrees with various theoretical predictions [75, 86, 87, 88], they are often referred to as triaxial strongly deformed (TSD) bands. In the literature, these TSD bands are interpreted as based on the deformation driven either by the $i_{13/2}$ proton intruder orbital, *e.g.*, for cases in several even-N Lu isotopes [63, 73, 74, 75, 76, 77, 78, 79, 81], or by the $i_{13/2}$ proton orbital coupled to different neutron orbitals, *e.g.*, for cases in odd-N Lu nuclei [76, 80]. Further, very recently, some of the observed TSD bands in nuclei of the region, *i.e.*, ^{161,163,165,167}Lu, have been identified as so-called "wobbling bands" [63, 77, 79, 81, 89], the spectroscopic representation of the wobbling mode (excitation) which is generally considered as the other unambiguous fingerprint for nuclear triaxiality.

It was first suggested by Bohr and Mottelson that a natural and unique consequence of a rotating triaxial nucleus is the occurrence of the wobbling excitation. In triaxial nuclei, where different moments of inertia ($\Im_x > \Im_y \neq \Im_z$) are associated with the three principal axes, rotation about the three axes is quantum mechanically possible. The wobbling mode, analogous to the classical motion of an asymmetric spinning top in which perturbations are superimposed on the main rotation around the principal axes (as shown in Figure 3.3), is indicative of the three-dimensional nature of collective nuclear rotation [9]. In the quantum

picture, the low-spin spectrum of such a system corresponds to that of the well-known Davydov asymmetric rotor. However, the low spin data do not allow a clear distinction between a rigid rotor and a system that is soft with respect to triaxial deformation. In the high-spin limit ($I \gg 1$), although rotation about the axis with the largest moment of inertia ($\Im_x$) is favored, the contributions from rotations about the other two axes can force the rotation angular momentum vector (R) off the principal axis to create a precession or wobbling mode. As a result, a triaxialy-deformed nucleus will exhibit a family of rotational cascades, called wobbling bands, each of which is associated with a wobbling phonon number ($n_w = 0, 1, 2, ...$) [90]. So far, wobbling bands with n_w up to 2 have been observed in Lu nuclei [79]. The energy of levels in a wobbling band can be given by:

$$E_R(I, n_\omega) = \frac{I(I+1)}{2\Im_x} + \hbar\omega_w(n_w + \frac{1}{2}),$$

(3.1)

where $\hbar\omega_w = \hbar\omega_{rot}\sqrt{(\Im_x - \Im_y)(\Im_x - \Im_z)/(\Im_y\Im_z)}$ with $\hbar\omega_{rot} = I/\Im_x$ [9]. In the intrinsic system (x, y, z), the quadrupole moments can be written as [9]:

$$Q_0 \equiv \langle \sum_k (2z^2 - x^2 - y^2)_k \rangle;$$

(3.2)

$$Q_2 \equiv \langle \sqrt{3/2} \sum_k (x^2 - y^2)_k \rangle,$$

(3.3)

and $\tan\gamma = \sqrt{2}(Q_2/Q_0)$. The strength of interband transitions,

$$B(E2; n_w, I \to n_w - 1, I - 1) = \frac{5}{16\pi}e^2\frac{n_w}{I}(\sqrt{3}Q_0 x - \sqrt{2}Q_2 y)^2,$$

(3.4)

is smaller than the one of inband transitions,

$$B(E2; n_w, I \rightarrow n_w, I - 2) \approx \frac{5}{16\pi} e^2 Q_2^2, \qquad (3.5)$$

by a factor of n_w/I, which represents the square of the amplitude of the precessional (wobbling) motion [9].

The characteristics of a wobbling band family have been summarized [77, 78] as: (1) the bands are associated with very similar intrinsic structure, $i.e.$, alignment, moment of inertia, quadrupole moment, $etc.$ Each excited band with the quantum number $n_w = 1, 2, ...$ can be seen as a wobbling phonon excitation built on the yrast $n_w = 0$ band; (2) the $\Delta I = \pm 1$ interband transitions, $n_w \rightarrow n_w - 1$ with $n_w = 1, 2, ...$, possess large values of $B(E2)_{out}$ (in contrast, small values of $B(M1)$), in competition with $B(E2)_{in}$ of the inband $\Delta I = 2$ transitions. The quantal phonon rule for transition probability implies that $B(E2; n_w = 2 \rightarrow n_w = 1) = 2B(E2; n_w = 1 \rightarrow n_w = 0)$ and the transitions with $\Delta n_w = 2$ are forbidden; (3) the bands are all associated with large ε_2 values and, hence, large quadrupole moments, Q_t, because of being built on a TSD minimum.

The following sections in this chapter will focus on the investigation of the TSD bands in the ^{163}Tm nucleus and the possibility of finding wobbling in this nucleus.

3.2   TSD band structures in ^{163}Tm

3.2.1   Motivation

Until very recently, the fact that wobbling bands had only been observed in several ($A = 161, 163, 165, 167$) Lu isotopes, and not in any other element remained
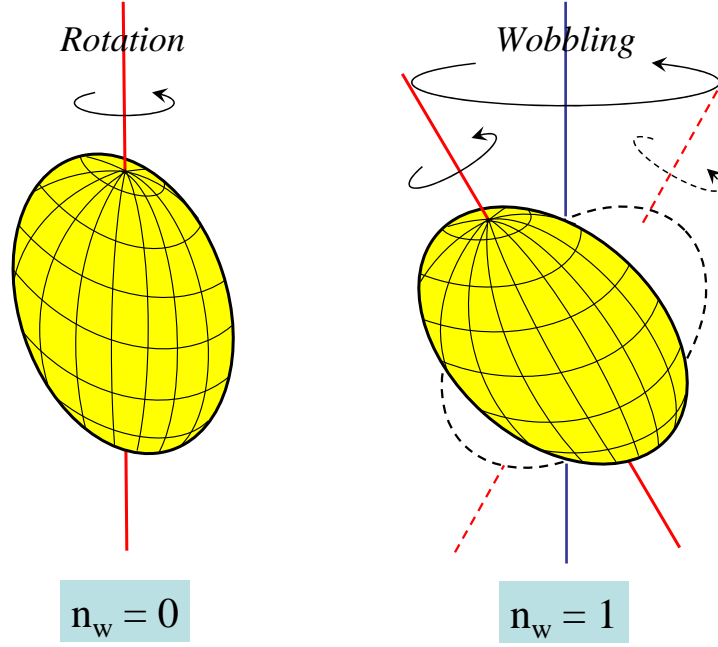
Figure 3.3. A schematical illustration of the wobbling motion of a rotating nucleus with triaxial shape in the classical view. n_w is the wobbling quantum number. The left ($n_w = 0$) and right ($n_w = 1$) panels correspond to the yrast and the first excited wobbling bands, respectively.

somewhat of a puzzle. Indeed, a number of TSD bands have been reported in many of the neighboring Ta and Hf nuclei of the region [82, 83, 84, 85, 91, 92], (up to 8 TSD bands in case of ^{174}Hf!), many of which may be grouped into possible families based on similarities of their dynamic moments of inertia, but none of them was found to exhibit deexcitation properties characteristic of the wobbling mode. In particular, the important $\Delta I = 1$, $E2$ interband transitions that provide a clear signature for wobbling in the Lu isotopes are absent.

A possible resolution of this issue has been proposed in our recent work of exploring the TSD band structures in the ^{163}Tm nucleus, which was recently published [93]. In this work, two strongly interacting TSD bands were identified. However, the linking transitions between TSD bands did not exhibit properties similar to the ones characteristic of wobbling. Rather, they seemed akin to what would be expected for collective structures associated with particle-hole (p-h) excitations in a TSD well. Still, this ^{163}Tm case represents the first time that two TSD bands with interconnecting transitions have been observed in any element other than Lu. The results of the work of Ref. [93] are discussed in some detail in the next two subsections.

3.2.2   Experiment and data

A typical Gammasphere "stand-alone" experiment was carried out with the 170-MeV ^{37}Cl beam, provided by the 88-inch cyclotron facility at the LBNL, and an isotopically enriched ^{130}Te target foil of about 0.5-mg/cm^2 thickness, *i.e.*, a so-called "thin" target. A total of about one billion events was accumulated. The data analysis was performed using the standard techniques, introduced in Sec. 2.5 of Chapter 2, and resulted in a partial level scheme of ^{163}Tm expanded
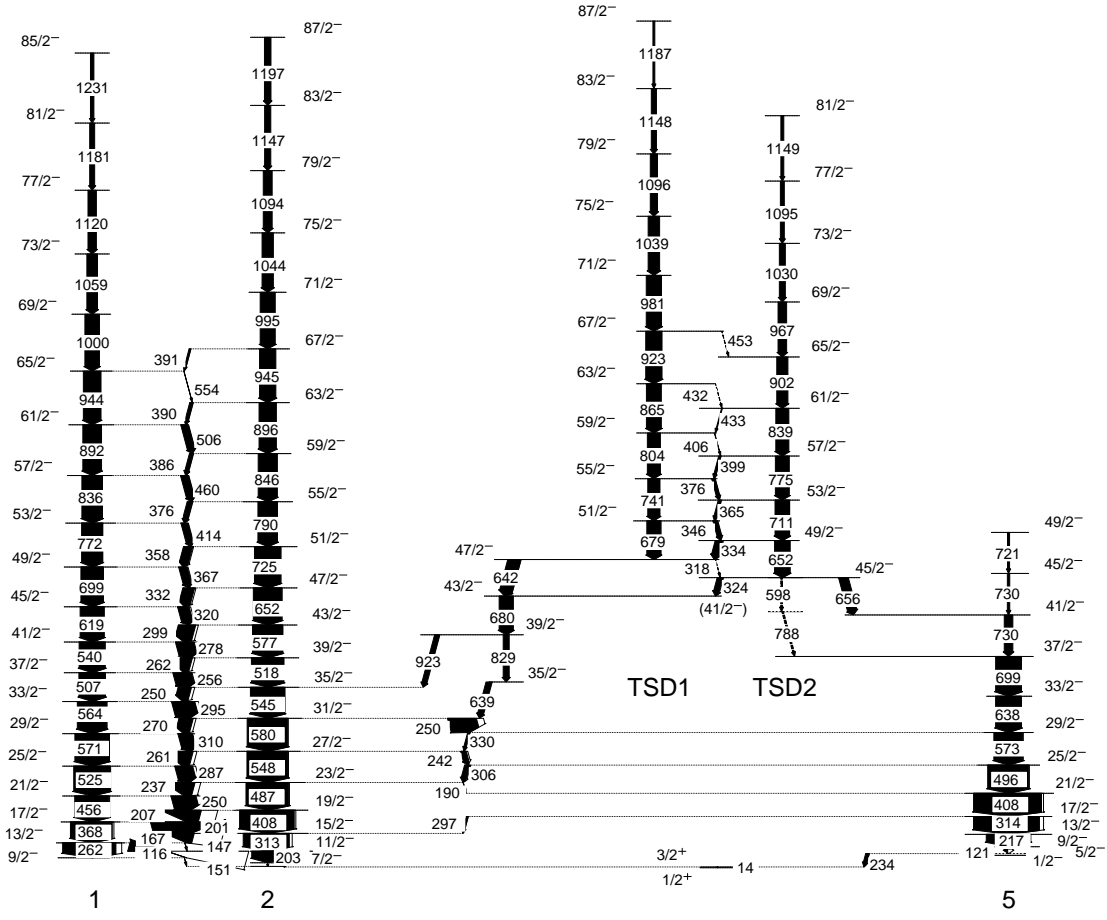
Figure 3.4. Partial level scheme of ^{163}Tm, showing the TSD bands as well as the yrast bands. Adapted from Ref. [93].

with respect to earlier work [94]. As can be seen in this level scheme (Figure 3.4), the two known yrast cascades [94], *i.e.*, bands 1 and 2, are now extended up to spins $85/2^-$ and $87/2^-$, respectively, and two new excited bands (labeled as TSD1 and TSD2) are observed as well. The relevant supporting spectra can be found in Fig. 2 in Ref. [93].

From the established level scheme, the alignment, i_x, and the dynamic moment of inertia, $\Im^{(2)}$, for each band have been extracted and are plotted as a function

of rotational frequency, $\hbar\omega$, in Figure 3.5. Both the alignments and the dynamic moments of inertia indicate that these four bands can be grouped into two families, *i.e.*, bands 1 and 2 in one, and, bands TSD1 and TSD2 in the other. As discussed below, the TSD1 and TSD2 bands are proposed to be associated with Triaxial Strongly Deformed (TSD) structures.

In the top panel of Figure 3.6, the experimental excitation energies of these proposed TSD bands as well as the yrast bands are shown, while the corresponding values calculated in the Cranked Nilsson-Strutinsky (CNS) model [95, 96, 97] and the Tilted-Axis Cranking (TAC) model [64, 98, 99] are presented in the bottom panel. It is worth pointing out here that the TAC model is an approach seeking the solutions to the time-dependent Schrödinger equation of a single particle in the intrinsic frame of nucleus (*i.e.*, Eq. 1.46 in Sec. 1.3.3 of Chapter 1) in the case of uniform rotation about an axis that is tilted with respect to the principal axes of the deformed density distribution [64]. Usually, three Euler angles θ, ϕ and ψ are used to specify the orientation of the principal axes in the body-fixed frame, denoted by $\hat{1}$, $\hat{2}$ and $\hat{3}$, with respect to the laboratory system, denoted by x, y and z. As can be seen in Figure 3.7, $\psi(=\omega t)$ is the angle that increases as the nucleus rotates around the z-axis, while the angles θ and ϕ determine the orientation of the rotation axis, *i.e.*, the z-axis. The CNS model is a special case of the TAC approach with the rotation axis fixed along one of the principal axes, *i.e.*, the interpolation technique into the cranked shell correction approach for the so-called Principal-Axis Cranking (PAC) solutions [64] (the correspnding orientation angles satisfy $\theta = 0, \pi/2$ and $\phi = 0, \pi/2$).

The measured excitation energies of TSD bands in ^{163}Tm are quite different from the ones of the wobbling bands seen in Lu (see for example, Fig. 14 in
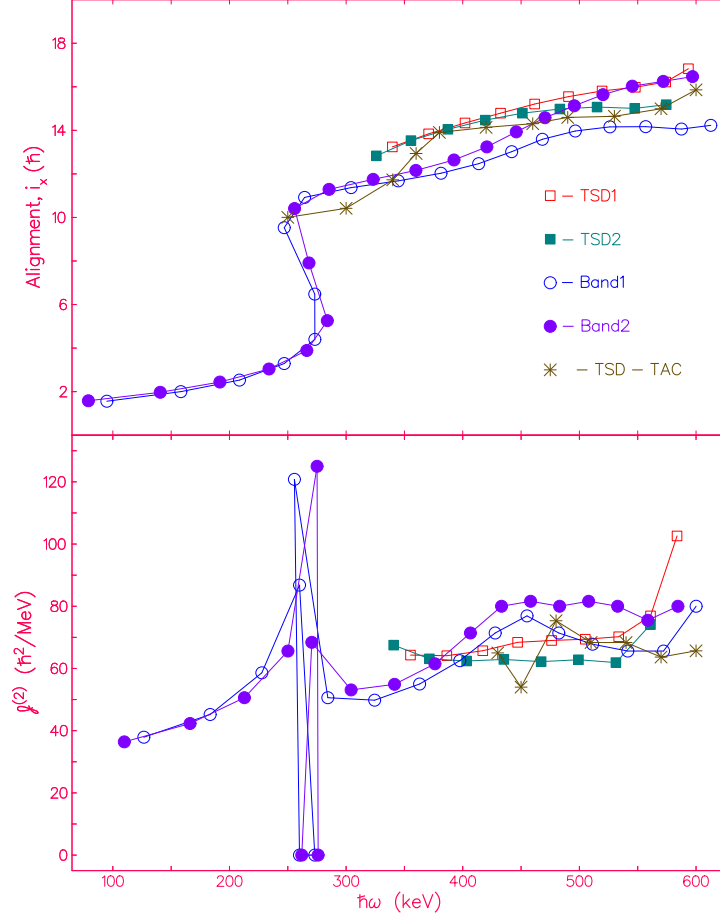
Figure 3.5. Aligned spins i_x (upper panel) and the experimental dynamic moments of inertia $\Im^{(2)}$ (lower panel) for the two TSD bands in ^{163}Tm as a function of rotational frequency. The subtracted reference for the alignment is $I_{ref} = J_0\omega + J_1\omega^3$ with the Harris parameters $J_0 = 30\hbar^2 MeV^{-1}$ and $J_1 = 40\hbar^4 MeV^{-3}$. The theoretical values for alignments and moments of inertia were obtained from the calculations in the TAC model. Adapted from Ref. [93].
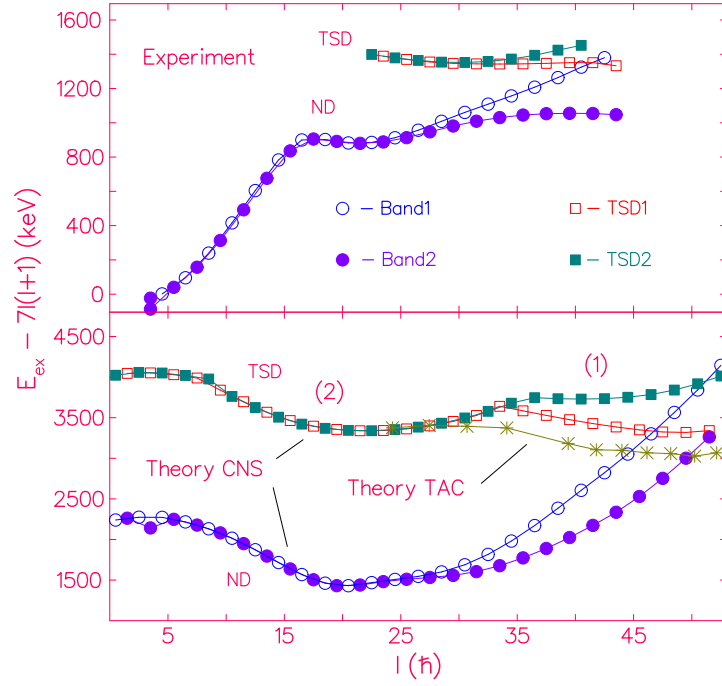
Figure 3.6. Excitation energies relative to a rotational reference for the two TSD bands and the two ND bands (1 and 2) in ^{163}Tm: the experimental data (top) and the calculated result in the CNS and the TAC models (bottom). The numbers (1) and (2) with the CNS calculation refer to the two associated TSD minima, respectively (presented in Figure 3.8). Adapted from Ref. [93].
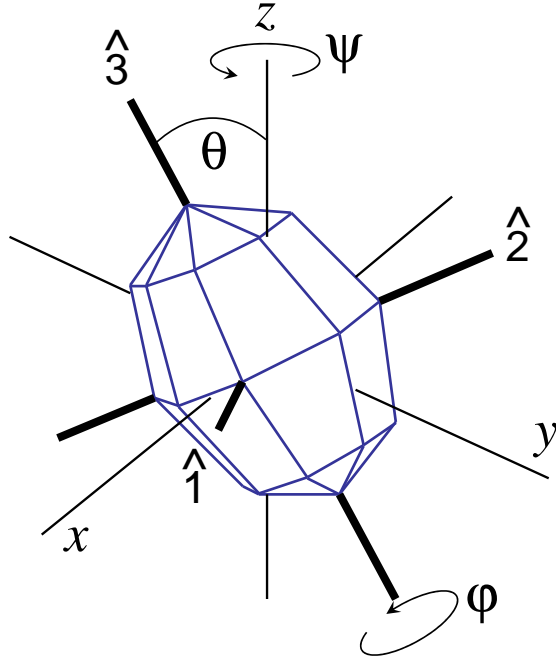
Figure 3.7. The Euler angles specifying the orientation of the triaxial density distribution in the laboratory frame. A polyeder shape is shown, which makes the geometry more visible. The principal axes $\hat{1}$, $\hat{2}$ and $\hat{3}$ are the thick lines and the laboratory axes x, y, z are thin ones. Adapted from Ref. [99].

Ref. [78]). This observation seems to suggest a different nature for the two TSD bands in ^{163}Tm, which is further supported by the structure of the linking transitions. These transitions connecting the two TSD bands in ^{163}Tm are not similar to the ones characteristic of wobbling, $i.e.$, the linking transitions go both ways between the two TSD bands in ^{163}Tm, whereas the connecting transitions always proceed only from a wobbling band to another with a lower n_w value in Lu.

3.2.3 Interpretation and discussion

In order to understand the observed properties of these bands in ^{163}Tm, the calculations in both the CNS and the TAC models were carried out. The potential energy surface (see Figure 3.8), resulting from the CNS calculations for a configuration with $(\pi, \alpha) = (-, -1/2)$ (see details below) at spin $I^\pi = 63/2^-$, indicates a prolate minimum at normal deformation (ND) ($\varepsilon_2 \approx 0.21$) and two triaxial strongly deformed (TSD) minima. The two TSD minima have nearly the same energy. It can be seen clearly in the bottom panel of Figure 3.6 that minimum 2 is energetically favored at low spin while minimum 1 becomes lower at high spin. The two minima have almost the same value of ε_2 and $|\gamma|$, indicating that both are associated with the same shape. The axis of rotation is the short one in minimum 1 (with $\gamma > 0$), while it is the intermediate one for minimum 2 (with $\gamma < 0$). Thus, the CNS calculations suggest that at $I = 24$, where minimum 1 goes below minimum 2, the orientation of the rotational axis flips from the intermediate axis to the short one. This sudden flip is caused by the inherent assumption in the CNS model that the rotational axis must be a principal one, and in fact indicates that this assumption of rotation about a principal axis is inappropriate in this case. Therefore, the TAC calculations, which do not re-

strict the orientation of the rotational axis, should be adopted to interpret the observations in this experiment. As expected, a tilted solution with lower energy was found, which smoothly connects minimum 2 with minimum 1. For $I > 23$, the angular momentum vector moves away from the intermediate axis toward the short axis. It does not quite reach it within the considered spin range. (For $I \sim 50$, the angle with the intermediate axis is still about 20°.) This solution is assigned to bands TSD1 and TSD2. In accordance with the experiment, it corresponds to a $\Delta I = 1$ band without signature splitting. As can be seen in Figure 3.6, the observed onset of signature splitting at the highest spins is consistent with the calculated approach of the TAC solution in minimum 1 of the CNS result. At large frequency, the calculated TSD bands have a lower energy than the ND ones, while the data show that only band 1 crosses band TSD1 above $I = 40$ (band 2 remains yrast up to the highest spins), $i.e.$, the experimental energy difference between the ND and TSD minima is somehwat larger than the calculated values at the highest spins. Moreover, Figure 3.5 demonstrates that the calculated alignments and the dynamic moments also agree with the measured ones. Hence, all experimental observables for the TSD bands in ^{163}Tm are well reproduced by the TAC calculations.

Further, the single proton routhians in both of the TSD minima were calculated and are shown in Figure 3.9. The configurations that we assign to the obseved TSD bands (indicated by the large filled circles in Figure 3.9) are the lowest with negative parity and small signature splitting, in agreement with the experiment. As discussed in Ref. [93], the CNS calculations also predict four competing TSD configurations (named TSD3, TSD4, TSD5, and TSD6 in the discussion below) at somewhat lower energy than TSD1 and TSD2. The positive-parity configurations
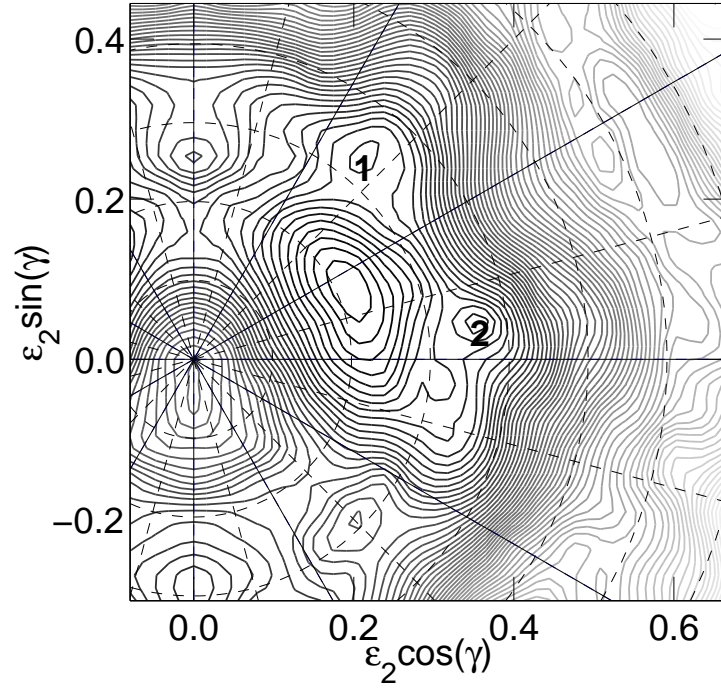
Figure 3.8. Potential energy surface for ^{163}Tm calculated in the CNS model at spin $63/2^-$. The two TSD minima are marked by 1 and 2, consistent with the labels used in Figure 3.6. Adapted from Ref. [93].

TSD3 and TSD4 have the odd proton on one of the [411]1/2 routhians and have both $h_{11/2}$ signatures occupied; they are predicted by the CNS calculations to lie about 500 keV below TSD1 at spin 20 and have a larger energy above spin 50. However, as can be seen in Fig. 10 of Ref. [94], some residual proton pair correlations in the lower-spin part will disfavor the configurations TSD3 and TSD4 with respect to TSD1 and TSD2. The configurations TSD5 and TSD6, with both signatures of the $h_{11/2}$ orbital occupied and the odd proton on one of the two $h_{9/2}$ routhians, would correspond to two well-separated $\Delta I = 2$ sequences with little resemblance to the experiment. The favored signature branch, TSD5, is predicted by the CNS calculations to lie about 500 keV below TSD1 at spin 20 and to have a larger energy than TSD1 above spin 40. We note here that the location of the $h_{9/2}$ orbital has been a longstanding open problem in calculations using the modified oscillator potential (cf. the discussion in Ref. [94]).

The relevant single-proton routhians in the ND minimum can be found in Ref. [100]. Comparing them with the routhians in the TSD minima (see Figure 3.9), one finds that the $h_{11/2}$ orbital has a larger splitting between the two signatures, which reflects the proposed smaller deformation. Further, the $h_{11/2}$ levels are shifted up by about 2 MeV. Hence, bands 1 and 2 are interpreted as the signature partners of a configuration with an odd proton on the $h_{11/2}$ level at the Fermi surface and a pair of protons on the [411]1/2 orbitals. This assignment is further supported by the fact that the observed signature splitting between bands 1 and 2 is consistent with the CNS calculation based on the above configuration (shown in Figure 3.6). It is also worth pointing out that, in contrast with previous calculations with $Z > 69$ and $N{\sim}94$ [63, 77, 78, 79, 81, 89], the $i_{13/2}$ proton level is empty in ^{163}Tm, which means that this level is not essential in forming the TSD
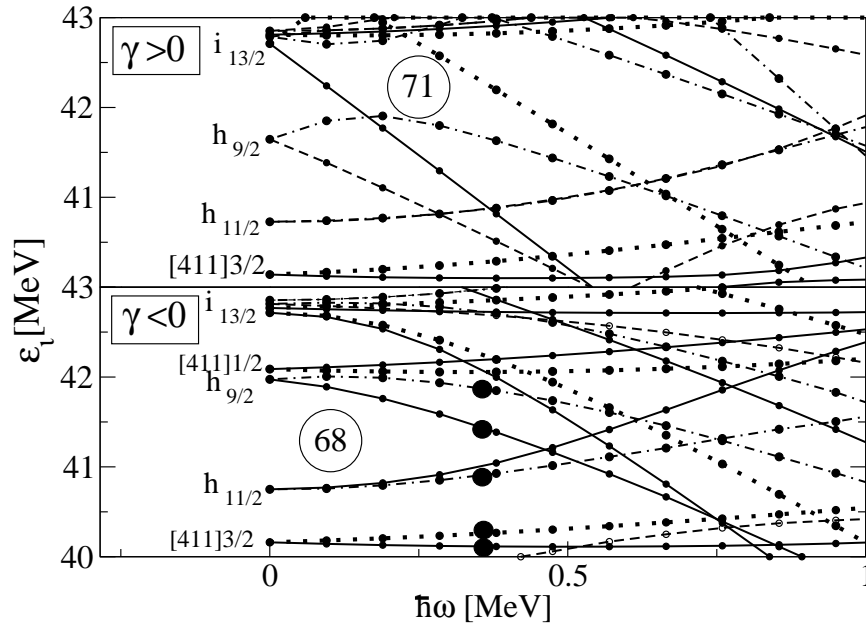
Figure 3.9. Single-proton routhians as function of rotational frequency in TSD minima 1 (top) and 2 (bottom). The line convention is: $(\pi, \alpha) = $ (+,1/2) full, (+,-1/2) dot, (-,1/2) dash, (-,-1/2) dash dot. The deformation parameters used in the calculations are: $\epsilon_2 = 0.39$, $\epsilon_4 = 0.05$, $|\gamma| = 17°$. Adapted from Ref. [93].

minima. Rather, it is the $N = 94$ gap in the neutron routhians at $\varepsilon_2 = 0.39$, $|\gamma| = 17°$ (see Figure 3.10) that stabilizes the TSD shape. We will return to this point further below.

A natural explanation is provided by the calculated single-proton routhians in Figure 3.9 for the presence of collective wobbling excitations in the Lu isotopes with $Z = 71$ and their absence in ^{163}Tm with $Z = 69$. The TSD configurations of nuclei with $Z > 69$ belong typically to minimum 1 with $\gamma > 0$ [100]. For $Z = 71$, the Fermi level is the signature $\alpha = 1/2$ routhian of $i_{13/2}$ parentage in the frequency range $250~keV < \hbar\omega < 450~keV$. The lowest TSD band is observed in this frequency range and has parity and signature $(+, 1/2)$. The lowest particle-hole (p-h) excitation of the same parity lifts the odd proton onto the other signature, $\alpha = -1/2$ of this $i_{13/2}$ level, which lies at a relatively high energy ($\sim 1~MeV$ at $\hbar\omega = 0.4~MeV$)). This brings the collective wobbling excitation, which has an energy of about $0.3~MeV$, well below the lowest p-h excitations. For $Z = 69$, however, the two signatures of the $h_{11/2}$ state are quite close together (see Figure 3.6). Therefore, the wobbling excitation lies above the p-h excitations, likely too high in excitation energy to be populated with observable strength in the reaction employed in the present study. It is also worth mentioning that the relative energy of the collective wobbling mode and of the p-h excitations in ^{163}Lu has been studied by means of the particle-rotor model [102], where the p-h excitations have been called the "cranking mode" [77]. They are found to be located well above the one-phonon wobbling excitation. With the level order suggested in Figure 3.9, one can expect, for $Z = 69$, that a band structure similar to the wobbling bands seen in $Z = 71$ is positioned at somewhat higher energy. It may be obtained by lifting the last proton from
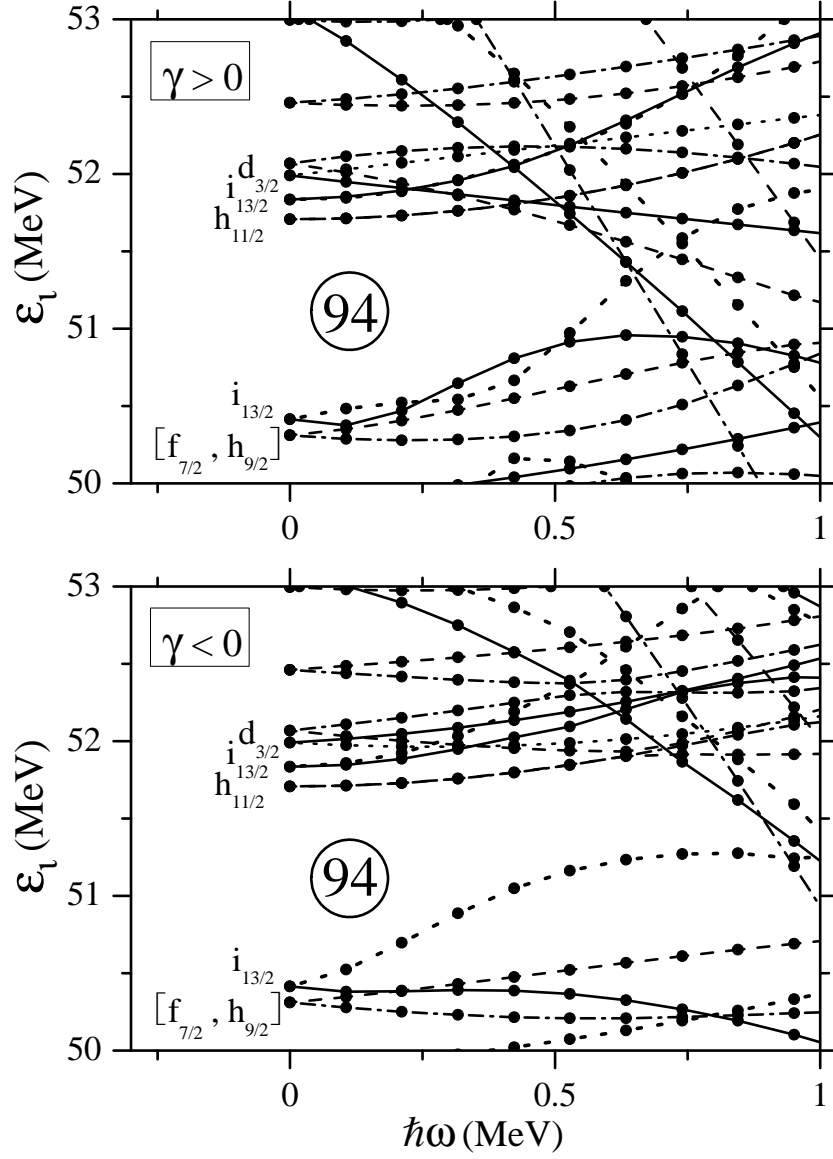
Figure 3.10. Single-neutron routhians as function of rotational frequency in TSD minima 1 (top) and 2 (bottom). The line convention is: $(\pi, \alpha) = (+, 1/2)$ full, $(+, -1/2)$ dot, $(-, 1/2)$ dash, $(-, -1/2)$ dash dot. The deformation parameters used in the calculations are: $\epsilon_2 = 0.39$, $\epsilon_4 = 0.05$, $|\gamma| = 17°$. Adapted from Ref. [101].

the $h_{11/2}$ into the $i_{13/2}$ orbital. For $Z = 73$, several TSD bands of both parities with similar energy are also expected. The possibility to experimentally identify a wobbling band is restricted by the competition of this collective excitation with the p-h excitations, $i.e.$, the wobbling band may become the first excitation mode above the yrast line, if its energy is lower than the energy of the p-h excitations. Such a case appears to occur in several odd-A Lu isotopes. Moreover, a large gap at $N = 94$, which is found in the neutron diagrams (Figure 3.10) prevents the neutron p-h excitations from competing with the wobbling mode in the Lu isotopes. The opposite scenario occurs in ^{163}Tm, where the energy for the p-h excitations between the signature partners of the $h_{11/2}$ orbital is smaller than the wobbling energy. In our experiment, only the first excited band, which corresponds to the p-h excitations, appears to have received sufficient intensity to be observed. However, the apparent absence of the wobbling mode does not necessarily imply a near-axial shape. If this was the case, there would be a conflict with the above calculations as well as with earlier ones [100].

3.3 Lifetime measurements of TSD bands in ^{163}Tm

3.3.1 Motivation

In the earlier structure work (see Sec. 3.2 as well as Ref. [93]), the interpretation of the two ^{163}Tm sequences as TSD bands rested solely on indirect experimental indications (such as the magnitude and evolution with frequency of the moments of inertia) and on the agreement with the calculations. Therefore, with the purpose to verify directly that the proposed TSD bands are associated with a larger deformation than the yrast sequences as well as to further test how well the TAC model predicts or reproduces the experimental observations in the region, another

experiment with the 165 MeV ^{37}Cl beam and a "thick" ^{130}Te target was performed using the ATLAS facility at ANL. The detailed configuration of the target used has been described in Sec. 2.4.2 of Chapter 2. In this experiment, the lifetimes and, hence, the quadrupole moments for the four ^{163}Tm bands were measured by means of the DSAM technique (see Sec. 2.4.2 of Chapter 2).

3.3.2   Experiment and data

The details of the performed DSAM experiment have been given in Sec. 2.4.2 of Chapter 2. In the six-day run, over 1.5×10^9 coincidence events with fold ≥ 3 were collected by Gammasphere. Since the DSAM technique involves the detection of γ rays during the slowing down process in the thick target, the relation between the average energy shifts and detector angles needs to be determined. For this purpose, the raw data were sorted into several BLUE database files. Subsequently, the background-subtracted spectra at a given detector angle under specific coincidence requirements, required by the DSAM mesurement, were achieved conveniently with the method introduced in Sec. 2.5.3 in Chapter 2. It is worth to point out that the proper method of subtracting background is a key factor in the success of such DSAM measurements. Recalling the effect of background subtraction in the process of generating coincidence spectra, as illustrated by Figure 2.15 in Chapter 2, it becomes rather obvious that accurate background subtraction is essential in a process where the crucial information, *i.e.*, the Doppler shift at a given angle, is derived from the determination of peak centroids. In addition, a thorough understanding of the spectra is very important as well since a measured centroid could potentially be in error if the peak is an unresolved doublet of two transitions.

The four rotational bands of interest in the present measurements are the bands 1 ($85/2^-$ – $9/2^-$ sequence) and 2 ($87/2^-$ – $7/2^-$ cascade) associated with the [523]$7/2^-$ configuration and the bands TSD1 ($87/2^-$ – $47/2^-$ sequence) and TSD2 ($81/2^-$ – $45/2^-$ cascade), shown in Figure 3.4. From a first inspection of the coincidence data, it was established that the transitions with energy $E_\gamma \leq 600\ keV$ in bands 1 and 2 did not exhibit any measurable shift or broadening as a function of detector angle. In other words, these deexcitations must have occurred after the recoiling nuclei have come to rest in the Au layer of the target. These "stopped" transitions could thus be used as a starting point to obtain coincidence spectra for each band at ten detector angles, from which energy shifts would subsequently be determined. The use of "stopped" transitions alone proved to be insufficient. Hence, angle-dependent coincidence gates had to be placed on band members in an iterative procedure starting with the lowest γ ray exhibiting a shift and moving up in the band one transition at each step. This procedure could be applied not only to bands 1 and 2, but also to the TSD1 and TSD2 sequences, since the latter deexcite into bands 1 and 2. In the process of selecting appropriate gating conditions, special care was taken to avoid numerous contaminant lines from either other ^{163}Tm band structures or other reaction products, as well as some in-band doublet γ rays. Actually, from the data analysis process it became clear that the cases of contamination can be grouped into two types: (1) the real γ ray of interest can be seen free of contaminant lines in certain spectra with appropriate gating conditions; and (2) the real γ ray of interest can not be distinguished from contaminant lines in any spectroscopic gating technique. For the latter case, *e.g.*, the 680-keV doublet in band TSD1, which corresponds to the $51/2^- \rightarrow 47/2^-$ transition and to the $43/2^- \rightarrow 39/2^-$ transition (see Figure 3.4), the

impact from contaminant can be weakened mostly through a procedure applied in the process of a linear fit to obtain the corresponding $F(\tau)$ value. This method will be discussed later in this subsection. For the transitions affected by contaminants of the first case (distinguishable type), the impact from the contaminant lines can be eliminated and, hence, the real γ rays of interest can be studied accurately in spectra generated with specific gating conditions, as illustrated in Figure 3.11 with the example of the 944-keV line in band 1 and the 945-keV transition in band 2, which affect each other.

Proceeding in this careful manner, an optimized spectrum was obtained at each detector angle by summing up all clean double-gated coincidence spectra with the appropriate gating conditions. These optimized spectra for all four bands (presented in Figures 3.12 – 3.15) were used to determine the centroid of γ-ray peaks of interest at each available detector angle, except for those corresponding to distinguishable contaminated lines. For such transitions, other specific spectra, described above, were used instead. In this context, the analysis of band TSD2 proved to be particularly challenging as it is the one most affected by the closeness in energy of many in-band transitions with either those in band 2 or other contaminant peaks. Hence, as can be seen in Figure 3.15, the peak positions of γ rays in band TSD2 are the most difficult to determine, compared with the ones in the other three bands, because of the relatively poor quality of spectra.

The fractions of full Doppler shift $F(\tau)$ and the associated errors were subsequently extracted for transitions in the four ^{163}Tm bands of interest through linear fits of the shifts measured at 10 angles with the transformed expression of
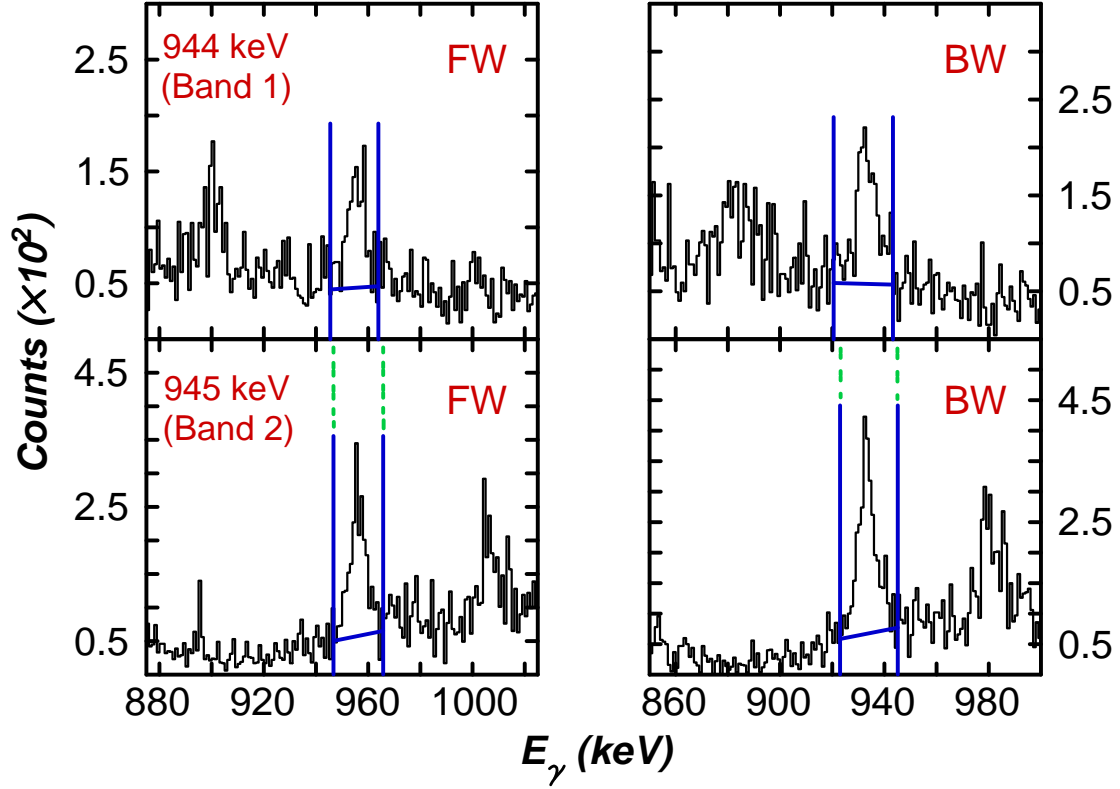
Figure 3.11. Representative summed spectra for accurately determining the peak positions of distinguishable contaminated transitions, the 944-keV line in band 1 and 945-keV line in band 2, at 2 detector angles: 35° (FW) and 145° (BW). The double gates used for producing the two spectra at the top are the combinations of the 1000-keV line in band 1 and any one of the other inband transitions of band 1, while the gates for the two spectra at the bottom are the 896-keV transition in band 2 plus any one of the other inband lines of band 2. The drawn low- and high-limit mark lines for each peak indicate the tiny shift of position from the 944-keV transition to the 945-keV transition.
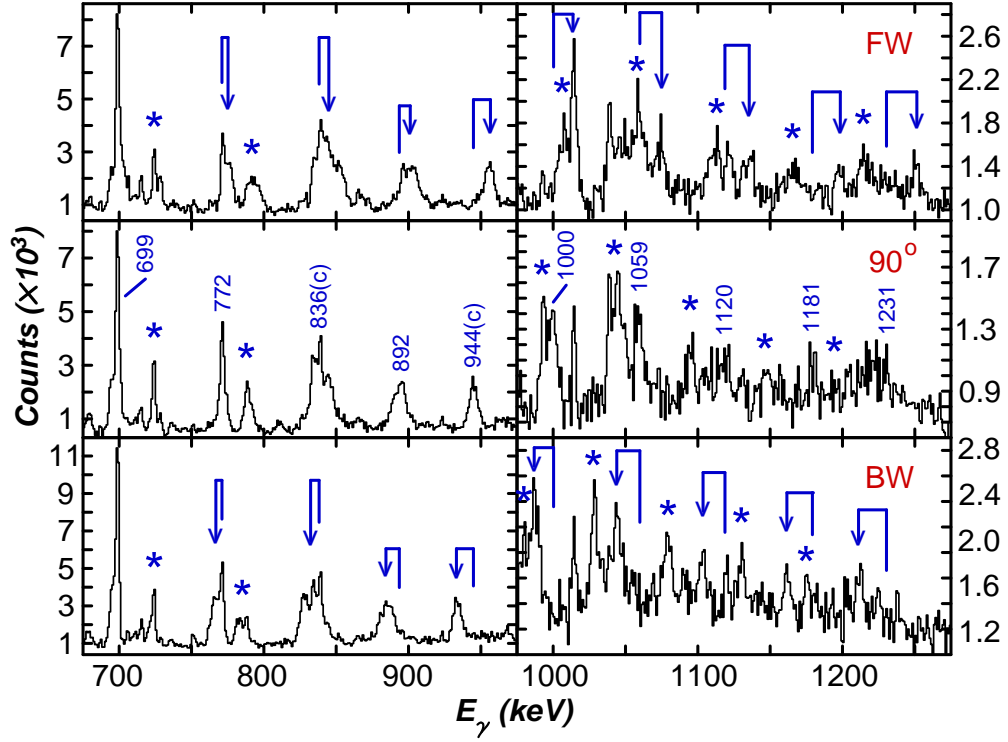
Figure 3.12. Sum of spectra gated on in-band transitions for band 1 at 3 detector angles: 35° (FW), 90°, and 145° (BW). The positions of unshifted and shifted γ rays are marked by energy values and arrows, respectively. Note that transitions from band 2 appear in these spectra (marked with ⋆ symbols) due to the fact that intense connecting transitions occur between the two structures. The transitions labeled by signs in the form of "energy value(c)" are the contaminated lines which need to be taken care of separately (see text for details).
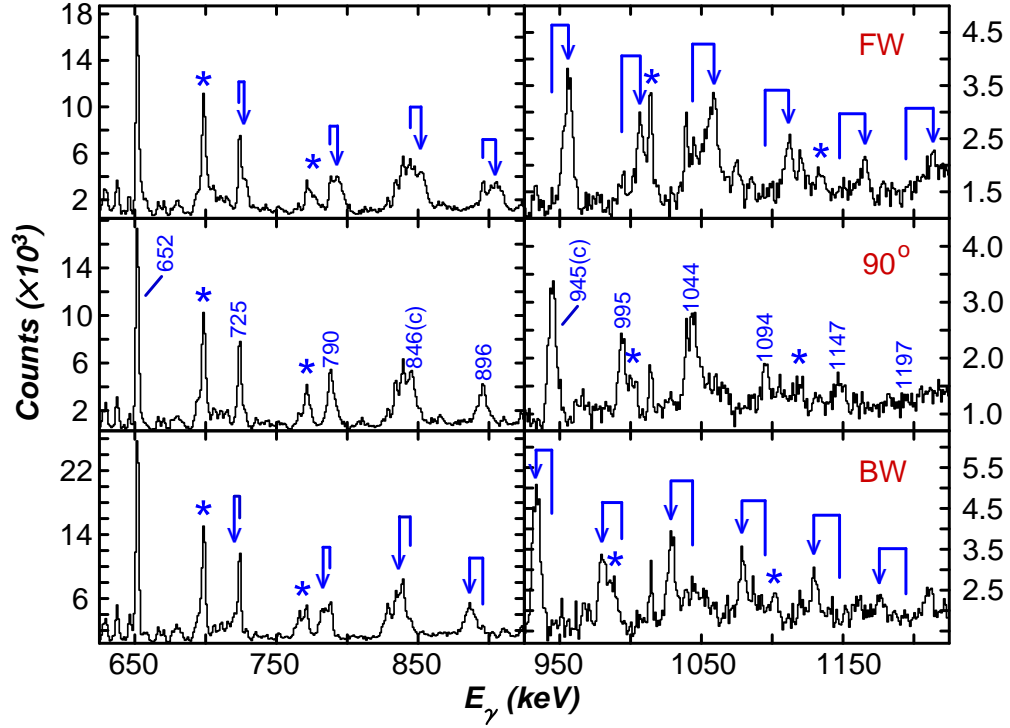
Figure 3.13. Sum of spectra gated on in-band transitions for band 2 at 3 detector angles: 35° (FW), 90°, and 145° (BW). The positions of unshifted and shifted γ rays are marked by energy values and arrows, respectively. Note that transitions from band 1 appear in these spectra (marked with ⋆ symbols) due to the fact that intense connecting transitions occur between the two structures. The transitions labeled by signs in the form of "energy value(c)" are the contaminated lines which need to be taken care of separately (see text for details).
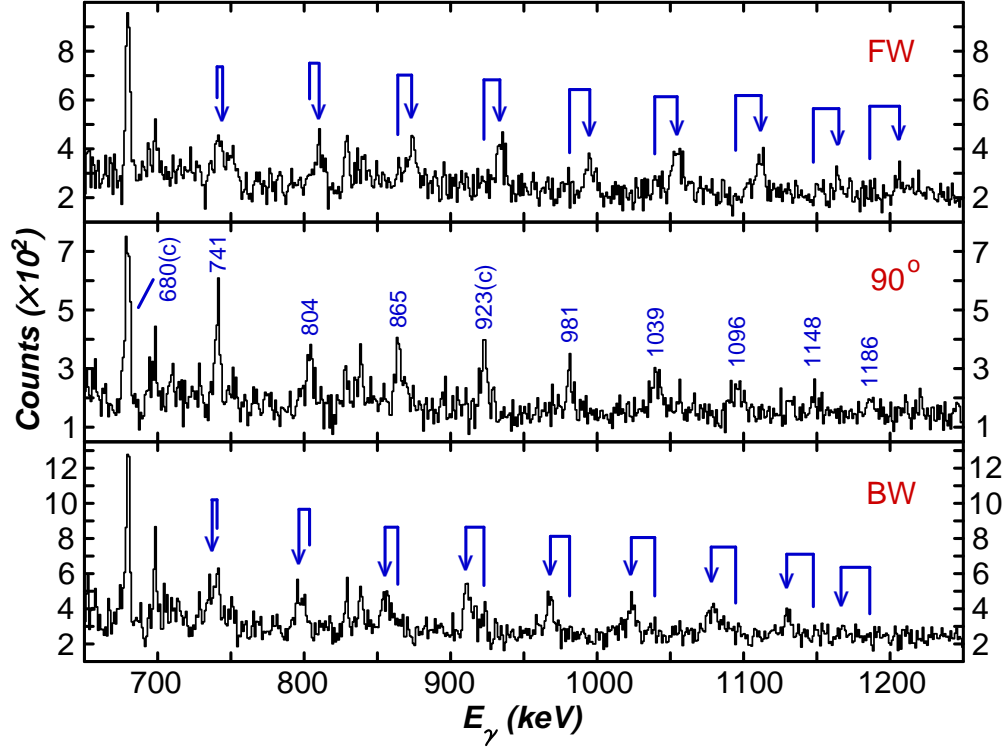
Figure 3.14. Sum of spectra gated on in-band transitions for band TSD1 at 3 detector angles: 35° (FW), 90°, and 145° (BW). The positions of unshifted and shifted γ rays are marked by energy values and arrows, respectively. Note that the transitions labeled by signs in the form of "energy value(c)" are the contaminated lines which need to be taken care of separately (see text for details).
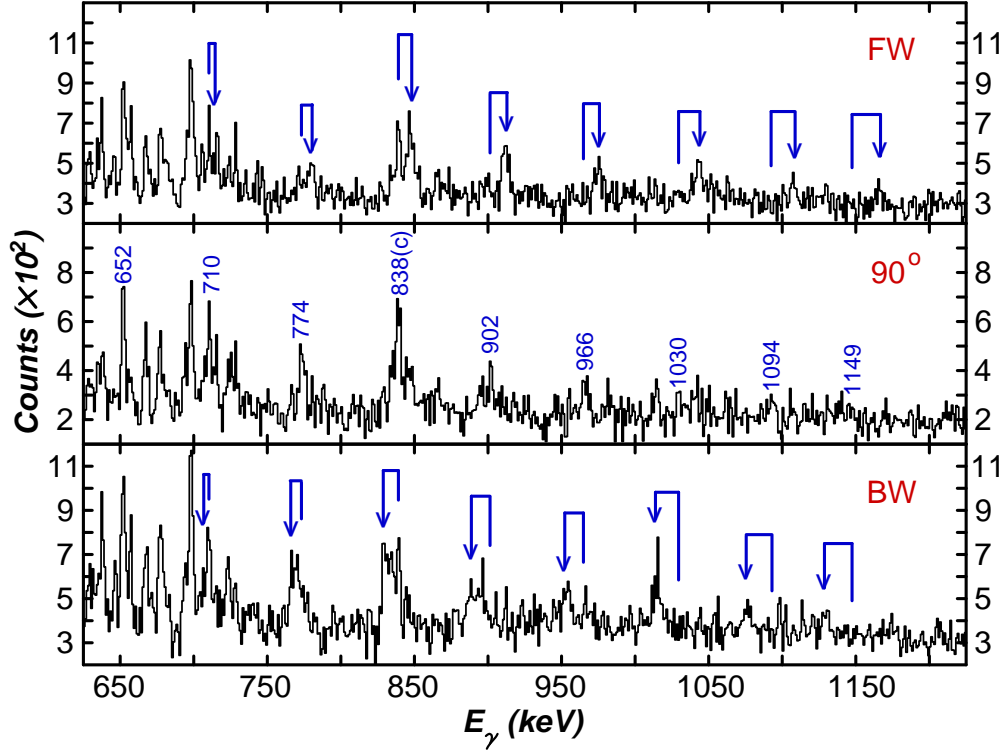
Figure 3.15. Sum of spectra gated on in-band transitions for band TSD2 at 3 detector angles: 35° (FW), 90°, and 145° (BW). The positions of unshifted and shifted γ rays are marked by energy values and arrows, respectively. Note that the transitions labeled by signs in the form of "energy value(c)" are the contaminated lines which need to be taken care of separately (see text for details).

Eq. 2.11 in Sec. 2.4.2 of Chapter 2:

$$F(\tau) = \frac{\overline{E_\gamma} - E_{\gamma 0}}{E_{\gamma 0}\beta_0 \cos(\theta)}. \tag{3.6}$$

Here, for every transition $E_{\gamma 0}$ is the nominal γ-ray energy, $\overline{E_\gamma}$ is the measured energy at the angle θ, and β_0 is the initial recoil velocity of the ^{163}Tm residues formed in the center of the ^{130}Te target layer. This quantity was calculated to be $\beta_0 = v_0/c = 0.021$ with the help of the stopping powers computed with the code SRIM 2003 [51]. Illustration of the linear fits can be seen in Figure 3.16 for bands 1, 2, TSD1 and TSD2.

It has been described earlier in this section that for some of the transitions contaminated by the non-distinguishable lines, such as the 680-keV doublet in band TSD1 and the 838-keV γ ray in band TSD2, the impact from contaminations can be weakened or eliminated through the process of a linear fit. The principle of this method is explained in the example of the 680-keV doublet. As can be seen in the spectra for band TSD1 (figure 3.14), the 680-keV transition is characterized by a marked Doppler shift clearly visible at the detector angles far away from 90°, *e.g.*, 35° (FW) and 145° (BW). In this doublet, the lower-spin 680-keV line, located in the decay sequence of bands TSD1 and TSD2 towards bands 1 and 2, is a "stopped" (no Doppler shift at every angle) transition, while the higher-spin 680-keV line is an in-band transition of band TSD1. The latter is the only possible source of the observed Doppler shift in the spectra. Considering both reliability and accuracy, two fits were performed for this transition (shown in Figure 3.17), *i.e.*, a fit (Fit 1) covering the data points at all angles and second fit (Fit 2) covering the data points only at three angles (θ): 35° (the largest Doppler shift), 90° (always zero Doppler shift for any transition), and 145° (the
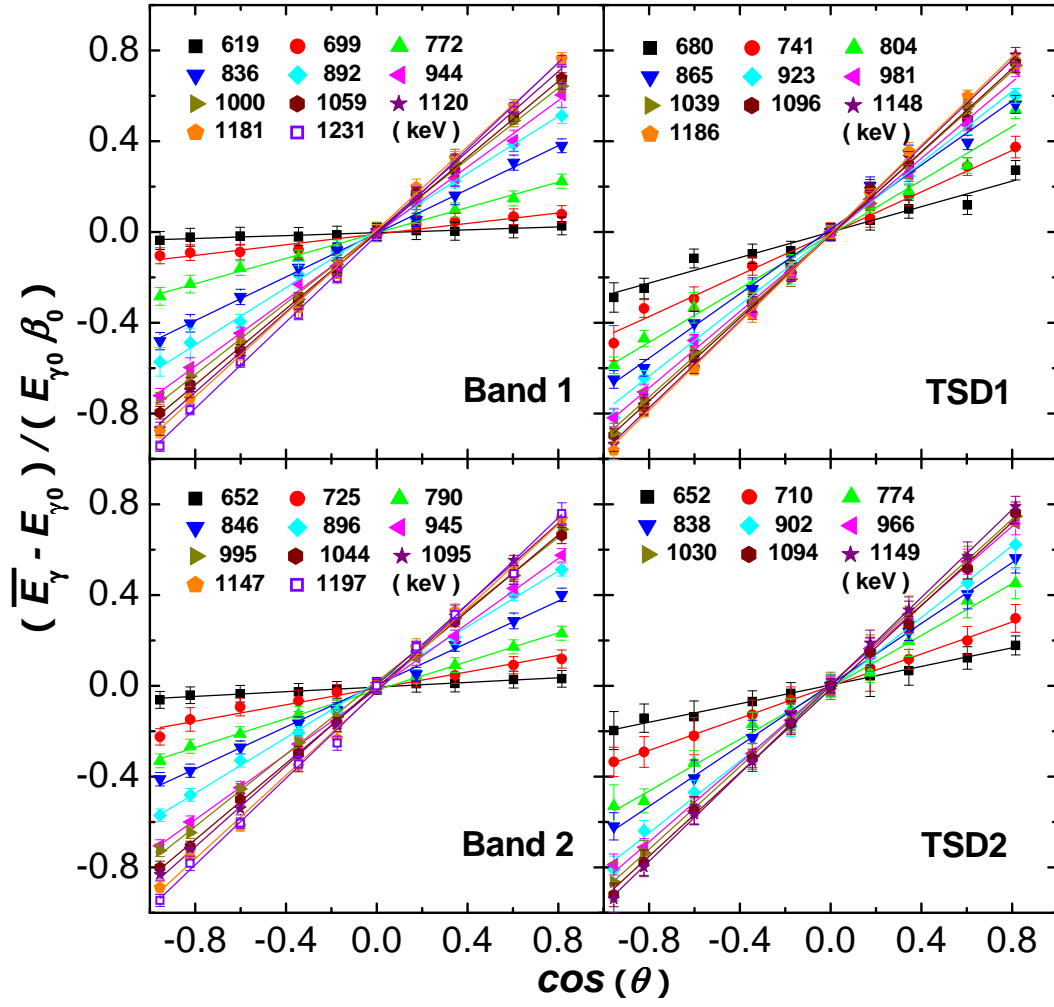
Figure 3.16. Linear fits to the γ-ray energy shifts as a function of $cos(\theta)$ for bands 1, 2, TSD1 and TSD2.

corresponding largest Doppler shift at backward angles). The adopted $F(\tau)$ value for the 680-keV transition in band TSD1 is the average of the slopes of the two fits, while the corresponding error combines the errors obtained in both fits and the variation between the two extracted slopes. As a result, the error bars for the $F(\tau)$ values for such a contaminated transition are considerably larger than those for the neighboring, contaminant-free transitions. This effect is clearly indicated in Figure 3.24, in which the measured $F(\tau)$ values are presented as a function of the γ-ray energy for all four bands.

A cursory inspection of this figure indicates two families of $F(\tau)$ curves: for similar transition energies bands 1 and 2 have distinctly smaller $F(\tau)$ values than bands TSD1 and TSD2. It is also worth noting that the larger $F(\tau)$ uncertainties associated with band TSD2 relate to the difficulty of obtaining suitable spectra as discussed above.

The intrinsic transition quadrupole moments Q_t of the four bands were extracted from the measured $F(\tau)$ values using the new Monte Carlo computer code MLIFETIME, developed by E. F. Moore at ANL. The model of the cascade used in fitting the measured data points is illustrated schematically in Figure 3.18 as a reference for the reader. The following assumptions have been made: (1) all levels in a given band have the same transition quadrupole moment Q_t; (2) the sidefeeding into each level in a band is modeled as a single cascade with a common, constant quadrupole moment Q_{sf}, and characterized by the same dynamic moment of inertia $\Im^{(2)}$ as the main band into which they feed; the number of transitions in each sidefeeding band is proportional to the number of transitions in the main band above the state of interest; (3) the sidefeeding intensity profile and the pattern of the decay out of the main band are determined directly

119
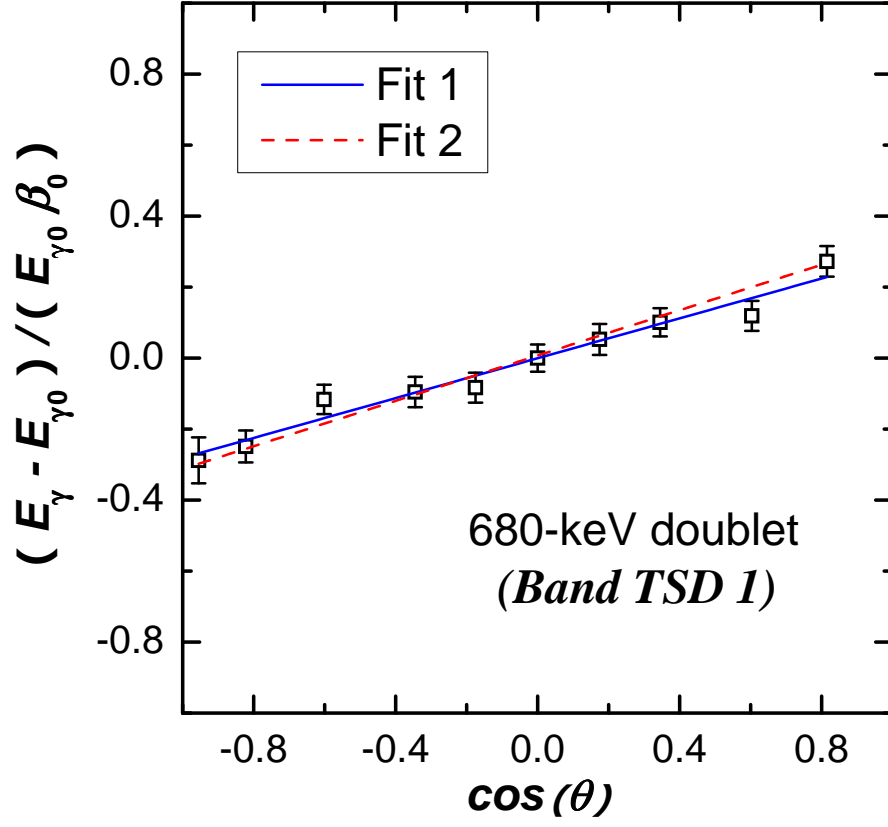
Figure 3.17. Linear fits to the γ-ray energy shifts as a function of $cos(\theta)$ for the 680-keV doublet in band TSD1. Fit 1 covers all data points and Fit 2 considers data points only at three angles (θ): 35°, 90°, and 145°. See text for details.

from the measured γ-ray intensities within the bands; (4) the internal conversion coefficients (α) are also taken into account, and (5) a one-step delay at the top of all feeder bands was parameterized by a single lifetime T_{sf}. The lifetimes of the individual states of interest depend on E_γ (transition energy), I_γ (intensity of the transition), α, Q_t, Q_{sf} and T_{sf}, in which E_γ and I_γ are the quantities measured directly from the spectra. In the simplest case, the mean lifetime T_γ for a particular state, which deexcites only by a $E2$ γ ray, is:

$$T_\gamma = \frac{8.210565 \times 10^6}{Q_t^2 E_\gamma^5 \langle IK20|(I-2)K\rangle^2}, \tag{3.7}$$

where T_γ is in femto-second (fs), E_γ in MeV and Q_t in electron-barn (eb).

In order to determine the average recoil velocity at which the decay from a particular state occurs, the detailed slowing-down histories of the recoiling ^{163}Tm ions in both the target and the Au backing were calculated using the SRIM 2003 [51] Monte Carlo code. The initial positions and velocity vectors for each of 10,000 starting ions were calculated in a Monte Carlo fashion which included the broadening of the recoil cone due to the evaporation of neutrons from the ^{167}Tm compound nucleus. The production cross section was assumed to be constant over the range of energies due to the beam slowing down in the target. This resulted in an even distribution for the starting positions of the ^{163}Tm ions throughout the target thickness. The initial ^{163}Tm ion positions in the target, ion energies, and recoil direction were supplied as input to the SRIM 2003 code, which then transported each ion through the target and the backing. The detailed recoil history for each ion was written out to a computer file which listed the energy, direction, and position at which each collision of the recoiling ^{163}Tm ions with the target and backing atoms occurred. The lifetime code then read in this file and tracked each
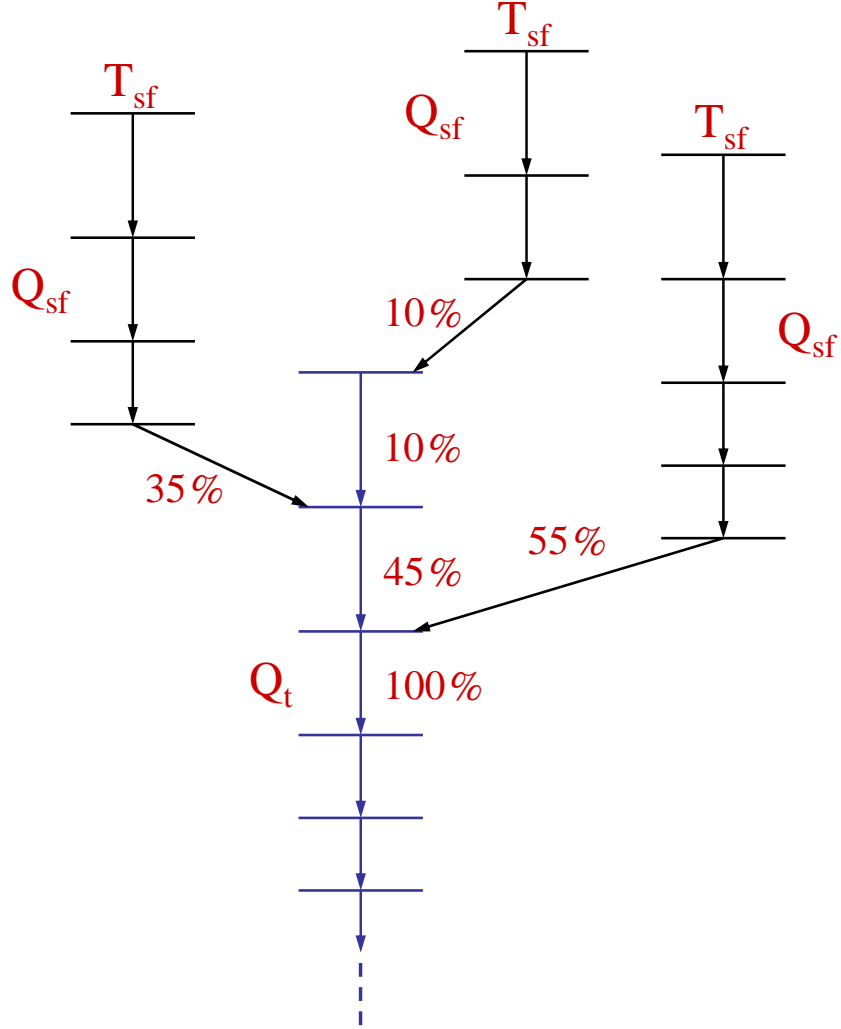
Figure 3.18. A schematic illustration of the model of the cascade used in the analysis to determine the quadrupole moments Q_t. The marked numbers (as examples) represent the relative intensities of associated transitions which affect the fit of the measured $F(\tau)$ values. Adapted from Ref. [50].

ion history in one femto-second (1 fs) time steps from the initial formation until the ion came to rest.

In order to compute the Doppler shifted energies of each γ ray emitted by the recoiling [163]Tm ions in a Monte-Carlo fashion, feeder bands into each state in the main band were randomly populated according to the measured intensity distribution, as shown in Tables 3.1, 3.2, 3.3 and 3.4 (refer to Figure 3.18 for obtaining the relative intensity of the sidefeeding). It is necessary to point out here that the energy of the beam for the thick-target experiment (165 MeV) is slightly different from that for the thin-target run (170 MeV). Hence, in the process of fitting $F(\tau)$ values, we adopted the intensity values measured in our DSAM experiment instead of the values obtained in the earlier thin-target measurement. In order to validate this approach, the intensity distributions for bands 1 and 2 obtained in the thick-target experiment were compared with those from the thin-target data, as illustrated in Figures 3.19 and 3.20. This comparison indicates that the intensity distribution varies slightly between the two experiments. It appears that there is slightly more γ-ray intensity at higher angular momentum in the thin-target data, as would be expected since the higher beam energy translates in an higher angular momentum in the compound nucleus. Further, the intensity distribution for bands 1 and 2, and for bands TSD1 TSD2 are compared in Figures 3.21 and 3.22. The populated intensity of bands TSD1 and TSD2 is approximately 5% relative to the one of bands 1 and 2 in the DSAM experiment. Since these bands are either signature partners (bands 1 and 2) or members of a single TSD family (bands TSD1 and TSD2), the populated intensity for one band should be close to that of the partner band, which is a feature exhibited by the data as seen in Figures 3.21 and 3.22. This observation provides further support for the validity

of the data analysis.

The subsequent decay profile through the feeder and main band was tracked in 1 fs steps, with the decay probability given by the radioactive decay law using the T_{sf} parameter and lifetimes generated from each Q_{sf}, Q_t parameter set (see Eq. 3.7). The velocity vector of the γ emitting ion was recorded at the time of decay of each state of interest. The calculated average fraction of the full Doppler shift was generated by accumulating a large number of histories. In the present analysis, each of the 10,000 ion histories was used 10 times, resulting in better than 1% statistical uncertainty in the calculated $F(\tau)$ values.

A χ^2 minimization using the computer code MINUIT with the fit parameters Q_t, Q_{sf} and T_{sf} was performed to the measured $F(\tau)$ values for the four bands. The results of the fitting process are summarized in Table 3.5, where the quoted errors include the covariance between the fit parameters. In order to illustrate the sensitivity of the $F(\tau)$ values to the values of the parameters Q_t and Q_{sf}, the data points of $F(\tau)$ for band TSD1 are compared to the calculated values with the best-fit parameters as well as to those with other values of Q_t and Q_{sf} in Figure 3.23. The four fit lines with either the best-fit Q_t value and various Q_{sf} values or with various Q_t parameters and the best-fit Q_{sf} value clearly lie away from data points, and the correponding χ^2 values are large. In contrast, the curve with the best-fit parameters agrees well with almost all data points and the corresponding χ^2 value reaches its minimum. As can be seen from Figure 3.24, the fit of the $F(\tau)$ data is satisfactory in all cases. This is illustrated further in the case of band TSD1 in the insert to Figure 3.24, where contours of χ^2 values are presented in a (Q_t, Q_{sf}) plane and a clear minimum can be seen. The corresponding error bars are determined by allowing the total χ^2 of the fit to increase by 1 relative to its
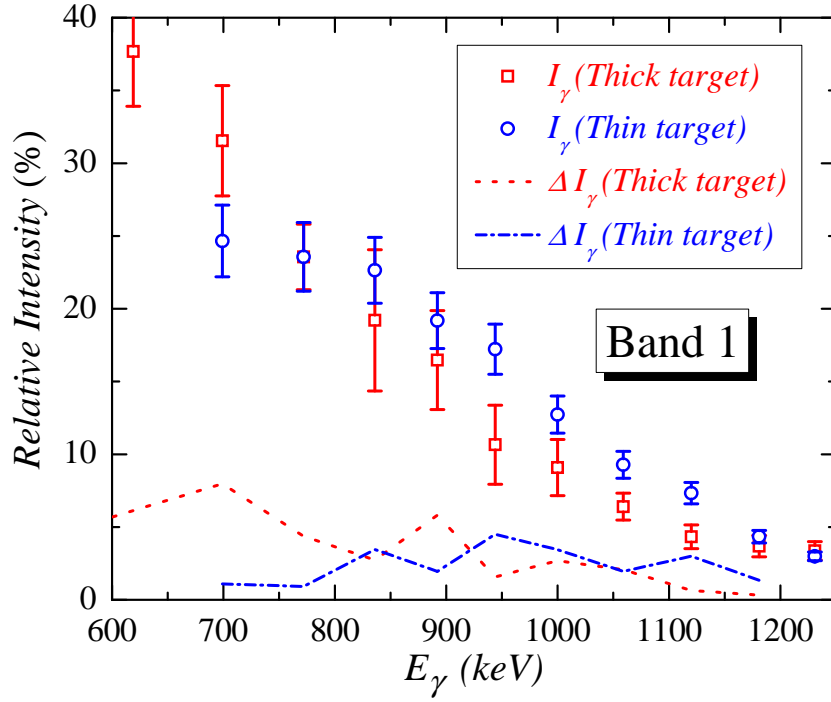
Figure 3.19. The intensity distribution (I_γ) for inband transitions of band 1 obtained in our thick-target experiment, compared with the one from the thin-target data. The parameter, $\Delta I_\gamma = I_\gamma(J{\rightarrow}J-2) - I_\gamma(J+2{\rightarrow}J)$ (J is the spin of level in band 1), represents the strength of the feeding for this band.

minimum (χ^2_{min}) and projecting the contour of ($\chi^2_{min} + 1$) onto the Q_t and Q_{sf} axes [52]. This determination of the error bars is illustrated in Figure 3.25 for the case of band TSD1.
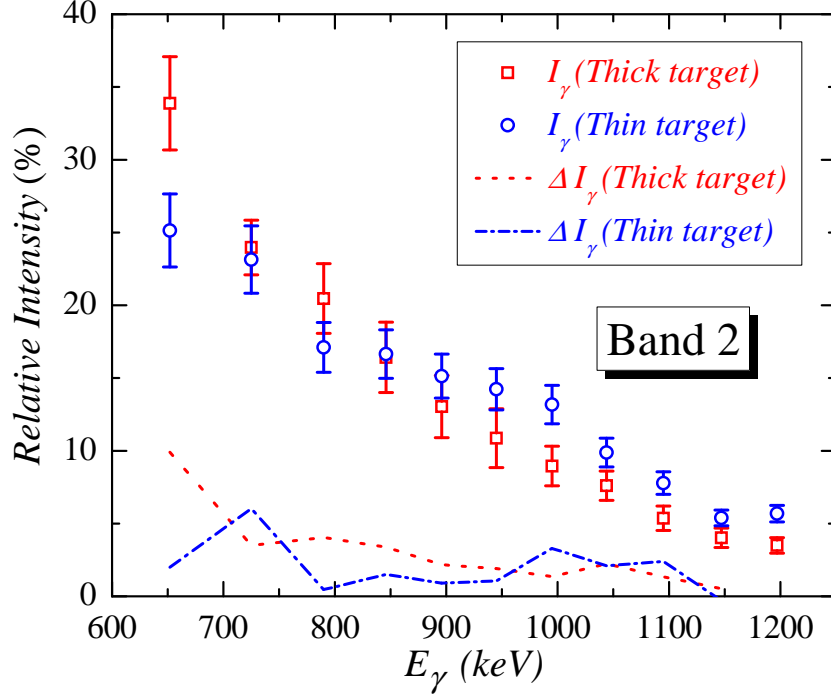
Figure 3.20. The intensity distribution (I_γ) for inband transitions of band 2 obtained in our thick-target experiment, compared with the one from the thin-target data. The parameter, $\Delta I_\gamma = I_\gamma(J{\rightarrow}J-2) - I_\gamma(J+2{\rightarrow}J)$ (J is the spin of level in band 2), represents the strength of the feeding for this band.
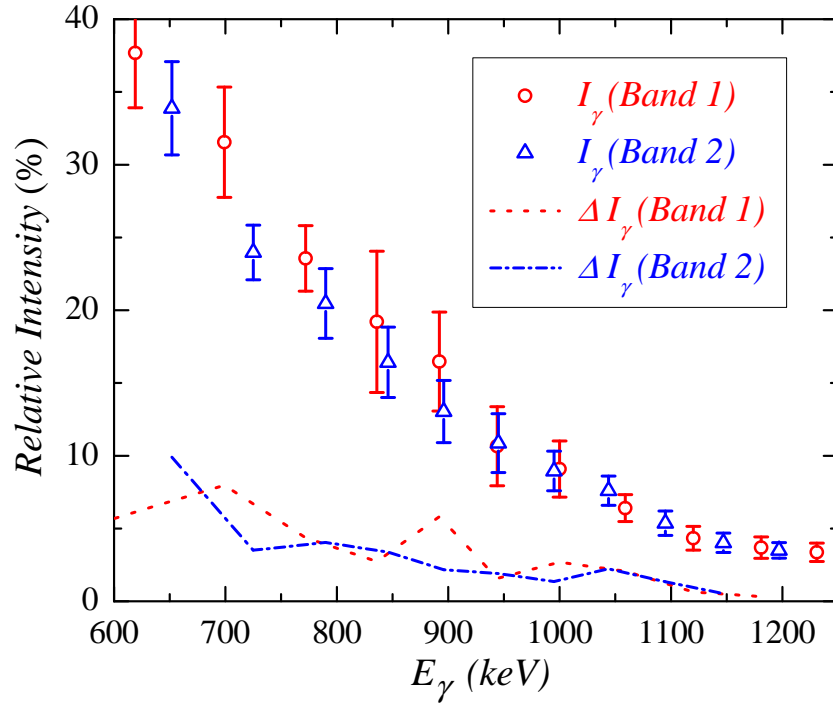
Figure 3.21. The intensity distribution (I_γ) for inband transitions of bands 1 and 2 obtained in our DSAM experiment. The parameter, $\Delta I_\gamma = I_\gamma(J{\to}J-2) - I_\gamma(J+2{\to}J)$ (J is the spin of level in band 1 or 2), represents the strength of the feeding for each band.
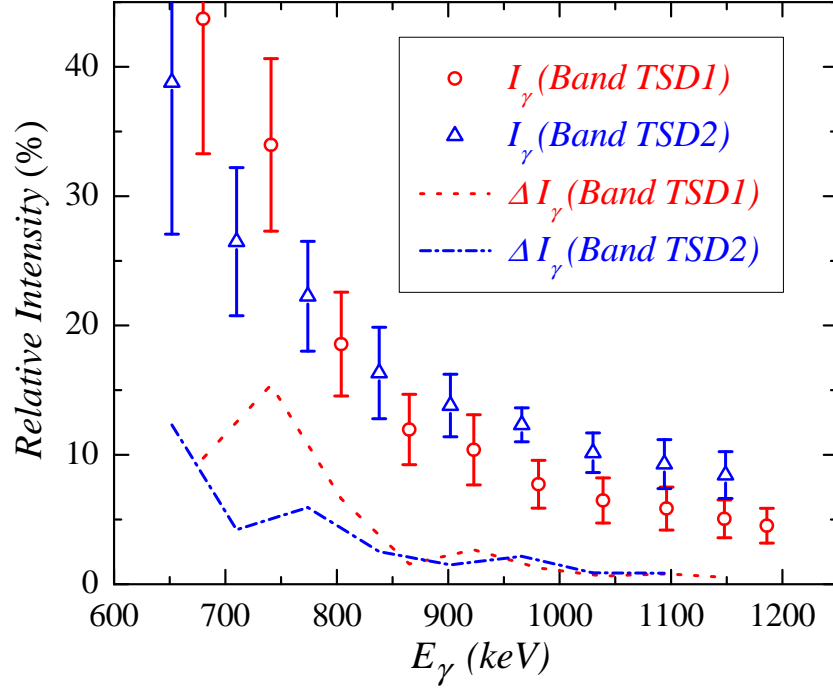
Figure 3.22. The intensity distribution (I_γ) for inband transitions of bands TSD1 and TSD2 obtained in our DSAM experiment. The parameter, $\Delta I_\gamma = I_\gamma(J{\to}J-2) - I_\gamma(J+2{\to}J)$ (J is the spin of level in band TSD1 or TSD2), represents the strength of the feeding for each band.

TABLE 3.1

THE RELATIVE TOTAL INTENSITY (*i.e.*, CORRECTED FOR
EFFICIENCY AND INTERNAL CONVERSION) AND ERROR OF
EACH TRANSITION OF INTEREST IN BAND 1 OF ^{163}Tm,
MEASURED IN THE DSAM EXPERIMENT

E_γ (keV)	Intensity (%)	Error (%)
619	38	4
699	32	4
772	24	2
836	19	5
892	16	3
944	11	3
1000	9	2
1059	6.4	0.9
1120	4.3	0.8
1181	3.7	0.7
1231	3.4	0.6

TABLE 3.2

THE RELATIVE TOTAL INTENSITY (*i.e.*, CORRECTED FOR
EFFICIENCY AND INTERNAL CONVERSION) AND ERROR OF
EACH TRANSITION OF INTEREST IN BAND 2 OF ^{163}Tm,
MEASURED IN THE DSAM EXPERIMENT

E_γ (keV)	Intensity (%)	Error (%)
652	34	3
725	24	2
790	20	2
846	16	2
896	13	2
945	11	2
995	9	1
1044	7.6	1.0
1095	5.4	0.8
1147	4.0	0.7
1197	3.5	0.5

TABLE 3.3

THE RELATIVE TOTAL INTENSITY (*i.e.*, CORRECTED FOR
EFFICIENCY AND INTERNAL CONVERSION) AND ERROR OF
EACH TRANSITION OF INTEREST IN BAND TSD1 OF ^{163}Tm,
MEASURED IN THE DSAM EXPERIMENT

E_γ (keV)	Intensity (%)	Error (%)
680	44	10
741	34	7
804	19	4
865	12	3
923	10	3
981	8	2
1039	7	2
1096	6	2
1148	5	2
1186	5	1

TABLE 3.4

THE RELATIVE TOTAL INTENSITY (*i.e.*, CORRECTED FOR
EFFICIENCY AND INTERNAL CONVERSION) AND ERROR OF
EACH TRANSITION OF INTEREST IN BAND TSD2 OF ^{163}Tm,
MEASURED IN THE DSAM EXPERIMENT

E_γ (keV)	Intensity (%)	Error (%)
652	39	12
710	26	6
774	22	4
838	16	4
902	14	2
966	12	1
1030	10	2
1094	9	2
1149	8	2

TABLE 3.5

SUMMARY OF QUADRUPOLE MOMENTS RESULTING FROM
DSAM CENTROID SHIFT ANALYSIS FOR THE 4 BANDS IN ^{163}Tm.
IN ALL CASES THE VALUE OF T_{sf} IS VERY SMALL, *i.e.*,
$T_{sf} \sim 1 \, fs$. THE ERROR BARS ARE STATISTICAL ONLY, *i.e.*,
THEY DO NOT INCLUDE THE $\sim 15\%$ ERROR ASSOCIATED
WITH THE SYSTEMATIC UNCERTAINTY IN THE STOPPING
POWERS (SEE TEXT FOR DETAILS)

Band	Q_t (eb)	Q_{sf} (eb)	χ^2_{min}
1	$6.4^{+0.6}_{-0.3}$	$6.7^{+0.7}_{-0.8}$	6.51
2	$6.4^{+0.3}_{-0.3}$	$7.0^{+0.9}_{-0.6}$	8.01
TSD1	$7.4^{+0.4}_{-0.4}$	$10.2^{+1.8}_{-1.3}$	1.81
TSD2	$7.7^{+1.0}_{-0.6}$	$9.7^{+2.9}_{-2.3}$	1.15
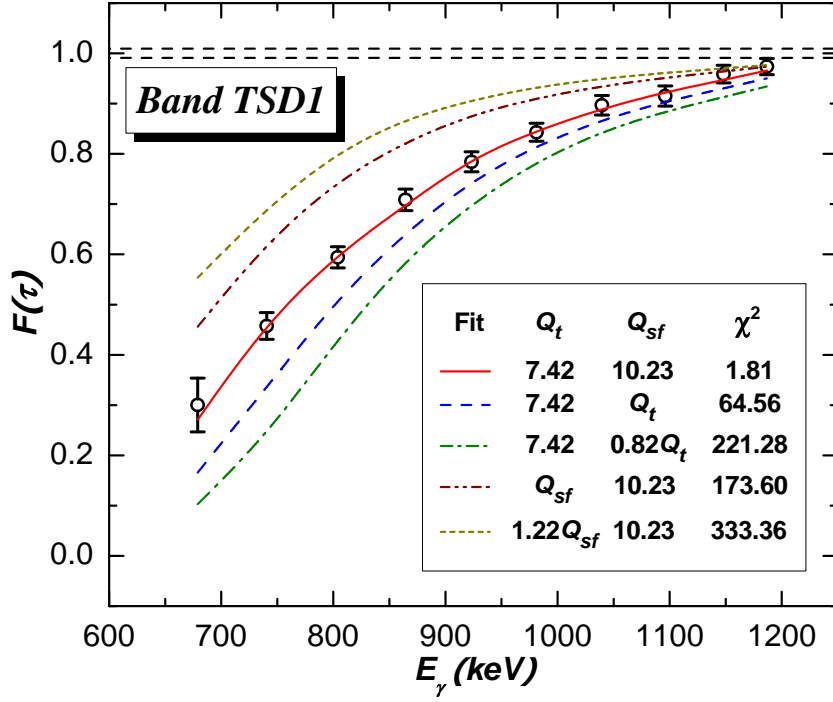
Figure 3.23. The $f(\tau)$ data points for band TSD1 as well as the fit line with the best-fit parameters which resulted from the running of the computer code MINUIT and four fit curves with some other values of Q_t and Q_{sf} (either the best-fit Q_t value and various Q_{sf} values or various Q_t parameters and the best-fit Q_{sf} value). See text for explanation. The two horizontal dashed lines show the range of initial recoil velocities within the ^{130}Te target layer.
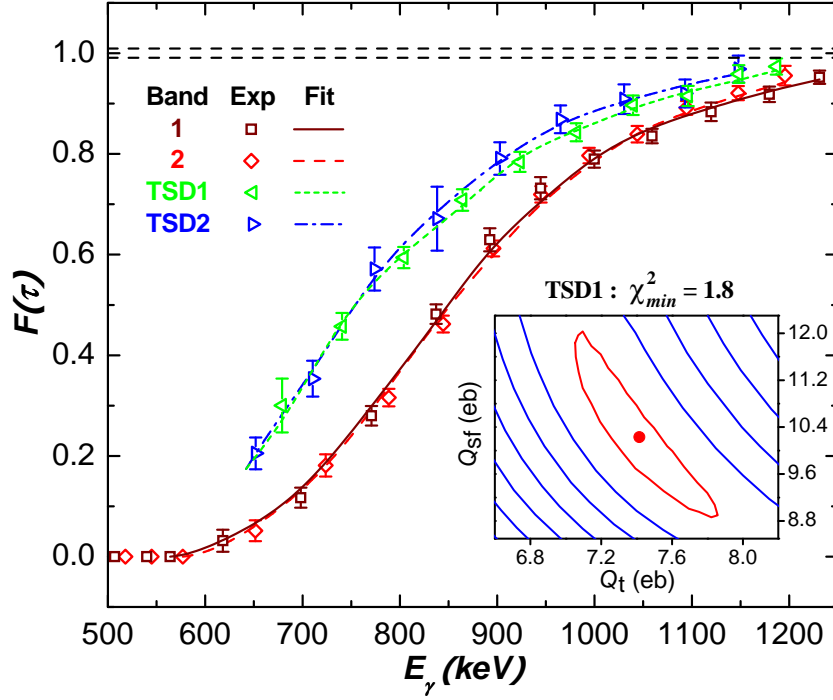
Figure 3.24. Measured $F(\tau)$ values with best-fit curves as described in the text for the four bands in [163]Tm. The two horizontal dashed lines show the range of initial recoil velocities within the [130]Te target layer. Insert: plot of the $\chi^2(Q_t, Q_{sf})$ surface for band TSD1. The central dot indicates the location of the minimum ($\chi^2_{min} = 1.8$), with the first contour plotted in an increment of one.
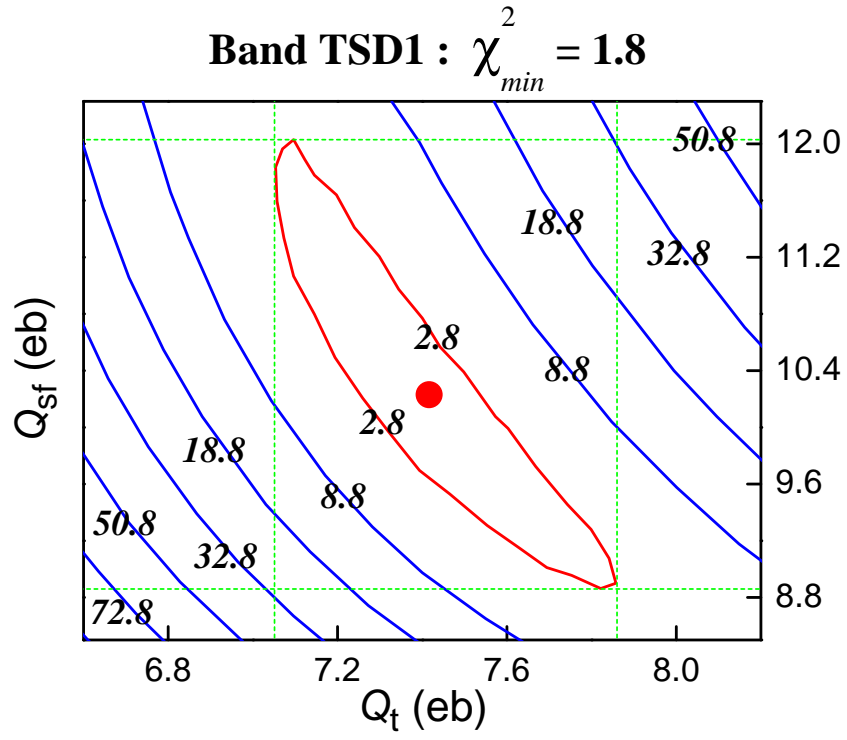
Figure 3.25. An illustration (using the example of band TSD1) of the method used in present work to determine the error bars for the parameters Q_t and Q_{sf}. See text for details.

3.3.3 Interpretation and discussion

Before discussing the significance of the difference in the measured Q_t values for bands 1 and 2, on the one hand, and the TSD1 and TSD2 sequences on the other, it is worth to examine the relevance of the results through a comparison with other nuclei in the region. Since bands 1 and 2 are based on the $[523]7/2^-$ configuration, a search of the literature was undertaken for quadrupole moment measurements of this configuration in neighboring nuclei. The results are given in Table 3.6. The $[523]7/2^-$ configuration is yrast in ^{163,165}Ho, and, perhaps more importantly, in ^{163}Lu, one of the isotopes where TSD and wobbling bands are known as well. It should be noted that the ^{163}Lu yrast sequence had first been associated with the $[514]9/2^-$ configuration [73]. However, following the work of Ref. [74], the $[523]7/2^-$ configuration was adopted on the basis of the $B(E2)$ and $B(M1)$ transition probabilities deduced from the measured lifetimes and branching ratios.

As can be seen from Table 3.6, the Q_t moments have been obtained using a number of techniques ranging from the analysis of $F(\tau)$ values, such as those in the present work, and full line shape analyses of data taken using the DSAM technique, to measurements with the recoil distance method (*e.g.*, so-called plunger data), and even to laser resonance ionization as well as detection of the characteristic X rays of kaonic, pionic or muonic atoms. It can be concluded from Table 3.6 that the moments measured in the present work for bands 1 and 2 ($Q_t \sim 6.4$ *eb*) are in good agreement with those reported for the same configuration in the literature. This observation provides further confidence in the analysis presented above.

The Q_t moments of bands 1 and 2 can then also be compared with the calculations first outlined in the earlier ^{163}Tm spectroscopy work [93]. These predict the value to be $Q_t = 5.8$ *eb* at spin $I = 30$, with an associated axial quadrupole

TABLE 3.6

QUADRUPOLE MOMENTS OF ND BANDS BASED ON THE $[523]7/2^-$ CONFIGURATION IN Tm, Ho, AND Lu NUCLEI. THE LAST COLUMN PROVIDES THE REFERENCE AND IDENTIFIES THE METHOD USED TO MEASURE THE MOMENTS BY THE FOLLOWING SYMBOLS: FT - DSAM $F(\tau)$; LS - DSAM LINE SHAPE; RD - RECOIL DISTANCE; LRIMS - LASER RESONANCE IONIZATION; KaX - KAONIC X-RAY; PiX - PIONIC X-RAY; MuX - MUONIC X-RAY. THE ERROR BARS ARE STATISTICAL ONLY AND DO NOT INCLUDE THE SYSTEMATIC UNCERTAINTY IN THE STOPPING POWERS. NOTE THAT FOR SOME ENTRIES IN THE TABLE, A RANGE OF VALUES IS GIVEN. THE READER IS REFERRED TO THE CITED REFERENCE FOR FURTHER DETAILS

Nuclide	Band	Q_t (eb)	Method [REF]
^{163}Tm	1	$6.4^{+0.6}_{-0.3}$	FT [present work]
^{163}Tm	2	$6.4^{+0.3}_{-0.3}$	FT [present work]
^{163}Ho	ND	6.78 ± 1.13	LRIMS [103]
^{165}Ho	ND1	$6.42 \pm 0.15, 6.78 \pm 0.04$	KaX, PiX [104]
		6.74 ± 0.04	PiX [32]
		6.57 ± 0.06	MuX [105]
^{165}Ho	ND2	5.76 ± 0.07	MuX [105]
^{163}Lu	ND1	$4.88^{+1.36}_{-0.68} - 6.78^{+2.66}_{-1.39}$	LS + RD [74]
^{163}Lu	ND2	$2.13^{+0.62}_{-0.43} - 6.72^{+0.77}_{-0.40}$	LS + RD [74]

deformation of $\epsilon_2 = 0.21$. Considering the fact that the errors quoted for the Q_t moments in Table 3.5 are statistical only and do not include the additional systematic error of $\sim 15\%$ due to the uncertainties in the stopping powers, the agreement between experiment and theory can be considered as satisfactory. Nevertheless, the fact remains that deformations calculated with the Cranked Nilsson-Strutinsky (CNS) model [96], the Tilted-Axis Cranking (TAC) model [99] or the Ultimate Cranker (UC) code [62], all using the same Nilsson potential, tend to be systematically somewhat smaller than the values derived from experiment, an observation that warrants further theoretical investigation.

The present data clearly indicate that the deformation associated with bands TSD1 and TSD2 is larger than that of the yrast structure: as can be seen from Table 3.5, the Q_t moments of bands TSD1 and TSD2 (~ 7.5 eb) exceed those for bands 1 and 2 by ~ 1 eb. The larger deformation agrees with the interpretation proposed in the earlier work [93]. However, the magnitude of the increase in Q_t moments is not reproduced as the TAC calculations indicate a transitional quadrupole moment increasing slightly from 8.7 eb at spin $I = 24$ to 9.6 eb for $34 < I < 50$. At present, this discrepancy between data and calculations is not understood. It is, however, not unique to ^{163}Tm. Table 3.7 compares Q_t moments for TSD bands in all nuclei of the region where this information is available. Just as was the case above, the systematic uncertainty associated with the stopping powers has been ignored. Nevertheless, three rather striking observations can be made from Table 3.7: (1) the Q_t values for the TSD bands in ^{163}Lu and ^{163}Tm are essentially the same, (2) the Q_t moments of the TSD bands decrease from ^{163}Lu and ^{163}Tm to ^{165}Lu, an observation already made for Lu isotopes in Refs. [106, 107], and (3) all the TSD bands in Hf nuclei are characterized by

139

Q_t moments that are larger than those in Lu and Tm by $\sim 4 - 6$ eb, possibly pointing to a rather different nature for these bands. Just as in the present ^{163}Tm case, a discrepancy between the measured and calculated Q_t moments was found for the Lu isotopes: the UC calculations predicted values of $Q_t \sim 9.2$ eb and 11.5 eb for positive and negative values of the deformation parameter γ, and these values were computed to be essentially the same for the three Lu isotopes ($A = $ 163, 164, 165) [106, 107], but with the configuration associated with a rotation about the short axis ($\gamma > 0$) being lower in energy; while the calculations in the TAC model gave the similar Q_t moments ($\sim 9.7 - 10.3$ eb) for the TSD bands in ^{163}Lu. As stated above, the physical origin of the discrepancy between theory and experiment is at present unclear, although it was pointed out in Refs. [106, 107] that the exact location in energy of the $i_{13/2}$ and $h_{9/2}$ proton- and $i_{11/2}$ neutron-intruder orbitals is crucial for the deformation. These orbitals are deformation driving and, hence, might have a considerable impact on the Q_t moments. It is possible that the use of the standard Nilsson potential parameters, questioned above for normal deformed configurations, needs also to be reconsidered for the precise description of TSD bands.

In Ref. [106] it was argued that the fact that the measured Q_t moments in the ^{163}Lu TSD bands are smaller than the calculated values points towards a positive γ deformation because the latter is associated with the smaller computed moments. As already discussed in the earlier ^{163}Tm paper [93] as well as in the discussion above, the same conclusion can not be drawn in the case of ^{163}Tm. Indeed, TAC calculations, which do not restrict the orientation of rotational axis to one of the principal axes, point to a tilted solution that smoothly connects two minima of opposite sign in γ deformation. The average deformation parameters are $\epsilon_2 = $

TABLE 3.7

QUADRUPOLE MOMENTS OF TSD BANDS IN Tm, Lu, AND Hf NUCLEI. THE LAST COLUMN PROVIDES THE REFERENCE AND IDENTIFIES THE METHOD USED TO MEASURE THE MOMENTS BY THE FOLLOWING SYMBOLS: FT - DSAM $F(\tau)$; LS - DSAM LINE SHAPE. THE ERROR BARS ARE STATISTICAL ONLY AND DO NOT INCLUDE THE SYSTEMATIC UNCERTAINTY IN THE STOPPING POWERS. NOTE THAT FOR SOME ENTRIES IN THE TABLE, A RANGE OF VALUES IS GIVEN. THE READER IS REFERRED TO THE CITED REFERENCE FOR FURTHER DETAILS

Nuclide	Band	Q_t (eb)	Q_{sf} (eb)	Method [REF]
^{163}Tm	TSD1	$7.4^{+0.4}_{-0.4}$	$10.2^{+1.8}_{-1.3}$	FT [present work]
^{163}Tm	TSD2	$7.7^{+1.0}_{-0.6}$	$9.7^{+2.9}_{-2.3}$	FT [present work]
^{163}Lu	TSD1	$7.4^{+0.7}_{-0.4}$, $7.7^{+2.3}_{-1.3}$	$6.7^{+0.7}_{-0.7}$, $7.0^{+0.7}_{-0.7}$	FT [107]
		$7.63^{+1.46}_{-0.88} - 9.93^{+1.14}_{-0.99}$		LS [108]
^{163}Lu	TSD2	$6.68^{+1.70}_{-1.02} - 8.51^{+0.95}_{-0.73}$		LS [108]
^{164}Lu	TSD1	$7.4^{+2.5}_{-1.3}$	$6.7^{+0.7}_{-0.7}$	FT [107]
^{165}Lu	TSD1	$6.0^{+1.2}_{-0.2}$, $6.4^{+1.9}_{-0.7}$	$5.4^{+0.5}_{-0.5}$, $5.8^{+0.6}_{-0.6}$	FT [107]
^{167}Lu	TSD1	$6.9^{+0.3}_{-0.3}$	$4.4^{+0.4}_{-0.2}$	FT [109]
^{168}Hf	TSD1	$11.4^{+1.1}_{-1.2}$	$10.5^{+1.7}_{-1.6}$	FT [82]
^{174}Hf	TSD1	$13.8^{+0.3}_{-0.4}$	$8.4^{+0.3}_{-0.3}$	FT [85]
^{174}Hf	TSD2	$13.5^{+0.2}_{-0.3}$	$8.0^{+0.3}_{-0.2}$	FT [85]
^{174}Hf	TSD3	$13.0^{+0.8}_{-0.4}$	$10.3^{+0.6}_{-0.8}$	FT [85]
^{174}Hf	TSD4	$12.6^{+0.8}_{-0.8}$	$10.2^{+1.6}_{-1.3}$	FT [85]

0.39, $|\gamma| = 17°$. For $I > 23$ the angular momentum vector gradually moves away from the intermediate axis ($\gamma < 0$) toward the short one ($\gamma > 0$), without reaching the latter by $I = 50$.

The TAC calculations of Ref. [93] have also been extended to the case of ^{163}Lu and the computed Q_t moments for the TSD bands are larger than the measured ones, in agreement with the general findings discussed above. These Q_t moments in ^{163}Lu were also found to decrease slightly from 10.3 eb at $I = 20$ to 9.7 eb at $I = 40$ just as in ^{163}Tm. Moreover, the ^{163}Lu values are also somewhat larger than the corresponding ones in ^{163}Tm, reflecting the additional drive towards larger deformation brought about by the $i_{13/2}$ proton orbital which is occupied in this case. However, it should be pointed out that within the framework of these calculations [93], the occupation of the $i_{13/2}$ proton orbital is not a necessary condition to achieve a TSD minimum. Rather, the deformation is driven mainly by the $N = 94$ neutron gap (the same point has been indicated in the earlier work [93]), as is illustrated in Figure 3.10, where the single-neutron routhians are presented and the large $N = 94$ gap associated with the TSD shapes at positive and negative γ values is clearly visible. The corresponding single-proton routhians can be seen in Figure 3.9. The occupation of the $i_{13/2}$ proton level in the Lu isotopes adds an additional degree of shape driving towards larger deformation. However, as stated above, the data indicate that its impact is rather minor. This is borne out by the calculations where average deformations of $\epsilon_2 = 0.39$, $|\gamma| = 17°$ for ^{163}Tm should be compared with computed values of $\epsilon_2 = 0.41$, $\gamma = +19°$ for ^{163}Lu. The nearly equal deformations find their origin in the following physical effect: ^{163}Lu does not make full use of the $N = 94$ gap, because it has two fewer neutrons, but this absence is compensated by the additional drive provided by the

$i_{13/2}$ proton. As argued in the earlier paper [93], the large $N = 94$ gap makes it unlikely that the ^{163}Tm TSD bands involve a three-quasiparticle structure with a proton coupled to a neutron particle-hole excitation. The possibility that these bands correspond to configurations with the odd proton occupying the [541]1/2$^-$ level (labeled as $h_{9/2}$ in Figure 3.9) is also unlikely. This orbital is characterized by a large signature splitting and small $B(M1)$ values for inter-band transitions, in clear contradiction with the ^{163}Tm data [93]. While it is possible that combining the occupation of the [541]1/2$^-$ level with a neutron particle-hole excitation would alter these observables, it would result in an excitation energy much larger than seen experimentally because of the large $N = 94$ gap. Furthermore, as can be seen in Figure 3.9, there are no other low-lying proton excitations that lead to small signature splitting.

Finally, it is worth noting that the values of the Q_{sf} moments associated with the sidefeeding differ significantly between bands 1 and 2, $Q_{sf} \sim 6.8$ eb, and bands TSD1 and TSD2, $Q_{sf} \sim 10$ eb (see Table 3.5). This change in Q_{sf} values is in part responsible for the large difference in the $F(\tau)$ curves as a function of energy seen in Figure 3.24. It implies that the γ-ray intensity responsible for the feeding of the bands originates from states associated with different intrinsic structures. The calculations presented in Ref. [93] suggested that several other TSD bands, corresponding to various p-h excitations, should be present in ^{163}Tm at excitation energies comparable to those of bands TSD1 and TSD2. It is plausible that these other TSD bands are part of the final stages in the deexcitation process towards the yrast TSD bands. If this is the case, the present observations suggest that the average deformation associated with the feeding TSD bands is larger than that of their yrast counter parts. Conversely, the feeding of bands 1 and 2 then appears

to occur from levels associated with a smaller deformation, similar to that of the bands themselves.

3.4 Conclusions and outlook

In summary, two new bands observed in the ^{163}Tm nucleus have been identified to be the triaxial strongly deformed (TSD) bands built on a minimum with calculated deformation parameters: $\varepsilon_2 \sim 0.39$, $|\gamma| \sim 17°$. The measured intrinsic properties, $e.g.$, alignments and moments of inertia, of these two TSD bands appear to be similar to the ones of other TSD bands observed in the region and have been reproduced by TAC calculations with parameters representative of a triaxial shape. It has been confirmed that these two TSD bands are associated with a larger deformation than the yrast (ND) bands, $i.e.$, $Q_t(\text{TSD}) \sim 7.5 \ eb$ and $Q_t(\text{ND}) \sim 6.4 \ eb$. Within the framework of present calculations, the deformation of the TSD bands is driven mainly by a large neutron gap at $N = 94$. The data also indicates that the feeding of these two TSD bands is associated with states of larger deformation ($Q_{sf} \sim 10 \ eb$). A surprising discrepancy ($\sim 20 - 30\%$) between data and calculations for the quadrupole moments of the TSD bands, which seems to be a general feature in the region, requires further investigation. The TSD bands in ^{163}Tm, which are distinctly different from the wobbling bands, have been interpreted by the TAC calculations to be structures associated with particle-hole excitations in the TSD well. Perhaps more importantly, the TAC calculations performed in present work provide a natural explanation for the presence of wobbling bands in the $_{71}$Lu isotopes and the absence of such bands in all neighboring $_{69}$Tm, $_{72}$Hf and $_{73}$Ta nuclei. The explanation is related to: (I) the level density around the Fermi surface; (II) the presence of a strong shell gap at

$N = 94$; and (III) the shape driving effects of the $i_{13/2}$ proton orbital.

CHAPTER 4

OCTUPOLE CORRELATIONS IN ^{238,240,242}Pu

4.1 Reflection asymmetry in nuclei

4.1.1 Introduction

For most deformed nuclei, a description in terms of an axial- and reflection-symmetric shape is adequate to interpret the observed band structures. Since such a shape is symmetric under space inversion, all levels in the associated rotational bands should have the same parity. However, the observation of negative-parity states near the ground level in even-even Ra and Th nuclei, which was first made by a Berkeley group in the 1950s [110, 111, 112], indicated that some nuclei might have a shape asymmetric under reflection, such as a pear shape, for example. Further measurements showed that these negative-parity states form bands with a spin-parity sequence 1^-, 3^-, 5^-, ... They are also characterized by a principal quantum number $K = 0$. These observations were interpreted as signatures for octupole vibrations about a spheroidal equilibrium shape [111, 112] (illustrated in Figure 4.1). Soon after the discovery of octupole vibrations, suggestions were made regarding the possibility of the onset of stable octupole deformation in nuclei [35, 113] (illustrated in Figure 4.1).

Interest in octupole correlations and octupole deformation was revived in the early 1980s by two theoretical developments. First, microscopic many-body calcu-

146
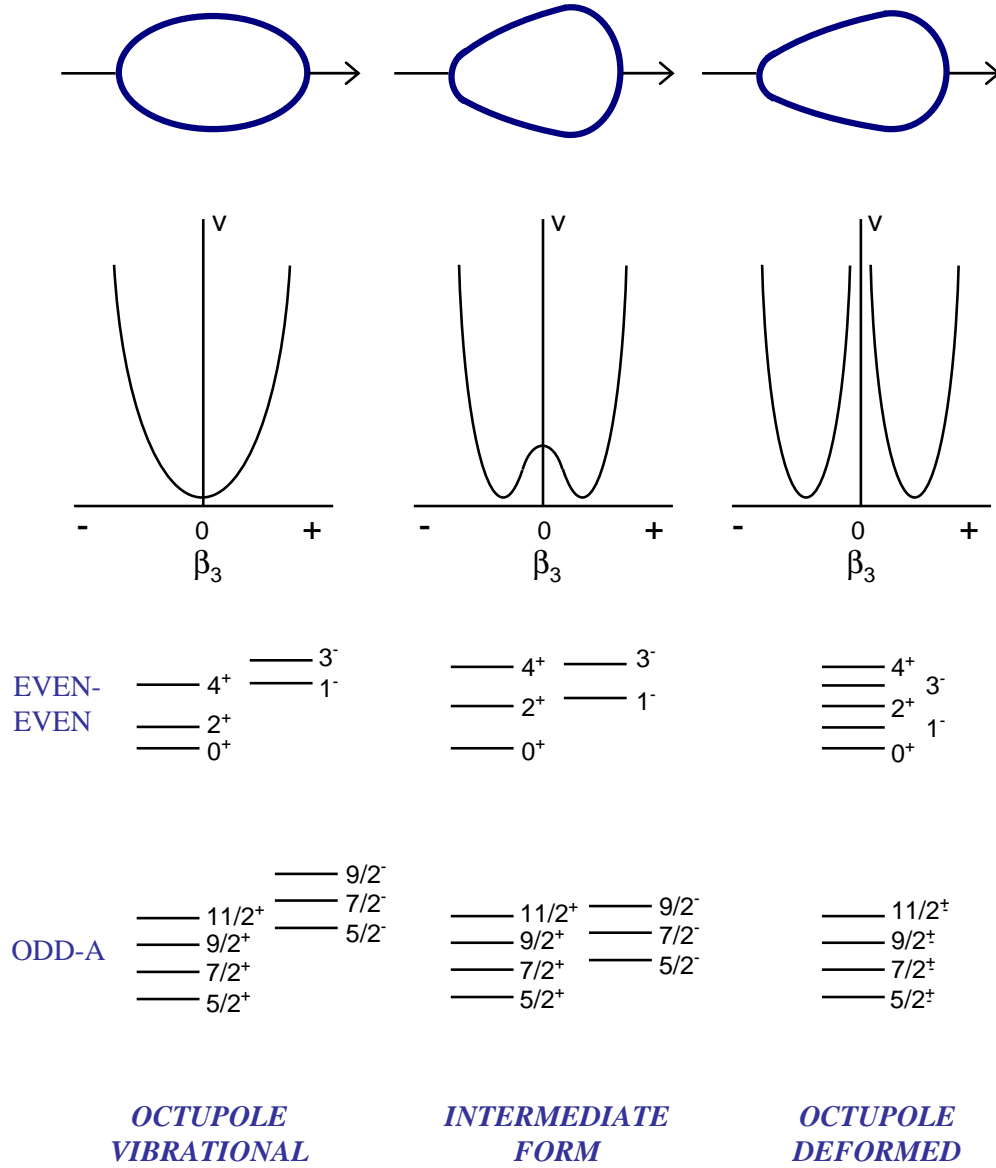
Figure 4.1. Energy level diagram and potential energy as a function of β_3 deformation for different axially symmetric ($K = 0$) shapes. The left panel (octupole vibration) represents a nucleus which has a spheroidal equilibrium shape in its ground state, which is relection symmetric as well. The right panel (octupole deformed) shows a nucleus with a rigid octupole shape (pear shape used as an example here). The middle panel (intermediate form) represents a soft pear-shaped nucleus, with deformation parameters: $\beta_2 \sim 0.15$ and $\beta_3 \sim 0.09$. Taken from Ref. [114].

lations by Chasman [115, 116] predicted the presence of parity doublets in several odd-mass Th, Ac and Pa nuclei as a sign of strong octupole deformation. Second, calculation of atomic masses with the Strutinsky method indicated that, in some nuclei, the addition of octupole deformation in the parameterization of the potential resulted in extra binding, typically of the order of $\sim 1.5\ MeV$ in the $A{\sim}224$ region [13].

4.1.2 Reflection-asymmetric shape

As described in Sec. 1.2.2 of Chapter 1, the nuclear shape is often parameterized in terms of a spherical harmonic expansion like Eq. 1.4:

$$R(\theta, \phi) = R_0 \left(1 + \alpha_{00} + \sum_{\lambda=1}^{\infty} \sum_{\mu=-\lambda}^{\lambda} \alpha_{\lambda\mu} Y_{\lambda\mu}(\theta, \phi) \right).$$

The requirement that the radius is real imposes the condition: $\alpha_{\lambda-\mu} = (-1)^{\mu}\alpha_{\lambda\mu}$. For axially symmetric shapes, all deformation parameters $(\alpha_{\lambda\mu})$ with $\mu{\neq}0$ vanish. The remaining shape parameters $\alpha_{\lambda 0}$ are usually called β_{λ}, $i.e.$, $\beta_{\lambda} \equiv \alpha_{\lambda 0}$. For nuclei with reflection symmetry, only β_{λ} terms with even λ have nonzero values; on the other hand β_3 $(\lambda = 3)$ represents the magnitude of octupole deformation of an axially reflection-asymmetric nucleus. It is worth noting that the terms octupole shape and reflection-asymmetric shape are used interchangeably in this thesis.

Attempts to find a unique parameterization of a pure-octupole shape ($i.e.$, without involving the quadrupole deformation) turned out to be less successful [117]. The octupole deformation is often seen in quadrupole deformed nuclei. The general quadrupole-octupole shape is described by two quadrupole shape parameters. $i.e.$, α_{20} and α_{22}, or β_2 and γ, and seven independent octupole param-

eters $\alpha_{3\mu}$ ($\mu = 0, \pm1, \pm2, \pm3$). Figure 4.2 displays four shapes resulting from the superposition of axial quadrupole and octupole deformation with $\mu = 0, 1, 2,$ and 3. A general parameterization of the combined quadrupole-octupole field, covering all possible shapes without double counting, was proposed by Rohoziński [118].

It was found that the contribution of the β_6 degree of freedom on binding energies is comparable to the contribution from the β_3 deformation [119]. Calculations with average potentials that included β_2–β_7 deformation parameters found that the β_5 mode helps stabilize the reflection-asymmetric shape, and the well depth was determined to be $\sim 1~MeV$ [120]. This is small compared to the gain in the binding energy of 10 MeV due to the quadrupole deformation [121] (see Figure 4.3).

Unlike for the quadrupole deformation, the magnitude of octupole deformation is difficult to determine from direct measurements. Several experimental signatures associated with octupole correlations will be discussed later in Sec. 4.1.4. The three shapes and the potential energy plots for nuclei associated with octupole correlations are illustrated in Figure 4.1. The situation seen in the left panel occurs for a nucleus with a spheroidal equilibrium shape in its ground state for which a vibrational band develops at an the excitation of $\sim 1~MeV$ in the corresponding level diagram; this corresponds to the so-called "octupole vibrator". The other limit (in the right panel) occurs when the nucleus has a sizable β_3 deformation in its ground state and there is an infinite barrier between the reflection-asymmetric shape and its mirror image; this is the so-called "octupole rotor" and is associated with "stable octupole deformation". The level diagram characteristic of a nucleus with such a shape, shown in the bottom of Figure 4.1, will be discussed further in Sec. 4.1.4. The third possible shape (in the middle

Quadrupole-octupole shapes
$\beta_2{=}0.6$, $\beta_{3\mu}{=}0.35$
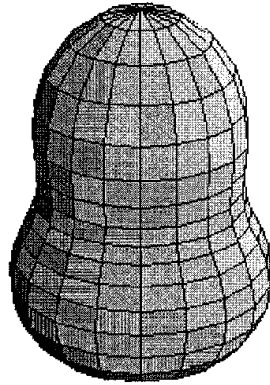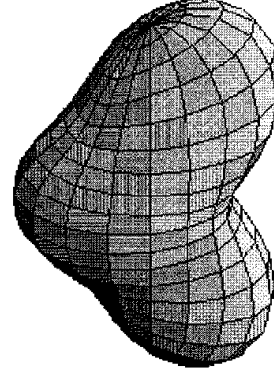
$\mu{=}0$ $\mu{=}1$
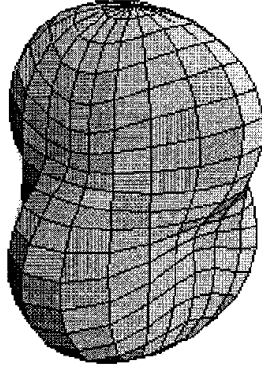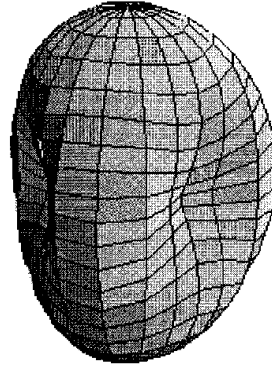
$\mu{=}2$ $\mu{=}3$

Figure 4.2. Four quadrupole-octupole shapes correspond to octupole deformation with $\mu = 0$, 1, 2, 3. In all cases, the same axial quadrupole $\alpha_{20} = \beta_2 = 0.6$ is assumed for illustration purposes. Taken from Ref. [117].
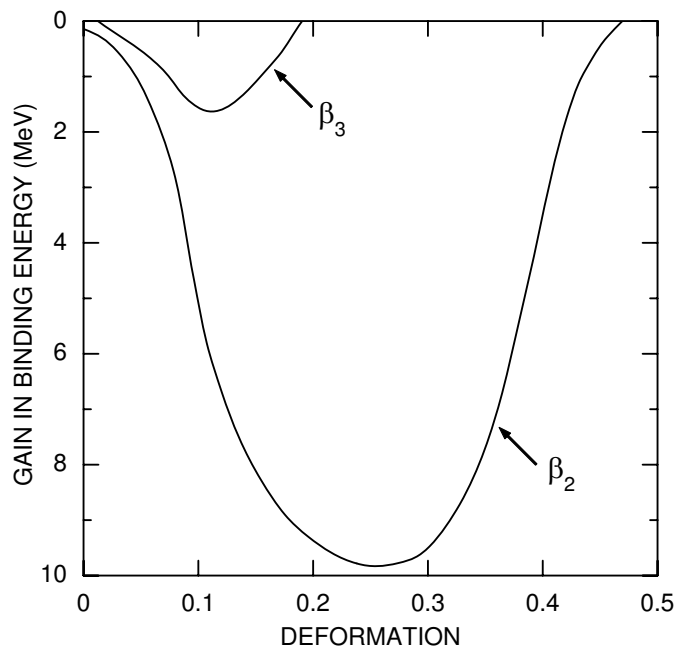
Figure 4.3. Calculated gain in binding energy as a function of deformation for an actinide nucleus. The bottom curve shows the gain in binding energy as a spherical nucleus develops β_2 deformation. The upper curve shows the gain with increase in β_3 deformation in an actinide nucleus with some β_2 deformation. Taken from Ref. [114].

panel) is intermediate between the two limits. Here, a finite barrier ($< 0.5\ MeV$) exists between the reflection-asymmetric shape and its mirror image and tunneling motion is possible between the two mirror shapes [114].

One of the most distinct differences in the properties of reflection-symmetric and reflection-asymmetric nuclei is the value of the electric dipole moment. The nuclear electric dipole moment ($\vec{D}$) is a measure of the shift between the center of charge and the center of mass of the nucleus. It can be written as:

$$\vec{D} = e\frac{ZN}{A}(\vec{r}_{p,c.m.} - \vec{r}_{n,c.m.}) \tag{4.1}$$

(*i.e.*, Eq. 12 in Ref. [117]), where e is the charge of electron, $\vec{r}_{p,c.m.} = \vec{r}_p/Z$ and $\vec{r}_{n,c.m.} = \vec{r}_n/N$ are the center-of-mass coordinates for protons and neutrons, respectively. For reflection-symmetric nuclei, the nucleonic (proton and neutron) densities have three symmetry planes, so that $|\vec{r}_n| = |\vec{r}_p| = 0$, and, hence, $|\vec{D}| = 0$. However, $\vec{r}_{p,c.m.} \neq \vec{r}_{n,c.m.}$ generally if the density distributions are reflection asymmetric. Thus, a large static $E1$ moment may arise. For an axially deformed system in the reflection-asymmetric case, the intrinsic dipole moment is aligned along the symmetry axis (z axis), and its value D_0 can be calculated directly from Eq. 4.1. In the most general case of triaxial and reflection-asymmetric density distributions, the intrinsic dipole moment is characterized by three spherical components, $D_{\pm 1}$ and D_0.

4.1.3   Theoretical description

Octupole correlations in nuclei are produced by the long-range, octupole-octupole interaction between nucleons. These correlations depend on the matrix elements of Y_0^3 between single-particle states with $\Delta j = \Delta l = 3$ and the energy

spacings between them. As can be seen in Figure 4.4, certain intruder states (defined in Sec. 1.2.1 of Chapter 1) with l, j quantum numbers lie close in energy to other states with $(l-3)$, $(j-3)$ quantum numbers. These pairs of orbits can be stongly coupled by the octupole correlations. The most important couplings are $(1g_{9/2} \rightarrow 2p_{3/2})$, $(1h_{11/2} \rightarrow 2d_{5/2})$, $(1i_{13/2} \rightarrow 2f_{7/2})$ and $(1j_{15/2} \rightarrow 2g_{9/2})$, highlighted in red color in Figure 4.4. Nuclei with a Fermi surface close to these pairs of states are particularly affected by strong octupole correlations. For spherical or near spherical nuclei, the corresponding nucleon numbers for these coupled orbits are 34, 56, 88 and 134, and these numbers have been labeled in Figure 4.4. For nuclei with large quadrupole deformation, the strong octupole correlations resulting from the coupled orbits generally have an impact over a range of several nucleon numbers. It can also be seen in Figure 4.4 that the octupole-driving $\Delta j = \Delta l = 3$ orbits are close together for larger particle numbers. Thus, nuclei with $Z \sim 88$ and $N \sim 134$ (the light actinides) are expected to possess the largest octupole correlations.

In order to reproduce and predict octupole correlations in nuclei, a number of theoretical approaches, microscopic as well as macroscopic, have been developed since the $K^\pi = 0^-$ octupole vibrational bands in the actinides were discovered in early 1950s. One model that explained the octupole vibrational bands in heavier actinides satisfactorily is the Random Phase Approximation (RPA) model by Neergård and Vogel [122, 123]. This model was later extended to the so-called "the Cranking plus RPA" method [124] through combining the approach with the cranked shell model, introduced in Sec. 1.3.3 of Chapter 1. In the RPA model based on the Cranked Nilsson potential, the Hamiltonian can be written as [125]:

$$H = H_{Nilsson} - \omega J_x - \frac{1}{2} \sum_K \chi_{3K} Q''^\dagger_{3K} Q''_{3K}, \qquad (4.2)$$
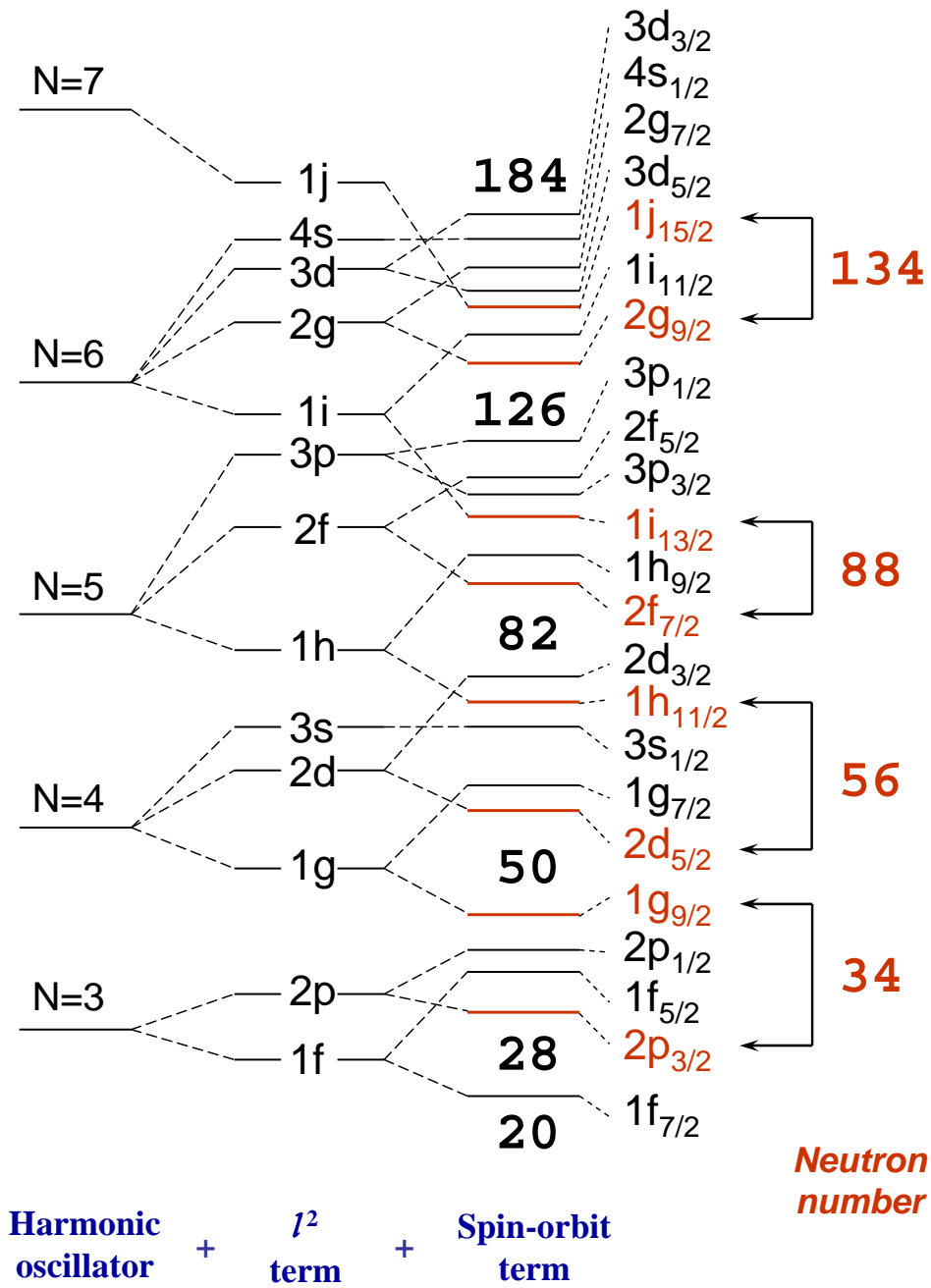
Figure 4.4. Partial energy scheme of single-particle levels of the shell model for neutrons showing the locations of the octupole-driving $\Delta j = \Delta l = 3$ coupled orbits, highlighted in red color. The numbers on the right correspond to the neutron numbers for which octupole correlations are strongest. The proton single-particle scheme is quite similar. Adapted from Figure 1.2 in Chapter 1.

where $H_{Nilsson}$ is a Nilsson Hamiltonian, defined in Eq. 1.13 of Chapter 1, and Q''_{3K} are the doubly stretched octupole operators defined by coordinates $x''_i = (\omega_i/\omega_0)x_i$ with $i = 1$, 2 and 3 [126]. Here ω_i/ω_0 denotes the ratios of the frequencies of the deformed harmonic-oscillator potential to that of the spherical one, while K represents the components of angular momentum on the symmetry axis of the potential. The force-strengths χ_{3K} can be determined from the self-consistency conditions between the potential and the density, once the single-particle potential at the equilibrium (for example, Nilsson potential, described in Sec. 1.2.3 of chapter 1) is given [126]. For the cases in which the pairing interactions are not negligible, another term, the pairing Hamiltonian (see Eq. 1.39 in Chapter 1), needs to be added in Eq. 4.2. With some appropriate assumptions and deductions [124, 125], the RPA energy eigenvalues, the so-called "Octupole strength", $S(Q''_{3K}, \omega)$ [125], and, hence, the neutron and proton single-particle routhians can be calculated as functions of the rotational frequency ω. The octupole vibrational states are then described in terms of a superposition of many particle-hole excitations. Thus, individual vibrations can be classified according to the different degrees of freedom of the particle-hole pairs. The detailed description of the RPA method is beyond the scope of this thesis work, but can be found in Refs. [124, 127]. The present work focuses mostly on the observation for octupole bands in Pu isotopes. Therefore, RPA calculations based on the cranked shell model, which can account well for the interplay between octupole vibrations and collective quasi-particle excitations under the stress of rotation, were carried out in Japan by T. Nakatsukasa of RIKEN.

Other models, such as microscopic many-body calculations, the particle-plus-rotor model, shell correction calculations, algebraic models, *etc.*, are also available

and may perhaps interpret the data better for nuclei with more intense octupole correlations (*i.e.*, nuclei that may be octupole deformed rather than octupole vibrational). Readers with further interest are referred to Refs. [114, 117] for details.

4.1.4 Experimental evidence

Though the existence of reflection asymmetry in nuclei is hard to prove conclusively, some of the experimental evidence, discussed below, can be reproduced well by theoretical calculations including octupole correlations.

As discussed at the beginning of this chapter, the observation of low-lying 1^- and 3^- states in the even-even Ra and Th nuclei provided the first experimental evidence that some nuclei may possess reflection-asymmetric shapes. In this mass region, the observed 1^- and 3^- states remain higher in energy than the 2^+ and 4^+ levels, respectively (as can be seen in Figure 4.5), an observation which conflicts with a well-known property of octupole deformed nuclei, *i.e.*, the positive- and negative-parity states are perfectly interleaved in a single rotational band. Hence, this observation leads to the hypothesis that these nuclei are not rigidly octupole deformed. Rather, they may fluctuate back to a reflection-symmetric shape. Figure 4.5 indicates that the energies of negative-parity states are the lowest in the even-even isotopes of Rn, Ra, Th and U with $N\sim134$, where a reflection-asymmetric shape is predicted to occur due to strong octupole correlations. It can be seen in this figure that the lowest-lying states are also very localized in N. As yet, in none of these nuclei has the lowest 1^- state been observed to be lower in energy than the lowest 2^+ state. Phenomena similar to those described above were also observed in the region of the lanthanide nuclei (Xe, Ba,

Ce, Nd, Sm and Gd) with $N\sim88$ (see Fig. 13 in Ref.[117]), even though the octupole correlations appear to be somewhat less intense. The systematic behavior of excited negative-parity states has been discussed by several authors. It has been concluded that a vibrational interpretation in terms of RPA calculations is most often appropriate. Further discussion of the theoretical attempts to describe the properties of the low-lying 1^- and 3^- states can be found, along with references, in the review article of Butler and Nazarewicz [117].
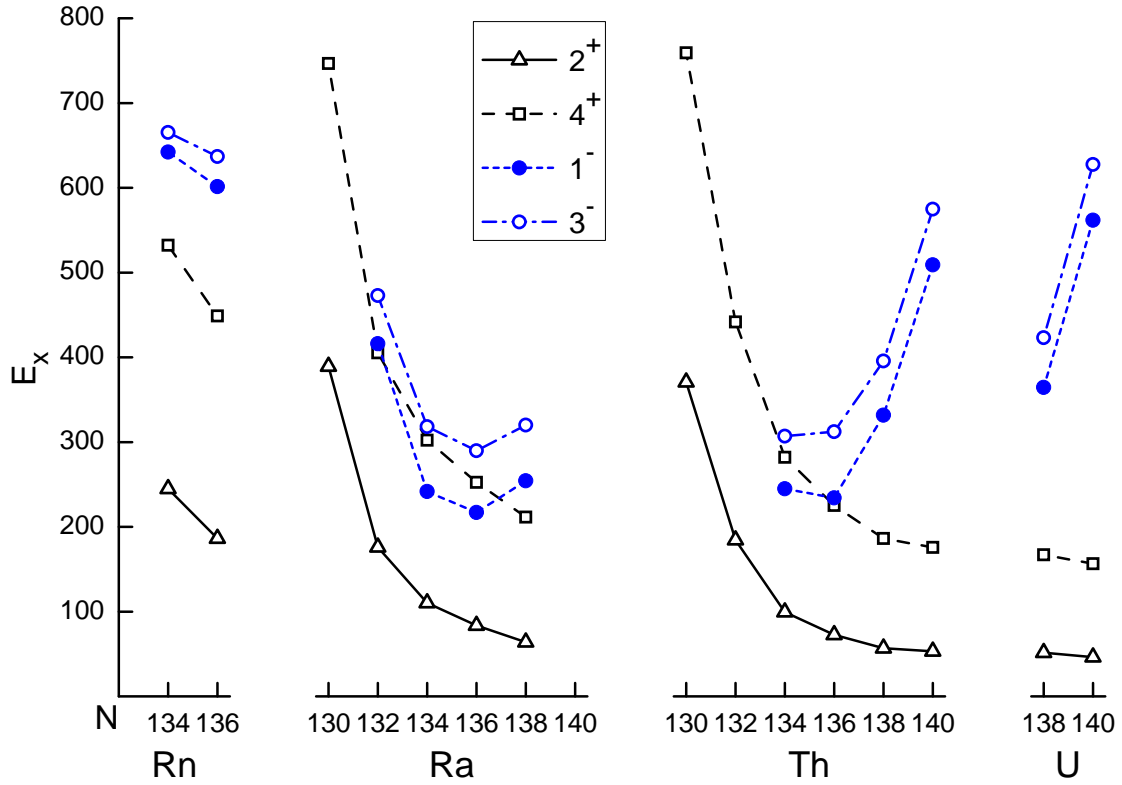
Figure 4.5. Excitation energies (keV) of the yrast 2^+, 4^+, 1^-, and 3^- states in the $Z = 86$–92 region. Adapted from Fig. 14 in Ref. [117].

The presence of a rotational band consisting of states with alternating parity, $e.g.$, I^+, $(I+1)^-$, $(I+2)^+$,..., is widely agreed to be one of the signatures for octupole deformed nuclei. The first observations of this striking feature in heavy, even-even nuclei were reported in ^{218}Ra [128] and ^{222}Th [129, 130]. In the medium-mass region, band structures with similar features were seen much earlier, for example, in ^{152}Gd [131] and in ^{150}Sm [132]. Figure 4.6 shows a typical example, ^{226}Th, in which the sequence has been observed up to spin $20\hbar$ [133, 134]. Structures similar to those of even-even octupole nuclei are observed in transitional odd-mass and odd-odd nuclei in which the odd particles are weakly coupled to the core. This situation exists, for example, in ^{219}Ra [135] and ^{216}Fr [136]. Bands of this type have been observed in over 50 nuclei.

In reflection-asymmetric nuclei, the $E1$ transitions observed between the yrast positive- and negative-parity bands, for example, $(I+1)^-{\rightarrow}I^+$ and $I^+{\rightarrow}(I-1)^-$, compete favorably with the $E2$ in-band γ rays, since they exhibit relatively large transition probabilities, $B(E1)$. Typical $B(E1)$ values are less than 10^{-4} Weisskopf units (W.u.), defined in Sec. 1.4.3 of Chapter 1, but the $B(E1)$ values in the mass regions where octupole correlations are strong, for example, in the actinides, range from 10^{-3} to 10^{-2} W.u. This phenomenon was first described by Bohr and Mottelson [137, 138], and Strutinsky [139] in terms of the macroscopic liquid-drop model. The related models are reviewed in Ref. [117] and the calculations using them reproduced the data of dipole moments (D_0) in both actinide and lanthanide nuclei. The relations between electric moments (D_0 and Q_0) and transition rates for $E1$ and $E2$ transitions have been described by Eqs. 1.81 and 1.82 in Chapter 1. In most cases, absolute values of $B(E1)$ probabilities are not available, and the D_0 moments have to be extracted from the branching ratios $I_\gamma(J{\rightarrow}J{-}1)/I_\gamma(J{\rightarrow}J{-}2)$
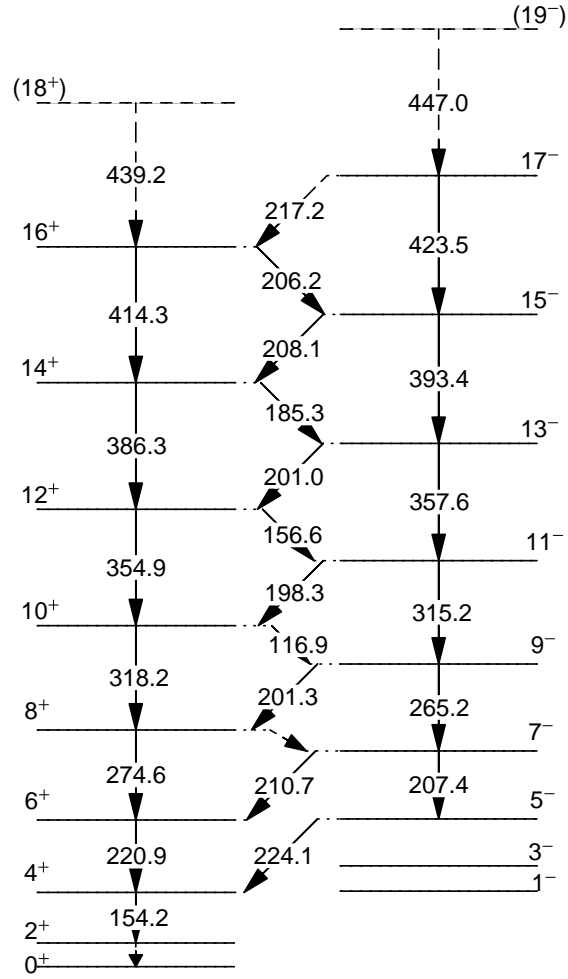
Figure 4.6. Partial level scheme of ^{226}Th displaying a characteristic sequence of states with alternating parity. Taken from Ref. [133].

(I_γ is the γ-ray intensity), which are related to $B(E1)/B(E2)$ ratios in the form of Eq. 1.84. It is worth noting that many nuclei in the mass regions of interest are not good rotors, hence, the use of formulae for axial-symmetric nuclei, Eqs. 1.81 and 1.82, is questionable [117]. Nevertheless, they provide a consistent way to extract the D_0 moments from the data.

In nuclei with one of the other two shapes shown in Figure 4.1, *i.e.*, with the octupole vibrational shape or the intermediate form, the states in the two bands with opposite parity are not interleaved. However, the displacement in energy of a state, I^-, from the middle point between two adjacent states with opposite parity, $(I-1)^+$ and $(I+1)^+$, often decreases with an increase in spin. Actually, even in the well-defined reflection-asymmetric nuclei with strong octupole correlations, *e.g.*, ^{226}Th, the states are not interleaved at low spin ($I < 5$). This observation suggests that, in reality, the extreme of stable octupole deformation is never reached at the ground state. The barriers between two degenerate octupole minima are finite, like depicted for nuclei with intermediate shapes in Figure 4.1. An important parameter, $S(I)$, *i.e.*, the energy staggering factor, is defined as:

$$S(I) = E_I - \frac{(I+1)E_{I-1} + IE_{I+1}}{2I+1}, \qquad (4.3)$$

in Ref. [114], where E_I, E_{I-1} and E_{I+1} are the energy of states I^-, $(I-1)^+$ and $(I+1)^+$, respectively. This quantity is a measure of the extent of that the two sequences of opposite parity are interleaved in spin and can be regarded as a single octupole rotational band. The values of the energy staggering for the yrast cascade and the lowest-lying band with opposite parity are observed to be zero at spins around $10\hbar$ in octupole deformed nuclei, for example in ^{223}Th and ^{220}Ra, while they tend to reach zero at high spin ($I \sim 30$) in some of nuclei that

are characteristic of octupole vibrations at low spin, such as ^{239,240}Pu (see Fig. 4b in Ref. [140] or Figure 4.9 in Sec. 4.2.2). In both cases, it seems that rotation acts to enhance the strength of the octupole correlations. In other words, rotation appears to stabilize octupole deformation. An explanation for the occurrence of this phenomenon has been presented in Ref. [117]: (a) the octupole shape has weaker pairing correlations, which increases the moments of inertia; and (b) the rotational motion perturbs the single-particle states of opposite parity, which makes the octupole driving ($\Delta l = \Delta j = 3$) orbitals approach each other with increasing frequency of rotation.

It is important to point out another experimental fingerprint for octupole deformation in odd-A and odd-odd nuclei: the so-called parity doublets. These were first discussed in Ref. [9] and re-emphasized later by Chasman [116]. The definition of parity doublets is that bands come in pairs close in energy with states of the same spin, but opposite parity. In other words, there is always another band close in energy with the same value of K and opposite parity for each band, and the bands of different parity and signature are connected by strong $E1$ and $M1$ transitions. A good example is the level structures of the odd-even ^{223}Th nucleus [141], shown in Figure 4.7, and the odd-odd nucleus, ^{224}Ac [142], for example.

In a nucleus with a stable reflection-asymmetric shape, the signature (α) and parity (p), defined in Chapter 1, are no longer good quantum numbers. The only remaining symmetry is a combination of them, known as simplex (S) [143, 144], which has properties similar to those of the signature quantum numbers in the absence of reflection symmetry [145]. Simplex is equivalent to reflection in a plane containing the symmetry axis (more generally, S represents the symmetry with respect to a plane perpendicular to the rotational axis), and is defined as the
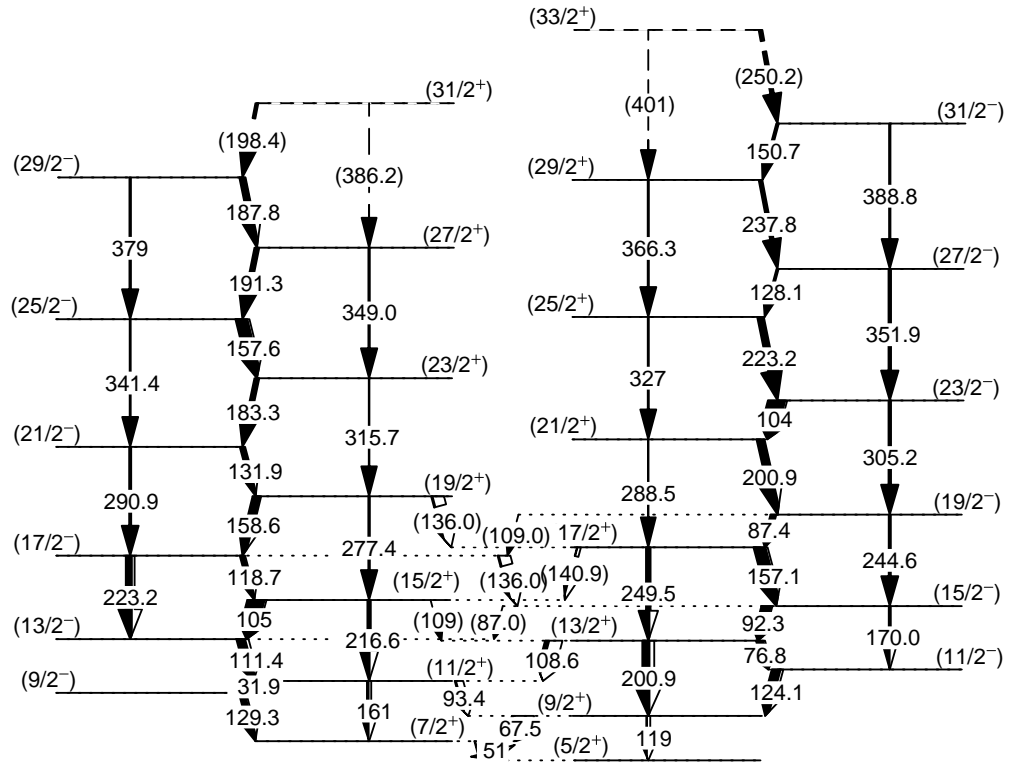
Figure 4.7. Partial level scheme of ^{223}Th. Taken from Ref. [141].

eigenvalue of the S operator, $S = \mathcal{P}\mathcal{R}^{-1}$, where $\mathcal{P}$ is the space-reversing operator (its eigenvalue p is parity) and $\mathcal{R}$ is the rotation operator. The rotational band with simplex s is characterized by states with spin I of alternating parity p [9],

$$p = se^{-i\pi I}. \tag{4.4}$$

Thus, for a reflection-asymmetric nucleus with even mass number, the sequences are:

$$s = +1, \quad I^p = 0^+, 1^-, 2^+, 3^-, ..., \tag{4.5}$$

$$s = -1, \quad I^p = 0^-, 1^+, 2^-, 3^+, ..., \tag{4.6}$$

while in the case of an odd-A nucleus, they are:

$$s = +i, \quad I^p = 1/2^+, 3/2^-, 5/2^+, 7/2^-, ..., \tag{4.7}$$

$$s = -i, \quad I^p = 1/2^-, 3/2^+, 5/2^-, 7/2^+, ... \tag{4.8}$$

As discussed in Chapter 1, the experimental aligned angular momentum can be transfered to the intrinsic frame of the nucleus and then be compared with calculations. In an investigation of alignments up to high spin in several isotopes of Rn, Ra and Th [146, 147], some features of the behavior of alignment as a function of rotational frequency ($\hbar\omega$) for structures associated with octupole correlations have been summarized. The difference of aligned angular momentum, $\Delta i_x = i_x^- - i_x^+$, between the positive- and negative-parity bands was extracted by subtracting a smoothed, interpolated value of i_x for positive-parity states from the i_x value for each negative-parity state at the same value of $\hbar\omega$. In an octupole-vibrational

nucleus, where the negative-parity states are described in terms of an octupole phonon coupled to the positive-parity band, the value of Δi_x is approximately $3\hbar$, as the octupole phonon quickly aligns with the rotation axis as the rotational frequency increases. For a nucleus with stable octupole deformation, the value of Δi_x should be zero because the positive- and negative-parity states are perfectly interleaved of energy in an octupole rotational sequence.

Some other experimental observations, which can be associated with reflection asymmetry in nuclei, for example, relatively large $E3$ transition rates, $B(E3)$, or enhanced α-decay probabilities to low-lying (1^-) states, are not discussed here. The interested reader is referred to dedicated review articles [114, 117] and the references therein.

4.2   Motivations of present work

4.2.1   Regions of strong octupole correlations

As pointed out earlier in this chapter, nuclei with proton and neutron numbers close to 34, 56, 88 and 134 are predicted to possess strong octupole-octupole interactions. The heavy nuclei in the lanthanide ($Z\sim60$, $N\sim90$) and actinide ($Z\sim90$, $N\sim140$) regions attracted much attention since they have shown evidence for the predicted strong octupole correlations. Nuclei in these regions offer the golden possibility to investigate the interplay between collective rotation and octupole degrees of freedom, because they are also characterized, at the minimum, by a modest quadrupole deformation.

The present work concentrates on the actinide region. In this region, nuclei are difficult to populate experimentally, but, many of them exhibit properties associated with more or less intense octupole correlations. As a result, some observed

bands are interpreted as structures built on an octupole vibration (vibrator) or an octupole deformation (rotor). As can be seen in Figure 4.8, among all these nuclei, the Ra and Th isotopes are the ones that have been studied most thoroughly, since they exhibit the strongest octupole correlations based on both the experimental evidence and theoretical calculations. In Figure 4.8, the thick line represents the predicted boundary of octupole deformation [14, 148], while the shaded squares highlight the nuclei in which octupole correlations have been investigated experimentally. In the area within this boundary and nearby, for even-even nuclei, ^{220}Ra [149, 150] and ^{222}Th [129] are two of the best examples of octupole rotors, and, some negative-parity cascades observed, for example, the ones found in ^{228}Th [133] and ^{230,232}Th [147], have been associated with the octupole vibration; while, the alternating-parity bands observed in ^{216}Fr [136] and ^{220}Ac [151, 152] and the parity doublets established in ^{221}Ra [153] and ^{223}Th [141] represent the occurrence of reflection asymmetry in odd-odd nuclei and in odd-A ones, respectively. Further, it was found that octupole correlations also have a significant impact on the properties of some nuclei away from the region defined above. For example, the low lying negative-parity bands observed in ^{238}U [41] and ^{240}U [154] have been interpreted as structures built on an octupole vibration. In these heavier actinide nuclei (U, Np, Pu, Am,... isotopes with $A > 236$), octupole correlations may still play an important role in explaining many observations. However, thus far, there is little information regarding octupole correlations in these nuclei, compared with the nuclei within or close to the bounded area illustrated in Figure 4.8. From this point of view, the present work, which is centered on the Pu isotopes ($Z = 94$) with $A{\sim}240$, expands the limited knowledge of octupole correlations in the actinides, and, some characters of octupole degrees of freedom in the heavier actinide

nuclei different from those in the lighter ones might be revealed as well.

4.2.2 Direct motivations

A few years ago, a study of the properties of the yrast and lowest negative-parity bands in a number of Pu isotopes ($A \sim$ 238–244) was performed by I. Wiedenhöver, *et al.* [43]. It was suggested in this work that strong octupole correlations lead to the absence (in $A =$239, 240) or delay in frequency (in $A =$ 238) of the strong proton alignment observed in the heavier ($A =$ 241, 242, 243 and 244) Pu isotopes. Further, the ^{240}Pu nucleus was found to possibly evolve from an octupole vibrator at low spin to an octupole rotor at high spin, in agreement with theoretical predictions by Jolos and von Brentano [155, 156]. The evidence was based mostly on (but not limited to) (a) the fact that, at the highest spins in ^{238,239,240}Pu, the energy staggering values become very small and comparable to the ones in ^{220}Ra and ^{222}Th, two of the best examples of static octupole rotors, as shown in Figure 4.9, *i.e.*, the states in the yrast band with positive parity become interleaved with the states in the octupole band with negative parity; (b) the comparison of aligned spins as a function of angular frequency ($\hbar\omega$) of the yrast bands in several Pu isotopes and other neighboring nuclei; and (c) the strength of the connecting transitions between the octupole and yrast bands.

The above suggestion received further support from a later work by Sheline and Riley [157]. It was pointed out in their paper that a smaller depression of the excitation energies of the lowest 1^- states was found at neutron numbers of 144 and 146 for Pu isotopes, *i.e.*, ^{238,240}Pu, which is similar with the deep 1^--state depression observed in the region of neutron numbers from 132 to 140 for Ra and Th nuclei (the region where strong octupole correlations lead to stable octupole
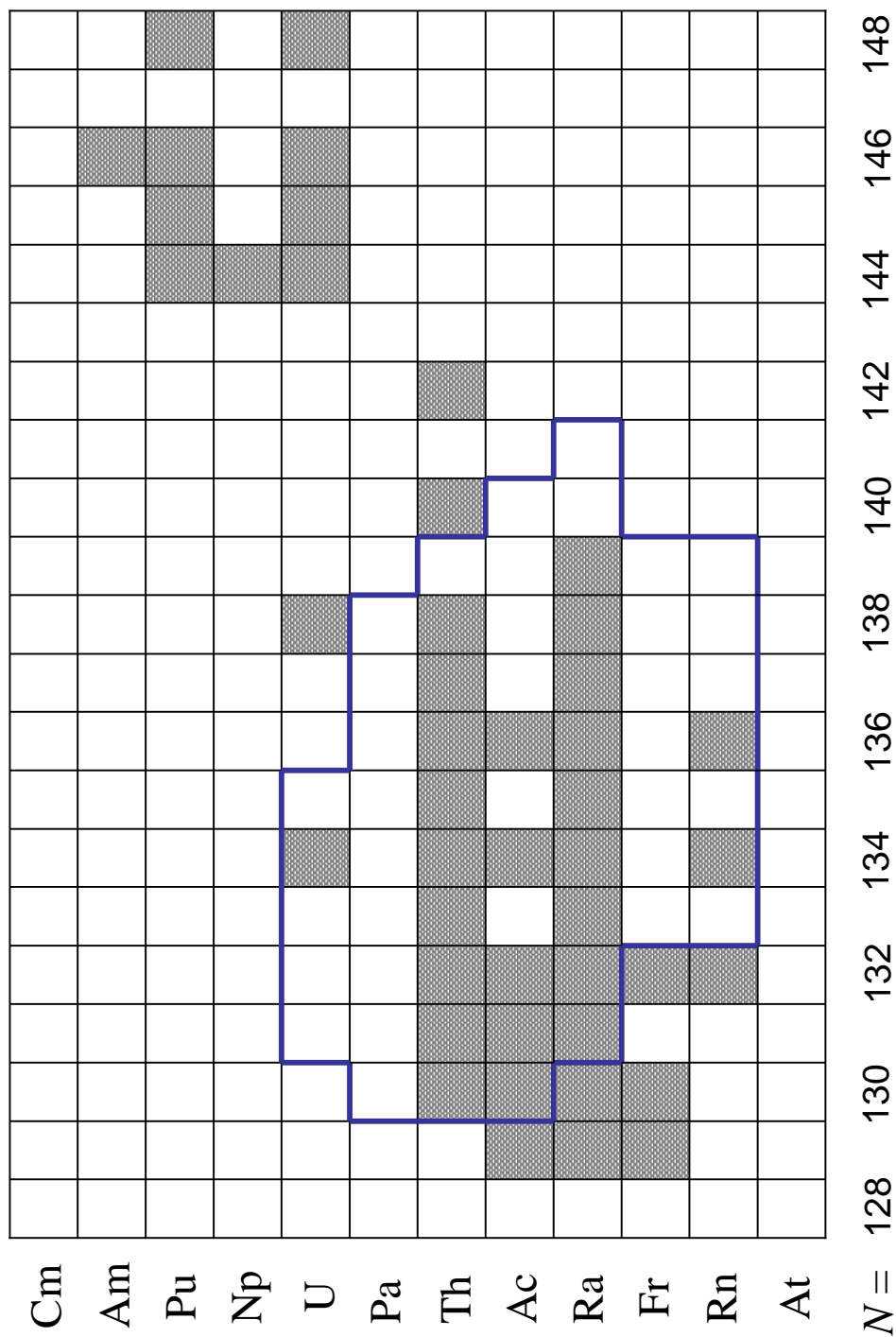
Figure 4.8. The partial actinide region of the nuclear chart with the purpose to illustrate the impact of octupole correlations. The thick line represents the predicted boundary of octupole deformation [14, 148], while the shaded squares are located at the nuclei in which octupole correlations have been investigated experimentally.
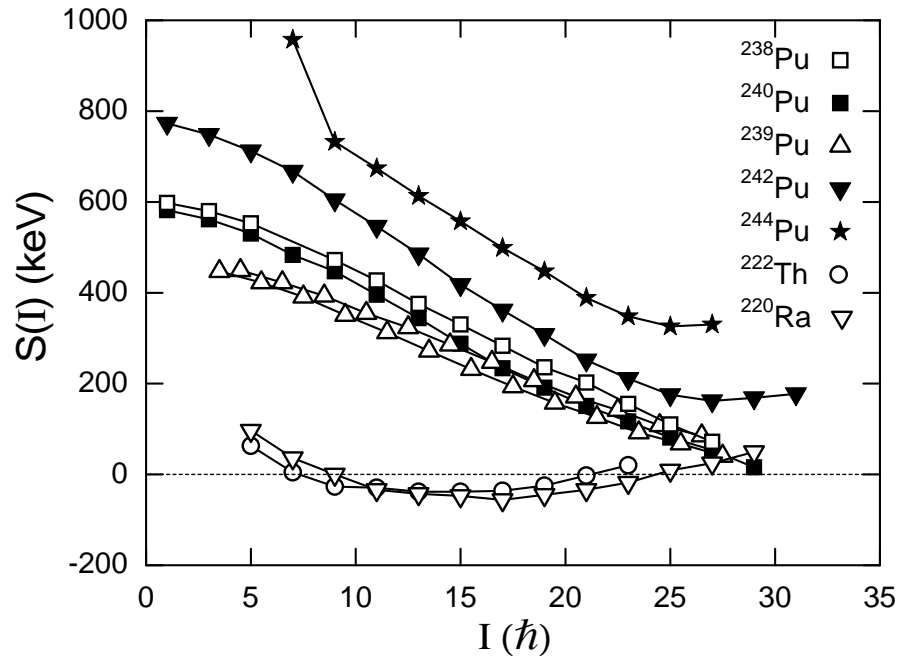
Figure 4.9. Comparison of the energy staggering $S(I)$ as a function of spin I in the Pu isotopes and in ^{220}Ra and ^{222}Th. Taken from Ref. [43].

deformation), as can be seen in Fig. 1(a) of Ref. [157].

Very recently, the properties of the odd-A ^{239}Pu nucleus, which was also proposed to have strong octupole correlations, was investigated and compared with its isotone ^{237}U and other associated neighboring nuclei by Zhu *et al.* [140]. The resulting level scheme of ^{239}Pu is shown in Figure 4.10. This is the first observation of negative-parity bands in an odd-A nucleus that would be associated with an octupole vibration. In contrast to its isotone ^{237}U, the energy differences in ^{239}Pu between states of same spin and opposite parity are getting smaller at high spin. Hence, the observed positive- and negative-parity bands, connected by strong $E1$ transitions at lower spins, tend to form parity doublets (defined in Sec. 4.1.4), one of the most important signatures for octupole deformation in odd-A nuclei, at the highest spins ($\frac{53}{2}\hbar$). More experimental evidence supporting the occurrence of strong octupole correlations at high spin in ^{239}Pu, for example, the aligned spins of the yrast and octupole bands in ^{239}Pu compared with those in several neighboring nuclei, were also presented in the paper [140].

The present work focuses on the octupole correlations in three even-even Pu nuclei (A = 238, 240, 242). We are especially interested in the strong octupole correlations in ^{240}Pu, which are proposed to be enhanced with the increase in angular momentum and be sufficiently strong to result in a transition from an octupole vibration at low spin to octupole deformation at high spin. Hence, the purpose of this work includes: (a) establishing the possible existence of an octupole rotational band consisting of states with alternating parity and spin, I^{+}, $(I+1)^{-}$, $(I+2)^{+}$,..., which are connected by strong $E1$ transitions, at high spin in ^{240}Pu as this is one of the best fingerprints for stable octupole deformation in even-even nuclei, and it could not be established in the earlier work [43] due to the lack of
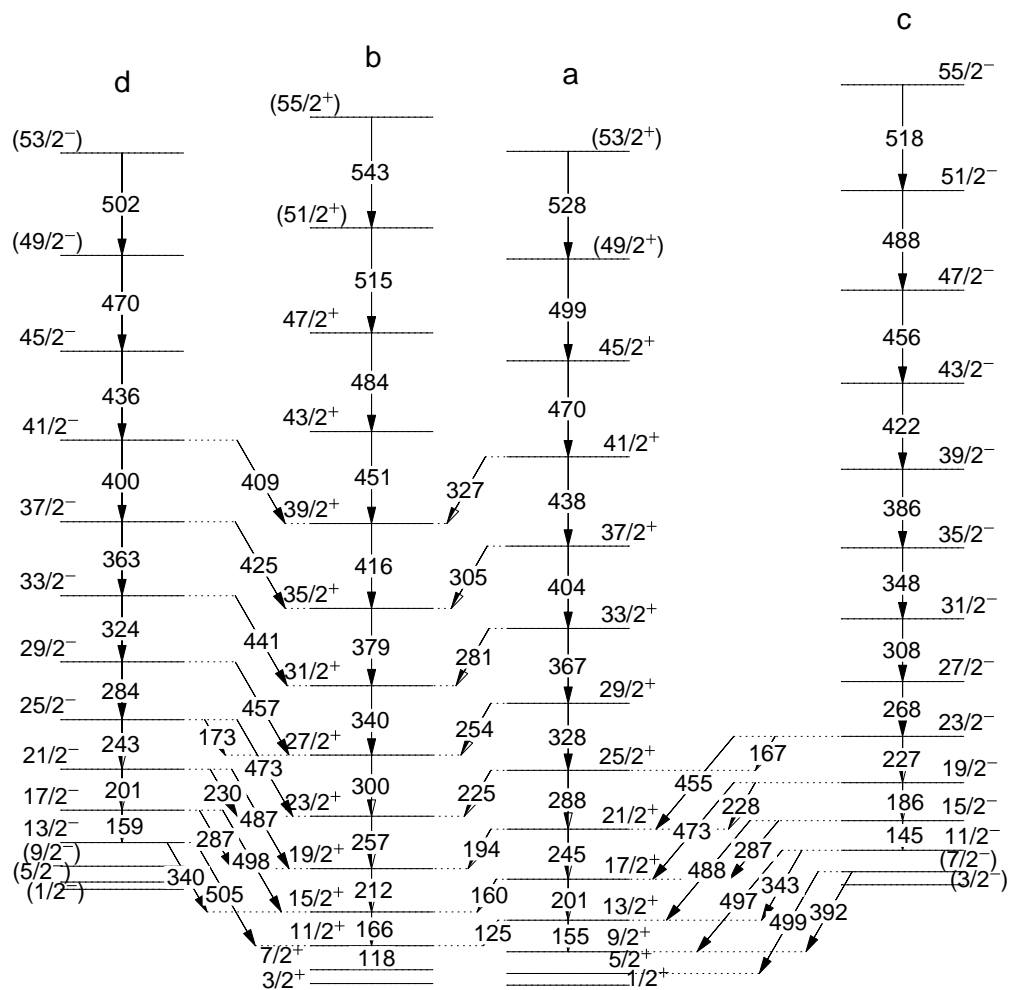
Figure 4.10. Partial level scheme of ^{239}Pu. Bands c and d are the octupole bands of interest. Taken from Ref. [140].

statistics; (b) exploring the magnitude of octupole correlations and its impact on the intrinsic structures of three Pu nuclei by extracting the relevant properties of the observed bands, such as alignments, routhians, *etc.*, and compairng them with results from RPA calculations including octupole interactions; and (c) searching for new levels and new band structures in the three Pu isotopes in order to get a more complete understanding of their intrinsic structures.

4.3   Experiment and data analysis

A series of "unsafe" Coulomb excitation experiments (for ^{240,242}Pu) as well as a single-neutron transfer measurement (for ^{238}Pu) have been carried out at ATLAS with Gammasphere (GS). The number of Compton-suppressed HPGe detectors in working condition was 99 in the ^{240}Pu experiment and 101 for the two other measurements. The so-called "unsafe" Coulomb excitation (Coulex) technique, which has been discussed in detail in Sec. 2.1.3 of chapter 2, was used in order to enhance the feeding of the highest-spin states. In the cases of ^{240}Pu and ^{242}Pu, beams of ^{208}Pb ions at an energy of 1300 MeV bombarded targets consisting of 0.35-mg/cm^2 layers of ^{240}Pu or ^{242}Pu (98% enriched), electroplated onto 50-mg/cm^2 Au backing foils. In addition, each target also had a thin (0.05-mg/cm^2) Au layer in front of the Pu material in order to avoid sputtering of the activity into the scattering chamber. For the single-neutron transfer reaction, an odd-neutron ^{207}Pb beam at 1300 MeV was used in conjunction with a ^{239}Pu target with characteristics similar to those just described.

About 1.2×10^9, 3×10^9 and 0.4×10^9 events with fold three or higher were collected for ^{239}Pu, ^{240}Pu and ^{242}Pu targets, respectively. In the subsequent data analysis, the raw data were converted into both the traditional Radware format

(Cube and Hypercube) and the latest Blue database format. The Cube and Hypercube were used to search for new band structures, while the Blue database made an important contribution in extending the states in the observed bands up to the highest spins. The application of the Blue database technique in the present work also made it convenient to produce spectra at different detector angles for the important angular distribution analysis, which will be discussed later in this section. As discussed in Sec. 2.1.3 of chapter 2, one of the drawbacks of the unsafe Coulex technique is that the transitions at high spin are usually emitted when the recoiling nuclei are still moving in the thick backing (Au) or in the target (Pu), and, as a result, they can be hard to resolve because of Doppler shifts and/or broadening. On the other hand, stable octupole deformation, experimentally exhibited in the form of the presence of a single band structure of states with alternating spins (even and odd) and parities ("+" and "−") in even-even nuclei, appears to occur at high spin in ^{240}Pu based on previous experimental observations [43]. Hence, these in-band and inter-band transitions at high spin, affected by Doppler broadening and shift, are very critical for the success of the present work. In other words, the higher in spin both the yrast and octupole vibrational bands are extended, the larger the probability that evidence for an octupole rotor will be found is. The best solution so far to overcome the difficulty of observing high-spin transitions is to make use of the Blue database analysis technique, so that the inspection of data angle by angle becomes possible. Because of its unique data structure, the Blue database is very useful and powerful for dealing with the thick-target data of γ rays with Doppler-shift and/or -broadening. This has been proven above in the ^{163}Tm DSAM measurement (see Chapter 3). With this technique, individual gating conditions can be set conveniently on γ rays at each

detector angle during the process of generating γ-ray histograms from the data. Then, the resulting spectra with appropriate background subtraction would have excellent quality providing, perhaps, the opportunity to observe the transitions of interest at high spin. Moreover, as discussed in Sec. 2.5.3 of Chapter 2, a coincidence requirement with additional conditions on γ-ray time, total multiplicity and sum-energy in the event and an appropriate subtraction of random signals in the data analysis are also important for achieving reliable coincidence spectra. This is essential because of the negative influence of the strong contaminations from Coulomb excitation of the Au backings. This background will be effectively eliminated or at least strongly suppressed. Therefore, any spectrum used in the following analysis of the Pu data was generated with these additional gating conditions. The method of extending the sequence of states up to higher spins in the Blue database as well as the way of searching for new band structures in Radware have been described in Sec. 2.5 of Chapter 2 and in Sec. 3.3.2 of Chapter 3. It is also worth noting here that only the Radware Hypercube (γ-γ-γ-γ) was used for developing the level scheme of ^{238}Pu, while the γ-γ-γ Cube was applied mostly in the analysis of band structures in ^{240}Pu and ^{242}Pu. Indeed, since the ^{238}Pu data was obtained from the weak, single-neutron transfer channel in the reaction with a ^{207}Pb beam bombarding a ^{239}Pu target, another coincidence gate was set on one of the strongest transitions in ^{208}Pb, the reaction partner of ^{238}Pu, to enhance the channel of interest.

The example of the 260.7-keV ($10^+\rightarrow8^+$) transition in band 1 of ^{242}Pu (see Figure 4.21) is used here to introduce the manner in which the relative intensities of transitions of interest (shown in the column "I_γ" of Tables 4.1–4.11) were extracted from the data. Given that the relative intensity of the 211.3-keV ($8^+\rightarrow6^+$)

transition in band 1 ($I_{\gamma1}\pm\delta I_{\gamma1}$) is known from the total projection spectrum, a spectrum double gated on the two lines below the 211.3-keV transition (the 102.8-keV and 158.5-keV lines) was calibrated with the efficiency curve (see Sec. 2.5.1 of Chapter 2) and, then, adopted after inspecting the level scheme (Figure 4.21). As can be seen in Figure 4.11, the peak areas (shaded areas) for the 211.3-keV ($\gamma1$) and the 260.7-keV lines ($\gamma2$) obtained from the analysis of this spectrum are $S_{\gamma1}$ and $S_{\gamma2}$, respectively. Thus, the relative intensity of the 260.7-keV transition ($I_{\gamma2}$) was calculated by: $I_{\gamma2} = \frac{S_{\gamma2}}{S_{\gamma1}}I_{\gamma1}$. The errors of $S_{\gamma1}$ and $S_{\gamma2}$ ($\delta S_{\gamma1}$ and $\delta S_{\gamma2}$) reflect the statistical fluctuations only, while the determination of the error of $I_{\gamma2}$ ($\delta I_{\gamma2}$), which is a function of $I_{\gamma1}$, $I_{\gamma2}$, $S_{\gamma1}$, $S_{\gamma2}$, $\delta I_{\gamma1}$, $\delta S_{\gamma1}$ and $\delta S_{\gamma2}$, obeys the general rules of propagation of errors [52]. The coincidence gates needed to generate the appropriate spectra were set either on the lines above or on the lines below the transition of interest depending on whether this transition shares the same initial or final state with the reference transition. The real gates used in the data analysis for getting the intensity values will be described in the following sections.

In order to assign or confirm the spins and parities of the observed states, the multipolarities of related transitions were studied by obtaining their angular distribution coefficients (shown in the columns "A_2" and "A_4" of Tables 4.1–4.11). The general process of extracting the A_2 and A_4 coefficients for the transitions of interest from the data is described using the example of the 260.7-keV ($10^+\rightarrow8^+$) transition in band 1 of ^{242}Pu. The nine summed spectra, shown in Figure 4.12, represent the γ-ray signals collected by the detectors at nine angles with the gating conditions set on two of 11 transitions in band 1 of ^{242}Pu (102.8-keV − 511.0-keV lines, excluding the 260.7-keV line). The detectors in 16 rings of GS (no detector installed in ring 1) were arranged into nine groups (rings 2–3, rings 4–5, ring
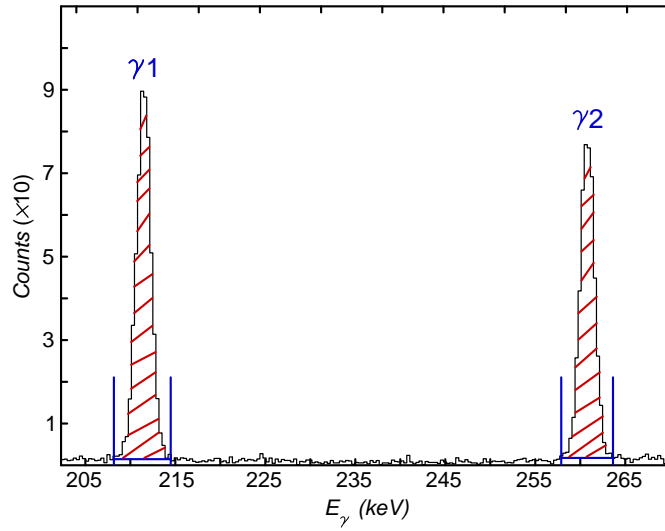
Figure 4.11. Coincidence spectrum double gated on the 102.8-keV and 158.5-keV transitions in band 1 of ^{242}Pu. The 211.3-keV and 260.7-keV γ rays above the gate lines are the transitions of interest, labeled as γ1 and γ2, respectively. See text for details.

6, rings 7–8, ring 9, rings 10–11, ring 12, rings 13-14, rings 15–17) in the data analysis. This implies that detectors in some neighboring rings were placed in one group in order to achieve sufficient statistics for each spectrum. Hence, nine values of peak areas (shaded areas) for the 260.7-keV transition were obtained. As seen in Table 2.1 of Chapter 2, each detector ring has its own angle (θ_i for ring i). From the calibration (see Sec. 2.5.1 of Chapter 2) done earlier, the relative efficiency for detecting γ rays with energies in the range ~ 260 keV for each detector ring has been obtained (the efficiency for ring i is Eff_i). The effective efficiency for a group consisting of detectors in more than one ring, for example, rings 15–17, is the sum of the efficiencies for all involved ring ($Eff_{15} + Eff_{16} + Eff_{17}$). And, the effective angle for such a group is the weighted mean value of the angles of all involved rings with the efficiency of the individual ring as the weighting factor.

For example,

$$\cos(\theta_{eff}) = \frac{Eff_{15}\cos\theta_{15} + Eff_{16}\cos\theta_{16} + Eff_{17}\cos\theta_{17}}{Eff_{15} + Eff_{16} + Eff_{17}}$$

for rings 15–17. Then, the process of fitting the measured intensity (peak area) as a function of $\cos(\theta)$ (θ is the detector angle or effective angle for each group) in the formula of Eq. 2.23, introduced in Sec. 2.5.4 of Chapter 2, was fulfilled by running the codes "Legft" of the Radware software package. An input file for "Legft" is composed of the values of the peak areas, effective angle ($\cos(\theta)$) and effective efficiency obtained above, while the output of "Legft" gives the A_0 (amplitude), A_2 and A_4 coefficients with the errors for the best fit. Examples of angular distribution curves can be seen in Figures 4.14, 4.22 and 4.31. The gating conditions to generate the appropriate spectra for the angular distribution analysis were either both placed on transitions in the same band (for studying in-band lines) or one set on the in-band transitions in one band and the other placed on the lines in the other band (for studying inter-band lines). The actual gates used in the present work will be described in the following sections.

The errors on the γ-ray energies given in the column "E_γ" of Tables 4.1–4.11 include the statistical errors associated with the peak fitting and the systematic ones associated with the calibration of the γ-ray energy. The error arising from the energy calibration (see Sec. 2.5.1 of Chapter 2) can be studied through comparing the energy values translated from the measured channel numbers with the adopted energy values for the γ rays from the standard radioactive sources. These errors are usually small, typically less than 0.1 keV over a wide range of γ-ray energies (10 keV − 2 MeV).

It should be noted that, due to the weak γ-ray intensity, the strong contamina-

176
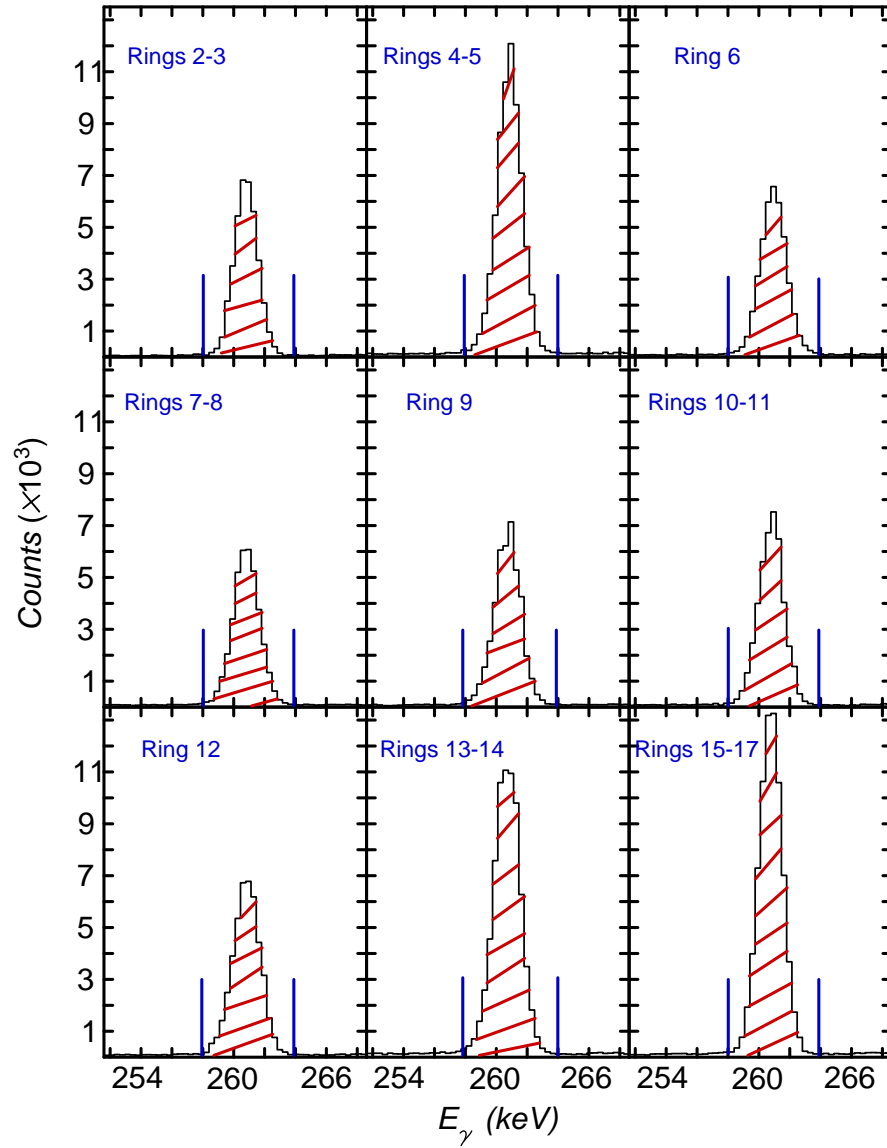
Figure 4.12. The summed spectra gated on two of 11 transitions in band 1 of ^{242}Pu at nine detector angles. The peak area (shaded area) of the 260.7-keV transition in each spectrum was obtained for the subsequent angular distribution analysis. See text for details.

tion, *etc.*, the values of the γ-ray intensity (I_γ) and angular-distribution coefficients (A_2, A_4) for some transitions are missing in Tables 4.1–4.11.

4.4 ^{240}Pu data

The level scheme of ^{240}Pu resulting from the above data analysis is presented in Figure 4.13. The three bands, observed in our experiment, are labeled as bands 1, 2 and 3, respectively, and will be discussed in detail one by one below. In the level scheme, a state is labeled by its spin, parity and excitation energy relative to the ground state (unit: keV), while a transition is labeled by its energy (unit: keV) only. The states and transitions drawn as dashed lines or labeled by the energy, spin-parity symbols in parentheses are tentative. This means of labeling states and transitions in the level scheme was also adopted in the ^{242}Pu and ^{238}Pu cases below.

For calculating the values of relative intensity in the column "I_γ" of Tables 4.1, 4.2 and 4.3, the 249.9-keV (10^+→8^+) transition in band 1 was taken as the "standard", and its intensity has been normalized to "1000" for convenience. Based on the relative γ-ray intensities obtained, the population of bands 2 and 3 relative to band 1 in this experiment was estimated to be 10% and 2%, respectively. Representative angular distributions for in-band and inter-band transitions associated with each band in ^{240}Pu are compared in Figure 4.14, *i.e.*, the examples of the 249.9-keV (10^+→8^+) and 499.2-keV (24^+→22^+) lines in band 1, the 377.9-keV (19^-→17^-) line in band 2, the 498.7-keV (13^-→12^+) transition linking bands 1 and 2, the 381.2-keV (20^+→18^+) line in band 3 and the 597.1-keV (14^+→13^-) transition linking bands 2 and 3. It was found in the analysis that the measured angular distribution coefficients (A_2 and A_4) for in-band and inter-band tran-
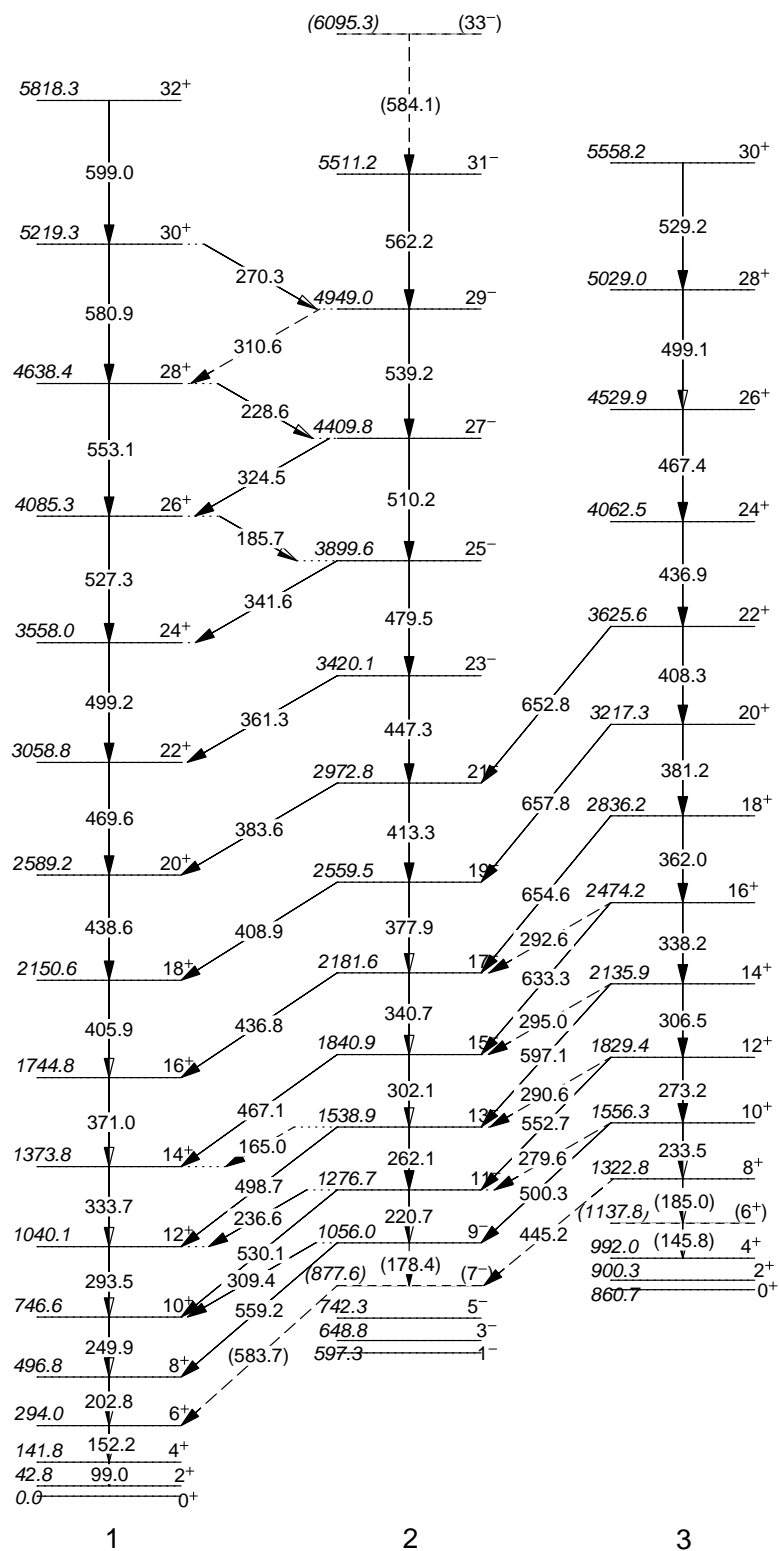
Figure 4.13. Partial level scheme of ^{240}Pu resulting from present work.
See text for details.

sitions in ^{240}Pu (see Tables 4.1, 4.2 and 4.3) are very close to the typical values expected for quadrupole and dipole γ rays, respectively (see Table 2.3 in Sec. 2.5.4 of Chapter 2).
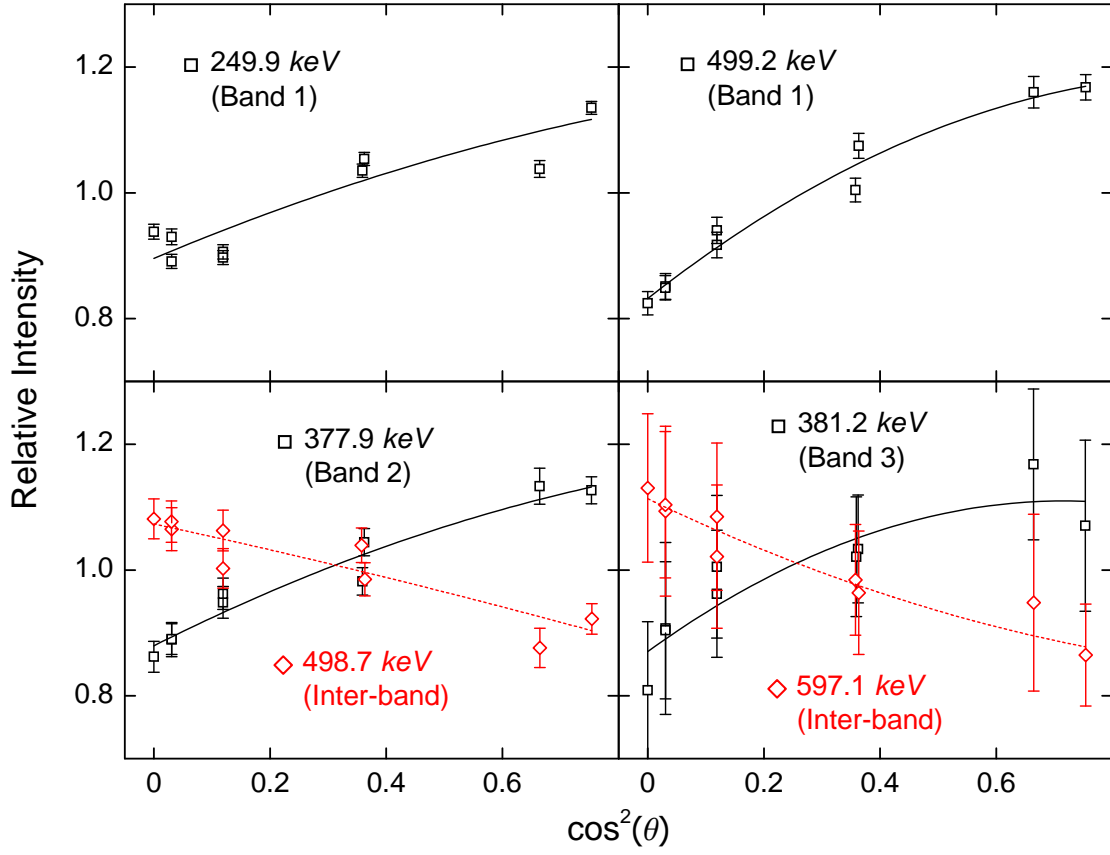
Figure 4.14. Samples of angular distributions for transitions in ^{240}Pu. The drawn curves (solid or dashed) represent the best fit of the data points. See text for details.

4.4.1 ^{240}Pu band 1

Band 1 in Figure 4.13 is the yrast band, which has been identified in several previous measurements [42, 158, 159, 160]. It consists of 16 transitions. The present work extends this band by three additional transitions with respect to the work of Ref. [42]. All in-band transitions of band 1 can be seen in Figure 4.15, with the exception of the 42.8-keV ($2^+\rightarrow0^+$) transition. The latter was not observed due to the high internal electron conversion probability in this low-energy range. The sum of spectra double gated on any two of the 11 in-band γ rays (from 152.2-keV to 527.3-keV) at all detector angles (rings 2–17), at forward angles (rings 2–8) and at backward angles (rings 10–17) are given in the top, middle and bottom panel, respectively. It is not surprising to see in the spectra that the 99.0-keV ($4^+\rightarrow2^+$) γ ray is contaminated by the $K\alpha$ characteristic X rays of Pu. From the comparison of these three spectra, it can be seen clearly that the transitions at high spin, $i.e.$, the 527.3-keV γ ray and all other lines above it, are associated with Doppler shifts and broadenings. This observation provides a direct indication that making use of the angular gating technique ($i.e.$, using individual gating conditions for each detector angle when generating the spectra with certain coincidence requirements) in the Blue database is absolutely necessary in order to see the transitions at the highest spins (as discussed in Sec. 4.3). Conversely, it is just the application of these proper data analysis techniques that makes the observation of such Doppler-shifted and -broadened transitions possible.

The intensities of the three low-lying transitions, $i.e.$, the 152.2-keV ($6^+\rightarrow4^+$), the 202.8-keV ($8^+\rightarrow6^+$) and the 249.9-keV ($10^+\rightarrow8^+$) transitions, were obtained from the total projection spectrum of the data. For the 293.5-keV ($12^+\rightarrow10^+$)

TABLE 4.1

THE EXCITATION ENERGIES (E_x) OF INITIAL STATES,
ASSIGNED SPINS, γ-RAY ENERGIES (E_γ), RELATIVE γ-RAY
INTENSITIES (I_γ) AND ANGULAR DISTRIBUTION
COEFFICIENTS (A_2 AND A_4) FOR THE TRANSITIONS
ASSOCIATED WITH BAND 1 IN ^{240}Pu

Band 1 in ^{240}Pu					
E_x (keV)	Assigned spin ($\hbar$)	E_γ (keV)	I_γ (rel.)	A_2	A_4
141.8	$4^+ \rightarrow 2^+$	99.0(3)			
294.0	$6^+ \rightarrow 4^+$	152.2(3)	370(10)	0.29(5)	-0.04(5)
496.8	$8^+ \rightarrow 6^+$	202.8(3)	844(21)	0.29(4)	-0.04(4)
746.6	$10^+ \rightarrow 8^+$	249.9(3)	1000(14)	0.19(4)	-0.03(5)
1040.1	$12^+ \rightarrow 10^+$	293.5(3)	966(23)	0.21(3)	-0.02(5)
1373.8	$14^+ \rightarrow 12^+$	333.7(3)	841(23)	0.21(2)	-0.04(3)
1744.8	$16^+ \rightarrow 14^+$	371.0(3)	705(20)	0.19(3)	-0.01(5)
2150.6	$18^+ \rightarrow 16^+$	405.9(3)	529(25)	0.19(4)	-0.05(5)
2589.2	$20^+ \rightarrow 18^+$	438.6(3)	347(29)	0.21(4)	-0.02(6)
3058.8	$22^+ \rightarrow 20^+$	469.6(3)	210(14)	0.19(5)	-0.02(6)
3558.0	$24^+ \rightarrow 22^+$	499.2(3)	125(13)	0.27(3)	-0.08(3)
4085.3	$26^+ \rightarrow 24^+$	527.3(3)	54(9)	0.33(5)	-0.05(5)
	$26^+ \rightarrow 25^-$	185.7(3)	6(3)		
4638.4	$28^+ \rightarrow 26^+$	553.1(3)	26(9)		
	$28^+ \rightarrow 27^-$	228.6(4)	7(4)		

TABLE 4.1 (contd.)

E_x (keV)	Assigned spin $(\hbar)$	E_γ (keV)	I_γ (rel.)	A_2	A_4
5219.3	$30^+ \to 28^+$	580.9(3)	19(7)		
	$30^+ \to 29^-$	270.3(4)			
5818.3	$32^+ \to 30^+$	599.0(3)	19(9)		
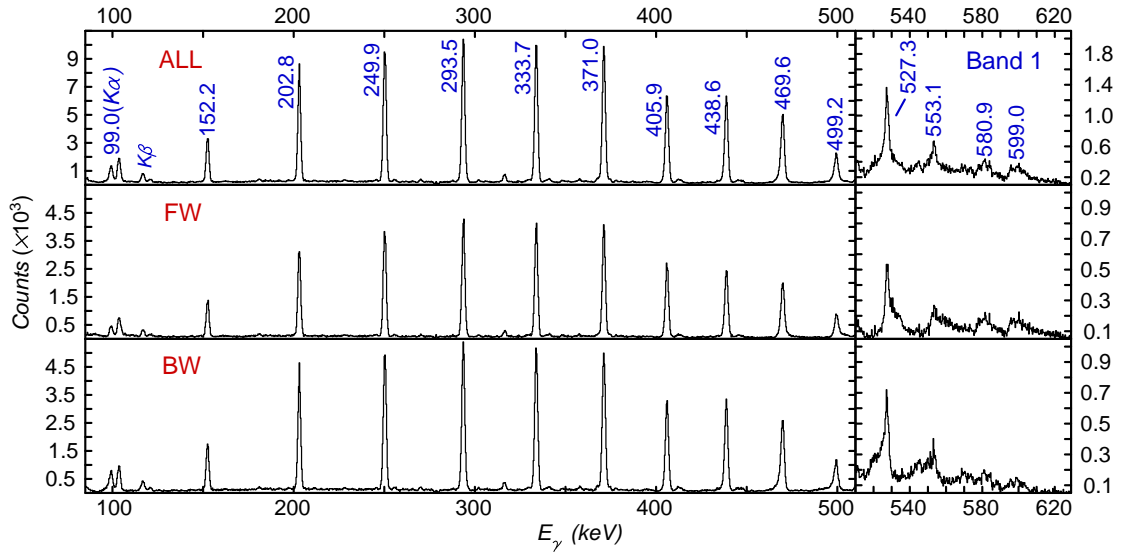
Figure 4.15. Three spectra representative of band 1 in ^{240}Pu. They are the sum of coincidence spectra, double gated on any two of 11 in-band γ rays (from the 152.2-keV line to the 527.3-keV transition) of band 1, at all detector rings (ALL), at rings 2–8 (FW) and at rings 10–17 (BW), respectively. $K\alpha$ and $K\beta$ denote the characteristic X rays of Pu.

transition, the coincidence spectrum double gated on the 152.2-keV line and the 202.8-keV γ ray was analyzed to achieve the ratio of intensity between the 249.9-keV and 293.5-keV transitions. The relative intensity of the 293.5-keV line was then obtained by the means described earlier in Sec. 4.3. Similarly, the intensities for the 333.7-keV and higher transitions were acquired from the appropriate spectra. For analyzing the angular distributions of the transitions in this band, the summed spectra with all available double gates were used. Nevertheless, when studying the intensity and angular distribution of transitions impacted by contamination, for example, the 527.3-keV ($26^+\rightarrow24^+$) transition that is contaminated by the 530.1-keV ($11^-\rightarrow10^+$) line, the use of gates that can lead to the observation of contamination, $i.e.$, any two of the 249.9-keV line and transitions located below, was carefully avoided.

The spin and parity of each state below the 26^+ level in this band, established in previous measurements [42, 159, 160], was confirmed here through the measured angular distributions. As the transitions above the 26^+ state form a natural extension of the lower-spin sequence in this band, the spin and parity for states above 26^+ was assigned based on an $E2$ multipolarity for these in-band transitions, although the information of A_2 and A_4 coefficients for them is not available in the present work. The fact that all these transitions below the 26^+ level in band 1 exhibit the expected angular distribution patterns can be viewed as support for the analysis techniques.

4.4.2 ^{240}Pu band 2

Band 2 in Figure 4.13, previously observed by Hackman et $al.$ [42], has been interpreted as the $K^\pi = 0^-$ octupole vibrational band. It consists of 16 transi-

tions. All transitions above the 7^- level in this band can be seen in Figure 4.16. In this spectrum, the 178.4-keV ($9^- \rightarrow 7^-$) γ ray is too weak to be observed clearly, and, the 584.1-keV ($33^- \rightarrow 31^-$) transition is hard to establish due to the impact of contamination and Doppler shift and/or broadening. As a result, these two transitions as well as the associated 7^- and 33^- states were assigned as tentative in the level scheme (Figure 4.13). The three bottom (below the 7^- level) transitions were not observed here due to the high internal electron conversion probability, but the associated energy levels, *i.e.*, the 1^-, 3^- and 5^- states, have been established in previous decay studies [158, 159]. Compared with the level scheme in Ref. [42], three new transitions at the highest spins (above 27^-) have been added, though the top transition at 584.1-keV ($33^- \rightarrow 31^-$) remains tentative. All of the transitions connecting bands 1 and 2, observed in previous experiment [42], are γ rays associated with the deexcitations from band 2 (octupole band) to band 1 (yrast band). They can be grouped into two types: $J^- \rightarrow (J-1)^+$ and $J^- \rightarrow (J+1)^+$, with the latter being much weaker in intensity (see Table 4.2). These inter-band transitions were also observed in the present work, as indicated in the main spectrum of Figure 4.16.

As described above, with the application of the angular gating technique in the Blue database, both the yrast band and the octupole sequence were extended towards higher spin. As a result, five additional $J^- \rightarrow (J-1)^+$ transitions between these two bands at higher spin, *i.e.*, the 383.6-, 361.3-, 341.6-, 324.5- and 310.6-keV lines, were found in the present work. All of these five γ rays are indicated in the inserted spectra of Figure 4.16, but, the highest lying one, *i.e.*, the 310.6-keV ($29^- \rightarrow 28^+$) transition, was taken as tentative because of the poor

TABLE 4.2

THE EXCITATION ENERGIES (E_x) OF INITIAL STATES,
ASSIGNED SPINS, γ-RAY ENERGIES (E_γ), RELATIVE γ-RAY
INTENSITIES (I_γ) AND ANGULAR DISTRIBUTION
COEFFICIENTS (A_2 AND A_4) FOR THE TRANSITIONS
ASSOCIATED WITH BAND 2 IN ^{240}Pu

Band 2 in ^{240}Pu					
E_x (keV)	Assigned spin ($\hbar$)	E_γ (keV)	I_γ (rel.)	A_2	A_4
877.6	$7^- \to 6^+$	583.7(4)			
1056.0	$9^- \to 7^-$	178.4(4)			
	$9^- \to 8^+$	559.2(3)	14(10)	-0.16(5)	-0.02(7)
	$9^- \to 10^+$	309.4(3)	5(5)	-0.20(5)	0.04(8)
1276.7	$11^- \to 9^-$	220.7(3)	4(2)	0.22(4)	-0.06(6)
	$11^- \to 10^+$	530.1(3)	18(9)	-0.14(5)	0.04(4)
	$11^- \to 12^+$	236.6(3)	7(4)		
1538.9	$13^- \to 11^-$	262.1(3)	21(10)	0.18(4)	-0.03(5)
	$13^- \to 12^+$	498.7(3)	28(18)	-0.15(3)	-0.01(5)
	$13^- \to 14^+$	165.0(3)	2(2)		
1840.9	$15^- \to 13^-$	302.1(3)	57(25)	0.23(3)	-0.05(4)
	$15^- \to 14^+$	467.1(3)	37(21)		
2181.6	$17^- \to 15^-$	340.7(3)	90(84)	0.17(4)	-0.03(4)
	$17^- \to 16^+$	436.8(3)	31(38)		
2559.5	$19^- \to 17^-$	377.9(3)	68(52)	0.21(3)	-0.04(4)
	$19^- \to 18^+$	408.9(3)	14(3)		

186

TABLE 4.2 (contd.)

E_x (keV)	Assigned spin $(\hbar)$	E_γ (keV)	I_γ (rel.)	A_2	A_4
2972.8	$21^-\rightarrow19^-$	413.3(3)	42(26)	0.16(5)	-0.04(5)
	$21^-\rightarrow20^+$	383.6(3)	9(2)		
3420.1	$23^-\rightarrow21^-$	447.3(3)	29(11)	0.19(3)	-0.04(5)
	$23^-\rightarrow22^+$	361.3(3)	6(2)		
3899.6	$25^-\rightarrow23^-$	479.5(3)	22(15)	0.19(4)	-0.07(3)
	$25^-\rightarrow24^+$	341.6(3)	7(3)		
4409.8	$27^-\rightarrow25^-$	510.2(3)	19(14)	0.24(5)	-0.12(4)
	$27^-\rightarrow26^+$	324.5(3)			
4949.0	$29^-\rightarrow27^-$	539.2(3)	13(9)		
	$29^-\rightarrow28^+$	310.6(4)			
5511.2	$31^-\rightarrow29^-$	562.2(3)	10(7)		
6095.3	$33^-\rightarrow31^-$	584.1(4)			
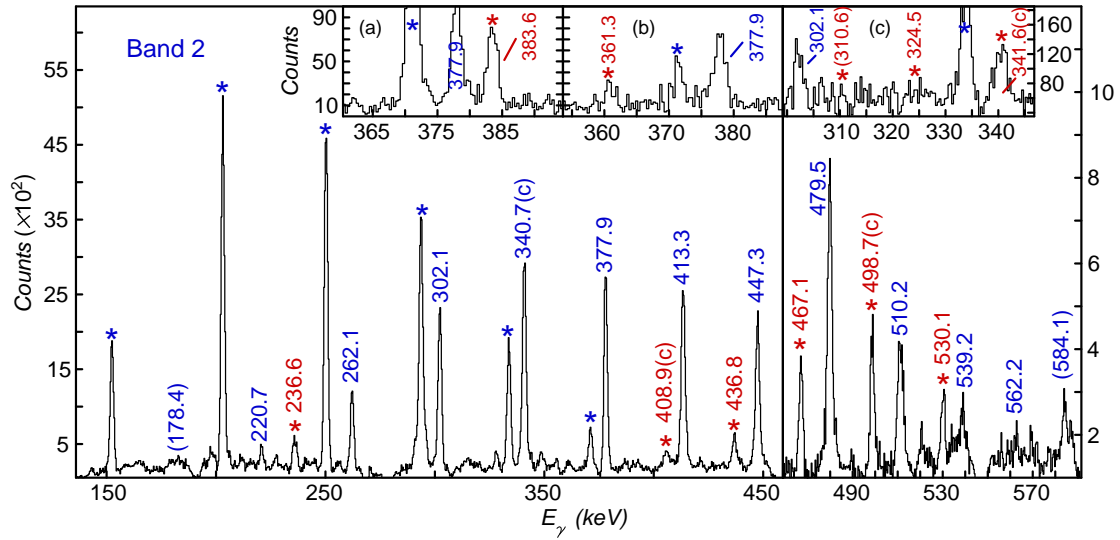
Figure 4.16. Spectra representative of band 2 in ^{240}Pu. The main spectrum is the sum of spectra double gated on any two of the 10 in-band γ rays (from 220.7-keV to 539.2-keV) of band 2. Insert (a, left): the spectrum gated on the 438.6-keV line in band 1 and the 447.3-keV line in band 2; insert (b, middle): the spectrum gated on the 469.6-keV line in band 1 and the 479.5-keV line in band 2; insert (c, right): the sum of spectra gated on the 499.2-keV line (band 1) / the 510.2-keV line (band 2), the 527.3-keV line (band 1) / the 539.2-keV line (band 2), the 527.3-keV line (band 1) / the 562.2-keV line (band 2) and the 553.1-keV line (band 1) / the 562.2-keV line (band 2). The in-band transitions in band 2 are labeled by their energy values. The in-band transitions in other bands (*e.g.*, band 1) of ^{240}Pu are highlighted by "⋆" symbols, while the inter-band transitions are marked with "⋆" symbols plus their energy values. The energy values followed by "(c)" symbols and such values placed in parentheses denote contaminated transitions and tentative ones, respectively.

associated statistics. More importantly, the linking transitions between bands 1 and 2 in an opposite direction, $i.e.$, $(J+1)^+ \to J^-$, were revealed for the first time in the present work. Three such transitions above spin $25\hbar$, $i.e.$, the 185.7-keV $(26^+ \to 25^-)$, 228.6-keV $(28^+ \to 27^-)$ and 270.3-keV $(30^+ \to 29^-)$ lines, are indicated in spectra (see Figure 4.17) with appropriate gating conditions, $i.e.$, one gate set on one of transitions in one band and the other gate placed on one of the lines in the other band. As can be seen in Figure 4.17, due to the range of spin in which they are located, these transitions are weak and have significant Doppler shifts and/or broadenings. As a result, they are hard to identify experimentally. However, by using the angular gating technique on the data with the Blue database format, the difficulty of observing those inter-band transitions was overcome in the present work. As described in Sec. 4.2.2, one of the purposes of present work is to establish the possible existence of an octupole rotational band consisting of states with alternating parity, connected by $E1$ transitions at high spin in ^{240}Pu. Therefore, the observation of these $J^- \to (J-1)^+$ and $(J+1)^+ \to J^-$ inter-band transitions, $i.e.$, the so-called "zig-zag" structure, at the $24\hbar$ and higher spins in the present work constitutes one of the most important evidence for fulfilling the above purpose. Its importance will be discussed further in Sec. 4.7.2.

In Ref. [42], the spins and parity of levels 9^- – 27^- were assigned taking advantage of the fact that these levels form a natural extension of a $K^\pi = 0^-$ level sequence $(1^-, 3^-, 5^-)$ previously identified in Refs. [158, 159]. Here, this assignment has been confirmed by the measured angular distribution coefficients for the transitions connecting bands 1 and 2 (indicative of dipole multipolarity) and the ones in band 2 (indicative of quadrupole multipolarity), see Table 4.2. The spins and parity for states above 27^- were assigned based on the fact that all

189
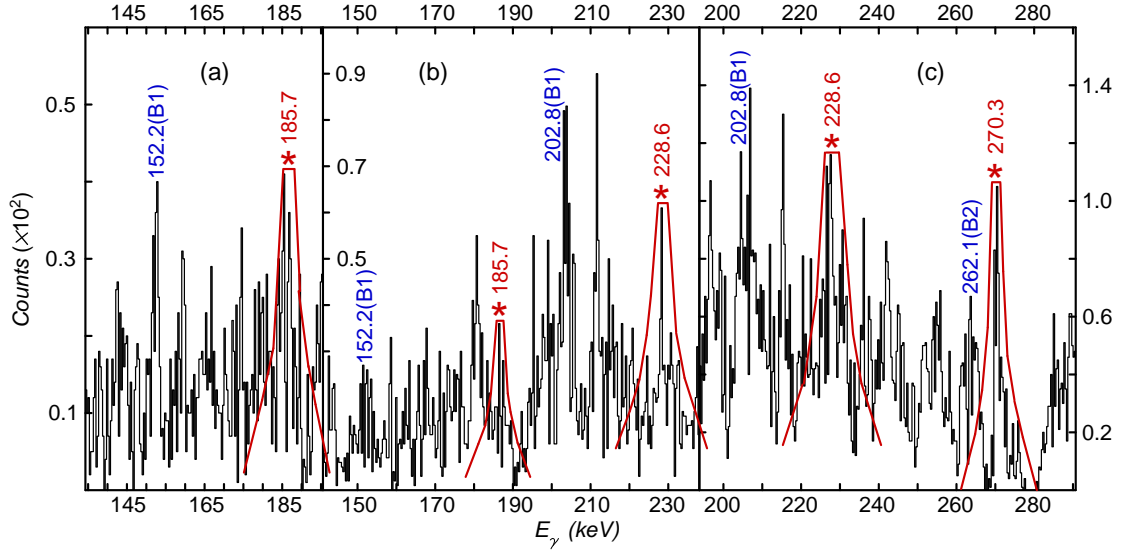
Figure 4.17. Coincidence spectra supporting the observation of three important $(J+1)^{+} \rightarrow J^{-}$ inter-band transitions. Gates for the panel (a) are set on the 553.1-keV transition in band 1 and one of the four lines (from 377.9-keV to 479.5-keV) in band 2; gates for the panel (b) are set on the 580.9-keV transition in band 1 and one of the five lines (from 377.9-keV to 510.2-keV) in band 2; gates for the panel (c) are set on the 599.0-keV transition in band 1 and one of the six lines (from 377.9-keV to 539.2-keV) in band 2. The energy values followed by "(B1)" and "(B2)" symbols represent the transitions in band 1 and in band 2, respectively. The red outlines indicate the estimated broadened shapes of these γ-ray peaks. See text for details.

transitions in a rotational band are associated with an $E2$ multipolarity, *i.e.*, the argument is similar to that used for the highest-spin states in band 1. The ratios of intensity between the transition in band 1 and the line connecting bands 1 and 2, which have a same final state, for example the 469.6-keV ($22^+ \rightarrow 20^+$) line and the 383.6-keV ($21^- \rightarrow 20^+$) transition, can be determined in the summed spectra double gated on the in-band transitions below the associated state of band 1 (the 20^+ level for the above example). Then, the relative intensities of these inter-band transitions can be calculated (see Table 4.2) since the ones of in-band lines of band 1 have been obtained earlier. The ratios of intensity between a transition in band 2 and the line connecting bands 1 and 2 which have a same initial state, for example the 413.3-keV ($21^- \rightarrow 19^-$) line and the 383.6-keV ($21^- \rightarrow 20^+$) γ ray, can also be extracted in the summed coincidence spectra double gated on the in-band transitions above the associated state of band 2 (the 21^- level for the above example). Similarly, the relative intensities of the transitions in band 2 can be obtained (see Table 4.2). The difference in the data analysis of bands 1 and 2 is that it is harder to pick proper gating transitions to generate coincidence spectra for band 2 because of the large number of contaminants and doublet transitions. This observation, together with the weaker intensity of band 2, explains why the quoted uncertainties in the relative intensities are often large.

4.4.3 ^{240}Pu band 3

The second positive-parity band, band 3, in Figure 4.13 consists of 15 transitions. Starting from the 6^+ level, none of the higher states of this band have been reported in the literature. The three bottom levels, on the other hand, were established previously by a decay study of ^{240}Np [159]. All of the in-band tran-

sitions up to spin $30\hbar$ as well as the transitions connecting bands 2 and 3 are indicated in Figure 4.18, except for the two γ rays at the lowest spins (below the 4^+ level). These were not observed in the present work due to the high internal conversion probability. Since the transitions associated with this band encounter intense contamination, such as the 408.3-keV ($22^+\rightarrow20^+$) transition being affected by the 405.9-keV ($18^+\rightarrow16^+$) line in band 1 and the 408.9-keV ($19^-\rightarrow18^+$) γ ray between bands 1 and 2, for example, the number of transitions that can be used as gates for generating proper coincidence spectra is very limited. Hence, the spectra in Figure 4.18 were obtained with appropriate gating conditions following careful and thorough checking of the gates. As can be seen in the main spectrum of Figure 4.18, the 145.8-keV ($6^+\rightarrow4^+$) and the 185.0-keV ($8^+\rightarrow6^+$) transitions are too weak to be identified firmly. Hence, these two transitions as well as the associated state, $i.e.$, the 6^+ level, were assigned as tentative in the level scheme (Figure 4.13).

Applying the same method that was used in the case of band 2, the relative intensity and angular distribution coefficients for the transitions associated with band 3 were obtained (see Table 4.3). When choosing the proper gates for generating certain spectra, extra caution was taken due to the weaker intensity and the more complex contaminations for this band, as described above. Compared with the typical values of γ-ray angular distribution coefficients (A_2 and A_4) given in Table 2.3 of Chapter 2, the A_2 and A_4 coefficients for the transitions connecting bands 2 and 3 and the ones in band 3 (given in Table 4.3) suggest their dipole and quadrupole nature, respectively. Hence, positive parity and even spins were assigned to the states of band 3 (the spins and parity for states above 20^+ were again assigned based on the fact that these transitions represent the natural ex-

tension of the lower-spin sequence in this band and all in-band transitions possess $E2$ multipolarity). As will be shown later in the present work, the routhian plot of this band (Figure 4.42 in Sec. 4.7.3) also suggests that the sequence of γ rays observed in the present work (above the 6^+ level) extrapolates well at lower angular frequency to the known 4^+, 2^+, and 0^+ levels (the excitation energy of the 0^+ state, E_x is 860.7 keV). This band head was interpreted to be associated with a β vibration in the decay work mentioned above [159]. The consistency of data points from the present work (at higher spin) with the ones from the decay study (at lower spin) supports, from another point of view, the assignment of spin and parity to this band proposed above. As in the case of band 2, the transitions connecting bands 2 and 3 can be grouped into two types: $J^+\rightarrow(J-1)^-$ and $J^+\rightarrow(J+1)^-$. The latter ones are also much weaker than the former in intensity (see Table 4.2). As can be seen in Figure 4.18, the 290.6-keV ($12^+\rightarrow13^-$) line, as an example of the weak $J^+\rightarrow(J+1)^-$ inter-band transitions, also faces strong contaminating γ rays (293.5-keV in band 1). These transitions were not observed clearly in the present work, and, hence, were taken as tentative in the level scheme. It is also interesting that band 3 was found to decay only to band 2. In other words, no linking transition between bands 1 and 3 was found, based on the observation that the maximum value of the relative intensity for virtual inter-band transitions connecting bands 1 and 3 was estimated to be 1 (the relative intensity of the 249.9-keV line in band 1 defined as 1000) in the present work.
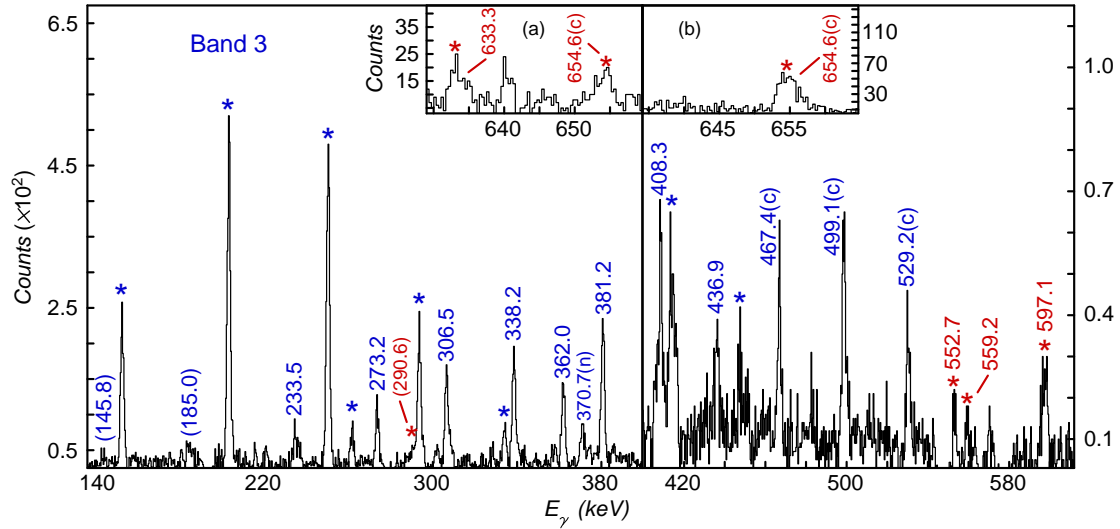
Figure 4.18. Spectra representative of band 3 in ^{240}Pu. The left panel of the main spectrum is the sum of several double-gated spectra. The gates were set on one of the two transitions with 273.2-keV and 306.5-keV energies, respectively, in band 3 and one of another three lines in the same band (306.5-keV, 338.2-keV and 362.0-keV), but, the two gates were not set on the 306.5-keV line at the same time. The right panel of the main spectrum is the spectrum double gated on the 338.2-keV and the 381.2-keV γ rays in band 3. Insert (a, left): the sum of spectra double gated on the 302.1-keV line in band 2 and one of the transitions above the 16$^+$ level in band 3; insert (b, right): the sum of spectra gated on the 340.7-keV line in band 2 and one of the γ rays above the 18$^+$ level in band 3. The related transitions shown in the spectra are labeled in the manner used in Figure 4.16. In addition, the energy value followed by the "(n)" symbol denotes a transition in the new band described in Sec. 4.4.4 and illustrated in Figure 4.19.

TABLE 4.3

THE EXCITATION ENERGIES (E_x) OF INITIAL STATES,

ASSIGNED SPINS, γ-RAY ENERGIES (E_γ), RELATIVE γ-RAY

INTENSITIES (I_γ) AND ANGULAR DISTRIBUTION

COEFFICIENTS (A_2 AND A_4) FOR THE TRANSITIONS

ASSOCIATED WITH BAND 3 IN ^{240}Pu

Band 3 in ^{240}Pu					
E_x (keV)	Assigned spin ($\hbar$)	E_γ (keV)	I_γ (rel.)	A_2	A_4
1137.8	$6^+ \rightarrow 4^+$	145.8(4)			
1322.8	$8^+ \rightarrow 6^+$	185.0(3)	1.2(8)		
	$8^+ \rightarrow 7^-$	445.2(4)			
1556.3	$10^+ \rightarrow 8^+$	233.5(3)	1.8(12)		
	$10^+ \rightarrow 9^-$	500.3(3)	2.6(17)	-0.18(3)	0.07(4)
	$10^+ \rightarrow 11^-$	279.6(4)			
1829.4	$12^+ \rightarrow 10^+$	273.2(3)	3.1(17)	0.18(2)	-0.12(4)
	$12^+ \rightarrow 11^-$	552.7(4)	2.8(15)	-0.23(4)	0.03(3)
	$12^+ \rightarrow 13^-$	290.6(4)			
2135.9	$14^+ \rightarrow 12^+$	306.5(3)	9(5)	0.26(2)	-0.10(4)
	$14^+ \rightarrow 13^-$	597.1(3)	7(4)	-0.20(2)	0.04(4)
	$14^+ \rightarrow 15^-$	295.0(3)	2.9(17)		
2474.2	$16^+ \rightarrow 14^+$	338.2(3)	13(12)	0.30(5)	-0.13(6)
	$16^+ \rightarrow 15^-$	633.3(4)	4(4)	-0.22(3)	0.02(5)
	$16^+ \rightarrow 17^-$	292.6(4)			

TABLE 4.3 (contd.)

E_x (keV)	Assigned spin $(\hbar)$	E_γ (keV)	I_γ (rel.)	A_2	A_4
2836.2	$18^+\rightarrow16^+$	362.0(3)	7(5)	0.22(5)	-0.14(6)
	$18^+\rightarrow17^-$	654.6(3)	2.3(18)		
3217.3	$20^+\rightarrow18^+$	381.2(3)	5(4)	0.18(5)	-0.11(7)
	$20^+\rightarrow19^-$	657.8(4)	0.9(6)		
3625.6	$22^+\rightarrow20^+$	408.3(4)			
	$22^+\rightarrow21^-$	652.8(4)	0.8(4)		
4062.5	$24^+\rightarrow22^+$	436.9(5)			
4529.9	$26^+\rightarrow24^+$	467.4(5)			
5029.0	$28^+\rightarrow26^+$	499.1(5)			
5558.2	$30^+\rightarrow28^+$	529.2(5)			

4.4.4 Sequence(s) not assigned

In the present ^{240}Pu data, another new band has been observed as illustrated in Figure 4.19. Three supporting spectra in Figure 4.20 were generated by triple gating on three of the four transitions at 303.5-, 340.3-, 370.7- and 405.8-keV. The transitions used as gates in these spectra could not be in mutual coincidence if they were not part of this new band. The coincidence relations shown in the spectra of Figure 4.20 suggest that this new cascade is coincident with the transitions in ^{240}Pu. Unfortunately, it was not possible to give any simple interpretation for this band. A thorough search was made in order to connect this cascade to the known states in ^{240}Pu and in neighboring nuclei, but without success. Hence, this new band could not be assigned in present work, but, it will perhaps be identified in future experiments.

196
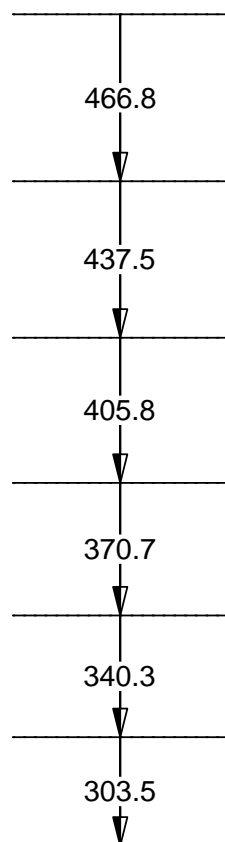
Figure 4.19. A γ-ray sequence that was not assigned in present work.
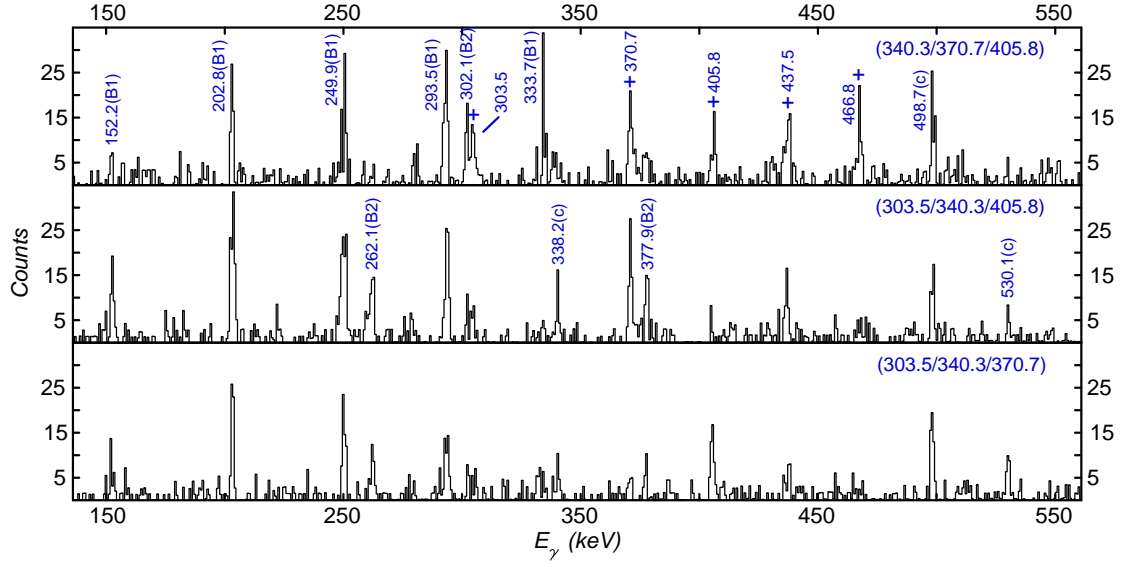
Figure 4.20. Triple gated spectra supporting the observation of the new band that was not assigned in present work. The gates used to generate these spectra are written in the corresponding panels. "B1", "B2", "+" and "(c)" symbols represent the transitions in band 1, in band 2, in this new band and the contaminated lines, respectively.

4.5 ^{242}Pu data

The level scheme of ^{242}Pu resulting from the present work is presented in Figure 4.21. The six bands, observed in our experiment, are labeled as bands 1 – 6 and will be discussed in detail one by one below. The states and transitions in the ^{242}Pu level scheme were labeled in a manner similar to that used in the ^{240}Pu case.

For computation of the relative intensities in the column "I_γ" of Tables 4.4– 4.9, the 102.8-keV $(4^+ \rightarrow 2^+)$ transition in band 1 was taken as the reference, and its intensity was normalized to "10000" for convenience. Based on the relative γ-ray intensities obtained, the population of bands 2 – 5 relative to band 1 in this experiment was estimated to be 7%, 2%, 1% and 1%, respectively. It was found that band 6 was populated even less than band 5. A definite number for its population is not available due to the lack of statistics, but the corresponding upper limit was estimated to be 0.5%. Representative angular distributions for in-band and inter-band transitions associated with each band (except band 6) in ^{242}Pu are compared in Figure 4.22, *i.e.*, the examples of the 158.5-keV $(6^+ \rightarrow 4^+)$ and 451.1-keV $(20^+ \rightarrow 18^+)$ lines in band 1, the 346.3-keV $(17^- \rightarrow 15^-)$ γ ray in band 2, the 531.8-keV $(19^- \rightarrow 18^+)$ transition linking bands 1 and 2, and the 367.6-keV $(17^- \rightarrow 15^-)$ line in band 3, the 907.8-keV $(15^- \rightarrow 14^+)$ transition linking bands 1 and 3, and the 312.8-keV $(16^+ \rightarrow 14^+)$ γ ray in band 4, the 1051.9-keV $(16^+ \rightarrow 14^+)$ transition linking bands 1 and 4, the 219.2-keV $(11^- \rightarrow 9^-)$ line in band 5, and the 800.1-keV $(11^- \rightarrow 10^+)$ transition linking bands 1 and 5. It was found in the analysis that the measured A_2 and A_4 coefficents for in-band and inter-band transitions in ^{242}Pu (see Tables 4.4–4.9) are very close to the typical values expected for quadrupole and dipole γ rays (see Table 2.3 in Sec. 2.5.4
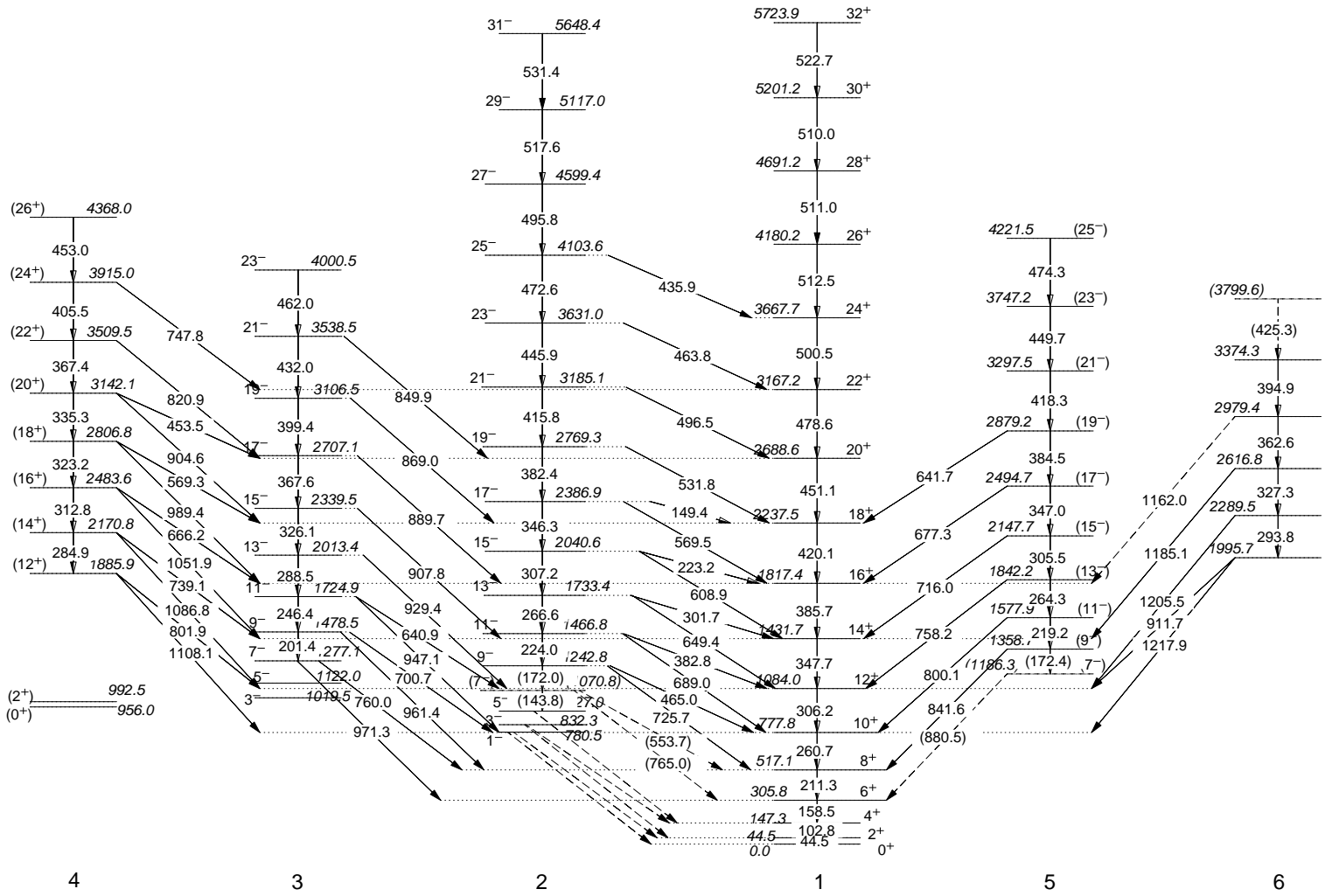
Figure 4.21. Partial level scheme of ^{242}Pu resulting from the present work. See text for details.

of Chapter 2), respectively. The only exception occurred in the case of γ rays linking bands 1 and 4. The measured A_2 and A_4 coefficients for them, such as the 1051.9-keV line (its angular distribution is illustrated in Figure 4.22), for example, suggest their quadrupole, rather than dipole, multipolarity. This exception will be discussed further in Sec. 4.5.4.

4.5.1 ^{242}Pu band 1

Band 1 in Figure 4.21 is the yrast band. The states with spin up to $26\hbar$ in this band have been identified in several previous measurements [43, 161, 162]. In the present work, three additional transitions above the previously known 26^+ level were observed, and these extend this band to spin $32\hbar$. All in-band transitions of band 1 below the 24^+ state, except the 44.5-keV $(2^+\rightarrow0^+)$ line, as well as some decay transitions from other bands in ^{242}Pu to band 1 can be seen in Figure 4.23. It is not surprising that the 44.5-keV transition was suppressed, due to its high internal electron conversion probability. In the process of analysing spectra double gated on high-spin transitions in the present work, it was found that the $26^+\rightarrow24^+$ line in band 1, which was considered as the available highest-spin one with 510.0-keV energy in the literature [161, 162], is actually a triplet, $i.e.$, three transitions having almost degenerate energy. Since energy values of the three lines located in the same band are very close, $i.e.$, 510.0-, 511.0- and 512.5-keV, they have not been separated before as the experiments were mostly carried out with thin targets and Doppler broadening contributed significantly. The three transitions in this high-spin triplet and an additional line (522.7-keV) above it as well as the transitions at lower spin in band 1 are confirmed here by three supporting coincidence spectra (Figure 4.24) generated with proper gating conditions. It can
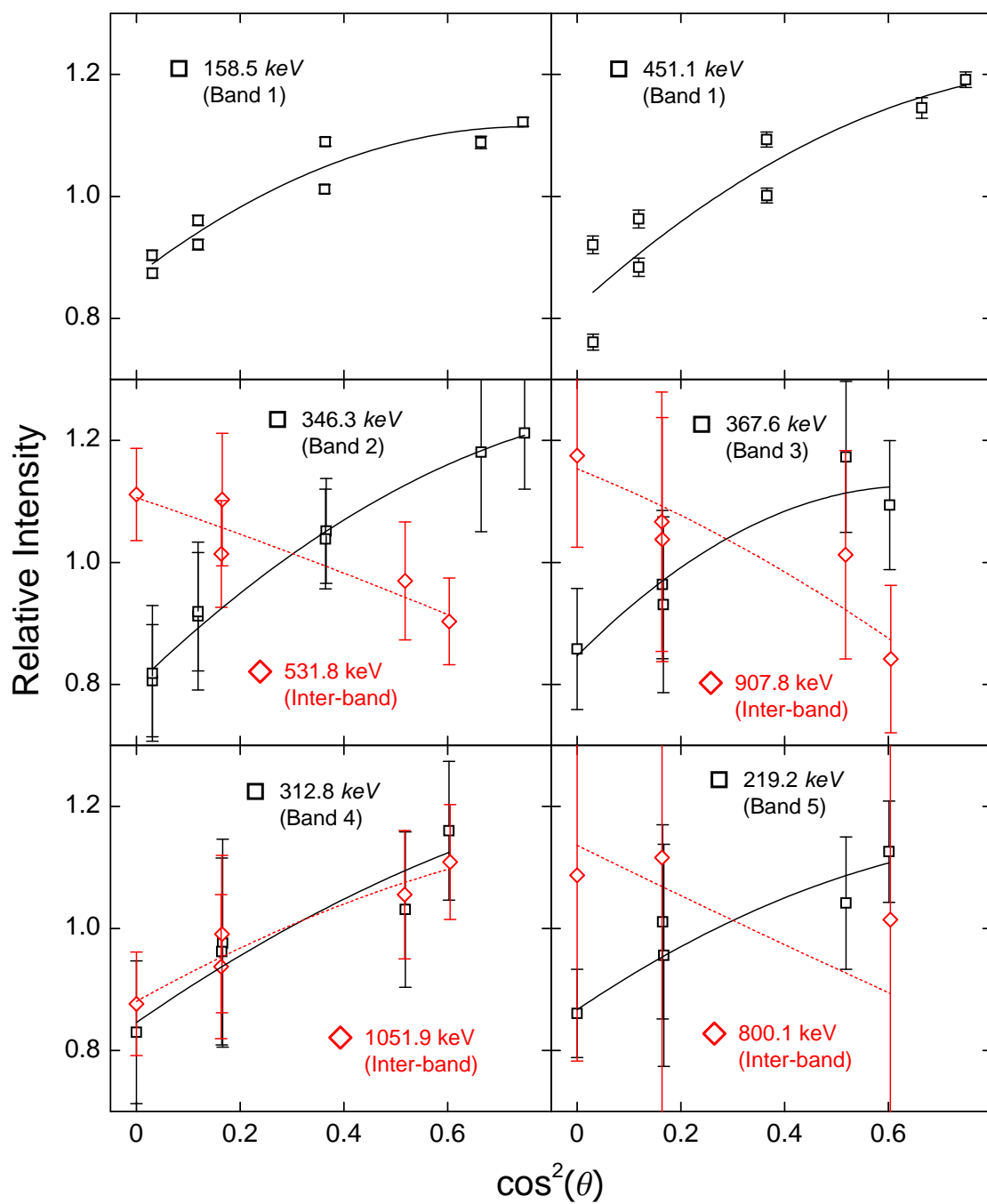
Figure 4.22. Samples of angular distribution for transitions in ^{242}Pu. The drawn curves (solid or dashed) represent the best fit of the data points. See text for details.

be seen that, for the peaks located at the energy value of this triplet ($\sim$ 511-keV), the width and the area are the largest in the bottom spectrum gated on the lowest-spin γ rays (both below triplet), and are the smallest in the top spectrum gated on the highest-spin lines (both in triplet). In the middle spectrum, generated with one gate set on a transition below the triplet (500.5-keV) and the other one placed on a line in the triplet (512.5-keV), both the width and area values for the peak of interest are intermediate. Furthermore, careful coincidence scans through the triplet provide additional evidence for the ordering proposed in the scheme (Figure 4.21). In addition, the higher-spin transition next to this triplet (522.7-keV) was observed most clearly in the top spectrum. As a result, it was concluded that there exists a triplet of γ rays with energy about 511 keV in this band. The relative intensity of each line in this triplet, obtained from fitting the peaks of interest in the spectra of Figure 4.24, is given in Table 4.4. The order in spin of the three transitions reflects the measured intensities.

The intensities of the three low-lying transitions, *i.e.*, the 102.8-keV ($4^+\rightarrow2^+$), the 158.5-keV ($6^+\rightarrow4^+$) and the 211.3-keV ($8^+\rightarrow6^+$) transitions, were obtained from the analysis of the total projection of the data. Using the method applied in the ^{240}Pu case, the relative intensity of the 260.7-keV ($10^+\rightarrow8^+$) transition was then obtained after getting the ratio of intensity between the 211.3-keV and 260.7-keV lines in the spectrum double gated on the 102.8-keV and 158.5-keV γ rays. Similarly, the intensities of the 306.2-keV transition and all others in the sequence were acquired from the appropriate spectra. The values of angular distribution coefficients (A_2 and A_4) for the in-band transitions of this band, obtained by analyzing the sum of angular spectra double gated on pairs of the 12 in-band lines (from 102.8-keV to 511.0-keV), can be found in Table 4.4. The spins and
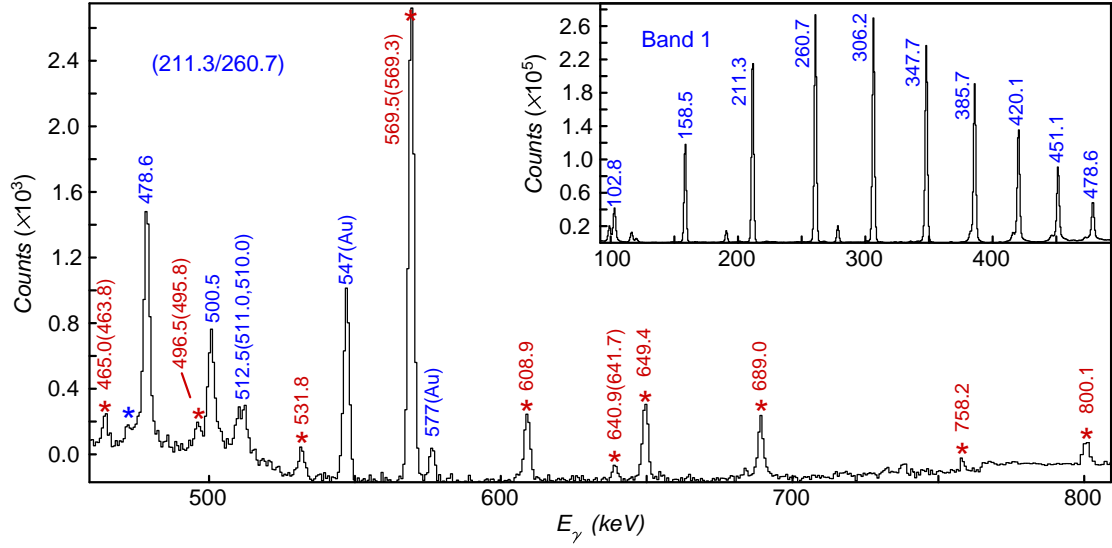
Figure 4.23. Spectra representative of band 1 in ^{242}Pu. The main panel
is the spectrum gated on the 211.3-keV and 260.7-keV lines in band 1.
Insert: the sum of spectra double gated on any two of the 11 in-band γ
rays (from 102.8-keV to 500.5-keV) of band 1. The related transitions
shown in the spectra are labeled in a manner similar to the one used in
Figure 4.16, except that the "(c)" symbols are replaced by the definite
energy values of contaminants in parentheses, and, "(Au)" symbols
denote the γ rays from Coulomb excitation of the Au backings.

parity of states up to 24^+ in this band, established in the work of Refs. [161, 162],
were confirmed in the present work. As the 512-511-510-keV sequence appears to
be the natural extension of the yrast band, $E2$ multipolarity is assigned to these
transitions as well although A_2 and A_4 coefficients could not be extracted in the
view of the spectral complexity discussed above.

TABLE 4.4

THE EXCITATION ENERGIES (E_x) OF INITIAL STATES,

ASSIGNED SPINS, γ-RAY ENERGIES (E_γ), RELATIVE γ-RAY

INTENSITIES (I_γ) AND ANGULAR DISTRIBUTION

COEFFICIENTS (A_2 AND A_4) FOR THE TRANSITIONS

ASSOCIATED WITH BAND 1 IN ^{242}Pu

Band 1 in ^{242}Pu					
E_x (keV)	Assigned spin ($\hbar$)	E_γ (keV)	I_γ (rel.)	A_2	A_4
147.3	$4^+\rightarrow2^+$	102.8(2)	10000(397)	0.30(3)	-0.12(5)
305.8	$6^+\rightarrow4^+$	158.5(2)	7474(441)	0.19(3)	-0.10(5)
517.1	$8^+\rightarrow6^+$	211.3(2)	10643(654)	0.21(4)	-0.05(5)
777.8	$10^+\rightarrow8^+$	260.7(2)	9064(830)	0.22(4)	-0.04(5)
1084.0	$12^+\rightarrow10^+$	306.2(2)	6716(815)	0.19(3)	-0.06(3)
1431.7	$14^+\rightarrow12^+$	347.7(2)	4730(487)	0.18(3)	-0.06(3)
1817.4	$16^+\rightarrow14^+$	385.7(2)	2899(319)	0.23(5)	-0.08(7)
2237.5	$18^+\rightarrow16^+$	420.1(2)	1631(172)	0.18(4)	-0.11(6)
2688.6	$20^+\rightarrow18^+$	451.1(2)	975(113)	0.30(7)	-0.09(10)
3167.2	$22^+\rightarrow20^+$	478.6(2)	488(80)	0.26(6)	-0.12(7)
3667.7	$24^+\rightarrow22^+$	500.5(2)	241(57)	0.32(10)	-0.12(14)
4180.2	$26^+\rightarrow24^+$	512.5(3)	76(19)		
4691.2	$28^+\rightarrow26^+$	511.0(5)	39(12)		
5201.2	$30^+\rightarrow28^+$	510.0(7)	12(4)		
5723.9	$32^+\rightarrow30^+$	522.7(4)	3.4(9)		
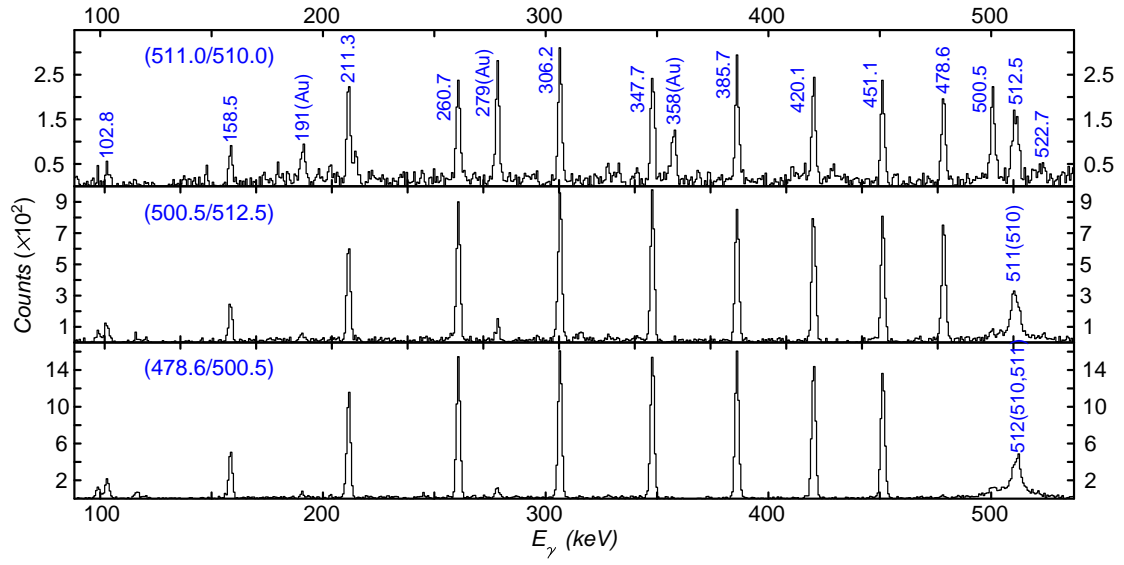
Figure 4.24. Spectra highlighting the high-spin triplet in band 1 of ^{242}Pu. The gates used to generate the three spectra (bottom, middle and top) are written in the corresponding panels. The related transitions shown in the spectra are labeled in the manner used in Figure 4.23. See text for details.

4.5.2 ^{242}Pu band 2

Band 2 in Figure 4.21, observed in previous measurements [43, 163], has been associated with a $K^\pi = 0^-$ octupole vibration. It consists of 15 transitions. All of the 12 transitions above the 7^- level can be seen in Figure 4.25. The inserted spectrum in this figure, generated with the gating conditions placed on the 445.9-keV γ ray and all other in-band lines above it, is presented here in order to highlight the high-spin $(19 - 31\hbar)$ part of this band. The 7^- level $(E_x = 1070.8 \ keV)$ was not identified in the literature [43, 163] because of insufficient statistics. In the present work, the 172.0-keV $(9^-\rightarrow7^-)$ transition, observed in Figure 4.25, is still too weak to determine its energy precisely, therefore, this transition as well as the associated 7^- state are indicated as tentative in the level scheme (Figure 4.21). The two bottom (below the 5^- level) γ rays were not observed here due to the high internal electron conversion probability, but the associated states, *i.e.*, 1^-, 3^- and 5^-, have been established in earlier work [163, 164]. Gamma rays associated with the deexcitation of this band to the yrast sequence (band 1) can be grouped into two types: $J^-\rightarrow(J-1)^+$ and $J^-\rightarrow(J+1)^+$, with the latter being much weaker in intensity (see Table 4.5). These inter-band transitions are also indicated in Figure 4.25. Additionally, as can be seen in the level scheme, the $(J+1)^+$ levels in band 1 are located, either, lower in energy $(J\leq21\hbar)$ than, or, very close $(\Delta E_x < 100 \ keV; J > 21\hbar)$ to the J^- states in band 2. Thus, no linking transitions between bands 1 and 2 in an opposite direction, like the $(J+1)^+\rightarrow J^-$ linking γ rays identified in the ^{240}Pu case, were observed in ^{242}Pu.

As was done in the analysis of ^{240}Pu data, the ratios of peak areas between the

TABLE 4.5

THE EXCITATION ENERGIES (E_x) OF INITIAL STATES,

ASSIGNED SPINS, γ-RAY ENERGIES (E_γ), RELATIVE γ-RAY

INTENSITIES (I_γ) AND ANGULAR DISTRIBUTION

COEFFICIENTS (A_2 AND A_4) FOR THE TRANSITIONS

ASSOCIATED WITH BAND 2 IN ^{242}Pu

Band 2 in ^{242}Pu					
E_x (keV)	Assigned spin ($\hbar$)	E_γ (keV)	I_γ (rel.)	A_2	A_4
1070.8	$7^-\rightarrow5^-$	143.8(10)	279(884)		
	$7^-\rightarrow6^+$	765.0(2)	279(41)		
	$7^-\rightarrow8^+$	553.7(2)	280(397)		
1242.8	$9^-\rightarrow7^-$	172.0(5)	23(19)		
	$9^-\rightarrow8^+$	725.7(2)	60(14)	-0.29(11)	0.11(9)
	$9^-\rightarrow10^+$	465.0(3)	46(25)		
1466.8	$11^-\rightarrow9^-$	224.0(3)	36(24)	0.26(9)	-0.10(16)
	$11^-\rightarrow10^+$	689.0(2)	92(17)	-0.24(8)	-0.08(10)
	$11^-\rightarrow12^+$	382.8(2)	24(19)		
1733.4	$13^-\rightarrow11^-$	266.6(2)	134(61)	0.34(20)	-0.07(25)
	$13^-\rightarrow12^+$	649.4(2)	121(21)	-0.22(10)	0.06(5)
	$13^-\rightarrow14^+$	301.7(2)	39(26)		
2040.6	$15^-\rightarrow13^-$	307.2(2)	357(114)	0.24(10)	-0.05(7)
	$15^-\rightarrow14^+$	608.9(2)	128(22)	-0.15(10)	0.03(5)
	$15^-\rightarrow16^+$	223.2(4)	30(17)		

TABLE 4.5 (contd.)

E_x (keV)	Assigned spin $(\hbar)$	E_γ (keV)	I_γ (rel.)	A_2	A_4
2386.9	$17^-\rightarrow15^-$	346.3(2)	638(322)	0.34(2)	-0.08(3)
	$17^-\rightarrow16^+$	569.5(2)	175(54)	-0.17(8)	0.02(4)
	$17^-\rightarrow18^+$	149.4(4)	9(10)		
2769.3	$19^-\rightarrow17^-$	382.4(3)	97(26)	0.19(8)	-0.08(10)
	$19^-\rightarrow18^+$	531.8(2)	53(9)	-0.22(11)	-0.01(14)
3185.1	$21^-\rightarrow19^-$	415.8(2)	124(43)	0.40(14)	-0.06(8)
	$21^-\rightarrow20^+$	496.5(2)	34(6)	-0.29(17)	0.02(21)
3631.0	$23^-\rightarrow21^-$	445.9(2)	105(52)	0.19(7)	-0.04(11)
	$23^-\rightarrow22^+$	463.8(3)	14(5)		
4103.6	$25^-\rightarrow23^-$	472.6(3)	77(45)	0.20(10)	-0.12(16)
	$25^-\rightarrow24^+$	435.9(3)	4(2)		
4599.4	$27^-\rightarrow25^-$	495.8(4)			
5117.0	$29^-\rightarrow27^-$	517.6(4)			
5648.4	$31^-\rightarrow29^-$	531.4(4)			
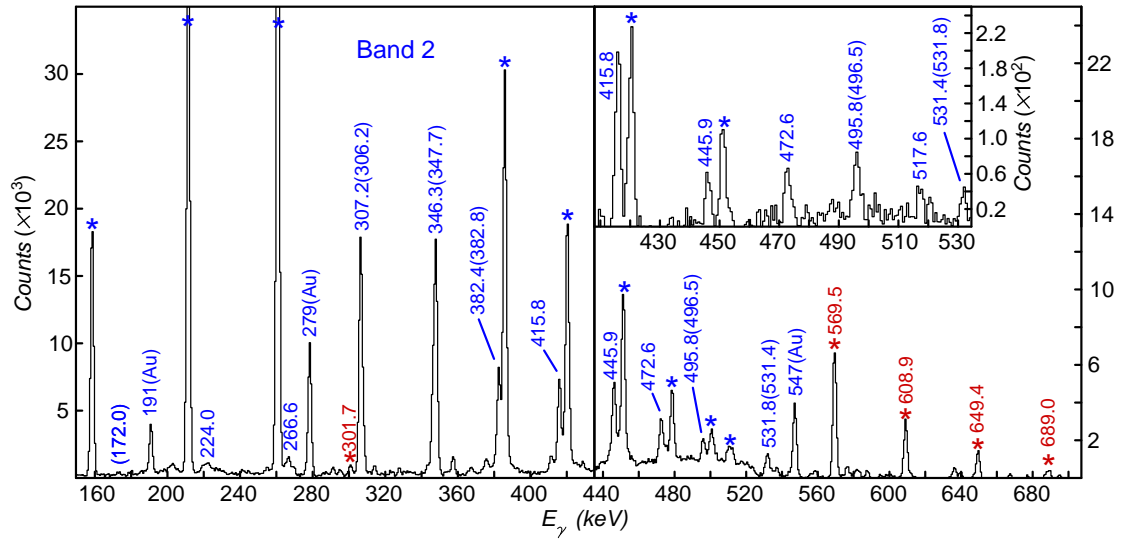
Figure 4.25. Spectra representative of band 2 in ^{242}Pu. Main panel: the sum of spectra double gated on any two of the 10 in-band γ rays (from 224.0-keV to 517.6-keV) of band 2. Insert: the sum of spectra gated on any two of the 445.9-keV, 472.6-keV and 495.8-keV lines in band 2. The related transitions are labeled in the manner used in Figure 4.23.

transitions with known intensities and those to be derived were extracted from the appropriate coincidence spectra. Thus, the relative intensities for the transitions associated with band 2 were obtained by, first, establishing the inter-band γ rays, and subsequently, the in-band transitions (see the related discussion in Sec. 4.4.2). For example, the relative intensity of the 569.5-keV ($17^-\rightarrow16^+$) inter-band line was acquired by analyzing the summed spectra double gated on the transitions below the 16^+ state in band 1. Then, the relative intensity of the 346.3-keV ($17^-\rightarrow15^-$) γ ray in band 2 was obtained by the analysis of the summed spectra double gated on the transitions above the 17^- state in band 2.

The spins and parity of states in this band, proposed originally in Ref. [43], were adopted in the present work (Figure 4.21). The assignment of the states up to the 25^- level was confirmed by the measured angular distribution coefficients for the transitions linking band 1 to band 2 (indicative of dipole multipolarity) and the ones in band 2 (indicative of quadrupole multipolarity), see Table 4.5, while the assignment of spins and parity of the 27^- level and the states above it is supported by the fact that all in-band transitions are associated with an $E2$ multipolarity (referring to what has been done for the high-spin states in band 1). It is worth to note that the gating conditions used to generate appropriate spectra (double-gated), in order to study the angular distributions of the weak inter-band transitions, were placed on one transition in both bands.

4.5.3 ^{242}Pu band 3

Due to their weak population and the presence of rather complex contaminations, the experimental evidence for bands 3 – 6 in ^{242}Pu cannot be provided through a single sample spectrum. Hence, for the supporting coincidence spectra

shown below (Figures 4.26 – 4.29), a figure generally consists of several panels. In each panel, one portion of an appropriate spectrum is illustrated with the purpose of highlighting a part of the related transitions only. The combination of all panels in a figure is then used to present all of the transitions observed in the band.

Band 3 in Figure 4.21 consists of ten transitions. The 7^- level and the states above it have been established for the first time in the present work. The seven in-band lines above the 7^- level as well as some inter-band transitions between bands 1 and 3 are indicated in Figure 4.26. The two lowest-spin γ rays ($5^- \to 3^-$ and $7^- \to 5^-$) were suppressed because of high internal electron conversion probabilities. However, the associated 3^- and 5^- states were established in previous work, more than two decades ago [163]. This band decays to band 1 (yrast band) only. In other words, no linking transition between this band and any sequence other than band 1, such as band 2, for example, was found. This is based on the observation that the upper limit for the relative intensity of any virtual inter-band transition connecting this band with any other, except band 1, was determined to be 5 (the relative intensity of the 102.8-keV line in band 1 is taken as 10000). The γ rays associated with the deexcitation of band 3 to 1 can also be grouped into two types: $J^- \to (J-1)^+$ and $J^- \to (J+1)^+$. Transitions with the same initial state in these two types have comparable intensities, as seen in Table 4.6.

The intensities and angular distributions for transitions associated with band 3 were studied in the method also used in the case of band 2. The results of the analysis are summarized in Table 4.6. The in-band and inter-band transitions (between bands 1 and 3) are indicative of quadrupole and dipole multipolarity, respectively, based on the measured A_2 and A_4 coefficients. As a result, negative parity and odd spins were assigned to the states of this band (the spins and parity

for states above 17^- were assigned based on the fact that these transitions appear to represent a natural extension of the lower-spin sequence in this band and all in-band transitions possess $E2$ multipolarity. This is similar to the reasoning use several times above). Further, the routhian plot of this band, indicated in Figure 4.50 (in Sec. 4.7.5), was obtained later using the method described in Sec. 1.3.4 of Chapter 1. This plot also suggests that the sequence of γ rays observed in the present work (above the 7^- level) extrapolates well at lower angular frequency to the known 5^-, 3^- levels ($E_x = 1019.5\ keV$ for the 3^- state). The consistency of data points from the present work (at higher spin) with the ones from the previous work [163] (at lower spin) supports, from another point of view, the above assignment of spin and parity.

4.5.4 ^{242}Pu band 4

Band 4 in Figure 4.21 is the second positive-parity band in ^{242}Pu. The 12^+ level and the states above it have been established here for the first time. The seven in-band lines above the 12^+ level as well as some inter-band transitions between bands 1 and 4 are indicated in Figure 4.27. The γ rays below the 12^+ state were not observed in the present work due to the lack of statistics and/or the high internal electron conversion probability, but the two bottom levels (0^+ and 2^+) have been reported in the literature [165, 166]. It was found that this band is connected with band 1 only. The linking transitions between the two bands can be grouped into two types: $J^+ \rightarrow (J-2)^+$ and $J^+ \rightarrow (J)^+$, with the latter being weaker in intensity (see Table 4.7). The maximum value of the relative intensity for virtual inter-band transitions connecting this band with any other, except band

TABLE 4.6

THE EXCITATION ENERGIES (E_x) OF INITIAL STATES,
ASSIGNED SPINS, γ-RAY ENERGIES (E_γ), RELATIVE γ-RAY
INTENSITIES (I_γ) AND ANGULAR DISTRIBUTION
COEFFICIENTS (A_2 AND A_4) FOR THE TRANSITIONS
ASSOCIATED WITH BAND 3 IN ^{242}Pu

		Band 3 in ^{242}Pu			
E_x (keV)	Assigned spin ($\hbar$)	E_γ (keV)	I_γ (rel.)	A_2	A_4
1277.1	$7^- \to 6^+$	971.3(5)	53(18)	-0.27(16)	0.06(19)
	$7^- \to 8^+$	760.0(5)	114(156)		
1478.5	$9^- \to 7^-$	201.4(3)	24(9)	0.19(11)	-0.07(14)
	$9^- \to 8^+$	961.4(4)	35(10)	-0.21(9)	0.02(5)
	$9^- \to 10^+$	700.7(4)	80(73)		
1724.9	$11^- \to 9^-$	246.4(2)	10(4)	0.27(17)	-0.13(11)
	$11^- \to 10^+$	947.1(2)	24(6)	-0.23(31)	0.04(39)
	$11^- \to 12^+$	640.9(3)	49(34)	-0.35(23)	0.10(13)
2013.4	$13^- \to 11^-$	288.5(2)	11(10)	0.22(14)	-0.10(18)
	$13^- \to 12^+$	929.4(2)	34(6)	-0.4(2)	-0.04(27)
2339.5	$15^- \to 13^-$	326.1(2)	15(9)	0.3(3)	-0.04(39)
	$15^- \to 14^+$	907.8(3)	21(5)	-0.3(2)	-0.05(26)
2707.1	$17^- \to 15^-$	367.6(2)	30(13)	0.20(12)	-0.15(17)
	$17^- \to 16^+$	889.7(4)	11(3)		

TABLE 4.6 (contd.)

E_x (keV)	Assigned spin ($\hbar$)	E_γ (keV)	I_γ (rel.)	A_2	A_4
3106.5	$19^-\rightarrow17^-$	399.4(3)			
	$19^-\rightarrow18^+$	869.0(4)	10(3)		
3538.5	$21^-\rightarrow19^-$	432.0(3)			
	$21^-\rightarrow20^+$	849.9(4)			
4000.5	$23^-\rightarrow21^-$	462.0(4)			
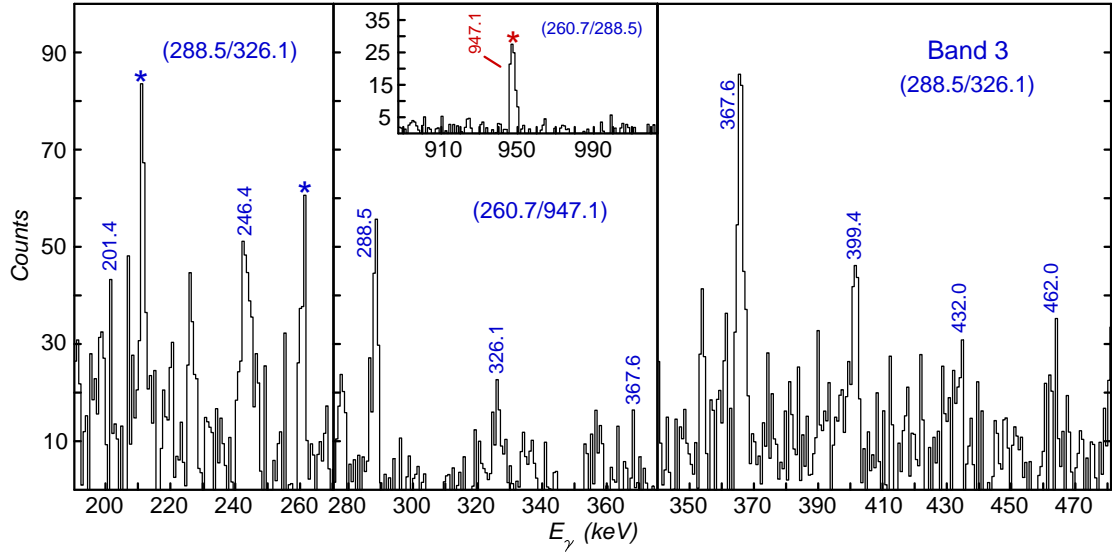
Figure 4.26. Spectra representative of band 3 in ^{242}Pu. The gates used to generate these spectra are written in the corresponding panels, respectively. The related transitions shown in the spectra are labeled in the manner used in Figure 4.23.

1, was estimated to be 3 (the relative intensity of the 102.8-keV line in band 1 was defined as 10000).

The results of data analysis for this band are summarized in Table 4.7. The measured A_2 and A_4 coefficients for the in-band transitions of band 4 are indicative of their quadrupole nature. It is worth noting that the measured A_2 and A_4 values for some of the transitions connecting band 1 with 4, for example, the 1051.9-keV (proposed $16^+ \rightarrow 14^+$) line, indicate their quadrupole rather than dipole character. In other words, the angular distributions for these inter-band γ rays linking bands 1 and 4 ($J^+ \rightarrow (J-2)^+$) are distinctly different from the ones of transitions connecting band 1 with bands 2 or 3. Rather, they are close to those for in-band γ rays, as illustrated in Figure 4.22. As a result, positive parity and even spins, $i.e.$, 12^+, 14^+,..., 26^+, were assigned to the states of band 4 (the spin and parity for the 22^+ level and the states above it were assigned based on the fact that these transitions represent a natural extension of the lower-spin sequence in this band and all in-band transitions possess $E2$ multipolarity.). This assignment is further supported by the fact that all of the measured A_2 and A_4 coefficients for transitions associated with band 4 (Table 4.7) can be explained well with the spins and parity assigned above. As will be shown later, the routhian plot of this band (Figure 4.44 in Sec. 4.7.3) also suggests that the sequence of γ rays observed here extrapolates at lower angular frequency to the known 2^+, 0^+ levels ($K = 0$; $E_x = 956.0 \ keV$ for the 0^+ state) [165, 166]. Nevertheless, the 4^+, 6^+, 8^+ and 10^+ levels have not been established yet; $i.e.$, the sequence of γ rays in this band cannot be rigorously followed to low spin. Therefore, all of the spins and parity assigned above to the states of this band are given as tentative in the level scheme (Figure 4.21).

TABLE 4.7

THE EXCITATION ENERGIES (E_x) OF INITIAL STATES,
ASSIGNED SPINS, γ-RAY ENERGIES (E_γ), RELATIVE γ-RAY
INTENSITIES (I_γ) AND ANGULAR DISTRIBUTION
COEFFICIENTS (A_2 AND A_4) FOR THE TRANSITIONS
ASSOCIATED WITH BAND 4 IN ^{242}Pu

Band 4 in ^{242}Pu					
E_x (keV)	Assigned spin ($\hbar$)	E_γ (keV)	I_γ (rel.)	A_2	A_4
1885.9	$12^+\rightarrow10^+$	1108.1(4)	8(3)		
	$12^+\rightarrow12^+$	801.9(2)	12(4)		
2170.8	$14^+\rightarrow12^+$	284.9(3)	15(8)	0.23(9)	-0.09(7)
	$14^+\rightarrow12^+$	1086.8(2)	12(4)	0.15(10)	-0.06(11)
	$14^+\rightarrow14^+$	739.1(2)	10(3)	-0.23(11)	-0.08(12)
2483.6	$16^+\rightarrow14^+$	312.8(3)	16(7)	0.27(15)	-0.05(20)
	$16^+\rightarrow14^+$	1051.9(2)	19(4)	0.21(7)	-0.04(9)
	$16^+\rightarrow16^+$	666.2(4)	9(3)		
2806.8	$18^+\rightarrow16^+$	323.2(2)	20(7)	0.13(17)	-0.15(22)
	$18^+\rightarrow16^+$	989.4(2)	24(5)		
	$18^+\rightarrow18^+$	569.3(3)			
3142.1	$20^+\rightarrow18^+$	335.3(2)	6(3)	0.27(16)	-0.15(21)
	$20^+\rightarrow18^+$	904.6(2)	13(3)		
	$20^+\rightarrow20^+$	453.5(3)			

TABLE 4.7 (contd.)

E_x (keV)	Assigned spin ($\hbar$)	E_γ (keV)	I_γ (rel.)	A_2	A_4
3509.5	$22^+ \rightarrow 20^+$	367.4(2)			
	$22^+ \rightarrow 20^+$	820.9(3)			
3915.0	$24^+ \rightarrow 22^+$	405.5(3)			
	$24^+ \rightarrow 22^+$	747.8(3)			
4368.0	$26^+ \rightarrow 24^+$	453.0(3)			

4.5.5 ^{242}Pu bands 5 and 6

The γ-ray sequences of bands 5 and 6, shown in Figure 4.21, are both new structures observed here for the first time. The eight transitions in band 5 and the five γ rays in band 6, as well as some associated inter-band transitions, are indicated in Figures 4.28 and 4.29. In the spectra, the 172.4-keV ($9^- \rightarrow 7^-$) in-band and the 880.5-keV ($7^- \rightarrow 6^+$) inter-band transitions, associated with band 5, and the 425.3-keV in-band and the 1162.0-keV inter-band transitions, associated with band 6, were not identified firmly because of insufficient statistics. Thus, these lines as well as the associated states were assigned as tentative in the level scheme (Figure 4.21). None of the low-spin (below the 7^- level for band 5 and below the 1995.7-keV level for band 6) γ rays was observed because of the lack of statistics and/or the high internal conversion probability. As was the case for bands 2 – 4, bands 5 and 6 are linked to band 1 only. The upper limit for the relative intensity of virtual inter-band transitions, connecting bands 5 or 6 with any sequence other than band 1, was estimated to be 3 (the relative intensity of the 102.8-keV line in band 1 is again taken as 10000).

Because of the poor statistics for band 5 in the data, the measured relative
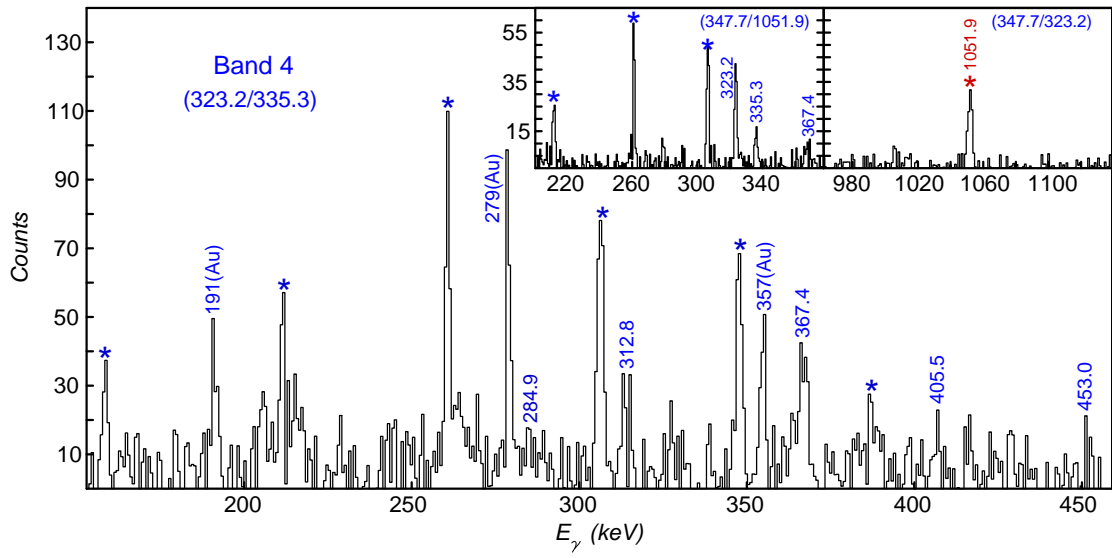
Figure 4.27. Spectra representative of band 4 in ^{242}Pu. The gates used to generate these spectra are written in the corresponding panels. The transitions are labeled in the manner used in Figure 4.23.

intensities are small quantities with relatively large errors, and the angular distribution coefficients (the errors are also relatively large) could be extracted for only a small portion of the related transitions (4 of 16). The intensities and the angular distribution coefficients for transitions associated with band 6 were not determined due to even poorer statistics. Despite the large uncertainties, the measured A_2 and A_4 coefficients for the in-band and inter-band transitions in band 5 (Table 4.8) indicate either quadrupole or dipole character depending on the case. Therefore, the levels in band 5 were assigned negative parity and odd spins (7^-, 9^-, ..., 25^-). Again, the spins and parity for the 15^- level and the states above it were assigned based on the continuation of the band through $E2$ transitions. Neither for band 5 or band 6, could the sequence be followed to low spin. In addition, none of the bandheads identified so far in the literature [167] could be considered as a reasonable extrapolation at lower angular frequency of the sequence of γ rays observed in the the present work. Therefore, all spin and parity values assigned above to the states of bands 5 are given as tentative in the level scheme and no quantum numbers are assigned to the levels of band 6.

4.6 ^{238}Pu data

The level scheme of ^{238}Pu resulting from this work is given in Figure 4.30. As pointed out above, the ^{238}Pu data was acquired from the weak, single-neutron transfer channel in the reaction of a ^{207}Pb beam with a ^{239}Pu target. The ratio of the number of events associated with ^{238}Pu to those of ^{239}Pu was roughly 1/8. As a result, it should come as no surprise that only two bands were observed in ^{238}Pu. These are labeled as bands 1 and 2 in Figure 4.30.

TABLE 4.8

THE EXCITATION ENERGIES (E_x) OF INITIAL STATES,

ASSIGNED SPINS, γ-RAY ENERGIES (E_γ), RELATIVE γ-RAY

INTENSITIES (I_γ) AND ANGULAR DISTRIBUTION

COEFFICIENTS (A_2 AND A_4) FOR THE TRANSITIONS

ASSOCIATED WITH BAND 5 IN ^{242}Pu

Band 5 in ^{242}Pu					
E_x (keV)	Assigned spin ($\hbar$)	E_γ (keV)	I_γ (rel.)	A_2	A_4
1186.3	$7^-\rightarrow6^+$	880.5(5)			
1358.7	$9^-\rightarrow7^-$	172.4(4)	24(16)		
	$9^-\rightarrow8^+$	841.6(5)	26(12)	-0.15(19)	0.06(24)
1577.9	$11^-\rightarrow9^-$	219.2(3)	43(16)	0.22(13)	-0.07(16)
	$11^-\rightarrow10^+$	800.1(2)	36(7)	-0.3(7)	0.01(90)
1842.2	$13^-\rightarrow11^-$	264.3(3)	26(16)	0.27(11)	-0.11(12)
	$13^-\rightarrow12^+$	758.2(3)	17(4)		
2147.7	$15^-\rightarrow13^-$	305.5(3)	25(56)		
	$15^-\rightarrow14^+$	716.0(4)	14(4)		
2494.7	$17^-\rightarrow15^-$	347.0(3)	23(57)		
	$17^-\rightarrow16^+$	677.3(5)	7(3)		
2879.2	$19^-\rightarrow17^-$	384.5(3)	33(57)		
	$19^-\rightarrow18^+$	641.7(5)			
3297.5	$21^-\rightarrow19^-$	418.3(3)	27(56)		
3747.2	$23^-\rightarrow21^-$	449.7(4)			
4221.5	$25^-\rightarrow23^-$	474.3(4)			

TABLE 4.9

THE EXCITATION ENERGIES (E_x) OF INITIAL STATES,
ASSIGNED SPINS, γ-RAY ENERGIES (E_γ) FOR THE
TRANSITIONS ASSOCIATED WITH BAND 6 IN ^{242}Pu

Band 6 in ^{242}Pu		
E_x (keV)	Assigned spin $(\hbar)$	E_γ (keV)
1995.7	$11^-\rightarrow10^+$	1217.9(3)
	$11^-\rightarrow12^+$	911.7(3)
2289.5	$13^-\rightarrow11^-$	293.8(3)
	$13^-\rightarrow12^+$	1205.5(3)
2616.8	$15^-\rightarrow13^-$	327.3(3)
	$15^-\rightarrow14^+$	1185.1(4)
2979.4	$17^-\rightarrow15^-$	362.6(3)
	$17^-\rightarrow16^+$	1162.0(4)
3374.3	$19^-\rightarrow17^-$	394.9(4)
3799.6	$21^-\rightarrow19^-$	425.3(4)

Figure 4.28. Spectra representative of band 5 in ^{242}Pu. The gates used to generate these spectra are written in the corresponding panels. The transitions are labeled in the manner used in Figure 4.23.
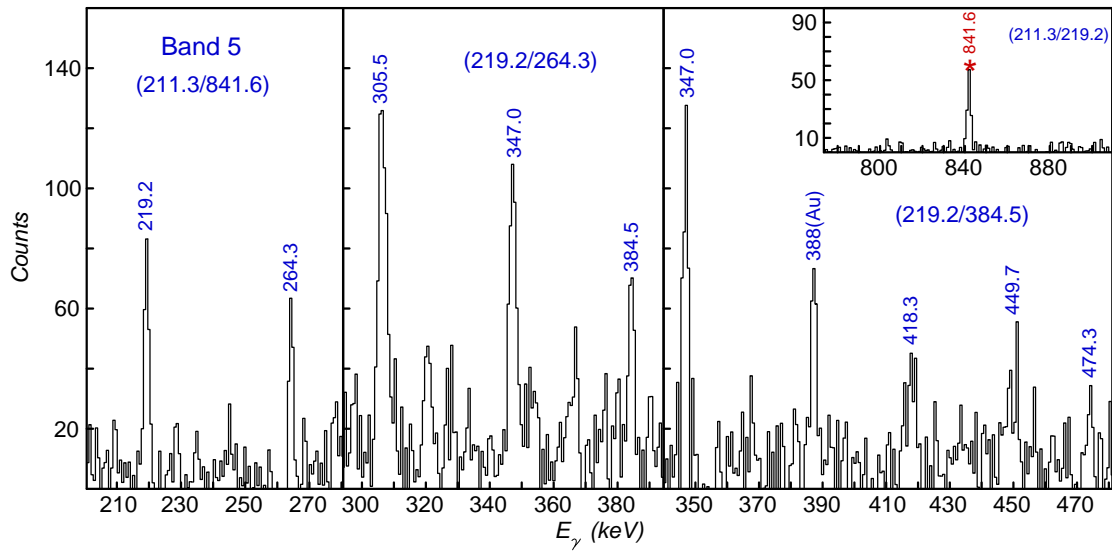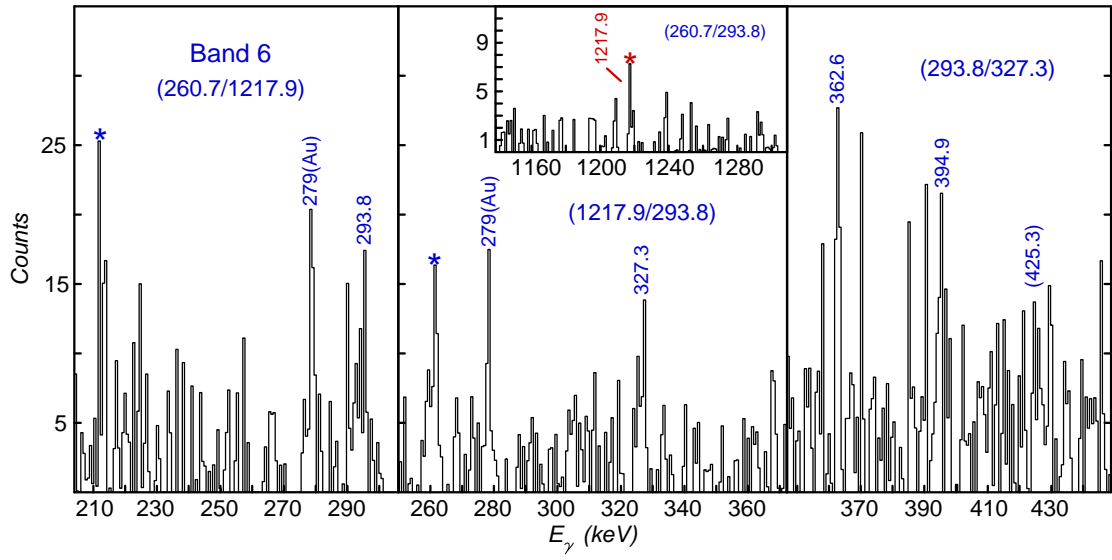
Figure 4.29. Spectra representative of band 6 in ^{242}Pu. The gates used to generate these spectra are written in the corresponding panels. The transitions are labeled in the manner used in Figure 4.23.
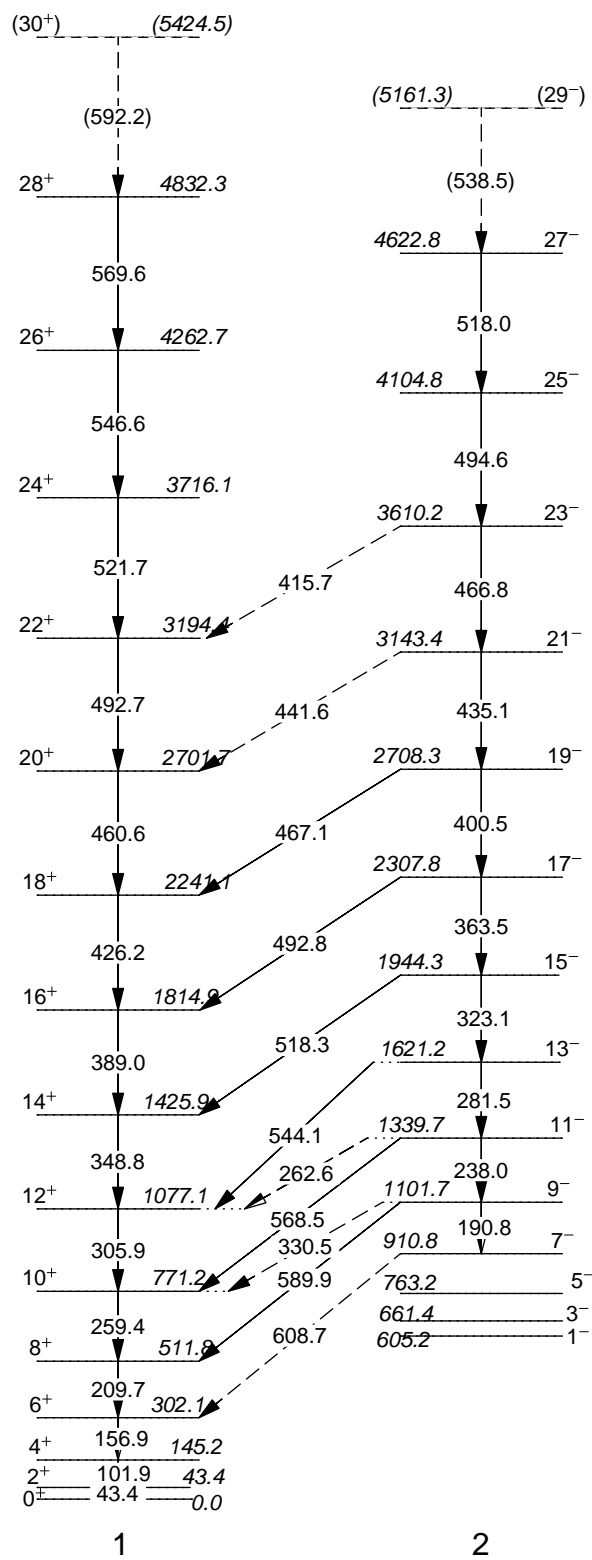
Figure 4.30. Partial level scheme of ^{238}Pu. See text for details.

As described in Sec. 4.3, triple coincidence gates, including one placed on one of the strongest transitions in ^{208}Pb, the reaction partner of ^{238}Pu, were always used to enhance the channel of interest. For calculating the relative intensities in the column "I_γ" of Tables 4.10 and 4.11, the 101.9-keV ($4^+\rightarrow 2^+$) transition in band 1 was taken as the reference, and its intensity was normalized to "1000" for convenience. Based on the measured relative γ-ray intensities, the population of band 2 relative to band 1 was determined to be $\sim$10%, while the upper limit for the population of any other possible bands, except bands 1 or 2, was estimated to be 2%. Representative angular distributions for in-band and inter-band transitions associated with each band in ^{238}Pu are compared in Figure 4.31. The examples include the 209.7-keV ($8^+\rightarrow 6^+$) line in band 1, the 400.5-keV ($19^-\rightarrow 17^-$) γ ray in band 2 and the 544.1-keV ($13^-\rightarrow 12^+$) and 568.5-keV ($11^-\rightarrow 10^+$) transitions linking bands 1 and 2. It was found in the analysis that the measured A_2 and A_4 coefficients for in-band and inter-band transitions in ^{238}Pu are very close to the typical values expected for quadrupole and dipole γ rays.

4.6.1 ^{238}Pu band 1

Band 1 in Figure 4.30 is the yrast band. It has been delineated up to a spin of $26\hbar$ in Refs. [168, 169]. Here, this band was extended by two additional transitions. The sum of spectra, given in Figure 4.32, was generared with the gating conditions placed on two of the in-band transitions and one of the strongest lines in ^{208}Pb (either 583 or 2611 keV). This band consists of fifteen transitions. All in-band transitions of band 1 are seen in Figure 4.32 except the 43.4-keV ($2^+\rightarrow 0^+$) line, which is suppressed due to the low detection efficiency at low energy and the high internal conversion probability. Some of the transitions in band 2 can be seen
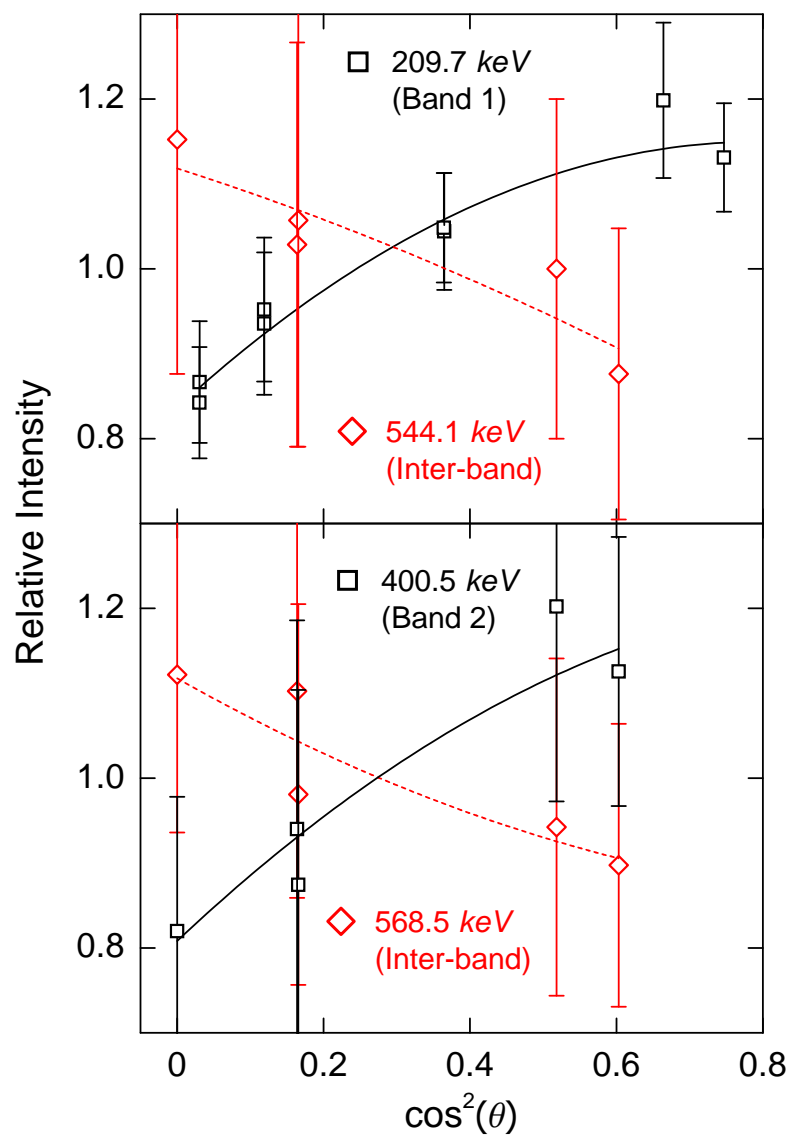
Figure 4.31. Samples of angular distributions for transitions in [238]Pu. The curves (solid or dashed) represent the best fit of the data points. See text for details.

in this figure as well because of the connections between the two sequences (see Figures 4.32 and 4.30). They will be discussed below.

The intensities of the three low-lying transitions, *i.e.*, the 101.9-keV ($4^+\rightarrow2^+$), the 156.9-keV ($6^+\rightarrow4^+$) and the 209.7-keV ($8^+\rightarrow6^+$) γ rays, were extracted from the total projection (single gated on one of the two lines in ^{208}Pb). Using the method applied in ^{240}Pu and ^{242}Pu, the relative intensity of the 259.4-keV ($10^+\rightarrow8^+$) transition was then obtained from the comparison of the peak area of the 209.7-keV line with that of the 259.4-keV γ ray in the spectrum triple gated on the 101.9-keV and 156.9-keV transitions together with one of the two ^{208}Pb lines. The intensities of the 305.9-keV γ ray and all other lines located above it were obtained from appropriate spectra in the same manner. The A_2 and A_4 coefficients for the in-band transitions, given in Table 4.10, were acquired at several angles from the sum of spectra generated with all available triple gates.

The spins and parity of the states up to 24^+, established in previous measurements [168, 169], were confirmed by the measured A_2 and A_4 coefficients of those associated γ rays here. As the transitions above the 24^+ state form a natural extension of the lower-spin sequence in this band, the spins and parity for states above 24^+ were assigned accordingly, even though the information of A_2 and A_4 coefficients for these high-spin lines is not available in the present work.

4.6.2 ^{238}Pu band 2

Band 2 in Figure 4.30 has been associated with the $K^\pi = 0^-$ octupole vibration in Refs. [170, 171, 172, 173], but the 7^- level and the states above it had not been established before. This band consists of fourteen transitions. All of the eleven transitions above the 7^- level can be seen in Figure 4.33. In this summed

TABLE 4.10

THE EXCITATION ENERGIES (E_x) OF INITIAL STATES,

ASSIGNED SPINS, γ-RAY ENERGIES (E_γ), RELATIVE γ-RAY

INTENSITIES (I_γ) AND ANGULAR DISTRIBUTION

COEFFICIENTS (A_2 AND A_4) FOR THE TRANSITIONS

ASSOCIATED WITH BAND 1 IN ^{238}Pu

Band 1 in ^{238}Pu					
E_x (keV)	Assigned spin ($\hbar$)	E_γ (keV)	I_γ (rel.)	A_2	A_4
145.2	$4^+\rightarrow2^+$	101.9(5)	1000(133)		
302.1	$6^+\rightarrow4^+$	156.9(5)	1252(247)	0.25(13)	-0.2(2)
511.8	$8^+\rightarrow6^+$	209.7(5)	1549(338)	0.24(3)	-0.11(4)
771.2	$10^+\rightarrow8^+$	259.4(5)	1636(364)	0.24(6)	-0.17(10)
1077.1	$12^+\rightarrow10^+$	305.9(5)	1346(347)	0.16(3)	-0.13(4)
1425.9	$14^+\rightarrow12^+$	348.8(5)	1117(302)	0.24(5)	-0.14(7)
1814.9	$16^+\rightarrow14^+$	389.0(5)	888(252)	0.18(11)	-0.08(17)
2241.1	$18^+\rightarrow16^+$	426.2(5)	569(166)	0.33(5)	-0.15(8)
2701.7	$20^+\rightarrow18^+$	460.6(5)	469(142)	0.24(4)	-0.04(6)
3194.4	$22^+\rightarrow20^+$	492.7(5)	260(96)	0.22(4)	-0.07(6)
3716.1	$24^+\rightarrow22^+$	521.7(5)	202(81)	0.20(9)	-0.15(11)
4262.7	$26^+\rightarrow24^+$	546.6(5)	141(61)		
4832.3	$28^+\rightarrow26^+$	569.6(6)	79(38)		
5424.5	$30^+\rightarrow28^+$	592.2(6)	20(14)		
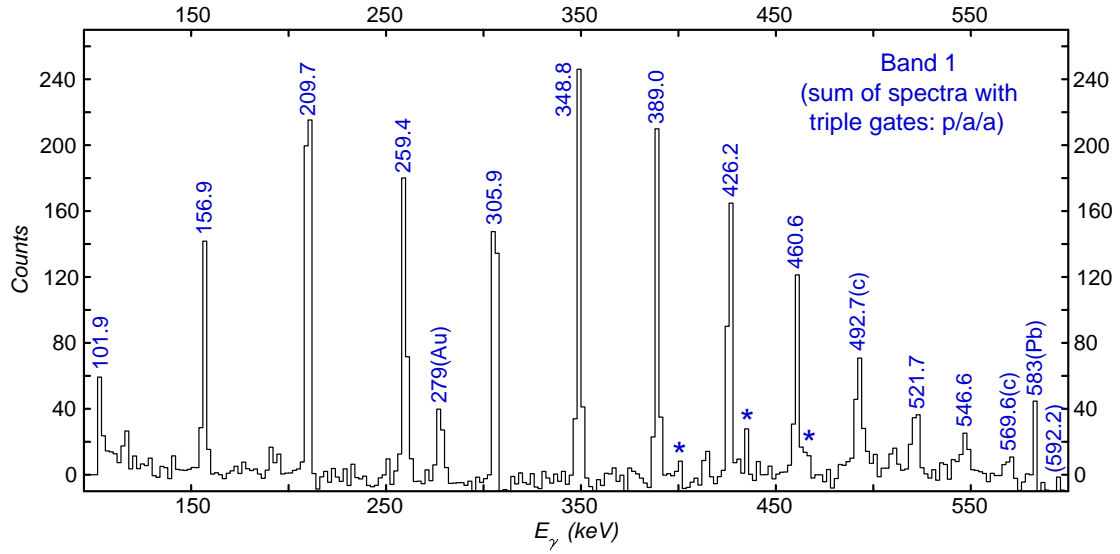
Figure 4.32. Spectrum representative of band 1 in ^{238}Pu. The triple coincidence gates are set on two of the 10 in-band transitions (from 209.7-keV to 546.6-keV) of band 1 in ^{238}Pu, $i.e.$, "a", and one of the strongest lines (583-keV or 2611-keV) in ^{208}Pb, $i.e.$, "p". The transitions are labeled in a manner similar to that used in Figure 4.16, except that "(Au)" and "(Pb)"symbols denote the lines of Au and Pb, respectively.

triple-gated spectrum, the 538.5-keV ($29^- \rightarrow 27^-$) transition is hard to confirm due to the lack of statistics combined with a sizeable Doppler shift and/or broadening. As a result, it was assigned on a tentative basis in the level scheme. The three transitions below the 7^- level were not observed because of the high internal conversion probability, but the associated 1^-, 3^- and 5^- states have been established in several previous measurements [170, 171, 172, 173]. The 7^- level ($E_x = 910.8 \ keV$), of which the energy was unknwon in the literature, has been identified for the first time in the present work, taking advantage of the observation of the 190.8-keV ($9^- \rightarrow 7^-$) transition in this band (see Figures 4.33 and 4.30). The γ rays linking this sequence to the yrast band (band 1) are indicated in Figure 4.33, and, they can also be grouped into two types: $J^- \rightarrow (J-1)^+$ and $J^- \rightarrow (J+1)^+$. The transitions of the latter type, *i.e.*, the 262.6- and 330.5-keV lines, are hard to verify in the spectra resulting from the above analysis, because of their low intensities, therefore, they are taken as tentative in the level scheme. This is also the case for some weak $J^- \rightarrow (J-1)^+$ inter-band transition, such as the 415.7-keV line, for example. It is also worth noting that no linking transitions between bands 1 and 2 in an opposite direction, like the $(J+1)^+ \rightarrow J^-$ lines seen in ^{240}Pu, were observed in ^{238}Pu, though the pattern of the difference in energy between the states of bands 1 and 2 at high spin in ^{238}Pu is quite similar to that in ^{240}Pu. The maximum value of the relative intensity for virtual $(J+1)^+ \rightarrow J^-$ transitions between bands 1 and 2 was estimated to be 5 (the relative intensity of the 101.9-keV line in band 1 is taken as 1000).

As in the ^{240}Pu and ^{242}Pu cases, the relative intensities of the inter-band transitions were extracted first, and, those of the in-band lines were obtained

231

TABLE 4.11

THE EXCITATION ENERGIES (E_x) OF INITIAL STATES,
ASSIGNED SPINS, γ-RAY ENERGIES (E_γ), RELATIVE γ-RAY
INTENSITIES (I_γ) AND ANGULAR DISTRIBUTION
COEFFICIENTS (A_2 AND A_4) FOR THE TRANSITIONS
ASSOCIATED WITH BAND 2 IN ^{238}Pu

	Band 2 in ^{238}Pu				
E_x (keV)	Assigned spin ($\hbar$)	E_γ (keV)	I_γ (rel.)	A_2	A_4
910.8	$7^- \rightarrow 6^+$	608.7(5)	99(25)		
1101.7	$9^- \rightarrow 7^-$	190.8(6)	84(26)		
	$9^- \rightarrow 8^+$	589.9(5)	140(33)	-0.4(2)	0.1(2)
	$9^- \rightarrow 10^+$	330.5(6)	49(16)		
1339.7	$11^- \rightarrow 9^-$	238.0(6)	130(44)	0.21(2)	-0.09(2)
	$11^- \rightarrow 10^+$	568.5(6)	175(51)	-0.20(14)	0.05(17)
1621.2	$13^- \rightarrow 11^-$	281.5(6)	163(63)	0.25(5)	-0.13(9)
	$13^- \rightarrow 12^+$	544.1(6)	119(53)	-0.26(16)	-0.02(22)
1944.3	$15^- \rightarrow 13^-$	323.1(5)	150(66)	0.22(6)	-0.10(8)
	$15^- \rightarrow 14^+$	518.3(5)	86(43)		
2307.8	$17^- \rightarrow 15^-$	363.5(5)	127(61)	0.4(3)	-0.05(45)
	$17^- \rightarrow 16^+$	492.8(5)	58(58)		
2708.3	$19^- \rightarrow 17^-$	400.5(5)	107(52)	0.31(16)	-0.1(2)
	$19^- \rightarrow 18^+$	467.1(5)	41(69)		

TABLE 4.11 (contd.)

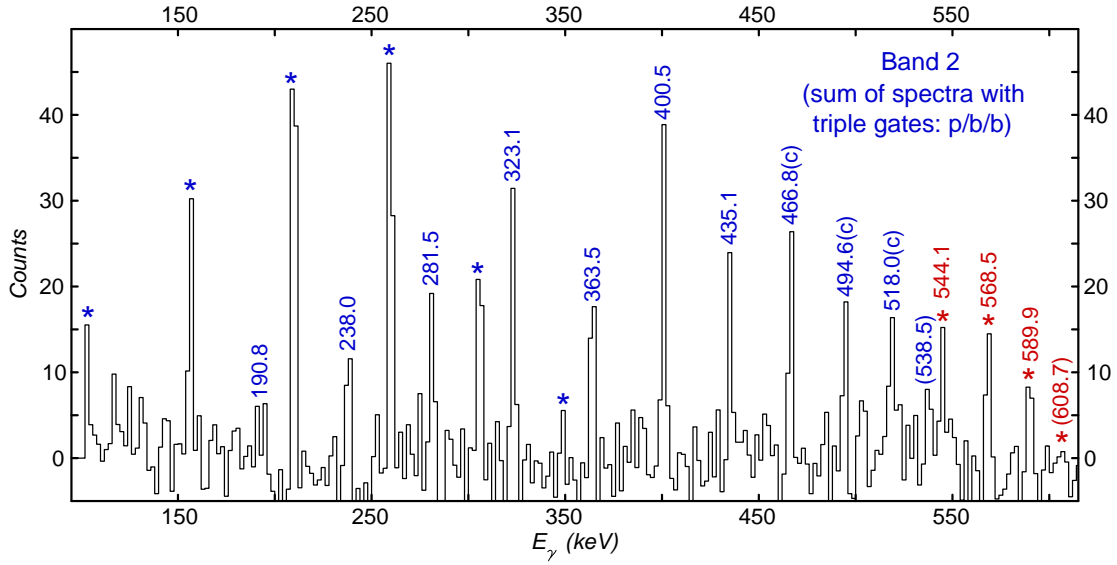| E_x (keV)	Assigned spin ($\hbar$)	E_γ (keV)	I_γ (rel.)	A_2	A_4
3143.4	$21^- \rightarrow 19^-$	435.1(5)	100(49)	0.14(18)	-0.09(24)
	$21^- \rightarrow 20^+$	441.6(5)	38(20)		
3610.2	$23^- \rightarrow 21^-$	466.8(5)	82(28)	0.4(2)	-0.2(3)
	$23^- \rightarrow 22^+$	415.7(5)	33(19)		
4104.8	$25^- \rightarrow 23^-$	494.6(6)	53(23)	0.5(3)	-0.1(5)
4622.8	$27^- \rightarrow 25^-$	518.0(7)	35(16)		
5161.3	$29^- \rightarrow 27^-$	538.5(7)			

Figure 4.33. Spectrum representative of band 2 in ^{238}Pu. The triple coincidence gates are placed on two of 9 in-band transitions (from 238.0-keV to 518.0-keV) in band 2, $i.e.$, "b", and one of the strongest lines (583-keV or 2611-keV) in ^{208}Pb, $i.e.$, "p". The transitions are labeled in a manner used in Figure 4.32.

subsequently. Further, the values of A_2 and A_4 coefficients for the transitions associated with band 2 were also derived. The rules of choosing proper coincidence gates are very similar to those applied in the analyses for band 2 in ^{240}Pu and in ^{242}Pu, except that triple (an additional gate placed on one of the strongest transitions in ^{208}Pb) instead of double gates were applied. The results of the above analysis are summarized in Table 4.11. The measured A_2 and A_4 coefficients for the inter-band transitions between bands 1 and 2 and the in-band ones of band 2 indicate their dipole and quadrupole nature, respectively. Hence, negative parity and odd spins were assigned to the levels of band 2 (the spins and parity for states above 25^- were adopted under the assumption that these transitions form the natural extension of the $E2$ sequence). As will be shown later, the resulting routhian plot (Figure 4.49 in Sec. 4.7.4) also suggests that the sequence of γ rays observed in the present work (above the 7^- level) extrapolates well at lower angular frequency to the known bandhead sequence of "5^-, 3^-, 1^-" states ($E_x = 605.2\ keV$ for the 1^- level). The consistency of the data points from the present work (at higher spin) with the ones from the previous work [170, 171, 172, 173] (at lower spin) supports, from another point of view, the assignment of spins and parity to this band.

4.7   Discussion and interpretation

Making use of the method described in Sec. 1.3.4 of Chapter 1, the experimental results for the three even-even Pu isotopes were used to extract essential physical quantities such as routhians and alignments, for example. In order to make meaningful comparisons between the intrinsic properties in different nuclei, common Harris parameters, $J_0 = 65\hbar^2 MeV^{-1}$ and $J_1 = 369\hbar^4 MeV^{-3}$, were

adopted for all nuclei compared in the present work. These parameters have proved suitable for most nuclei in the region [43, 174, 175]. In fact, these values keep the aligned spins i_x of the yrast bands in the even-even nuclei close to zero at all frequencies below the first band crossing (*i.e.*, backbending; see Sec. 1.3.3 in Chapter 1).

4.7.1 Yrast bands

Before discussing these measured alignments, it is necessary to briefly introduce the important concept of "Pauli blocking". In a rotating odd-even nucleus, as described in Sec. 1.3.2 of Chapter 1, the Coriolis force tends to break a pair of nucleons in an orbital of interest and align the individual angular momenta with the rotation axis. However, the presence of an aligned odd nucleon in the same orbital will prevent the occupation of this orbital, because of the Pauli exclusion principle: once the pair is broken, one of the nucleons will need to occupy a higher-lying orbital. In other words, this alignment will require more energy and will occur at much higher frequency. Hence, the alignment curve will remain constant in the frequency region where a sudden increase of the angular momentum occurs in the yrast bands in the neighboring even-even nuclei. In other words, the alignment is blocked. The phenomenon has been predicted and reproduced well by Cranked Shell Model (CSM) calculations. A more detailed discussion of the subject can be found in Refs. [19, 175].

Figure 4.34 (a), (b) and (c) compares the aligned spins i_x as a function of the rotational frequency $\hbar\omega$ for the yrast bands (band 1) in the ^{238}Pu, ^{240}Pu and ^{242}Pu isotopes with those seen in the neighboring even-even ^{244}Pu [43] and ^{238}U [41] nuclei. Comparisons are also provided with the bands built on the $j_{15/2}$ neutron

orbital in ^{237,239}U [140] and on the $i_{13/2}$ proton orbital in ^{237}Np and ^{241}Am [19, 175].

As can be seen in Figure 4.34 (a), a strong alignment occurs in ^{242,244}Pu at a frequency of $\hbar\omega{\sim}0.25\ MeV$. In the case of ^{244}Pu, the data show that the gain in angular momentum is essentially $10\hbar$. The alignment in the yrast band of ^{238}U exhibits a pattern similar to those of ^{242,244}Pu, but the rate of increase is smaller, probably reflecting differences in interaction strength between the aligned and ground configurations at the crossing point. In contrast, the bands built on the $j_{15/2}$ neutron orbital in the odd-A (odd-neutron) neighboring nuclei, such as ^{237,239}U, all exhibit alignments which follow those of the even-even cores, $i.e.$, no Pauli blocking occurs. The difference of i_x at low frequency between the even-even and odd-A nuclei, discussed above, simply reflects the contribution to the total spin due to the alignment with the rotation axis of the odd neutron.

In contrast, the alignments for the bands built on odd $i_{13/2}$ quasi-protons in ^{237}Np and ^{241}Am, illustrated in Figure 4.34 (b), do not exhibit any sudden gain within the $0.20\ MeV < \hbar\omega < 0.30\ MeV$ frequency range, $i.e.$, these alignments are blocked.

All of the above observations naturally lead to the conclusion that the gain in alignment (backbending) seen in these actinide nuclei is due to the alignment of a pair of $i_{13/2}$ quasi-protons. This settles a longstanding debate in the literature [161, 176, 177] about whether $i_{13/2}$ quasi-protons, or, $j_{15/2}$ quasi-neutrons are involved. Further detailed discussions about the impact of the proton $i_{13/2}$ and neutron $j_{15/2}$ orbitals on the alignment patterns in the actinide region are presented in Refs. [19, 175].

With the purpose of interpreting the above observations of alignment, the standard Cranked Shell Model (CSM) calculations with the Warsaw-Lund code
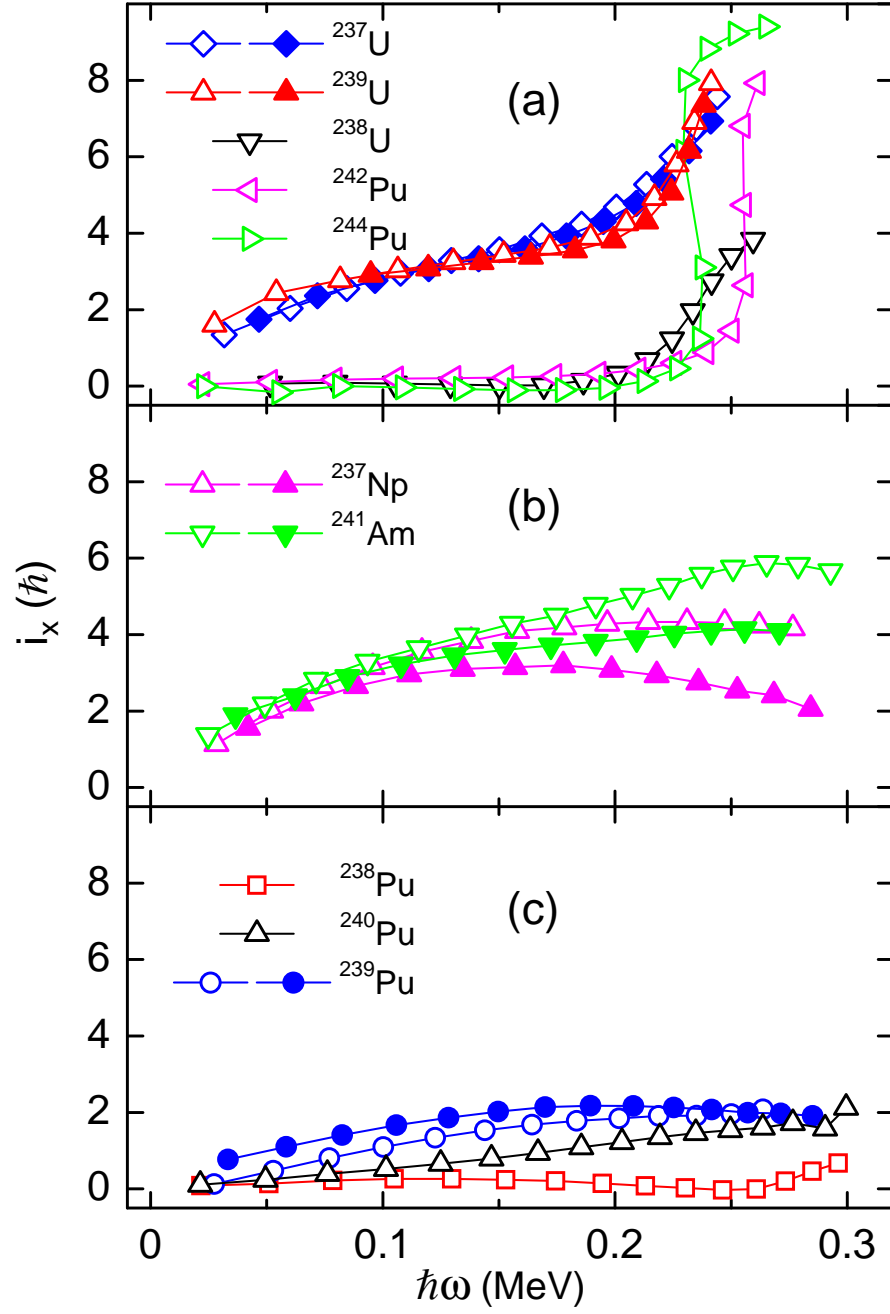
Figure 4.34. The aligned spins i_x of the yrast bands in the ^{238,240,242,244}Pu isotopes and in the neighboring even-even ^{238}U, odd-neutron ^{237,239}U and odd-proton ^{237}Np and ^{241}Am nuclei. See text for details.

using a Woods-Saxon potential were performed for the ^{238,240,242}Pu isotopes. The universal deformation parameters, $\beta_2 = 0.29$, $\beta_4 = 0.01$, $\gamma = 0°$, and a pairing strength (*i.e.*, the G_p and G_n factors for protons and neutrons, calculated from the fit of a large number of data [19]) at 90% of the full value were adopted in the present calculations. CSM calculations with these values of the parameters have been found to give the most satisfactory agreement with the data for most nuclei in the region [19]. The gain in alignment δi_x and the frequency $\hbar\omega_c$ where the alignment occurs for the $i_{13/2}$ quasi-protons in ^{238,240,242}Pu, extracted from the resulting quasi-proton routhian plots (at the left in Figure 4.35), are almost identical: $\delta i_x = 7.75\hbar$ and $\hbar\omega_a = 0.28~MeV$. Hence, in the ^{242}Pu case, the measured δi_x ($\sim 8 - 10\hbar$) and $\hbar\omega_a$ ($\sim 0.25~MeV$) values for the $i_{13/2}$ quasi-protons were reproduced well by the CSM calculations.

The performed CSM calculations (see the plots at the right in Figure 4.35) also indicate that the alignment of $j_{15/2}$ quasi-neutrons is expected in the same frequency range. As discussed above, the data do not provide much direct evidence for such neutron alignments. This issue remains unresolved at this time, although it has been suggested in Ref. [19] that a rather small neutron gap may have as a consequence a gradual, hardly visible alignment of the $j_{15/2}$ neutrons.

Because of the successful interpretation of the ^{242,244}Pu and ^{238}U data illustrated in Figure 4.34 (a) and (b) using the concepts of $i_{13/2}$ quasi-proton alignments and Pauli blocking, the experimental i_x curves for the yrast bands in ^{238,239,240}Pu become rather striking: there is no sign of any sudden gain in alignment throughout the entire rotation frequency range ($0.02~MeV < \hbar\omega < 0.30~MeV$). This observation indicates that the expected $i_{13/2}$ quasi-proton alignment is absent or, at least, severely delayed in frequency in ^{238,239,240}Pu. It is worth
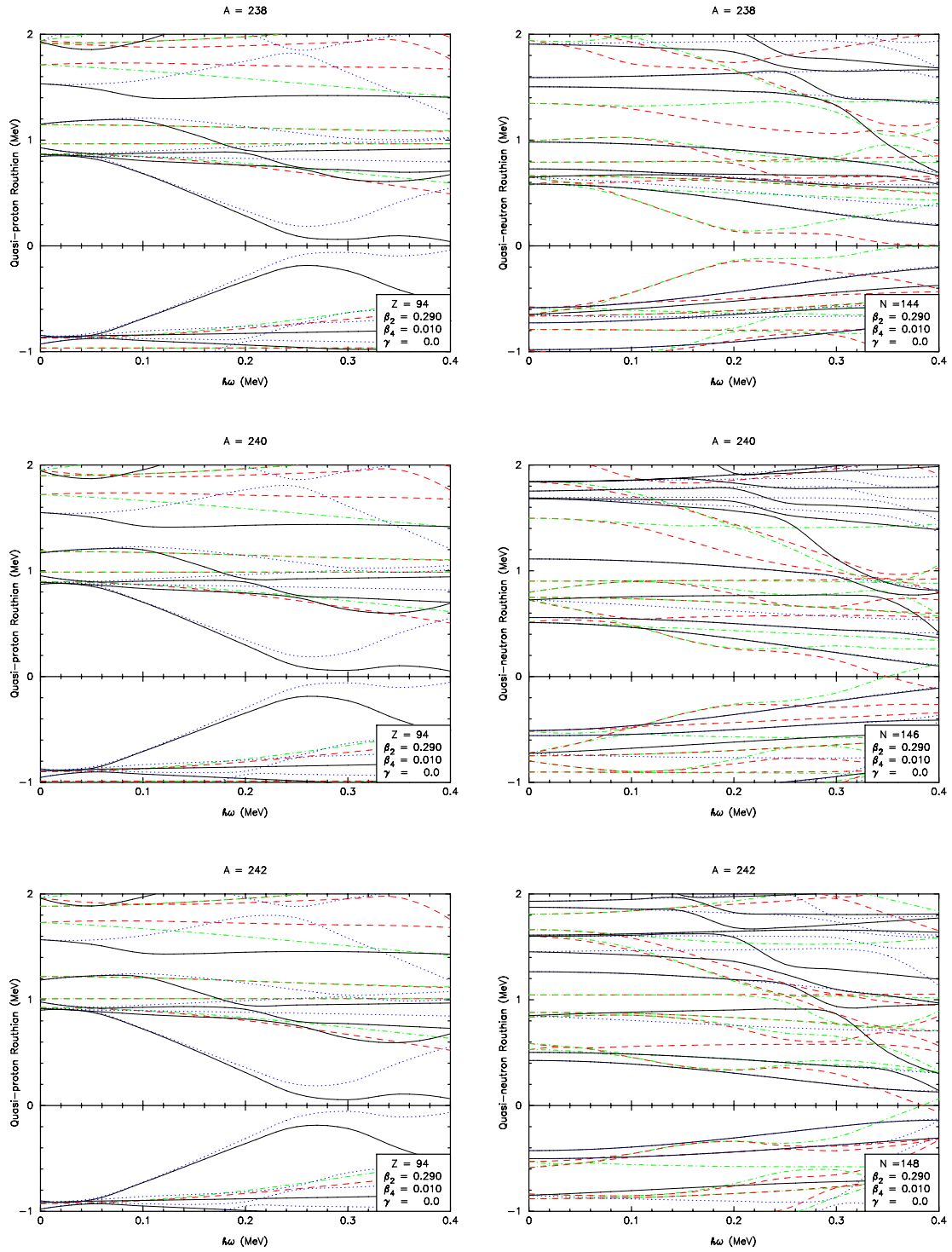
Figure 4.35. The quasi-proton and quasi-neutron routhians from the
Cranked Shell Model (CSM) calculations described in the text.

pointing out that this is not a small effect. For example, the absence of a sudden alignment in ^{240}Pu continues for at least five transitions beyond the point where it occurs in ^{242}Pu. To the best of our knowledge, the same strong $i_{13/2}$ quasi-proton alignment is predicted to occur at the same frequency ($\hbar\omega{\sim}0.25\ MeV$) by all available calculations [161, 176, 177]. The striking difference in pattern was revealed for the first time in the previous work of Wiedenhöver $et\ al.$ [43]. A natural explanation was suggested therein in terms of strong octupole correlations in ^{238,239,240}Pu, which would have a considerable impact on their intrinsic structure and result in the absence or delay of the strong proton alignment seen in the heavier Pu and neighboring U nuclei.

4.7.2   One-phonon octupole bands

The alignments of the negative-parity bands (band 2) in ^{238,240,242}Pu, which have been associated with a one-phonon octupole vibration, are illustrated in Figures 4.36, 4.37 and 4.38. The indicated patterns are consistent with those seen in their respective yrast (positive-parity) bands.

In ^{242}Pu, the aligned spin i_x of the octupole band (band 2) gradually increases until an upbending occurs at $\hbar\omega{\sim}0.25\ MeV$ just as in the yrast band. The difference of i_x between the yrast and octupole bands gradually rises with increasing frequency, until it becomes almost constant at $3\hbar$ over wide range of frequencies ($0.10\ MeV\ <\ \hbar\omega\ <\ 0.25\ MeV$). The value of $3\hbar$ corresponds to what would be expected for an octupole phonon. This negative-parity band upbends at essentially the same high frequency ($\hbar\omega{\sim}0.25\ MeV$), $i.e.$, the alignment processes occurring in the core are reflected in band 2 as well.

In order to understand the observations, a microscopic model that is able to
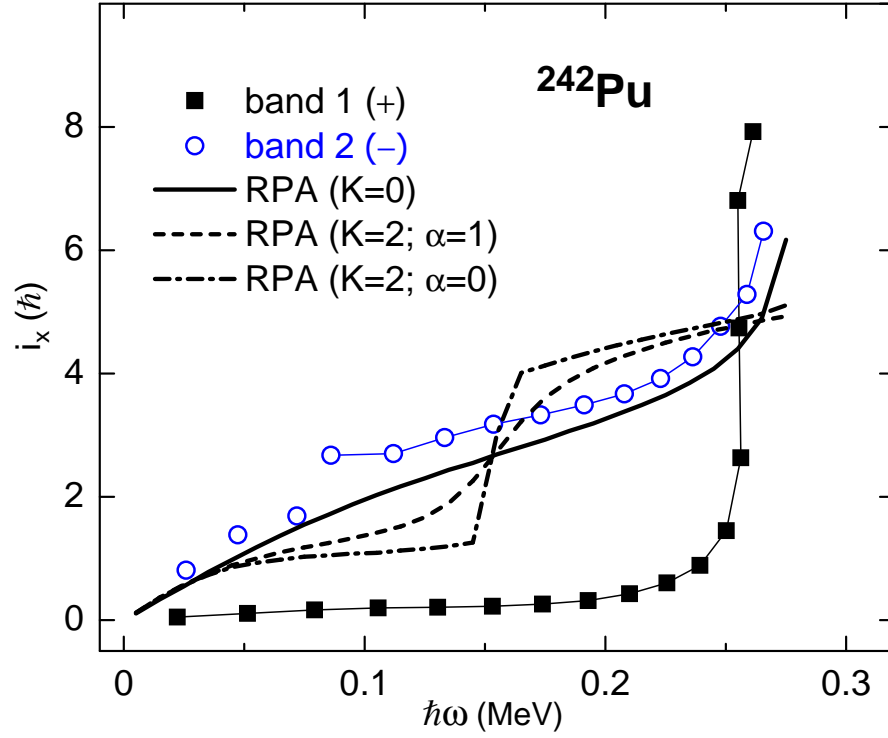
Figure 4.36. Spin alignments as a function of rotational frequency for bands 1 and 2 in ^{242}Pu. The + and − symbols in parentheses represent the parity of band. The data points connected by thin lines were obtained in the present work, while the separated points were adopted from the literature. The drawn thick lines are obtained from the cranked RPA calculations with different K and α quantum numbers. See text for details.

Figure 4.37. Spin alignments as a function of rotational frequency for bands 1 and 2 in ^{238}Pu from the data and from the RPA calculations. See text for details.
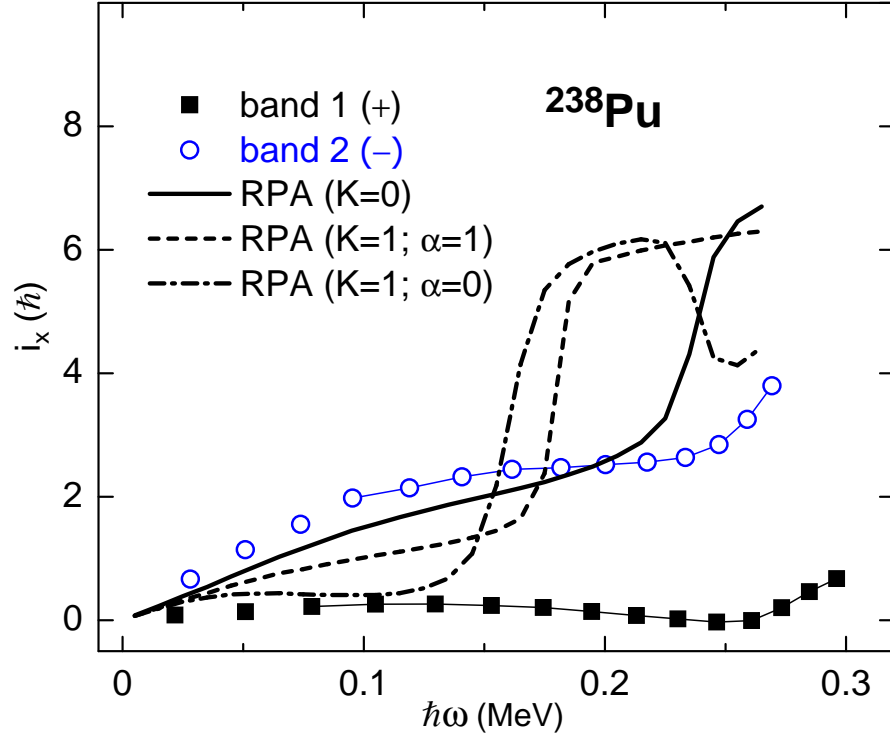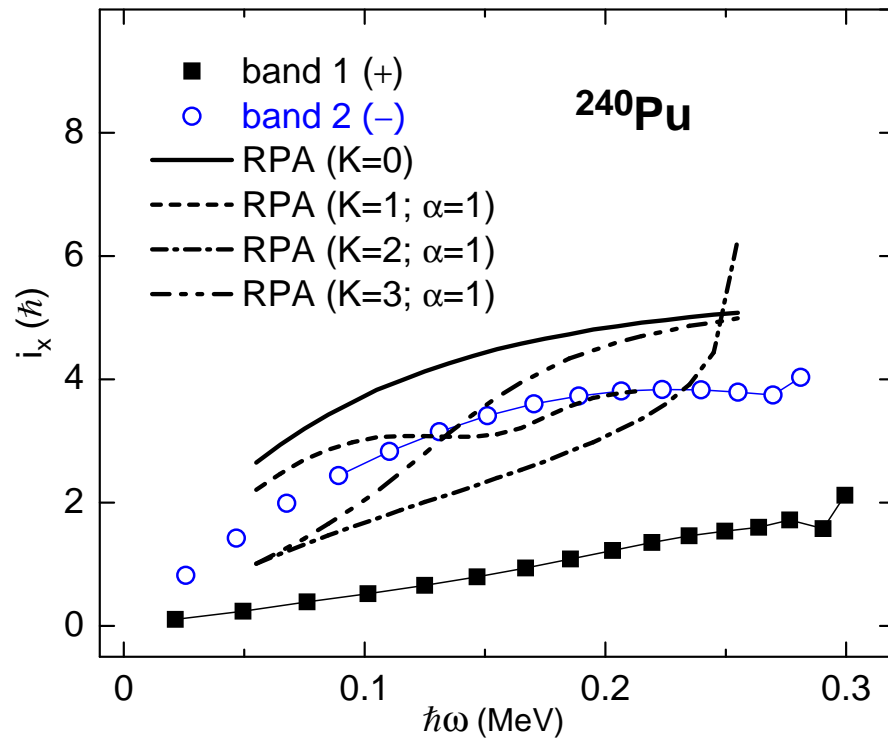
Figure 4.38. Spin alignments as a function of rotational frequency for bands 1 and 2 in ^{240}Pu from the data and from the RPA calculations. See text for details.

describe well different types of vibrations is necessary. As introduced in Sec. 4.1.3 of this chapter, the calculations with the Random Phase Approximation (RPA) model based on the cranked Nilsson potential, *i.e.*, the cranked RPA calculations, can account well for the interplay between octupole vibrations and collective quasi-particle excitations under the stress of rotation. Such calculations have proved to reproduce quite successfully the experimental observables in many nuclei of the region, such as ^{238}U [41], ^{248}Cm [42] and ^{232}Th [19], for example. Hence, similar calculations for the three Pu nuclei of interest were carried out by T. Nakatsukasa of RIKEN for the present work.

As seen in Figure 4.36, the cranked RPA calculations reproduce the alignment in band 2 of ^{242}Pu rather well: the magnitude of the alignment and its evolution with spin are accounted for, justifying the $K = 0$ octupole assignment.

In ^{238}Pu, the aligned spin of the octupole band, and, hence, the difference Δi_x between the yrast and octupole bands is close to zero at low frequency and gradually increases with increasing frequency, until it becomes flat around $3\hbar$ in the medium spin region ($0.10 \ MeV < \hbar\omega < 0.25 \ MeV$). Thus, the data indicate that this negative-parity band is associated with an octupole vibration. Around $\hbar\omega = 0.25 \ MeV$, there is indication of the start of an upbend. However, the experimental data do not allow to fully delineate the character of the alignment, although it seems to mirror the beginning of the upbend seen in the yrast sequence at somewhat higher frequency. As seen in Figure 4.37, the cranked RPA calculations with $K = 0$ do not reproduce the characteristics of this band as well as was the case in ^{242}Pu, especially at high frequency ($\hbar\omega > 0.20 \ MeV$).

The most striking pattern exhibited by the alignments is seen in ^{240}Pu. It has been pointed out earlier that the i_x curve of its yrast band is unique among those

of the yrast bands in $^{238-244}$Pu isotopes; *i.e.*, it forms an almost straight line with small and positive slope and no sign of a sudden alignment gain. At the same time, the alignment of its octupole band grows gradually from a small number ($\sim$0.5$\hbar$) at $\hbar\omega = 0.02\ MeV$ until it reaches the maximum of about 4$\hbar$ at $\hbar\omega\sim$0.20 MeV, before remaining almost constant at higher frequencies. As a result, the value of Δi_x of the negative-parity band relative to the yrast (positive-parity) sequence remains between 2 to 3$\hbar$ in the medium spin region, and, even decreases slightly with the increasing angular frequency for $\hbar\omega > 0.20\ MeV$. It is worth pointing out that the corresponding Δi_x in ^{220}Ra and ^{222}Th [147, 178], two of the best examples of nuclei with stable octupole deformation, also decreases from about 3$\hbar$ at $\hbar\omega\sim$0.10 MeV to a smaller value at higher frequencies ($\hbar\omega > 0.22\ MeV$). Hence, this characteristic behavior in Δi_x can be viewed as a first similarity with observations made in nuclei understood in terms of octupole deformation. As can be seen in Figure 4.38, none of the cranked RPA calculations can reproduce the alignment of band 2. This observation is consistent with that seen at high spin in ^{238}Pu, and is presumably due to the impact of strong octupole correlations.

As described in Sec. 4.7.1, it was seen in the data that the $i_{13/2}$ quasi-proton alignment is absent or at least severely delayed in frequency in the ^{240}Pu and ^{238}Pu yrast bands. This surprising phenomenon, suggested to be due to the impact of strong octupole correlations [43], has actually been predicted in theoretical work by Frauendorf and Pashkevich [144]. The CSM calculations therein indicate that, with the presence of octupole deformation, the pronounced backbending is absent at the frequency where it is observed in reflection-symmetric nuclei, and is calculated to occur at higher frequency. As shown above, the observed alignments in the octupole bands of ^{240}Pu and ^{238}Pu are not reproduced well by the cranked

RPA calculations, which have proved to do well for "normal" octupole vibrations, for example those in ^{242}Pu (in the present work), ^{238}U [41] and ^{232}Th [19]. These facts point to the additional stength of octupole correlations in ^{240}Pu and ^{238}Pu. To firmly establish this pattern of increased octupole correlations and to learn further about their impact in the two Pu nuclei, evidence other than the alignment properties discussed thus far is required.

Further evidence of the increased importance of octupole correlations in ^{240}Pu and ^{238}Pu comes from the ratios of dipole and quadrupole moments which can be extracted from the branching ratios between in-band and out-of-band transitions in bands 2 in the three Pu isotopes. Although such ratios were already reported and discussed in Ref. [43], the data from the present work extend to higher spin, and, in many instances, are of better accuracy. As seen clearly in Figure 4.39, the ratios of moments D_0/Q_0 in the three even-even Pu isotopes are close and grow gradually with increasing spin, up to angular momenta lower than $19\hbar$, but, they behave differently for higher spin values ($>19\hbar$). In ^{238}Pu and ^{240}Pu, the D_0/Q_0 ratios keep rising, while the values become essentially constant in ^{242}Pu. In other words, the inter-band $E1$ decays become increasingly competitive with the in-band $E2$ transitions, as the spin increases. The effect is most pronounced for ^{240}Pu. With the assumption that the Q_0 moments are constant, as would be expected for a rotational band, the resulting increase of D_0 moment in ^{238,240}Pu reflects the enhacement of octupole collectivity and this observation can be viewed as a second indication that enhanced octupole correlations indeed play a major role in these two nuclei.

In fact, the energy difference between the yrast and octupole bands ΔE, which is defined as $\Delta E = E_-(I) - (E_+(I+1) + E_+(I-1))/2$, is a measure of the extent
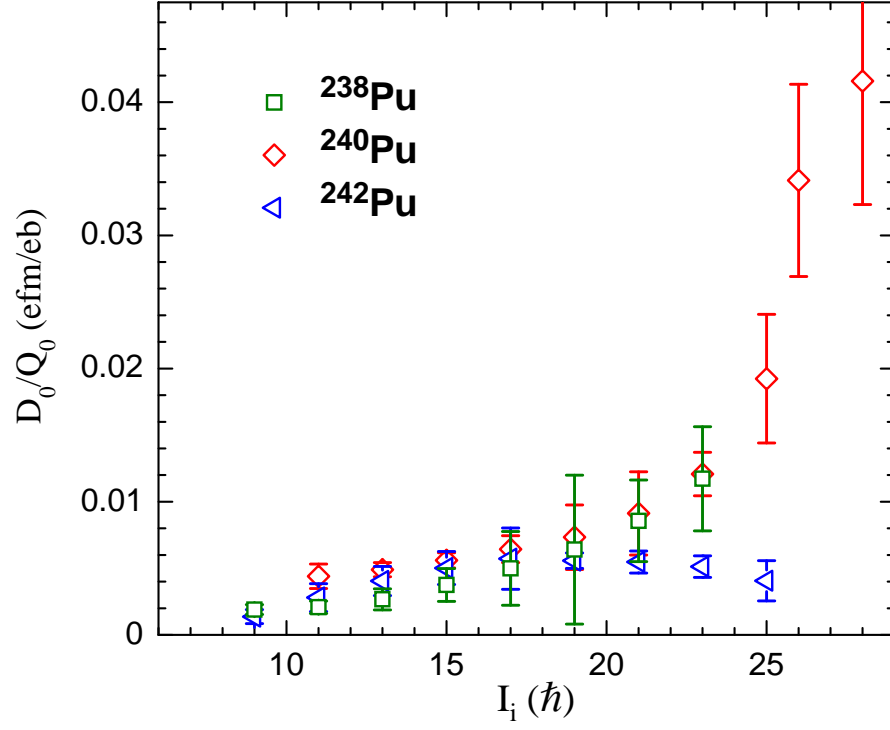
Figure 4.39. The ratios between the dipole and quadrupole moments extracted from the intensity balance between transitions linking the yrast and octupole bands and the in-band transitions in the octupole band.

to which the positive-parity levels of band 1 and the negative-parity levels of band 2 can be viewed as merging into a single rotational band. As can be seen in Figure 4.40, at the highest spins the situation in ^{238}Pu and ^{240}Pu is rather similar to that seen in the "octupole-deformed" ^{220}Ra and ^{222}Th nuclei: the measured ΔE values are very close to zero. In contrast, the negative-parity band in ^{242}Pu exhibits a different trajectory: it never merges with the yrast band and its ΔE pattern has similarities with that seen in ^{238}U.

More importantly, at spins $\geq 25\hbar$ in ^{240}Pu, a key sequence of $E1$ transitions, linking the alternating-parity states that are well interleaved in energy, $i.e.$, the "zig-zag" structure, is observed (see the level scheme of ^{240}Pu and the discussion in Sec. 4.4.2). These inter-band transitions are seen to go "both ways", $i.e.$, they go not only from band 2 to band 1, such as the $27^- \rightarrow 26^+$ line, but also from band 1 to band 2, see the $26^+ \rightarrow 25^-$ γ ray, for example. This unusual decay mode has been established for the first time in the present work (see Sec. 4.4.2). In ^{238}Pu, no such $E1$ transitions connecting the interleaved levels in the yrast (positive-parity) and octupole (negative-parity) bands at high spin were seen. In ^{242}Pu, the levels $(I+1)^+$ and I^- with $I \geq 25\hbar$ in the two bands with opposite parity have almost degenerate energies, and no inter-band lines were observed. Assuming a constant moment $Q_0 = 11.6$ eb adopted from a previous measurement of the $B(E2)$ rate for the $2^+ \rightarrow 0^+$ in the yrast band [179], the key values of D_0 for some of those linking transitions can be derived. Despite the relatively large errors, the D_0 values at high spin become quite large: $D_0 \geq 0.2$ efm for $I \geq 25\hbar$ in ^{240}Pu, and correspond to $B(E1)$ strength $\geq 2 \times 10^{-3}$ W.u. Such values are much larger than the $B(E1)$ strengths that are usually observed ($< 10^{-4}$ W.u.). They are of the same order as those observed in the light Ra and Th isotopes [133], which are among the best
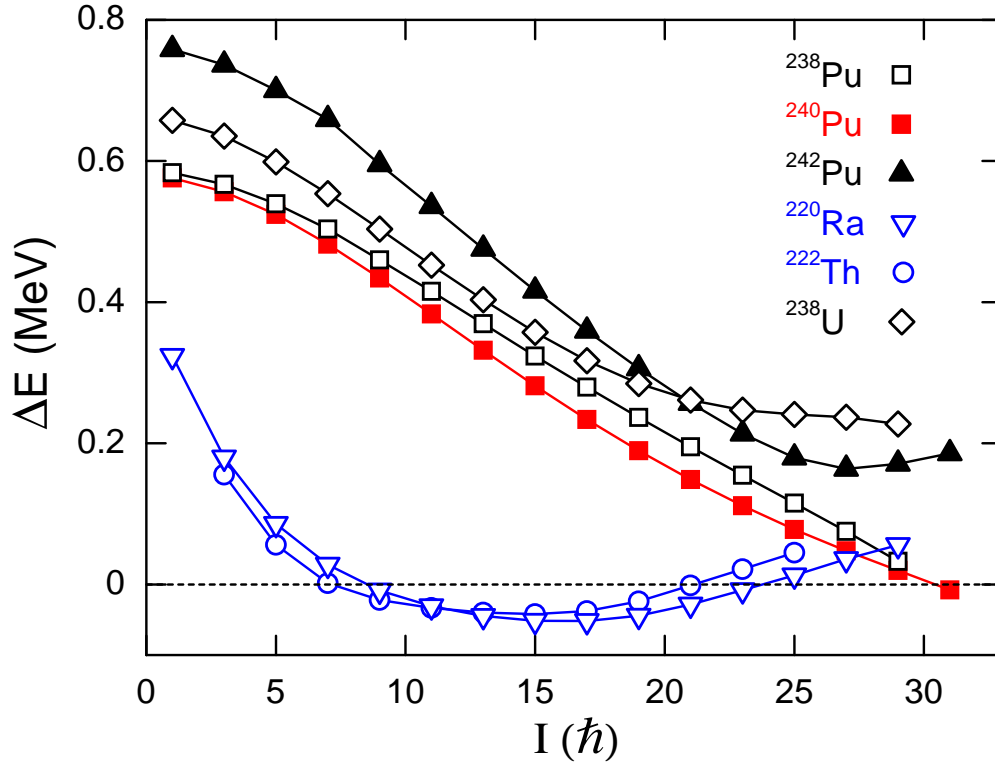
Figure 4.40. The plots of the energy difference between the yrast and one-phonon bands ΔE as a function of spin I for several even-even actinide nuclei. See text for details.

examples of octupole rotors [117].

From the discussion above, it is clear that, at high spin, the yrast (positive-parity) and the negative-parity bands in ^{240}Pu appear to merge into a single octupole rotational band (I^+, $(I+1)^-$, $(I+2)^+$, ...), which is widely viewed as one of the signatures for octupole deformed nuclei. This is the first observation of this unique feature in actinide nuclei located outside of the predicted boundary of the "island" of octupole deformation [14, 148], illustrated in Figure 4.8 in Sec. 4.2.1. It provides the most direct indication for the fact that the octupole correlations are enhanced considerably in ^{240}Pu by the rotation of nucleus and, perhaps, to

the point where static octupole deformation develops at sufficiently high angular momentum [155, 156].

4.7.3   Excited positive-parity bands in ^{240}Pu and ^{242}Pu

The three bottom levels in band 3 of ^{240}Pu were originally associated with a collective quadrupole vibration, mostly a β vibration with preserved axial symmetry [159], although a triaxial γ vibration with two phonons combining to a 0^+ state was proposed as well. However, it was pointed out by Hoogduin *et al.* [180] that a triaxial γ band would be expected to manifest itself at higher excitation energy. In the same work [180], another new experimental observation was provided: band 3 in ^{240}Pu does not decay by $E0$ transitions to band 1, unlike every other first excited even-spin, positive-parity band in the neighboring nuclei. Such strong $E0$ linking lines have been widely associated with β bands [181]. Furthermore, studies of (p,t) transfer reactions, carried out in the 1970s [165, 166], indicated that, while in most actinide nuclei (Th, U, Cm, ...) the (p,t) strength to excited 0^+ states is concentrated on a single state, this is not the case in ^{240}Pu; rather, the strength is split on two excited states: the 0_2^+ level at 862 keV and the 0_3^+ level at 1091 keV. Thus, from this discussion it results that band 3 cannot readily be associated with a β vibration, either.

As can be seen in the level scheme (Figure 4.13), the sequence of γ rays at higher spin built on the first excited 0^+ state in ^{240}Pu (*i.e.*, the in-band transitions of band 3) has been observed for the first time in the present work. Experimentally, this band only decays via $E1$ transitions to the negative-parity band (band 2). This is a very surprising and, to our knowledge, unique result. It is the only band of its kind in all three Pu isotopes studied here. Hence, the excited positive-parity
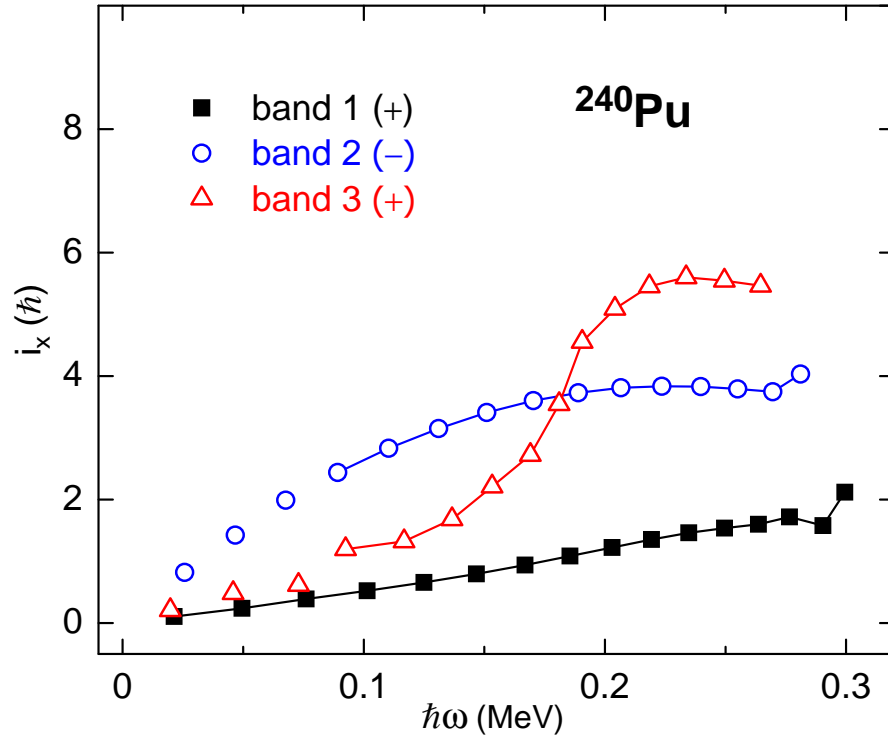
Figure 4.41. The aligned spins obtained from the present data for bands
1, 2 and 3 in ^{240}Pu.

band (band 3) sets the ^{240}Pu nucleus apart from all the others. The aligned spin
i_x of band 3 in ^{240}Pu is also interesting. As illustrated in Figure 4.41, it starts
from a low value ($< 1 \hbar$), but at the point where a $3\hbar$ alignment is achieved in
the negative-parity band (band 2), $i.e.$, $\hbar\omega{\sim}0.20 \ MeV$, a gain in alignment of $\sim$
$6\hbar$ has occurred in the excited positive-parity band. Furthermore, the i_x value of
band 3 remains essentially constant at $6\hbar$ for higher frequencies. The routhian
plot for this band (see Figure 4.42) changes its slope sharply at the point where
the sudden gain in alignment happens.

The first excited positive-parity band (band 4) in ^{242}Pu exhibits a markedly
different behavior. Experimentally, it only decays to the yrast band (instead of
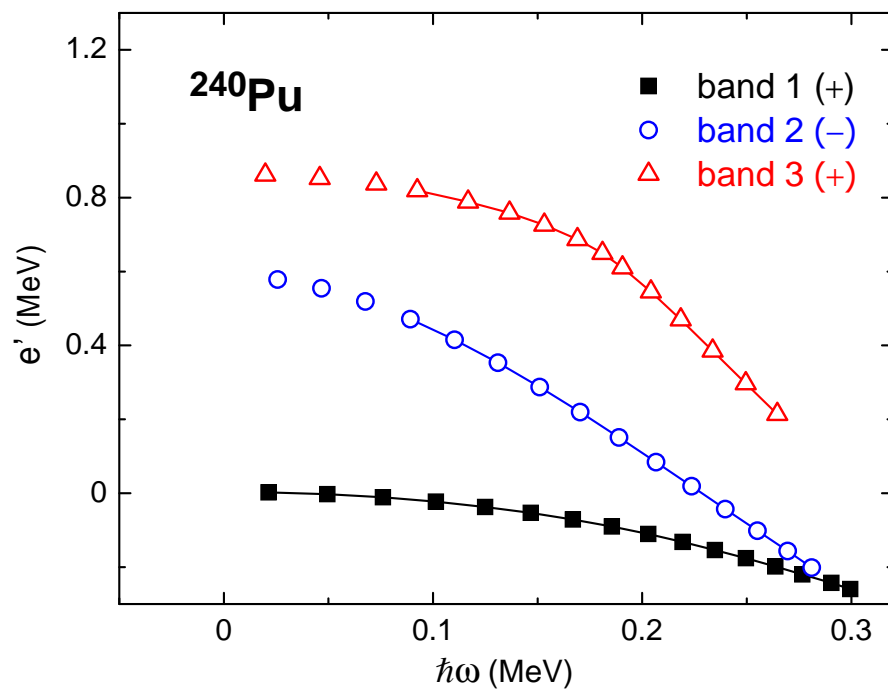
Figure 4.42. The routhians obtained from the present data for bands 1, 2 and 3 in ^{240}Pu.

to the negative-parity band in the ^{240}Pu case). Only a few states were identified, and this band was not traced down to low spin due to the lack of statistics. It can be seen clearly in Figure 4.43 that a gain in alignment of $\sim 8\hbar$ occurs around $\hbar\omega = 0.16\ MeV$. Thus, this band does not have any similarity with band 3 in ^{240}Pu, and its exact nature has not been thoroughly investigated here. A rather natural interpretation of this band might be that it starts out as a β vibration at low spin (where the 0_2^+ and 2_2^+ states are known from earlier work [165, 166]), which is crossed at higher frequency by a two quasi-particles excitation, possibly a quasi-neutron excitation. As can be seen in Figure 4.35, at least one possible crossing is calculated to occur in the routhian diagram below $\hbar\omega = 0.2\ MeV$. On the other hand, an extrapolation of the routhian of band 4 to higher frequency in Figure 4.44 would suggest that this band would cross band 1 at the frequency where the upbend occurs in latter. This observation would associate band 4 with a two quasi-protons excitation. Clearly, further elucidation of this issue will require a new data set where band 4 would be expanded to both higher and lower spin states.

In summary, the evidence for very strong octupole correlations in ^{240}Pu (and possibly also in ^{238}Pu) that has emerged in the present work includes: (a) the absence or severe delay of quasi-proton alignment in the yrast band (see Sec. 4.7.1); (b) the rising of the D_0 moment with increasing spin throughout the measured range of angular momentum (see Sec. 4.7.2); (c) the sequence consisting of interleaved levels with alternating spin and parity, which are connected by strong $E1$ transitions, $i.e.$, the "zig-zag" pattern (see Sec. 4.7.2); and, (d) an excited positive-parity band (band 3) that decays solely to the octupole band (band 2) via $E1$ transitions (see Sec. 4.7.3). In addition, there is further evidence for the
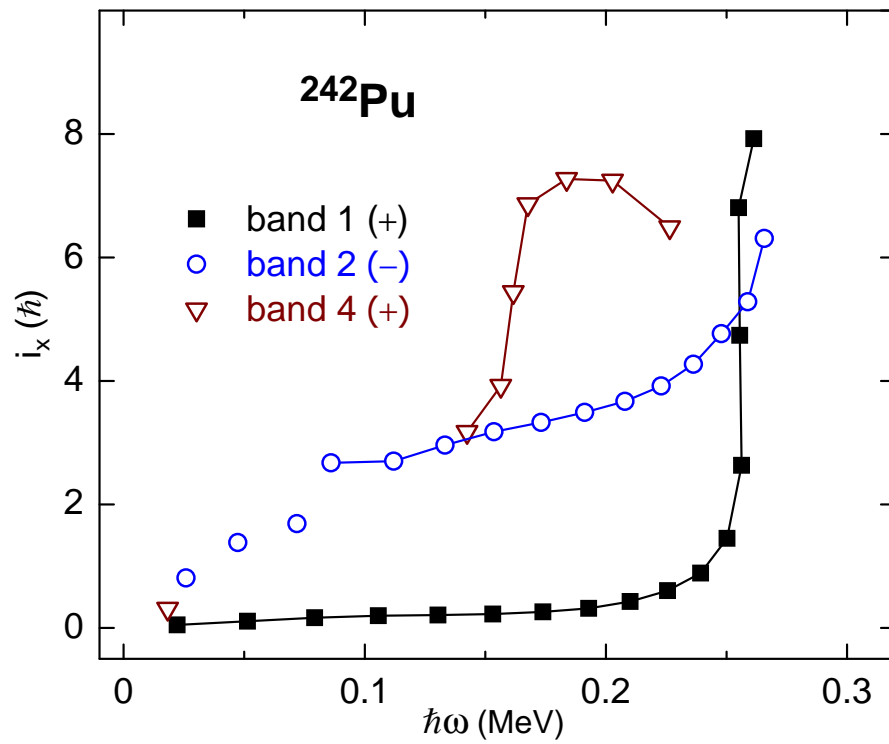
Figure 4.43. The aligned spins obtained from the present data for bands 1, 2 and 4 in ^{242}Pu.
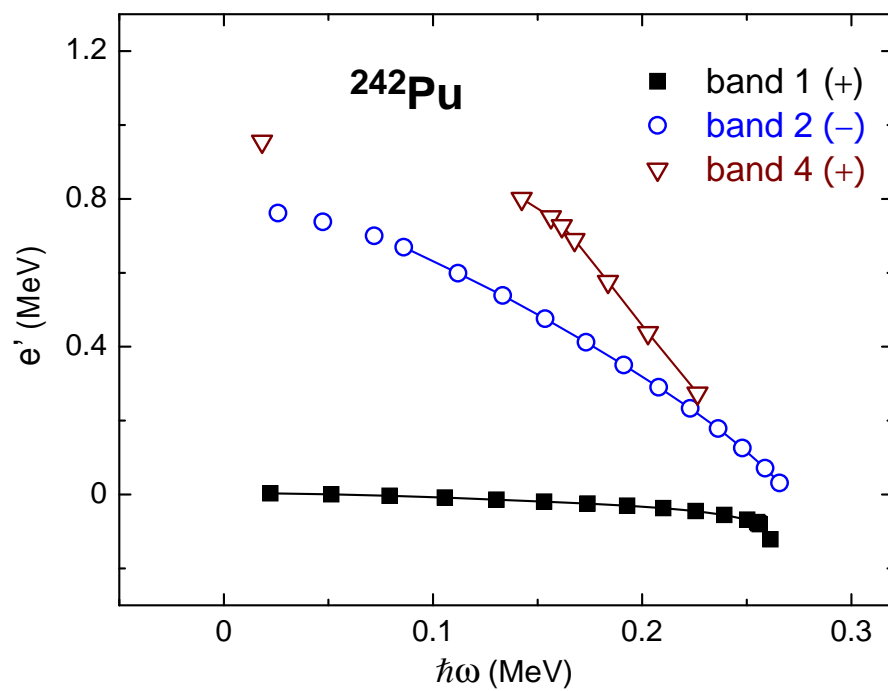
Figure 4.44. The routhians obtained from the present data for bands 1, 2 and 4 in ^{242}Pu.

strength of octupole correlations in ^{238}Pu and ^{240}Pu from α decay [157]. The hindrance factors (HFs) of α decay from the 0^+ ground states of ^{238}Pu and ^{240}Pu to the low-lying 1^- levels in the daughter nuclei are found to be small. In fact, these two nuclei form a minimum in HFs for the Pu isotopes, which can be related to large octupole correlations, according to Ref. [157]. Indeed, this observation of low HFs is one of the criteria for octupole deformation, which have been established by a large number of experiments (see Ref. [117]). All of these observations underline the need for a new interpretation.

4.7.4 Interpretation of observables using "Octupole Condensation"

As discussed earlier in this section, the RPA calculations appear to be inappropriate to deal with cases associated with strong octupole correlations, such as is the case here with ^{240}Pu and, perhaps, ^{238}Pu.

Recently, a new mechanism has been proposed by S. Frauendorf, entitled "condensation of rotational-aligned octupole phonons" [182]. In this work, first it is assumed that the quadrupole deformed nucleus is a rigid rotor with the moment of inertia, $\mathcal{J}$, and that the octupole vibration is harmonic with frequency Ω_3. Furthermore, it is postulated there is no interaction between the octupole phonons and the quadrupole deformed potential of the nucleus. The picture that then results is given in Figure 4.45: while the prolate nucleus rotates with a frequency ω_2, an "octupole" wave travels over its surface with a frequency ω_3 ($= \Omega_3/3$). Frozen "images" of the superposition of the two modes resemble in a striking way an octupole deformed nucleus. The running of the wave then gives the appearance of an octupole nucleus rotating or vibrating. The energy of the nucleus assuming this new collective mode is $E_n(I) = \hbar\Omega_3(n+1/2) + (I-ni)^2/(2\mathcal{J})$, where $I = ni + \omega\mathcal{J}$,

ω is the angular velocity, n is the number of octupole bosons, each boson carrying $3\hbar$ angular momentum ($i = 3\hbar$). The resulting energy spectrum is plotted as a function of I in Figure 4.46 (a). At $I_n = \Omega_3 \mathcal{J}/i + i(n + 1/2)$, it becomes energetically favorable to increase the spin I through exciting an aligned phonon rather than by a further increase of the angular velocity ω ($= \omega_2$). Thus, as shown in Figure 4.46 (b), a number of band crossings will occur. At each crossing, a band with a higher number of phonons crosses the yrast band. The routhians of these multiphonon states $E'_n - E'_0$ ($E'_n = E_n - \omega I$), illustrated in Figure 4.46 (b), become zero at the same point $\omega = \omega_c = \Omega_3/i$, $i.e.$, at a critical angular frquency. In this language, boson condensation occurs at ω_c, the point where ω_2 also equals ω_3.

The figure given above (Figure 4.46 (a)) is an idealized one. In reality, the anharmonicities of the octupole mode and the coupling to the quadrupole mode [9] lead to an interaction between states with different phonon numbers. Due to parity conservation, the states with even n (or with odd n) only mix with others with even n (or with odd n). The interaction causes a repulsion between crossing bands of the same parity. Figure 4.46 (c) illustrates the resulting pattern of condensation when moderate anharmonicities are included.

Assuming that bands 1, 2 and 3 can be assimilated with $n = 0$, $n = 1$ and $n = 2$ phonon bands, the experimental excitation energies E_x (Figure 4.47) and routhians e' (Figure 4.42) of the three bands in ^{240}Pu can be compared with Figures 4.46 (b) and (c), respectively. In Figure 4.42, the one-phonon octupole band (band 2) crosses the yrast band (band 1) at a frequency of $\sim 0.28\ MeV$. Due to the lack of statistics, the proposed two-phonon band (band 3) was not extended sufficiently to observe the crossing with the yrast band. However, if one extrapolates its trajectory while keeping the slope unchanged, such a crossing would not occur
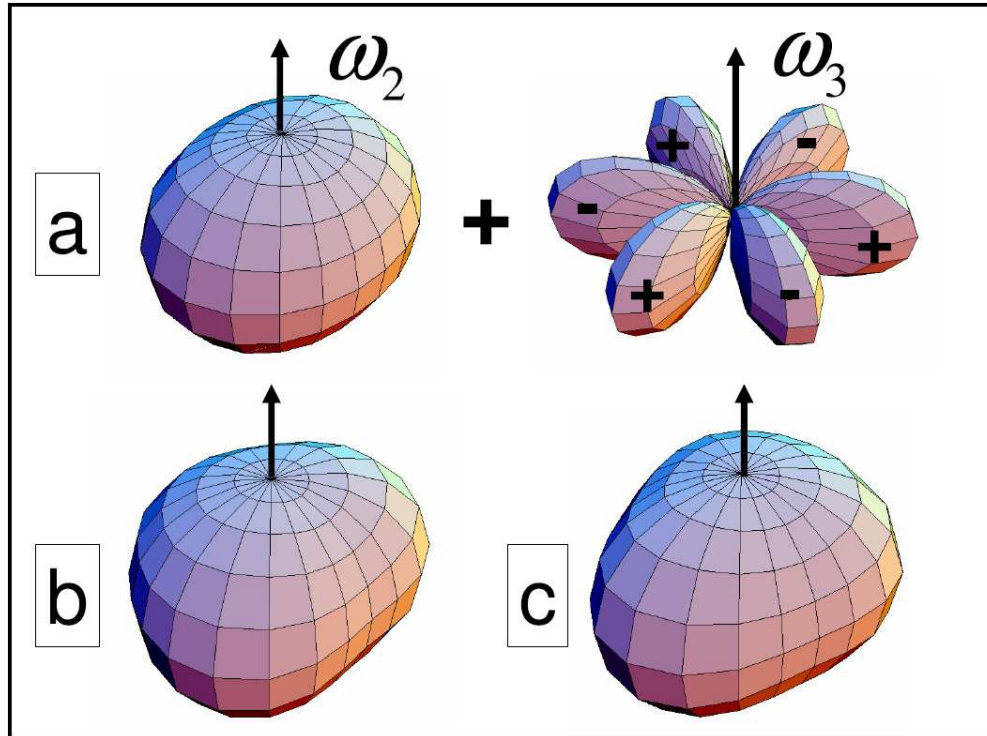
Figure 4.45. An octupole wave traveling over the surface of a quadrupole-deformed nucleus. In c), the octupole wave has turned by 90° as compared to b). See text for details. Taken from Ref. [182].
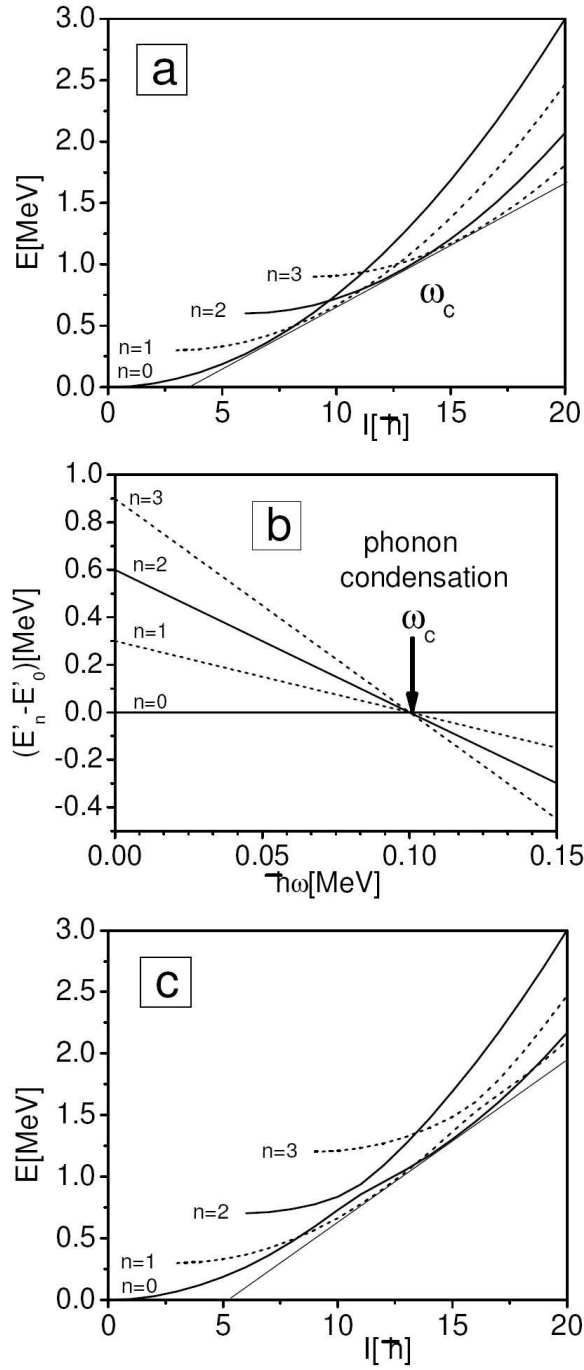
Figure 4.46. Top panel, (a): Energies of aligned octupole multiphonon bands. Full lines show $\pi = +$ and dashed lines $\pi = -$ states. Middle panel, (b): Energy in the rotating frame (routhian) relative to the zero-phonon band. Bottom panel, (c): As top, but, assuming an interaction between the phonons and an anharmonicity. See text for details. Taken from Ref. [182].

at the same frequency as that where bands 1 and 2 cross, but rather around 0.35 MeV. The disagreement between the observation and the ideal situation of octupole condensation, shown in Figures 4.46 (b), presumably reflects the involved anharmonicities. The excitation energies in ^{240}Pu (Figure 4.47) exhibit essentially the expected pattern at low-spin ($0 < I < 8\hbar$) as shown in Figures 4.46 (c), $i.e.$, the prediction for octupole condensation with band interaction. Unfortunately, the predicted full mixing between $n = 0$ and $n = 2$ phonons was not reached, even at the highest spin ($\sim 33\hbar$), in the present work. Based on the difference of the crossing frequency of $n = 0$ and $n = 1$ phonons with that of $n = 0$ and $n = 2$ phonons, the impact of anharmonicities can be quantified approximately. According to Ref. [182], at the point of condensation, the relation $E_n = \omega_c I$ applies for the n-phonon state. In the ^{240}Pu case, ω_c was extracted to be 0.28 MeV and 0.35 MeV for the $n = 1$ and $n = 2$ states, respectively. As pointed out above, the aligned spins for these two states are about $3\hbar$ ($n = 1$) and $6\hbar$ ($n = 2$), as would be expected for one- and two-phonon states. Hence, E_2 can be estimated to be $2.5E_1$, rather than the idealized value of $2E_1$. The discrepancy in E_2 directly points to the strengh of the involved anharmonicities. It should be noted also that the presence of sizable anharmonicities is also seen in the fact that the excitation energy of 0^+ state of band 3 (861 keV) is significantly lower than twice the excitation energy of the band 2 bandhead (597 keV).

The impact of octupole condensation also shows up in the plots of the energy difference ΔE as a function of spin I (Figure 4.40 in Sec. 4.7.2) and of the spin J_a as a function of the angular frequency $\hbar\omega$ (Figure 4.48). Following the discussion of Ref. [182] on octupole condensation in ^{220}Ra and ^{222}Th, the one-phonon band crosses the zero-phonon band before it feels much of an interaction with the two-
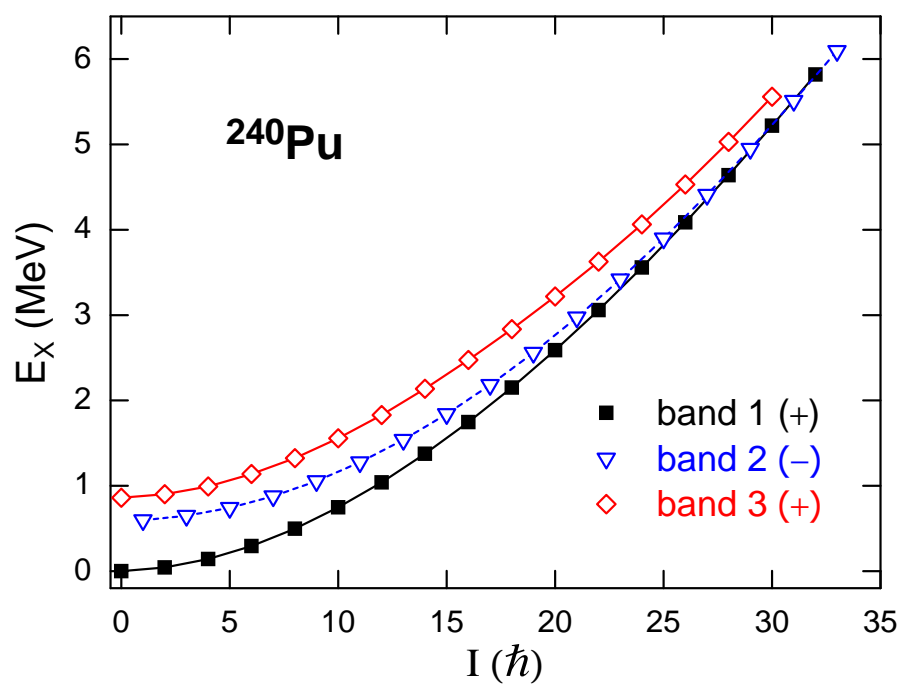
Figure 4.47. The excitation energies of states in bands 1, 2 and 3 of
^{240}Pu. See text for details.

phonon band (see Figure 4.46). At the crossing, the energy difference between the yrast and one-phonon bands, $i.e.$, $\Delta E = E_-(I) - (E_+(I+1) + E_+(I-1))/2$, changes sign. At higher frequency the two-phonon band encounters the zero-phonon one, and the two mix and exchange character. The level repulsion attenuates the growth of $-\Delta E$, and this quantity starts decreasing when the $\pi = +$ band has become predominantly of two-phonon character. At the crossing between the two- and one-phonon bands, ΔE changes sign again. According the same rule, the one- and three-phonon bands are mixed at higher spin and the next change of sign of ΔE would occur at the crossing of three- and two-phonon bands. In the ^{240}Pu case, presumably because of weaker octupole correlations, only the first change of sign of ΔE (the crossing of one- and zero-phonon bands) is seen at the highest spins, while the zero- and two-phonon bands have not yet started their mixing. It is worth pointing out that the observation of the yrast and one-phonon bands not merging, but crossing has been interpreted satisfactorily for the first time by this concept of octupole condensation. The indication of octupole condensation in the angular momentum J_a $(= I - 1/2)$ was also discussed using the example of ^{220}Ra and ^{222}Th in Ref. [182]. As can be seen in Figure 4.48, the one-phonon band starts with three units of angular momentum more than the zero-phonon band at the same $\hbar\omega$, as expected for one aligned octupole phonon. The difference decreases, when the two-phonon state, which carries six units of angular momentum, starts mixing into the zero-phonon band. The two observed bands have equal angular momentum at the frequency of full mixing where ΔE starts rising. Near the crossing of the two- and one-phonon bands at $I{\sim}24\hbar$ ($\hbar\omega{\sim}0.25$ MeV), where the mixing is small, the angular momentum difference is $-3\hbar$. It is also expected that the difference of J_a will be zero again when the full mixing between the one-

and three-phonon states is reached (see Figure 4.46). The J_a functions for the three bands of ^{240}Pu observed in the present work exhibit the expected pattern characteristic of octupole condensation in the stage before the occurrence of full mixing between the zero- and two-phonon states. The difference of J_a between the zero- and one-phonon bands remains $3\hbar$ at $\hbar\omega{\sim}0.28\ MeV$, and, then, starts decreasing because of the mixing of zero- and two-phonon states. This difference would reach zero at a frequency larger than $0.30\ MeV$ (the highest frequency in the observation) as shown by the extrapolation of the J_a curves of the zero- and one-phonon bands. The frequency where the difference of J_a may become $-3\hbar$ in ^{240}Pu (as seen in ^{220}Ra and ^{222}Th) is expected to be well beyond the measured range in the present work. In addition, the two- and one-phonon bands cross at $\hbar\omega{\sim}0.20\ MeV$ as expected. Therefore, both the ΔE and J_a behaviors support the onset of octupole condensation in ^{240}Pu.

It is also pointed out in Ref. [182] that, with the anharmonicities included, the $I^+{\rightarrow}(I{-}1)^-$ inter-band transitions have equal strength with the $I^-{\rightarrow}(I{-}1)^+$ ones, rather than being suppressed (in the case of excluding the anharmonicities). The consistency between this prediction and the observation of the "zig-zag" pattern of inter-band lines only in ^{240}Pu provides further confidence for the validity of the interpretation with octupole condensation.

Finally, it is worth pointing out as well that interband transitions are allowed only between states of bands differing by only one octupole phonon. This accounts for the experimental observations that the levels of band 3 solely decay to those of band 2 and that any deexcitation towards band 1 was beyond the detection limit of the measurements.

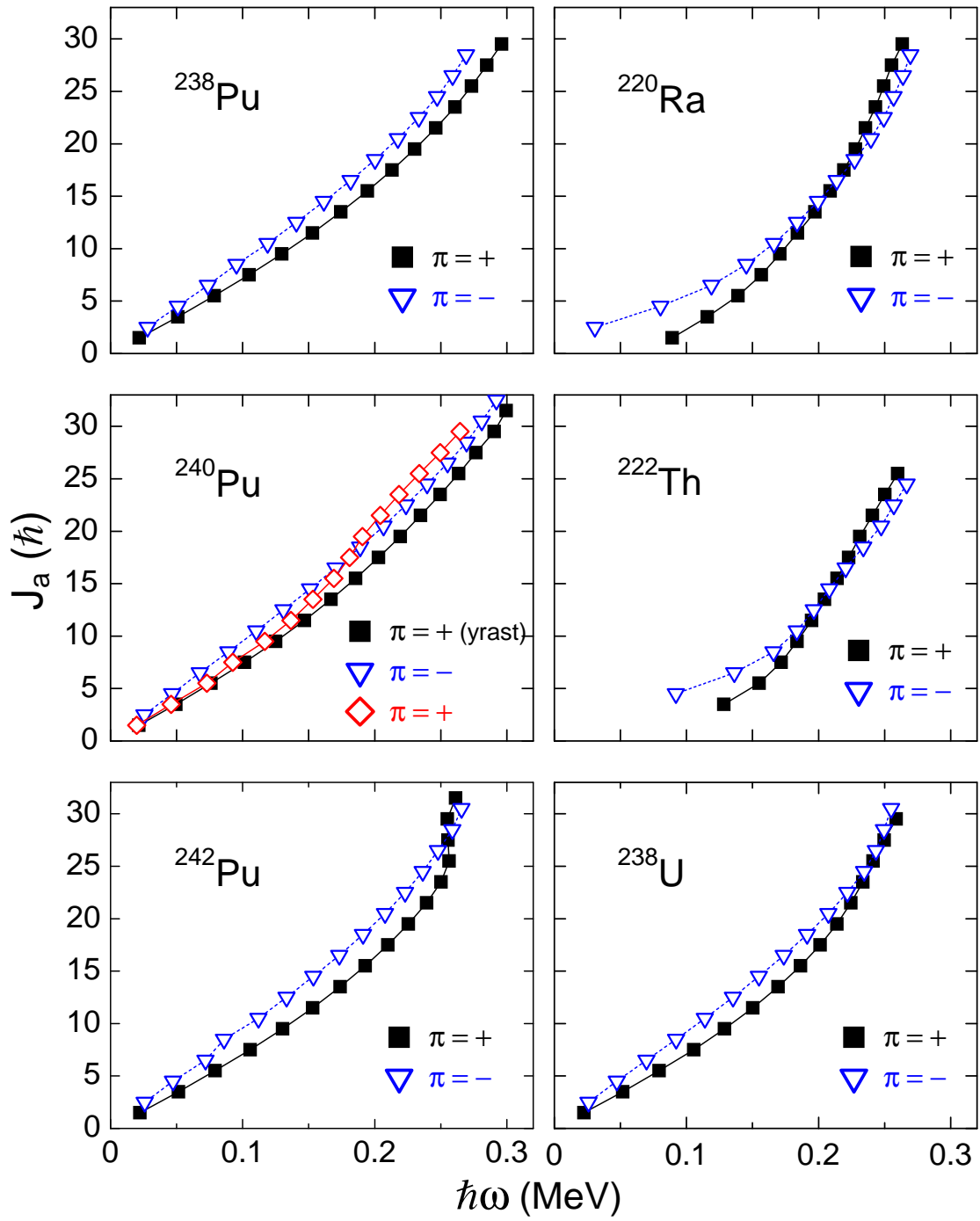As seen in both Figures 4.40 (in Sec. 4.7.2) and 4.48, the situation in ^{242}Pu

Figure 4.48. The plots of the angular momentum $J_a = I - 1/2$ as a function of angular frequency $\hbar\omega$ for the yrast and octupole bands in several even-even actinide nuclei. See text for details.

is very different. The first excited positive-parity sequence (band 4) in ^{242}Pu has been identified as a quasi-particle excitation, rather than a two-phonon octupole band. At the highest spins (or frequency) in the present work, the ΔE values remain almost constant at $\sim$0.2 MeV. The J_a curves of the yrast and one-phonon bands cross at $\hbar\omega\sim$0.25 MeV, but the reason for this crossing is the alignment of a pair of $i_{13/2}$ quasi-protons in the yrast band and the crossing has no similarity in pattern with those of phonon states. Both ΔE and J_a values in ^{242}Pu behave in an almost identical manner with those in ^{238}U, a well-known octupole vibrator (see Figures 4.40 and 4.48). In summary, the different scenarios in ^{240}Pu and ^{242}Pu indicate that the two-phonon octupole and the $i_{13/2}$ two quasi-protons bands are rather close in energy and compete with each other. In ^{240}Pu, the two-phonon octupole band is lower. The yrast (zero-phonon) band interacts with the two-phonon band. This effect results in the absence or delay of the $i_{13/2}$ quasi-protons alignment. In ^{242}Pu, the $i_{13/2}$ two quasi-protons band is at lower excitation energy. It interacts with the yrast band, and a strong alignment occurs. Unfortunately, the two-phonon octupole band could not be seen in this case.

Compared with the observations in ^{240}Pu and ^{242}Pu, the strength of octupole correlations in ^{238}Pu seems moderate. In its routhian diagram (Figure 4.49), due to the lack of statistics, the one-phonon octupole band (band 2) was not extended sufficiently to observe the crossing with the yrast band (band 1). However, the extrapolattion of its trajectory suggests that band 2 would cross the yrast band in a manner similar to that seen in the ^{240}Pu case, but, at a higher frequency ($\sim$ 0.30 MeV). The ΔE values (see Figure 4.40 in Sec. 4.7.2) keep decreasing and get very close to, but do not reach, zero at the highest observed spins. The difference of J_a (see Figure 4.48) between the yrast band and the one-phonon one
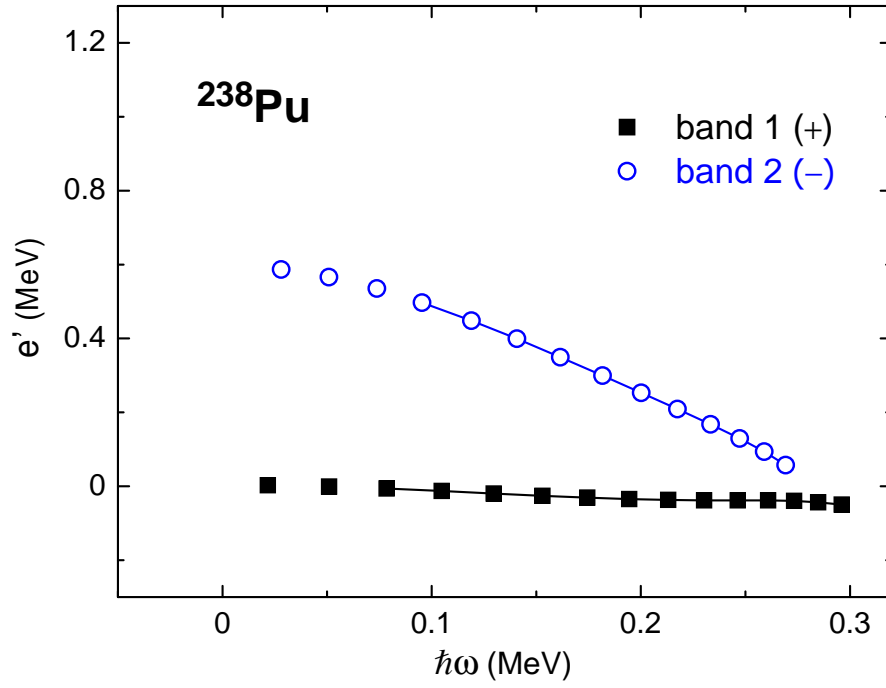
Figure 4.49. The routhians obtained from the present data for bands 1
and 2 in ^{238}Pu.

remains constant ($\sim 3\hbar$) at $\hbar\omega > 0.20$ MeV; $i.e.$, no sign of a decrease is seen. On the other hand, the proton alignment seen in ^{242}Pu is absent or delayed, as well. No inter-band transition was observed at high spin. It is possible that the two quasi-particle band and the two-phonon octupole band are located at almost the same energy, although neither of them is seen in the present work. The impact from both of these two bands on the yrast band could possibly result in the observed moderate pattern in ^{238}Pu, $e.g.$, the milder upbend of the alignment at higher frequency for the yrast and one-phonon octupole bands (see Figure 4.37 in Sec. 4.7.2).

4.7.5 Other bands in ^{242}Pu

Band 3 only decays to the yrast band experimentally. As can be seen Figure 4.50, the cranked RPA calculations for the negative-parity bands in ^{242}Pu reproduced this band reasonably well. Based on the experimental observables, such as the routhian (Figure 4.50) and the aligned spin (Figure 4.51), for example, and the comparisons with calculations, band 3 can probably be associated with an octupole vibration with $K = 3$ and $\alpha = 1$. Due to the large uncertainty on spin and parity value in band 5 and the unknown properties of band 6, these two bands were not compared with the RPA calculations and no further interpretation is given in the present work.

4.8 Conclusions and outlook

In the present work, the measured properties of ^{238,240,242}Pu and the comparison with neighboring nuclei indicate that octupole correlations in ^{240}Pu are very strong (although weaker than those in two of the best examples of "octupole rotors", ^{220}Ra and ^{222}Th). The octupole correlations appear to be enhanced with increasing spin and become even sufficient to give rise at high spin to structures similar to those traditionally associated with the rotation of an octupole deformed nucleus. Octupole correlations in ^{238}Pu seem to be substantial as well; $i.e.$, sufficient to delay the proton alignment. The octupole correlations appear weakest in ^{242}Pu, and do not affect the occurrence of the proton alignment.

The cranked RPA calculations reproduced reasonably well all experimental observables associated with weak octupole correlations (octupole vibrators). The behavior of ^{240}Pu can be understood by invoking octupole condensation.

It would be interesting to see if the yrast and one-phonon bands in ^{240}Pu
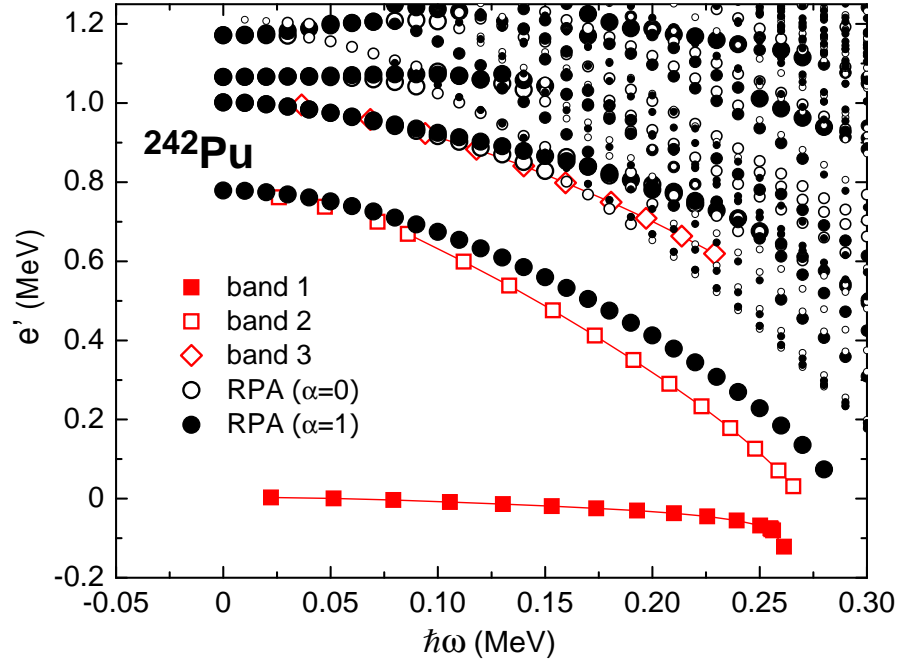
Figure 4.50. The routhians of bands 1, 2 and 3 from the present data and the cranked RPA calculations for the negative-parity bands in ^{242}Pu. The K quantum numbers of the octupole multiplets used in the RPA calculations from low to high in energy in the figure are: 0, 3, 2, 1. The open and filled circles denote that α (signature) $= 0$ and $= 1$, respectively. The size of the circle represents the strength of collectivity, $i.e.$, large - highly collective, medium - moderately collectively, and, small - non-collective.
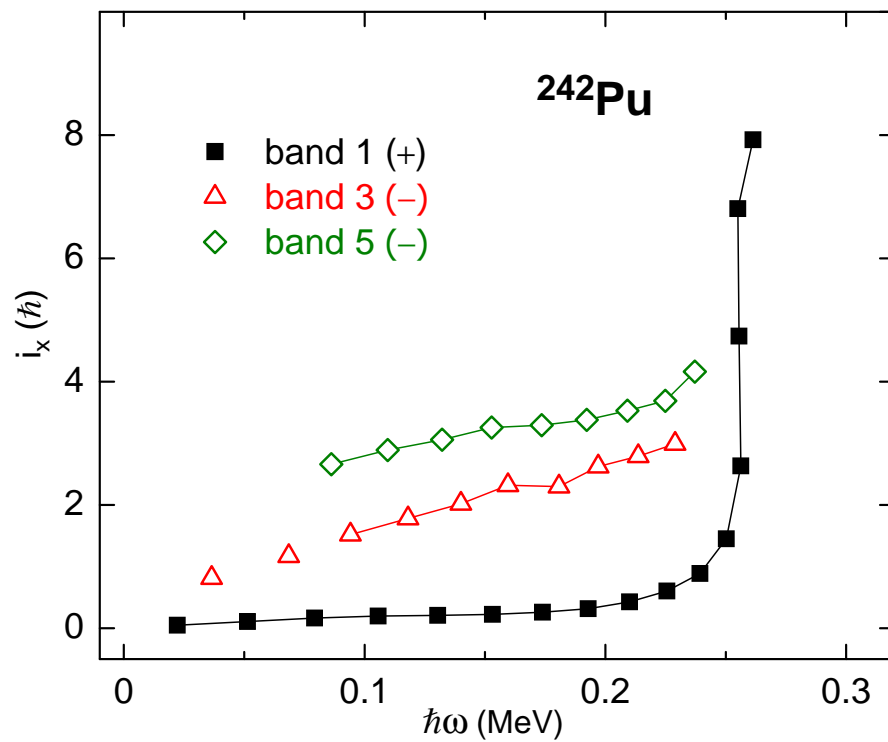
Figure 4.51. The aligned spins obtained from the present data for bands 1, 3 and 5 in ^{242}Pu.

behave in the expected manner; *i.e.*, in a way similar to that seen in ^{220}Ra and ^{222}Th, as predicted by the theory. This would require data at spins beyond the measured range in the present work.

CHAPTER 5

SUMMARY AND PERSPECTIVE

The purpose of this work was two-fold: explore the nuclear shape associated with new bands discovered in ^{163}Tm and provide new data to investigate the strength of octupole correlations in the Pu isotopes. These two objectives have now been met.

In ^{163}Tm, two excited bands were shown to be associated with quasi-particle excitations in a triaxial minimum rather than with the wobbling mode. This minimum was measured to correspond to a larger deformation than that characterizing the ground state. The data can be reproduced reasonably well by calculations which also provide an explanation for the presence of wobbling in the Lu isotopes and its absence in the neighboring isotopic chains of Ta, Hf and now also Tm.

The results obtained thus far lead naturally to a number of open questions deserving attention in the future. First, it was recognized in the present work that the measured quadrupole transition moments are significantly smaller than those calculated. This observation is not limited to ^{163}Tm: quadrupole moments smaller than those predicted have also been found in the Lu isotopes where wobbling is present. The origin of this discrepancy between experiment and theory remains to be clarified. Furthermore, specifically for ^{163}Tm, the data presented here indicate that the γ-ray intensity responsible for the feeding of the two triaxial strongly deformed bands originates from states associated with larger deformation

than that of the two bands themselves. The exact nature of these feeding levels warrants further attention, but would presumably require a detector system of larger resolving power than Gammasphere in order to extract the weak γ rays from the quasicontinuum of unresolved transitions. Finally, a systematic search for wobbling excitations in this region of the nuclear chart needs to continue in order to validate the present theoretical understanding in terms of specific shell gaps.

The new data available for the even-even $^{238-242}$Pu isotopes have clarified the role of octupole correlations in these nuclei and have led to a satisfactory interpretation in terms of octupole phonon condensation. Specifically, the special role of octupole correlations in ^{240}Pu is highlighted by the data. Not only has a pattern expected for the rotation of an octupole-deformed nucleus been experimentally established at high spin, but a seldom observed mode of deexcitation has been uncovered for a rotational band built on the first excited 0^+ level: the decay proceeds solely towards the octupole band.

The picture that emerges is one where strong octupole correlations are interpreted as rotation-induced condensation of octupole phonons having their angular momentum aligned with the rotational axis. The phonon condensate co-rotates with the prolate deformed nucleus. This new collective motion leads naturally to oscillations in the energy difference between the lowest positive- and negative-parity bands. Within this picture, the two excited bands observed here in ^{240}Pu are associated with one- and two-phonon excitations and the data extend to sufficiently high frequency to observe the first of the crossings predicted by theory. The ^{238}Pu data can be interpreted within the same framework. The extended level structure delineated in ^{242}Pu is the only one to exhibit the type of excitations seen

in other well-deformed actinide nuclei of the region, indicating that the octupole strength weakens considerably as the number of neutrons increases.

While a satisfactory picture emerges, additional work is highly desirable in this instance as well. If the rotational sequences, especially in ^{240}Pu, could be extended to higher spin, it would be possible to verify the theoretical predictions of a crossing between the yrast and the two-phonon bands. Also, expanding the level structure of ^{240}Pu would be of value. In particular, information on the excitation energy and the behavior with rotational frequency of quasi-particle excitations would provide further information on the strength of octupole correlations as well as on the interactions between the various modes. Exploration of other nuclei, not only in the actinide region, but also in other parts of the nuclear chart would also be important in order to assess whether this exotic collective mode is a rather general phenomenon.

Just as in the case of ^{163}Tm, progress demands the availability of a detection system with the intrinsic ability to detect weaker γ-ray transitions. Indeed, such a system, GRETA, an array of Ge detectors with tracking capability, is currently being developed. This array is expected to exceed the resolving power of Gammasphere by at least two orders of magnitude.

BIBLIOGRAPHY

1. E. Rutherford, Philosophical Magazine, Series 6 **vol. 21** (1911).

2. K. S. Krane, *Introductory Nuclear Physics* (John Wiley and Sons, New York, 1988).

3. M. G. Mayer, Phys. Rev. **75**, 1969 (1949).

4. O. Haxel, J. H. D. Jensen, and H. E. Seuss, Phys. Rev. **75**, 1766 (1949).

5. R. V. F. Janssens, Nature **435**, 897 (2005).

6. M. G. Mayer and J. H. D. Jensen, *Elementary Theory of Nuclear Shell Structure* (Wiley, New York, 1955).

7. S. Zhu, Ph.D. thesis, University of Notre Dame (2003).

8. S. G. Nilsson, Kgl. Dan. Viden. Selsk. Mat. Fys. Medd. **29**, 16 (1955).

9. A. Bohr and B. R. Mottelson, *Nuclear Structure*, vol. II (World Scientific, Singapore, 1998).

10. S. G. Nilsson and I. Ragnarsson, *Shapes and Shells in Nuclear Structure* (Cambridge University Press, Cambridge, 1995).

11. V. M. Strutinsky, Nucl. Phys. A **95**, 420 (1967).

12. V. M. Strutinsky, Nucl. Phys. A **112**, 1 (1968).

13. P. Möller and J. R. Nix, Nucl. Phys. A **361**, 117 (1981).

14. W. Nazarewicz, P. Olanders, I. Ragnarsson, J. Dudek, G. A. Leander, P. Möller, and E. Ruchowska, Nucl. Phys. A **429**, 269 (1984).

15. D. C. Rainwater, Phys. Rev. **79**, 432 (1950).

16. A. Bohr, Phys. Rev. **81**, 134 (1951).

17. A. Bohr and B. R. Mottelson, Kgl. Dan. Viden. Selsk. Mat. Fys. Medd. **27**, 16 (1953).

18. R. Bengtsson and J. D. Garrett, *Collective Phenomena in Atomic Nuclei*, vol. 2 (World Scientific Publishing Co., Singapore, 1984).

19. K. A. Saleem, Ph.D. thesis, Illinois Institute of Technology (2002).

20. P. T. Greenlees, Ph.D. thesis, University of Liverpool (1999).

21. J. Bardeen, L. N. Cooper, and J. R. Schreifer, Phys. Rev. **108**, 1175 (1957).

22. A. Bohr, B. R. Mottelson, and D. Pines, Phys. Rev **110**, 936 (1958).

23. R. F. Casten, *Nuclear Structure from a Simple Perspective* (Oxford University Press, Oxford, 1990).

24. B. R. Mottelson and J. G. Valatin, Phys. Rev. Lett. **5**, 511 (1960).

25. R. Bengtsson and S. Frauendorf, Nucl. Phys. A **327**, 139 (1979).

26. D. R. Inglis, Phys. Rev. **96**, 1059 (1954).

27. R. Bengtsson and J. y. Zhang, Phys. Lett. B **135**, 358 (1984).

28. A. Johnson, H. Ryde, and J. Sztarkier, Phys. Lett. B **34**, 605 (1971).

29. F. S. Stephens and R. S. Simon, Nucl. Phys. A **183**, 257 (1972).

30. S. G. Nilsson, C. F. Tsang, A. Sobiczewski, Z. Szymański, S. Wycech, G. Gustafsson, I. L. Lamm, P. Möller, and B. Nilsson, Nucl. Phys. A **131**, 1 (1969).

31. G. Hackman, T. L. Khoo, M. P. Carpenter, T. Lauritsen, A. Lopez-Martens, I. J. Calderin, R. V. F. Janssens, D. Ackermann, I. Ahmad, S. Agarwala, et al., Phys. Rev. Lett. **79**, 4100 (1997).

32. B. Olaniyi, A. Shor, S. C. Cheng, G. Dugan, and C. S. Wu, Nucl. Phys. A **403**, 572 (1983).

33. R. V. Jolos, P. von Brentano, A. Dewald, and N. Pietralla, Phys. Rev. C **72**, 024310 (2005).

34. J. M. Blatt and V. F. Weisskopf, *Theoretical Nuclear Physics* (Wiley, New York, 1952).

35. K. Alder, A. Bohr, T. Huus, B. Mottelson, and A. Winther, Rev. Mod. Phys. **28**, 432 (1956).

36. J. Cerny, ed., *Nuclear spectroscopy and reactions*, vol. Part C (Academic Press, New York, 1974).

37. S. Cohen, F. Plasil, and W. J. Swiatecki, Ann. Phys. **82**, 557 (1974).

38. N. Bohr, Nature **344**, 137 (1936).

39. H. Amro, Ph.D. thesis, North Carolina State University (1999).

40. J. M. Alexander and G. N. Simonoff, Phys. Rev. **133**, 93 (1964).

41. D. Ward, H. R. Andrews, G. C. Ball, A. Galindo-Uribarri, V. P. Janzen, T. Nakatsukasa, D. C. Radford, T. E. Dreake, J. DeGraaf, and Y. R. Shimizu, Nucl. Phys. A **600**, 88 (1996).

42. G. Hackman, R. V. F. Janssens, T. L. Khoo, I. Ahmad, J. P. Greene, H. Amro, D. Ackermann, M. P. Carpenter, S. M. Fischer, T. Lauritsen, et al., Phys. Rev. C **57**, R1056 (1998).

43. I. Wiedenhöver, R. V. F. Janssens, G. Hackman, I. Ahmad, J. P. Greene, H. Amro, P. K. Bhattacharyya, M. P. Carpenter, P. Chowdhury, J. Cizewski, et al., Phys. Rev. Lett. **83**, 2143 (1999).

44. K. A. Saleem, R. V. F. Janssens, M. P. Carpenter, F. G. Kondev, I. Wiedenhover, I. Ahmad, J. Caggiano, P. Chowdhury, J. A. Cizewski, D. Cline, et al., Phys. Rev. C **70**, 024310 (2004).

45. W. R. Leo, *Techniques for Nuclear and Particle Physics Experiments* (Springer-Verlag, Berlin, 1993).

46. R. H. Pehl and F. S. Goulding, Nucl. Instr. Meth. **81**, 329 (1970).

47. M. Riley, ed., *GAMMASPHERE, The Begining. . . 1993-1997* (GAMMASPHERE, 1998).

48. R. V. F. Janssens and F. S. Stephens, Nucl. Phys. News **6**, 9 (1996).

49. A. M. Baxter, T. L. Khoo, M. E. Bleich, M. P. Carpenter, I. Ahmad, R. V. F. Janssens, E. F. Moore, I. G. Bearden, J. R. Beene, and I. Y. Lee, Nucl. Instr. And Meth. A **317**, 101 (1992).

50. D. Nisius, Ph.D. thesis, Purdue University (1996).

51. J. F. Ziegler, J. P. Biersack, and U. Littmark, *The stopping and Range of Ions in Solids* (Pergamon, New York, 1985).

52. P. R. Bevington and D. K. Robinson, *Data Reduction and Error Analysis for the Physical Sciences* (McGraw-Hill, New York, 1992).

53. D. C. Radford, Nucl. Instr. And Meth. A **361**, 297 (1995).

54. D. C. Radford, ed., *Proceedings of the International Conference on the Frontier of Nuclear Spectroscopy* (World Scientific, Singapore, 1992).

55. M. Cromaz, T. J. M. Symons, G. J. Lane, I. Y. Lee, and R. W. MacLeod, Nucl. Instr. And Meth. A **462**, 519 (2001).

56. D. C. Radford, Nucl. Instr. And Meth. A **361**, 306 (1995).

57. K. Starosta, D. B. Fossan, T. Koike, C. Vaman, D. C. Radford, and C. J. Chiara, Nucl. Instr. And Meth. A **515**, 771 (2003).

58. D. C. Radford, `http://radware.phy.ornl.gov`.

59. B. Singh and J. C. Waddington, `http://www.nndc.bnl.gov/nndc/evalcorner/hijpi.pdf`.

60. J. Dudek, *Superdeformed Nuclear Shapes: New Features, Systematics and Predictions* (CRN preprint, Strasbourg, 1987).

61. W. Nazarewicz, G. A. Leander, and J. Dudek, Nucl. Phys. A **467**, 437 (1987).

62. R. Bengtsson, `http://www.matfys.lth.se/~ragnar/TSD-defsyst.html`.

63. G. Schönwaßer, H. Hübel, G. B. Hagemann, P. Bednarczyk, G. Benzoni, A. Bracco, P. Bringel, R. Chapman, D. Curien, J. Domscheit, et al., Phys. Lett. B **552**, 9 (2003).

64. S. Frauendorf, Rev. Mod. Phys. **73**, 463 (2001).

65. S. Frauendorf and J. Meng, Nucl. Phys. A **617**, 131 (1997).

66. S. Frauendorf and J. Meng, Z. Phys. A **356**, 263 (1997).

67. C. Vaman, D. B. Fossan, T. Koike, K. Starosta, I. Y. Lee, and A. O. Macchiavelli, Phys. Rev. Lett. **92**, 032501 (2004).

68. J. Timár, C. Vaman, K. Starosta, D. B. Fossan, T. Koike, D. Sohler, I. Y. Lee, and A. O. Macchiavelli, Phys. Rev. C **73**, 011301 (2006).

69. J. A. Alcántara-Núñez, J. R. B. Oliveira, E. W. Cybulska, N. H. Medina, M. N. Rao, R. V. Ribas, M. A. Rizzutto, W. A. Seale, F. Falla-Sotelo, K. T. Wiedemann, et al., Phys. Rev. C **69**, 024317 (2004).

70. T. Koike, K. Starosta, C. J. Chiara, D. B. Fossan, and D. R. LaFosse, Phys. Rev. C **67**, 044319 (2003).

71. K. Starosta, T. Koike, C. J. Chiara, D. B. Fossan, D. R. LaFosse, A. A. Hecht, C. W. Beausang, M. A. Caprio, J. R. Cooper, R. Krücken, et al., Phys. Rev. Lett. **86**, 971 (2001).

72. S. Zhu, U. Garg, B. K. Nayak, S. S. Ghugre, N. S. Pattabiraman, D. B. Fossan, T. Koike, K. Starosta, C. Vaman, R. V. F. Janssens, et al., Phys. Rev. Lett. **91**, 132501 (2003).

73. W. Schmitz, C. X. Yang, H. Hübel, A. P. Byrne, R. Müsseler, N. Singh, K. H. Maier, A. Kuhnert, and R. Wyss, Nucl. Phys. A **539**, 112 (1992).

74. W. Schmitz, H. Hübel, C. X. Yang, G. Baldsiefen, U. Birkental, G. Fröhlingsdorf, D. Mehta, R. Müßeler, M. Neffgen, P. Willsau, et al., Phys. Lett. B **303**, 230 (1993).

75. H. Schnack-Petersen, R. Bengtsson, R. A. Bark, P. Bosetti, A. Brockstedt, H. Carlsson, L. P. Ekström, G. B. Hagemann, B. Herskind, F. Ingebretsen, et al., Nucl. Phys. A **594**, 175 (1995).

76. P. Bringel, H. Hübel, H. Amro, M. Axiotis, D. Bazzacco, S. Bhattacharya, R. Bhowmik, J. Domscheit, G. B. Hagemann, D. R. Jensen, et al., Eur. Phys. J. A **16**, 155 (2003).

77. S. W. Ødegård, G. B. Hagemann, D. R. Jensen, M. Bergström, B. Herskind, G. Sletten, S. Törmänen, J. N. Wilson, P. O. Tjøm, I. Hamamoto, et al., Phys. Rev. Lett. **86**, 5866 (2001).

78. D. R. Jensen, G. B. Hagemann, I. Hamamoto, S. W. Ødegård, M. Bergström, B. Herskind, G. Sletten, S. Törmänen, J. N. Wilson, P. O. Tjøm, et al., Nuclear Physics A **703**, 3 (2002).

79. D. R. Jensen, G. B. Hagemann, I. Hamamoto, S. W. Ødegård, B. Herskind, G. Sletten, J. N. Wilson, K. Spohr, H. Hübel, P. Bringel, et al., Phys. Rev. Lett. **89**, 142503 (2002).

80. S. Törmänen, S. W. Ødegård, G. B. Hagemann, A. Harsmann, M. Bergström, R. A. Bark, B. Herskind, G. Sletten, P. O. Tjøm, A. Görgen, et al., Phys. Lett. B **454**, 8 (1999).

81. H. Amro, W. C. Ma, G. B. Hagemann, R. M. Diamond, J. Domscheit, P. Fallon, A. Görgen, B. Herskind, H. Hübel, D. R. Jensen, et al., Phys. Lett. B **553**, 197 (2003).

82. H. Amro, P. G. Varmette, W. C. Ma, B. Herskind, G. B. Hagemann, G. Sletten, R. V. F. Janssens, M. Bergström, A. Bracco, M. Carpenter, et al., Phys. Lett. B **506**, 39 (2001).

83. A. Neußer, H. Hübel, G. B. Hagemann, S. Bhattacharya, P. Bringel, D. Curien, O. Dorvaux, J. Domscheit, F. Hannachi, D. R. Jensen, et al., Eur. Phys. J. A **15**, 439 (2002).

84. M. K. Djongolov, D. J. Hartley, L. L. Riedinger, F. G. Kondev, R. V. F. Janssens, K. A. Saleem, I. Ahmad, D. L. Balabanski, M. P. Carpenter, P. Chowdhury, et al., Phys. Lett. B **560**, 24 (2003).

85. D. J. Hartley, M. K. Djongolov, L. L. Riedinger, G. B. Hagemann, R. V. F. Janssens, F. G. Kondev, E. F. Moore, M. A. Riley, A. Aguilar, C. R. Bingham, et al., Phys. Lett. B **608**, 31 (2005).

86. T. Bengtsson, Nucl. Phys. A **496**, 56 (1989).

87. T. Bengtsson, Nucl. Phys. A **512**, 124 (1990).

88. S. Åberg, Nucl. Phys. A **520**, 35 (1990).

89. P. Bringel, G. B. Hagemann, H. Hübel, A. Al-khatib, P. Bednarczyk, A. Bürger, D. Curien, G. Gangopadhyay, B. Herskind, D. R. Jensen, et al., Eur. Phys. J. A **24**, 167 (2005).

90. G. B. Hagemann and I. Hamamoto, Nucl. Phys. News **13**, 20 (2003).

91. M. S. Fetea and R. F. Fetea, Nucl. Phys. A **690**, 239 (2001).

92. D. G. Roux, M. S. Fetea, E. Gueorguieva, B. R. S. Babu, R. T. Newman, J. J. Lawrie, R. Fearick, D. G. Aschman, R. Beetge, M. Benatar, et al., Phys. Rev. C **63**, 024303 (2001).

93. N. S. Pattabiraman, Y. Gu, S. Frauendorf, U. Garg, T. Li, B. K. Nayak, X. Wang, S. Zhu, S. S. Ghugre, R. V. F. Janssens, et al., Phys. Lett. B **647**, 243 (2007).

94. H. J. Jensen, G. B. Hagemann, P. O. Tjøm, S. Frauendorf, A. Atac, M. Bergström, A. Bracco, A. Brockstedt, H. Carlsson, P. Ekström, et al., Z. Phys. A **340**, 351 (1991).

95. T. Bengtsson and I. Ragnarsson, Phys. Scr. **T5**, 165 (1983).

96. T. Bengtsson and I. Ragnarsson, Nucl. Phys. A **436**, 14 (1985).

97. A. V. Afanasjev, D. B. Fossan, G. J. Lane, and I. Ragnarsson, Phys. Rep. **322**, 1 (1999).

98. S. Frauendorf, Nucl. Phys. A **557**, 259 (1993).

99. S. Frauendorf, Nucl. Phys. A **677**, 115 (2000).

100. R. Bengtsson and H. Ryde, Eur. Phys. J. A **22**, 355 (2004).

101. X. Wang, R. V. F. Janssens, E. F. Moore, U. Garg, Y. Gu, S. Frauendorf, M. P. Carpenter, S. S. Ghugre, N. J. Hammond, T. Lauritsen, et al., Phys. Rev. C **75**, 064315 (2007).

102. I. Hamamoto, Phys. Lett. B **193**, 399 (1987).

103. G. D. Alkhazov, A. E. Barzakh, I. Y. Chubukov, V. P. Denisov, V. S. Ivanov, N. B. Buyanov, V. N. Fedoseyev, V. S. Letokhov, V. I. Mishin, and S. K. Sekatsky, Nucl. Phys. A **504**, 549 (1989).

104. C. J. Batty, S. F. Biagi, R. A. J. Riddle, B. L. Roberts, G. J. Pyle, G. T. A. Squier, D. M. Asbury, and A. S. Clough, Nucl. Phys. A **355**, 383 (1981).

105. R. J. Powers, F. Boehm, P. Vogel, A. Zehnder, T. King, A. R. Kunselman, P. Roberson, P. Martin, G. H. Miller, R. E. Welsh, et al., Nucl. Phys. A **262**, 493 (1976).

106. G. Schönwaßer, H. Hübel, G. B. Hagemann, J. Domscheit, A. Görgen, B. Herskind, G. Sletten, J. N. Wilson, D. R. Napoli, C. Rossi-Alvarez, et al., Eur. Phys. J. A **13**, 291 (2002).

107. G. Schönwaßer, H. Hübel, G. B. Hagemann, H. Amro, R. M. Clark, M. Cromaz, R. M. Diamond, P. Fallon, B. Herskind, G. Lane, et al., Eur. Phys. J. A **15**, 435 (2002).

108. A. Görgen, R. M. Clark, M. Cromaz, P. Fallon, G. B. Hagemann, H. Hübel, I. Y. Lee, A. O. Macchiavelli, G. Sletten, D. Ward, et al., Phys. Rev. C **69**, 031301 (2004).

109. G. Güdal, H. Amro, C. W. Beausang, D. S. Brenner, M. P. Carpenter, R. F. Casten, C. Engelhardt, G. B. Hagemann, C. R. Hansen, D. J. Hartley, et al., J. Phys. G **31**, S1873 (2005).

110. F. Asaro, F. S. Stephens, and I. Perlman, Phys. Rev. **92**, 1495 (1953).

111. F. S. Stephens, F. Asaro, and I. Perlman, Phys. Rev. **96**, 1568 (1954).

112. F. S. Stephens, F. Asaro, and I. Perlman, Phys. Rev. **100**, 1543 (1955).

113. K. Lee and D. Inglis, Phys. Rev. **108**, 774 (1957).

114. I. Ahmad and P. Butler, Annu. Rev. Nucl. Part. Sci. **43**, 71 (1993).

115. R. R. Chasman, Phys. Rev. Lett. **42**, 630 (1979).

116. R. R. Chasman, Phys. Lett. B **96**, 7 (1980).

117. P. A. Butler and W. Nazarewicz, Rev. Mod. Phys. **68**, 349 (1996).

118. S. G. Rohoziński, J. Phys. G **16**, L173 (1990).

119. R. R. Chasman, Phys. Lett. B **175**, 254 (1986).

120. A. Sobiczewski, Nucl. Phys. A **485**, 16 (1988).

121. R. R. Chasman, *Nuclear Structure, Reactions and Symmetries* (World Scientific, Singapore, 1986).

122. K. Neergård and P. Vogel, Nucl. Phys. A **149**, 209 (1970).

123. K. Neergård and P. Vogel, Nucl. Phys. A **149**, 217 (1970).

124. E. R. Marshalek, Nucl. Phys. A **266**, 317 (1976).

125. S. Mizutori, Y. R. Shimizu, and K. Matsuyanagi, Prog. Theor. Phys. **86**, 131 (1991).

126. H. Sakamoto and T. Kishimoto, Nucl. Phys. A **501**, 205 (1989).

127. P. Ring and P. Schuck, *The Nuclear Many-Body Problem* (Springer, 1990).

128. J. Fernández-Niello, H. Puchta, F. Riess, and W. Trautmann, Nucl. Phys. A **391**, 221 (1982).

129. D. Ward, G. D. Dracoulis, J. R. Leigh, R. J. Charity, D. J. Hinde, and J. O. Newton, Nucl. Phys. A **406**, 591 (1983).

130. W. Bonin, M. Dahlinger, S. Glienke, E. Kankeleit, M. Krämer, D. Habs, B. Schwartz, and H. Backe, Z. Phys. A **310**, 249 (1983).

131. D. R. Zolnowski, T. Kishimoto, Y. Gono, and T. T. Sugihara, Phys. Lett. B **55**, 453 (1975).

132. Z. Sujkowski, D. Chmielewska, M. J. A. D. Voigt, J. F. W. Jansen, and O. Scholten, Nucl. Phys. A **291**, 365 (1977).

133. P. Schuler, C. Lauterbach, Y. K. Agarwal, J. D. Boer, K. P. Blume, P. A. Butler, K. Euler, C. Fleischmann, C. Gunther, E. Hauber, et al., Phys. Lett. B **174**, 241 (1986).

134. B. Ackermann, H. Baltzer, C. Ensel, K. Freitag, V. Grafen, C. Gunther, P. Herzog, J. Manns, M. Marten-Tolle, U. Muller, et al., Nucl. Phys. A **559**, 61 (1993).

135. P. D. Cottle, M. Gai, J. F. Ennis, J. F. S. Jr., D. A. Bromley, C. W. Beausang, L. Hildingsson, W. F. Piel, D. B. Fossan, J. W. Olness, et al., Phys. Rev. C **33**, 1855 (1986).

136. M. E. Debray, J. Davidson, M. Davidson, A. J. Kreiner, D. Hojman, D. Santos, K. Ahn, D. B. Fossan, Y. Liang, R. Ma, et al., Phys. Rev. C **41**, R1895 (1990).

137. A. Bohr and B. R. Mottelson, Nucl. Phys. **4**, 529 (1957).

138. A. Bohr and B. R. Mottelson, Nucl. Phys. **9**, 687 (1958).

139. V. M. Strutinsky, At. Energ. **4**, 150 (1956).

140. S. Zhu, R. V. F. Janssens, G. J. Lane, I. Wiedenhover, M. P. Carpenter, I. Ahmad, A. P. Byrne, P. Chowdhury, D. Cline, A. N. Deacon, et al., Phys. Lett. B **618**, 51 (2005).

141. M. Dahlinger, E. Kankeleit, D. Habs, D. Schwalm, B. Schwartz, R. S. Simon, J. D. Burrows, and P. A. Butler, Nucl. Phys. A **484**, 337 (1988).

142. R. K. Sheline, J. Kvasil, C. F. Liang, and P. Paris, Phys. Rev. C **44**, R1732 (1991).

143. A. L. Goodman, Nucl. Phys. A **230**, 466 (1974).

144. S. Frauendorf and V. V. Pashkevich, Phys. Lett. B **141**, 23 (1984).

145. W. Nazarewicz, P. Olanders, I. Ragnarsson, J. Dudek, and G. A. Leander, Phys. Rev. Lett. **52**, 1272 (1984).

146. J. F. C. Cocks, P. A. Butler, K. J. Cann, P. T. Greenlees, G. D. Jones, S. Asztalos, P. Bhattacharyya, R. Broda, R. M. Clark, M. A. Deleplanque, et al., Phys. Rev. Lett. **78**, 2920 (1997).

147. J. F. C. Cocks, D. Hawcroft, N. Amzal, P. A. Butler, K. J. Cann, P. T. Greenlees, G. D. Jones, S. Asztalos, R. M. Clark, M. A. Deleplanque, et al., Nucl. Phys. A **645**, 61 (1999).

148. R. K. Sheline, Phys. Lett. B **197**, 500 (1987).

149. J. D. Burrows, P. A. Butler, K. A. Connell, A. N. James, G. D. Jones, A. M. Y. El-Lawindy, T. P. Morrison, J. Simpson, and R. Wadsworth, J. Phys. G **10**, 1449 (1984).

150. P. D. Cottle, J. F. Shriner, F. Dellagiacoma, J. F. Ennis, M. Gai, D. A. Bromley, J. W. Olness, E. K. Warburton, L. Hildingsson, M. A. Quader, et al., Phys. Rev. C **30**, 1768 (1984).

151. N. Schulz, V. R. Vanin, M. Aïche, C. Briançon, A. Chevallier, J. Chevallier, M. E. Debray, A. J. Kreiner, E. Ruchowska, and J. C. Sens, Z. Phys. A **335**, 107 (1990).

152. N. Schulz, V. R. Vanin, A. J. Kreiner, E. Ruchowska, M. Aïche, C. Briançon, A. Chevallier, J. Chevallier, M. E. Debray, and J. C. Sens, Z. Phys. A **339**, 325 (1991).

153. J. Fernández-Niello, C. Mittag, F. Riess, E. Ruchowska, and M. Stallknecht, Nucl. Phys. A **531**, 164 (1991).

154. T. Ishii, S. Shigematsu, M. Asai, A. Makishima, M. Matsuda, J. Kaneko, I. Hossain, S. Ichikawa, T. Kohno, and M. Ogawa, Phys. Rev. C **72**, 021301(R) (2005).

155. R. V. Jolos and P. von Brentano, Phys. Rev. C **49**, R2301 (1994).

156. R. V. Jolos and P. von Brentano, Nucl. Phys. A **587**, 377 (1995).

157. R. K. Sheline and M. A. Riley, Phys. Rev. C **61**, 057301 (2000).

158. H.-C. Hseuh, E.-M. Franz, P. E. Haustein, S. Katcoff, and L. K. Peker, Phys. Rev. C **23**, 1217 (1981).

159. P. P. Parekh, L. K. Peker, S. Katcoff, and E. M. Franz, Phys. Rev. C **26**, 2178 (1982).

160. K. Hardt, P. Schüler, C. Günther, J. Recht, and K. P. Blume, Nuclear Physics A **407**, 127 (1983).

161. W. Spreng, F. Azgui, H. Emling, E. Grosse, R. Kulessa, C. Michel, D. Schwalm, R. S. Simon, H. J. Wollersheim, M. Mutterer, et al., Phys. Rev. Lett. **51**, 1522 (1983).

162. D. Cline, Acta Phys. Pol. B **30**, 1291 (1999).

163. T. Elze and J. R. Huizenga, Nucl. Phys. A **187**, 545 (1972).

164. P. E. Haustein, H. C. Hseuh, R. L. Klobuchar, E. M. Franz, S. Katcoff, and L. K. Peker, Phys. Rev. C **19**, 2332 (1979).

165. J. V. Maher, J. R. Erskine, A. M. Friedman, J. P. Schiffer, and R. H. Siemssen, Phys. Rev. Lett. **25**, 302 (1970).

166. J. V. Maher, J. R. Erskine, A. M. Friedman, R. H. Siemssen, and J. P. Schiffer, Phys. Rev. C **5**, 1380 (1972).

167. Y. A. Akovali, `http://www.nndc.bnl.gov`.

168. M. A. Stoyer, Ph.D. thesis, University of California, Berkeley (1990).

169. M. Devlin, D. Cline, K. G. Helmer, R. Ibbotson, C. Y. Wu, P. A. Butler, A. J. Cresswell, G. D. Jones, M. A. Stoyer, and J. O. Rasmussen, Phys. Rev. C **47**, 2178 (1993).

170. F.Asaro and I.Perlman, UCRL **9566**, 50 (1960).

171. S. Bjørnholm, M. Lederer, F. Asaro, and I. Perlman, Phys. Rev. **130**, 2000 (1963).

172. B. Bengtson, J. Jensen, M. Moszynski, and H. L. Nielsen, Nucl. Phys. A **159**, 249 (1970).

173. A.Lorenz, IAEA Tech.Rept.Ser. p. No.261 (1986).

174. I. Wiedenhöver, R. V. F. Janssens, G. Hackman, I. Ahmad, J. P. Greene, H. Amro, M. P. Carpenter, D. T. Nisius, P. Reiter, T. Lauritsen, et al., in *Proceedings of the International Conference on Nuclear Structure '98, Gatlinburg, TN*, AIP Conf. Proc. (AIP, New York, 1999), pp. No.481, p. 527.

175. K. A. Saleem, R. V. F. Janssens, M. P. Carpenter, F. G. Kondev, I. Wiedenhover, I. Ahmad, J. Caggiano, P. Chowdhury, J. A. Cizewski, D. Cline, et al., Phys. Rev. C **70**, 024310 (2004).

176. J. Dudek, W. Nazarewicz, and Z. Szymański, Phys. Rev. C **26**, 1708 (1982).

177. J. Dudek, W. Nazarewicz, and Z. Szymanski, Phys. Scr. **T5**, 171 (1983).

178. J. F. Smith, J. F. C. Cocks, N. Schulz, M. Aïche, M. Bentaleb, P. A. Butler, F. Hannachi, G. D. Jones, P. M. Jones, R. Julin, et al., Phys. Rev. Lett. **75**, 1050 (1995).

179. C. E. Bemis, F. K. McGowan, J. L. C. Ford, W. T. Milner, P. H. Stelson, and R. L. Robinson, Phys. Rev. C **8**, 1466 (1973).

180. J. M. Hoogduin, E. Ditzel, A. Balanda, F. W. N. de Boer, H. Bokemeyer, J. Gerl, K. Heyde, J. van Klinken, A. Krasznahorkay, P. Salabura, et al., Phys. Lett. B **384**, 43 (1996).

181. A. S. Davydov and V. S. Rostovsky, Nucl. Phys. **60**, 529 (1964).

182. S. Frauendorf, arXiv:0709.0216v2 [nucl-th].